CORRELATIONS OF MICROSTRUCTURAL FEATURES BETWEEN NEUTRON AND SELF-ION IRRADIATED MA957

A Dissertation

by

JING WANG

Submitted to the Office of Graduate and Professional Studies of
Texas A&M University
in partial fulfillment of the requirements for the degree of

DOCTOR OF PHILOSOPHY

Chair of Committee,	Lin Shao
Committee Members,	Michael Demkowicz
	Sean McDeavitt
	Pavel Tsvetkov
Head of Department,	Ibrahim Karaman

August 2017

Major Subject: Materials Science and Engineering

ABSTRACT

Nuclear energy is a sustainable, efficient, carbon-neutral energy source to meet the ever-increasing global energy demands. Some current advanced reactor concepts require reactor core components, such as fuel cladding and ducts, to withstand up to 300–500 dpa neutron irradiation. Achieving such a dose level in test reactors would require years or even decades of radiation, which makes reactor irradiation impractical for materials development and testing. As an alternative approach to study high-dose irradiation effects in materials, ion irradiation techniques are regaining popularity due to their high damage production rate. To date, the correspondence between neutron and ion irradiation is still being investigated, and correlations of microstructural features between neutron and ion irradiated materials are still not well understood.

As a means to understand these correlations, the microstructures of neutron- and ion-irradiated steel alloy MA957 were examined and compared. This material was selected due to its high relevance to high-dose applications. The characterization relies heavily on atom probe tomography (APT). The results show that YTiO oxide particles in MA957 followed similar trends with irradiation temperature after neutron and ion irradiation but size and number density were not identical. The presence of alpha-prime phase has been confirmed at lower irradiation temperatures in both neutron and ion irradiations. Assessing effects on grain boundary segregation after ion irradiation is more challenging. Thus, only qualitative comparisons of segregation of Cr, Ti, and TiO were conducted between neutron and ion irradiation.

Rate theory calculations were carried out to investigate precipitate stability. The defect balance equation and precipitate stability models were reanalyzed using materials-specific and experiment-specific parameters. Precipitate nucleation was not included in the analysis, and so size change is more readily predicted with this model than number density change. Predicted results of particle stability were found to be in good agreement with our experimental results. The ratio of diffusivity to dose rate was identified as a

probable measure to determine whether application of temperature shift is necessary for reproducing microstructural evolution in ion irradiation. The dose rate dependence has been reanalyzed and temperature ranges where precipitate growth is independent of dose rate have been identified for future investigations.

DEDICATION

To my wife, Jia Liu, and to my family for their support.

ACKNOWLEDGEMENTS

I would like to thank my committee chair, Dr. Lin Shao, for his support and direction since I entered graduate school. His passion and hard-working spirit have always been a model for me to follow. He encourages me and others to find our own research interests and always gives us freedom to explore new ideas. His advice and help have been invaluable to my development as a researcher and in many aspects of life.

I would like to thank my mentor at Pacific Northwest National Laboratory, Dr. Mychailo B. Toloczko, for his financial support and his guidance that helped me quickly navigate and gain expertise in this dissertation topic during the past two and a half years. His meticulous and rigorous attitude towards research has set an example for me to follow.

I would like to thank Dr. Frank A. Garner for his patience, guidance, and encouragement. His knowledge and insights in the nuclear materials field are always educational and inspiring. His help and advice are not only beneficial in academics but also in other aspects like communication, presentation, professionalism, and writing. I would also like to thank Dr. Daniel Schreiber, who trained and led me into the field of atom probe tomography (APT). His expertise is admirable and his encouragement inspires me to keep pursuing better data analysis techniques for APT.

I would like to thank our collaborators at the Kharkov Institute of Physics for performing ion irradiation, and Dr. Nathan Bailey at the University of California, Berkeley, for providing some APT datasets. Thanks also go to Dr. Alicia Certain who characterized and analyzed some specimens before me, and Maura Zimmerschied for technical editing.

I would like to thank my committee members, Dr. Michael Demkowicz, Dr. Sean McDeavitt, and Dr. Pavel Tsvetkov, for providing their guidance, advice, and support and for broadening my knowledge throughout the course of this research.

Thanks also go to my friends and colleagues, Dr. Di Chen, Dr. Tianyi Chen, Jonathan Gigax, Hyosim Kim, Mrs. Xuemei Wang, and the department faculty and staff for helping me and making my time at Texas A&M University a great experience. I am also grateful for many wonderful friends and colleagues at Pacific Northwest National Laboratory.

Finally, thanks to my mother and father for their encouragement and to my wife for her patience and love.

CONTRIBUTORS AND FUNDING SOURCES

Contributors

This work was supervised by a dissertation committee consisting of Professors Lin Shao, Sean McDeavitt and Pavel Tsvetkov of the Department of Nuclear Engineering and Professor Michael Demkowicz of the Department of Materials Science and Engineering.

All ion irradiation experiments were carried out at the Kharkov Institute of Physics by our collaborators. Some APT raw datasets for neutron irradiated MA957 were provided by Dr. Nathan Bailey at the University of California, Berkeley. Several APT raw datasets about unirradiated MA957 were provided by Dr. Alicia Certain.

All work for the dissertation was completed by the student, under supervision of Dr. Mychailo B. Toloczko of Pacific Northwest National Laboratory.

Funding Sources

Graduate study was partially supported by fellowships from the Department of Materials Science and Engineering at Texas A&M University.

This work was made possible in part by the Fuel Cycle R&D Program Core Materials research area sponsored by the U.S. Department of Energy, Office of Nuclear Energy under Contract DE-AC06-76RLO 1830.

Microstructural characterizations in this research were supported by Environmental Molecular Science Laboratory through user proposal numbers 48665, 49117 and 49582.

Its contents are solely the responsibility of the authors and do not necessarily represent the official views of the U.S. Department of Energy, Office of Nuclear Energy.

NOMENCLATURE

α'	Alpha prime, a second phase particle
14YWT	a 14Cr nanostructured ferritic alloy with oxide dispersion
APT	Atom Probe Tomography
BCC	Body Centered Cubic
BR2	Belgian Reactor 2 (Mol. Belgium)
CEA	Commissariat à l'Énergie Atomique et aux Énergies Alternatives, the French Alternative Energies and Atomic Energy Commission
DFR	Bounreay Fast Reactor (United Kingdom)
dpa	Displacements Per Atom
EBR-II	Experimental Breeder Reactor II (Idaho)
EDM	Electric Discharge Machining
EDS	Energy Dispersive Spectroscopy
EFTEM	Energy filtered transmission electron microscopy
EMSL	Environmental and Molecular Science Laboratory (at PNNL)
EV	a heat of ODS ferritic alloy MA957
FCRD	Fuel Cycle Research and Development (Program)
FFTF	Fast Flux Test Facility (Hanford, Washington)
FIB	Focused Ion Beam
F/M	Ferritic/Martensitic
G-phases	Ni-Mn-Si-enriched precipitate
GB	Grain Boundary
GFR	Gas Fast Reactor
HIP	Hot Isotropic Pressing
HRTEM	High Resolution Transmission Electron Microscopy
HT-9	a Ferritic/Martensitic steel alloyed with Cr, Mo, V and W
HV	High-Voltage

INCO	International Nickel Company
IVAS	Integrated Visualization and Analysis Software
JANNuS	Joint Accelerators for Nano-science and Nuclear Simulation
JOYO	a sodium-cooled fast reactor located at Oarai, Japan.
K-S	Kolmogorov-Smirnov (test)
KIPT	Kharkov Institute of Physics and Technology
KP	Kinchin-Pease
LEAP	Local Electrode Atom Probe
LMFBR	Liquid Metal Fast Breeder Reactor
MA957	a 14Cr ferritic alloy strengthened by oxide dispersion
MOTA	Materials Open Test Assembly irradiation vehicle used in FFTF
NHM	Nelson, Hudson, Mazey model for precipitate evolution
NRT	Norgett, Robinson, and Torrens (model)
ODS alloy	Oxide Dispersion Strengthened alloy
ORNL	Oak Ridge National Laboratory
Phenix	a sodium-cooled fast breeder reactor at Marcoule, France
PKA	Primary Knock-on Atom
PNNL	Pacific Northwest National Laboratory
RED	Radiation Enhanced Diffusion
RIP	Radiation Induced Precipitation
RIS	Radiation Induced Segregation
SCWR	Supercritical Water Reactor
SEM	Scanning Electron Microscopy
SFR	Sodium-cooled Fast Reactor
SRIM	Stopping Range of Ions in Matter (software)
SRMA	Service de Recherches Métallurgiques Appliquées, Applied Metallurgical Research Service
SS	Stainless Steel
STEM	Scanning Transmission Electron Microscopy

TEM	Transmission Electron Microscopy
TWR	Traveling Wave Reactor
TX	a heat of ODS ferritic alloy MA957
VHTR	Very High Temperature Reactor

TABLE OF CONTENTS

Page

LIST OF FIGURES

Page

LIST OF TABLES

Page

1 INTRODUCTION

Nuclear energy is a sustainable, carbon-neutral source to supply the ever increasing global energy demand. Current developments in advanced reactors have been envisioned for better safety, economics, waste generation and nonproliferation. Reactor core component materials must be able to withstand extreme conditions including high fluence irradiation at high temperatures. Understanding radiation effects in materials for reactor core components is not only because of great scientific interests but also due to crucial technological importance. Figure 1-1 shows a roadmap for structural materials requirement in advanced reactor designs and current reactors [1].

Current requirements for structural materials have been set even higher. For example, core components (cladding and ducts) in sodium-cooled fast reactors (SFRs) must be able to safely operate at 360-650˚C to >200 dpa (displacement per atom). In the traveling-wave reactor (TWR) concept, requirements on core structural materials increased to more than 500 dpa during service [2]. Cladding and ducts in fast reactors are generally metals. The harsh in-reactor environment can adversely affect microstructural evolutions that lead to degradation of physical and mechanical properties [3-6]: e.g., void swelling typically occurs in a temperature range that overlaps with SFR core operation temperatures and can result in change of materials' dimensions; radiation-induced precipitation (RIP) can induce secondary phase formation which may lead to radiation-induced hardening and loss of ductility.

Traditionally, research on radiation effects in reactor core structural materials has been conducted in test reactors. However, there are several serious difficulties with using test reactors for radiation effects research. At one time, high dose neutron irradiations for the purposes of alloy development could be performed in the United States, but such facilities are no longer available. Currently the maximum dpa rate attainable by neutron irradiation is ~18 dpa per year and then only in Russia's BOR-60 fast reactor. The radiation damage cannot be created significantly faster in test reactors than in commercial reactors, which means materials problems may not be discovered far enough

in advance. In addition, characterization of highly radioactive samples is extremely expensive and time consuming.

To facilitate alloy developments for core component applications, interest in using ion irradiation as a surrogate technique to study radiation effects has been renewed. In general, heavy or self-ion irradiation introduce damage orders of magnitude faster than fast neutron irradiation. This testing enables accelerated assessments of radiation responses in testing newly developed materials. However, systematic investigations to evaluate the viability of such surrogate techniques are lacking.

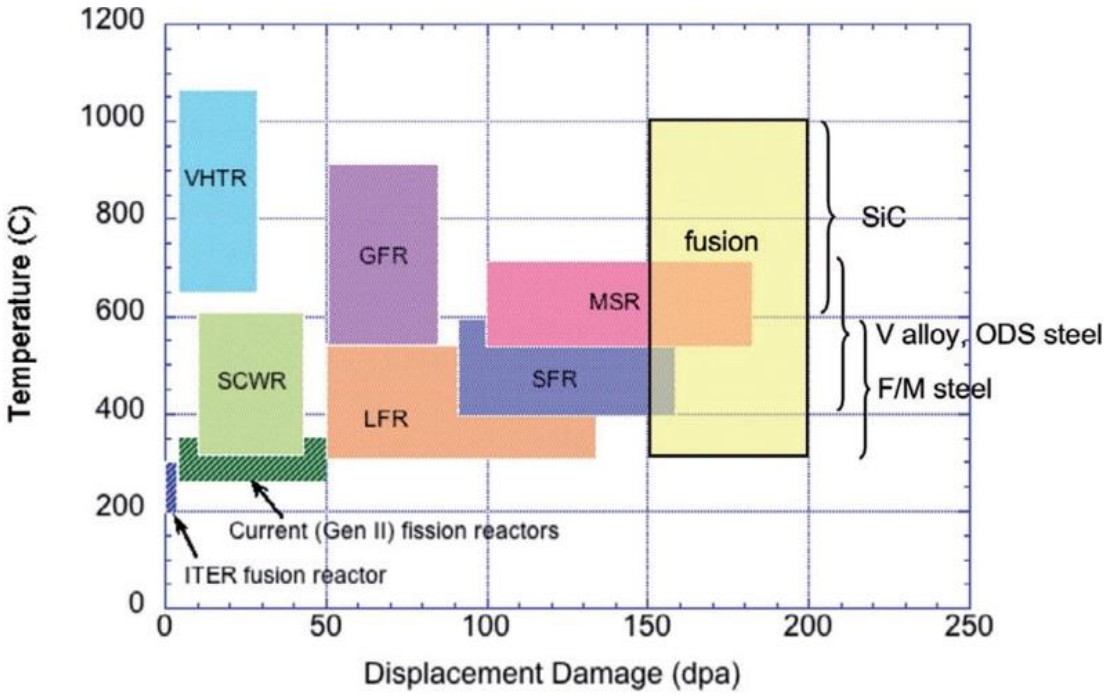

Figure 1-1. Overview of operating temperatures and displacement damage dose regimes for structural materials in current (Generation II) and proposed future (Generation IV) fission and fusion energy systems. The six Gen IV fission systems are Very High Temperature Reactor (VHTR), Super Critical Water Reactor (SCWR), Lead Fast Reactor (LFR), Gas Fast Reactor (GFR), Sodium Fast Reactor (SFR), and Molten Salt Reactor (MSR) [1].

Our ultimate objective is to evaluate the validity of using self-ion irradiations to gain information about neutron irradiation damage in nuclear reactor core structural materials. This dissertation carried out two integral approaches to achieve this goal in an oxide dispersion strengthened (ODS) ferritic alloy MA957:

- First, a systematic investigation was performed on microstructural features of neutron or ion irradiated target materials. For the scope of this study, oxide particles, second phase clusters and grain boundary chemistry were characterized and examined. Microstructural features were then compared and correlated between neutron and ion irradiations. Void swelling is generally minimal in ODS alloys for our irradiation conditions so it was not discussed. Dislocation structures (loops, lines or networks) were not characterized yet due to limited time.
- Second, rate theory calculations were performed in order to understand similarities and differences in observed microstructure, especially for precipitate stability, between neutron and ion irradiations. The concept of temperature shift and dose rate dependence were re-examined using parameters specific to our material and experiment within precipitate stability model frames. Due to complexity in nucleation and grain boundary segregation, they were not included in rate theory calculations yet.

2 BACKGROUND

2.1 Background on Radiation Damage

2.1.1 Overview of Radiation Damage Production

Energetic particles, typically neutrons or ions in our field of study, interact with atoms and incur energy and momentum transfer when traveling through materials. The transfer of kinetic energy to lattice atom creates primary knock-on atoms (PKA). A PKA will be displaced from its lattice site and collide with surrounding lattice atoms, creating subsequent collision events known as damage cascades. A typical illustration of damage cascade is shown in Figure 2-1.

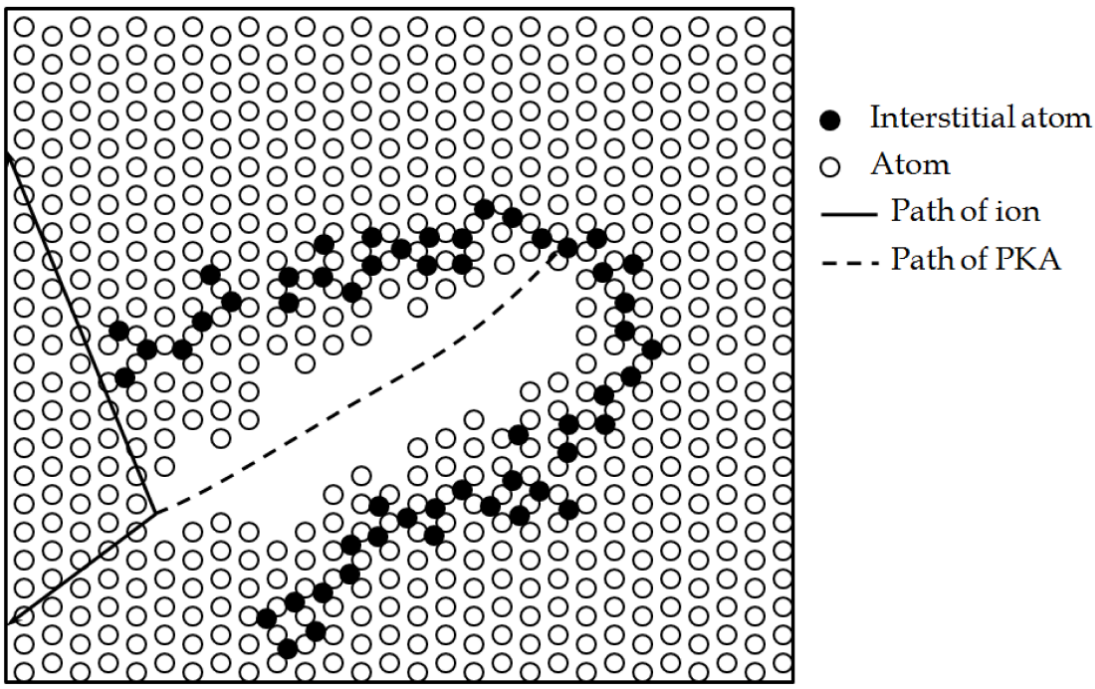

Figure 2-1. An illustration of damage cascade in solid materials [7].

During a damage cascade, some lattice atoms can be displaced to interstitial positions and leave vacancy positions behind; these are called Frenkel pairs. The increased average kinetic energy of atoms in the cascade region is equivalent to an effective high temperature zone. This process is called thermal spike. In a metallic system, a thermal spike is quickly quenched by dissipating thermal energy to lattice and electrons. At slightly longer time scale that defect migration is permitted, the remaining stable defects and some defect clusters will participate in diffusion and reaction. Typical characteristic duration lengths of each process are shown in Figure 2-2.

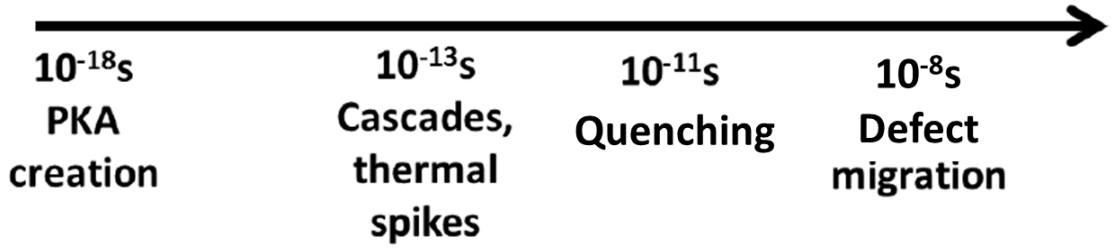

Figure 2-2. Approximate time scale for defect production processes in metallic materials [8].

The radiation damage dose received by materials is typically quantified as displacements per atom (dpa), the average number of displacements that each atom has experienced during irradiation. One simple theoretical method for calculating atomic displacements is the Kinchin-Pease (KP) model [9], which can be described by:

$$\nu(T) = \frac{T}{2E_d} \qquad for \quad 2E_d < T < E_c \tag{2.1}$$

where ν is number of displaced atoms per PKA, T is PKA energy, E_d is displacement threshold energy, and E_c is energy cut-off for energy loss by electron stopping. Figure 2-3 plots the number of displaced atoms based on the KP model. In this model, no displacement would be produced if PKA energy is lower than E_d. When $T < 2E_d$, kinetic energy transferred from PKA to another lattice atom will be smaller than E_d so that no

additional displacement will occur. Number of displacement is predicted to grow linearly with PKA energy for $T \geq 2E_d$.

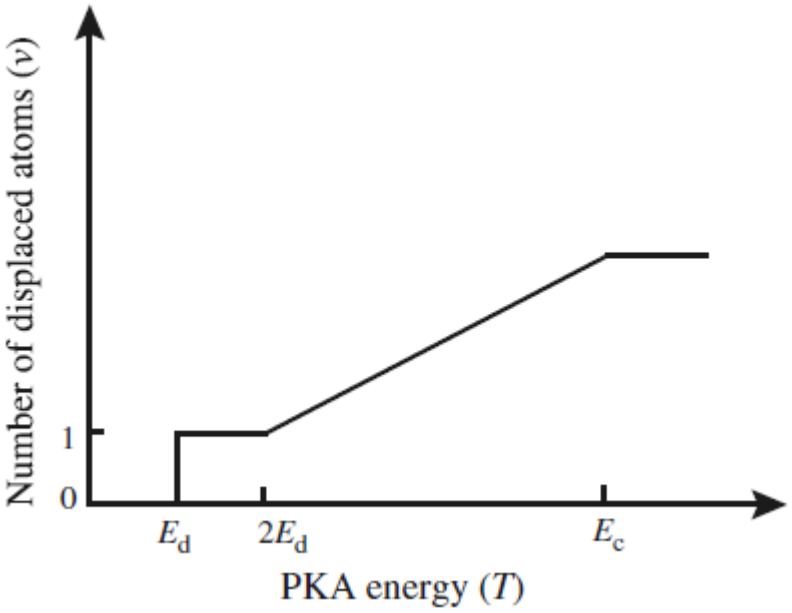

Figure 2-3. Number of displaced atoms as a function of PKA energy according to the Kinchin-Pease Model. E_d is displacement threshold energy and E_c is energy cut-off for energy loss by electron stopping [8].

Several modifications have been suggested for the simple KP model. One model developed by Norgett, Robinson, and Torrens (NRT) later became widely adopted internationally and is still a well-recognized standard for computing displacements per atom [10, 11]. The NRT model can be written as:

$$\nu_{NRT} = \frac{0.8T_d(E_{PKA})}{2E_d} \tag{2.2}$$

where ν_{NRT} is the number of stable Frenkel pairs, $T_d(E_{PKA})$ is the damage energy that represents the elastic portion of the PKA energy dissipated to lattice, and E_d is the displacement threshold energy, which is the minimum energy required to create a stable Frenkel pair. We need to mention that there is no "perfect" or "correct" value for dpa,

because it depends on choice of models. For example, comparing the NRT model with molecular dynamics (MD) simulation, numbers of stable Frenkel pairs differ by multiple times, since the NRT model does not consider in-cascade defect interactions. On the other hand, MD simulation cannot handle electronic energy loss due to lack of proper interatomic interactions for that purpose.

2.1.2 Overview of Defect Reaction and Transport

Stable point defects generated during irradiation may be annihilated to vanish or may agglomerate to form defect clusters. Most point defects vanish either by mutual recombination or by migration to be absorbed at defect sinks. Annihilated defects have little or no effect on material properties. Defects that remain may agglomerate into defect clusters, such as voids and dislocation loops, which could potentially adversely impact materials' properties. At very low irradiation temperature where both vacancy and interstitial diffusion are difficult, ballistic mixing induced by energetic particles becomes a significant driving force for diffusion [12].

In the body-centered cubic (BCC) Fe system, interstitials are more mobile than vacancies at low temperatures ($<0.3T_m$, T_m is melting temperature,) because they have a lower migration energy barrier. In this temperature regime, defect dynamics is controlled by interstitials. Interstitials tend to form dislocation loops or interstitial clusters that cause hardening and embrittlement. Radiation-induced void swelling is less likely in this temperature range due to low mobility of vacancies, which makes void nucleation and growth both difficult.

At intermediate temperatures ($0.3–0.5T_m$), vacancies become mobile and vacancy clusters can nucleate and grow. Radiation-induced precipitation and segregation could occur at these temperatures since vacancies and interstitials have different mobilities. Some defect sinks may be biased for absorbing either vacancies or interstitials and cause a net excess of the other type. Fracture toughness and ductility could be degraded by precipitation and segregation. In an SFR, core components are operated at 360-650°C, a range that spans both low and intermediate temperature ranges. Considering that

radiation damage is received by materials at a rate of ~20–50 dpa/year in an SFR core environment, both void swelling and mechanical property degradation are critical issues in BCC Fe-based alloys.

Defect self-diffusion is generally considered to be driven by concentration gradients. Other driving forces, such as stress strain fields and temperatures may also be responsible. In general, diffusion of multiple component entities in polycrystalline materials is complicated due to presence of grain boundaries (GBs), dislocations and other internal heterogeneities. The defect balance can be simplified and described by a system of partial differential equations based on diffusion. A more detailed description will be presented in section 5.

2.1.3 Similarities and Differences between Neutron and Ion Irradiations

Ion irradiation can be generally categorized into three types based on mass of ions: electrons, light ions (H, He), and heavy ions. For the purpose of studying high radiation damage, heavy (or self) ion irradiation is preferred since it can deliver very high dose in a reasonably short time of period, e.g., 50-600 dpa per day, depending on the accelerator design, which could have taken years or decades in test reactors. An advantage of ion irradiation is that experimental parameters, such as temperatures and damage rates, can be well controlled compared to conditions in a reactor, where highly controlled experiments are expensive and difficult. Materials under neutron irradiation in a reactor environment would usually experience temperature and flux fluctuations. Heavy ion irradiation experiments normally produce no residual radioactivity in specimens and thus post-irradiation examination is less expensive. Neutron irradiation also induces transmutation, which sometimes can noticeably alter a material's chemical composition.

Evaluating the viability of ion irradiation as a surrogate tool for neutron irradiation poses many challenges. Aside from materials' intrinsic differences, the microstructure is believed to be affected by numerous other factors, such as temperature, dose rate, gas injection and strain, etc. The intrinsic differences between ion irradiation

and neutron irradiation are called neutron-atypical variables. First of all, the primary recoil energy spectrum, which is directly linked to defect production, is different between ion and neutron irradiation [13]. Atomic-scale simulation studies showed that the damage cascade size and surviving defects are directly affected by PKA energy [14]. However, the influences of the primary recoil energy spectrum on long-term evolution of microstructures are still under discussion. For self-ion irradiation in steels, the recoil energy and the efficiency in producing freely migrating defects are more similar to those of neutrons than those of light-ion or electron irradiation [15], as illustrated in Figure 2-4.

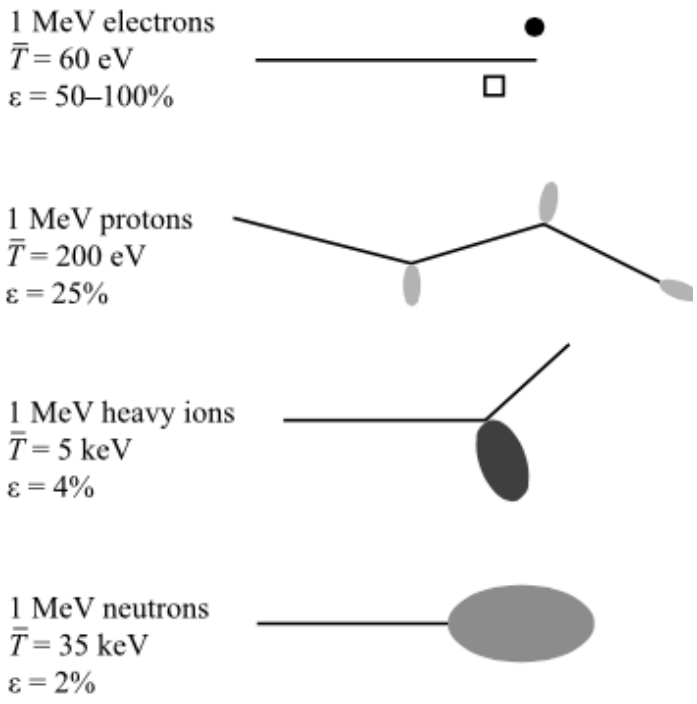

Figure 2-4. Comparison of average PKA energies, T, and defect production efficiencies, ε, between different ions and neutron [16]. During electron irradiation, average PKA energy is small and it only lead to production of isolated Frankel pairs. Heavy ion irradiation in general induce higher average PKA energies but a large fraction of created defects annihilated within damage cascade.

The second variable is the accelerated radiation damage rate in ion irradiation. Typical damage rate is ~10^{-4}-10^{-2} dpa/s for self-ion irradiation, in comparison to ~10^{-7}-10^{-6} in fast reactor. The difference is conventionally addressed by applying temperature shift to ion irradiation conditions. The concept of temperature shift was derived by the rate theory and was popularized by Mansur et al [17-20]. It suggests that the increased damage rate needs be accommodated with increased irradiation temperature to maintain an invariant defect flux. The model was first proposed to explain a shift in the peak swelling temperature observed in pure Nickel irradiated by neutron or ion [19]. Few experimental data are available for studying damage rate effects of heavy-ion irradiations in BCC Fe-based alloy systems, nor are there many systematic studies of other defect types, such as second phases and dislocations.

Recently, several more neutron-atypical variables have been identified and are under various stages of investigation [21-26]. Foremost of these is the effect of injected interstitials, operating not only as a physical entity but also as a chemical entity, changing the alloy composition toward the end of the ion stopping range. Injected interstitials are known to suppress both void nucleation and void growth even in pure metals, due to defect imbalance in ion irradiation [21, 24, 27, 28]. The free surface could also be a difficulty in ion irradiation study. Being strong a defect sink, a free surface could greatly affect microstructural evolution in the vicinity [29]. Ion irradiation could also induce various levels of surface sputtering depending on irradiation conditions. It could potentially change chemical composition in near-surface regions [30]. Another important but long-neglected effect is the ion beam mode used for irradiation. When applied to samples, an ion beam can be delivered in either raster-scan or defocused mode. Recently studies suggest raster-scan should be avoided for radiation effects research [23, 25].

Another distinctive difference between ion and neutron irradiations is that neutron-induced transmutation [31], [32], [33], [34], [35]. First of all, helium, which could lead to embrittlement [36], is a product of transmutation of certain elements, such as produced by ^{10}B through a (n, α) reaction. Another major source of helium in Ni-

bearing alloys is the two-step $^{58}Ni(n, \gamma)^{59}Ni(n, \alpha)^{56}Fe$ reaction, since ^{58}Ni comprises 67.8 % of natural Ni and it has large reaction cross sections.

Transmutation could also result in altering alloys' chemical compositions, depending on neutron energy spectra. Greenwood and Garner calculated transmutation of W, Re, V and Mo in various neutron spectra environments [31], [33], in which fast neutron spectra were based on FFTF and mixed neutron spectra were based on HFIR. Vanadium-51 transmutes to ^{52}V via (n, γ) reaction and then decays to ^{52}Cr. Under fast neutron spectra, less than 1% of V was transmuted to Cr up to 833 days, when irradiated at below core positions. However, the production of Cr is significant, reaching a level of 19.3% in mixed neutron spectra environments. Tungsten, mostly ^{184}W and ^{186}W, transmutes via (n, γ) reaction and leads to Re, most of which will subsequently transmute to Os. Transmutation of W is especially significant under mixed spectra and is moderate in FFTF below core positions. The transmutation of W could potentially be an issue since W is one of most important carbide formers in Fe-Cr-W F/M steels in the absence of Mo. Under both spectra types, molybdenum primarily transmutes via (n, γ) reaction, mostly ^{98}Mo to ^{99}Mo and ^{100}Mo to ^{101}Mo, which decay to ^{99}Tc and ^{101}Ru, respectively. Other reactions, (n, p) and (n, α), could also occur. Overall reduction of Mo was less than 1 % under fast spectra up to 833 days and under mixed spectra up to a year. In addition, Greenwood and Garner suggested that neutron self-shielding could significantly reduce the transmutation rate, but that the effect is highly dependent on the materials' geometry and needs further investigation [33].

2.2 Radiation Effects on Structural Materials

2.2.1 Radiation Induced Precipitation (RIP) and Phase Stability

Radiation introduced excess point defects in materials systems can sometimes induce precipitation of second phases, which otherwise would have not occurred under normal annealing. The exact mechanism is still not clear. It may accelerate the kinetic processes for phase separation, alter free energy formalisms, or both [37, 38]. A typical

microstructure of F/M steels HT-9 (one type of BCC Fe base alloy) with irradiation induced precipitations after high-dose irradiation is shown in Figure 2-5 (dislocation structures are not shown here). The energy-filtered transmission electron microscope (EFTEM) images show the existence of voids, Ni-Mn-Si-enriched precipitates (G-phase), and Cr-enriched alpha-prime (α′), neither of which exists before irradiation. Those irradiation-induced precipitates are considered responsible for increased hardness and reduced ductility.

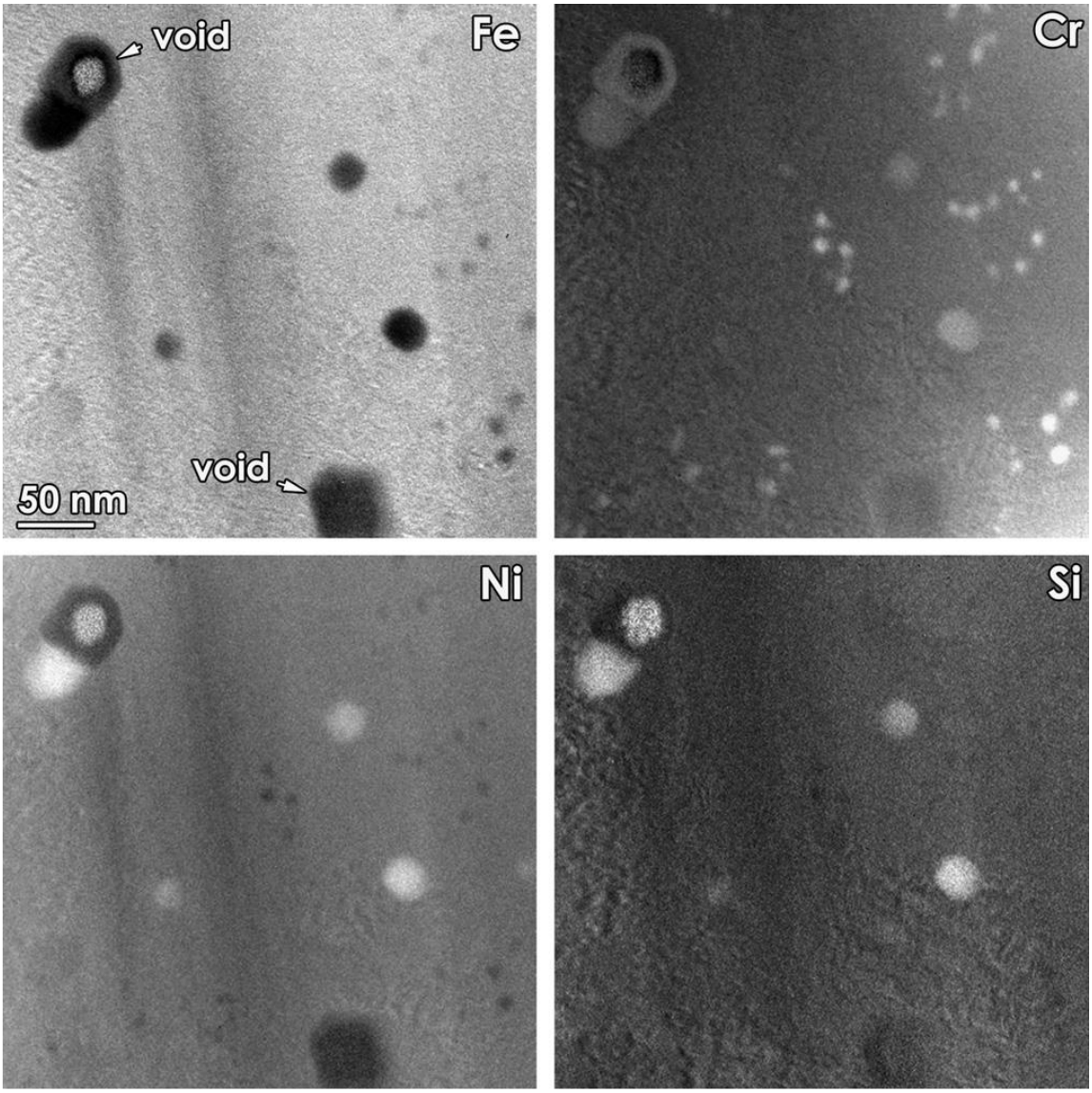

Figure 2-5. Energy-Filtered TEM (EFTEM) images of HT-9, 155 dpa at 440°C. Jump ratio images of Fe, Cr, Ni, and Si show G-phase and α′ precipitates as well as voids [6].

Some thermally stable phases, such as carbides, can be dissolved under irradiation. PKAs and recoils that gained enough kinetic energy can be ejected from existing phases into solution. This process is usually referred as irradiation induced atomic mixing or ballistic dissolution. Dissolution of pre-existing precipitates or second

phases can be detrimental to maintaining a material's designed performance. For ODS alloys, the importance of yttrium-titanium oxide to high temperature mechanical properties has kept the stability of those particles under irradiation a focus of studies.

2.2.2 Dimensional Stability

Void Swelling

Void swelling was first discovered in 1967 in the Dounreay Fast Reactor (DFR) in the United Kingdom, which was operated at 270–560 °C [39]. Void swelling was recognized as a major life-limiting factor of structural materials in reactor service when double-digit percentages of swelling in austenitic 304 stainless steel [40], [41] were observed in early experiments in Experimental Breeder Reactor II (EBR-II). Void formation and growth are conventionally described by rate theory [42], [18] and attributed to an excess of vacancies. At temperatures relevant to fast reactor operation, the difference between the mobilities of interstitials and vacancies is large. Interstitials preferentially migrate to certain types of defect sinks, such as dislocations, and are annihilated at recombination sites because vacancies and interstitials have a bias for defect sinks. As a result, a net excess of vacancies, which are also mobile in this temperature range, is present in the materials, and they tend to agglomerate into vacancy clusters that eventually nucleate into voids. However, at even higher temperatures, void swelling becomes unlikely again, since the difference between mobilities of vacancies and interstitials decreases and point defects tend to recombine with each other more efficiently.

Void swelling in steels is divided into two stages: an incubation stage with a very low swelling rate, and a steady-state swelling stage with a larger and constant swelling rate. The duration and swelling rate of the incubation stage depend on the irradiation conditions, microstructure, and composition. The steady-state swelling rate in face-centered cubic (FCC) steels is ~1%/dpa but that value is still debated for BCC steels. A general trend for void swelling is shown in Figure 2-6. Garner et al. pointed out that the

observed swelling resistance in BCC steels can be attributed to a much longer incubation period, while the steady-state swelling rate might be higher than previously expected [3]. In the same study, Garner et al. re-examined previous experimental data generated on Fe-Cr binary alloys in EBR-II and suggested the swelling rate is at least ~0.2%/dpa, a much higher number than previously expected in BCC structures. However, due to the fact that Fe-Cr binary alloys swell faster than other more complex alloys, the statement for other F/M steels has not yet been verified by neutron irradiation experiments.

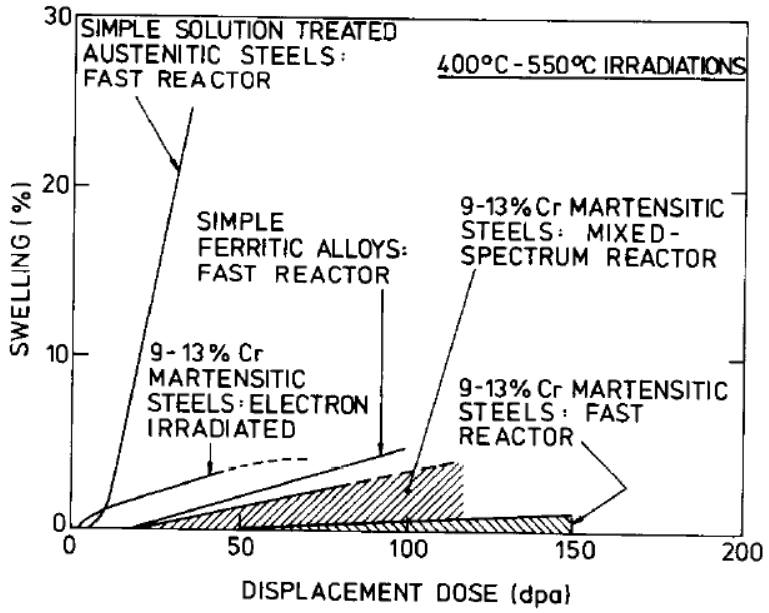

Figure 2-6. A typical schematic for void swelling in austenitic and F/M steels as a function of fluence [43].

Void swelling in ODS alloys is generally low. Toloczko et al. measured density change in MA957, a 14Cr ferritic ODS alloy, irradiated to 40-110 dpa at 400-750°C at the Fast Flux Test Facility (FFTF) and found minimal void swelling [44]. The same heat of alloy was recently irradiated by Cr ions to 500 dpa at similar temperatures. The result again confirmed excellent swelling resistance of ODS alloys [45].

Irradiation Creep

Creep is the time-dependent, permanent deformation of materials that occurs under the influence of mechanical stress. Irradiation creep, also known as in-reactor creep, is a creep process that occurs under the influence of simultaneous application of mechanical stress and irradiation. Both thermal creep, which occurs at elevated temperatures, and irradiation creep could happen in the ferritic steels during in-core service, but the latter is dominant in the lower temperature regime ($T < 0.5T_m$), which includes the materials' normal operating temperatures in fast reactors. Irradiation creep is an important process that must be accounted for in reactor designs. For example, irradiation creep could be beneficial to relax materials and relieve stress induced by void swelling. But shape deformation beyond design tolerance could also occur, even under normal stress [46]. The irradiation creep process is governed by interactions among point defects, the stress, and the material-specific properties. Irradiation introduces extra point defects beyond the equilibrium levels that are absorbed by dislocations. The absorption of point defects must be asymmetrical to induce dislocation climb, since the equal partitioning of vacancies and interstitials at dislocations would result in annihilation, and dislocation climb could not occur.

A number of theories, such as I-creep, stress-induced preferential absorption (SIPA), and preferred absorption glide (PAG), have been developed to explain interactions among supersaturating point defects, the stress, and the material during irradiation creep [47], [48], [49], [50],[51]. Regardless of mechanisms at the atomic scale, Garner et al. proposed a general mathematical description for irradiation creep, which involves transient creep, creep without swelling, and creep with swelling, shown in equation (2.3) [46], [52]:

$$\frac{\dot{\varepsilon}}{\sigma^n} = A\left[1 - e^{\frac{-dpa}{\tau}}\right] + B_0 + D\dot{S} \tag{2.3}$$

where $\dot{\varepsilon}$ is the effective strain rate per dpa, σ is the applied stress, n is a stress component, A and τ are empirical parameters for transient creep, B_0 is the creep

compliance, D is the creep-swelling coupling coefficient, and $\dot{S}$ is the swelling rate as a function of dpa.

Creep compliance, B_0, is the parameter that describes the irradiation creep rate at steady state without swelling. A limited number of creep studies exist for ODS alloys. Toloczko et al. reported that MA957 exhibited significantly better creep resistance at 600°C up to 100 dpa than traditional F/M steel HT-9, as shown in Figure 2-7 [53].

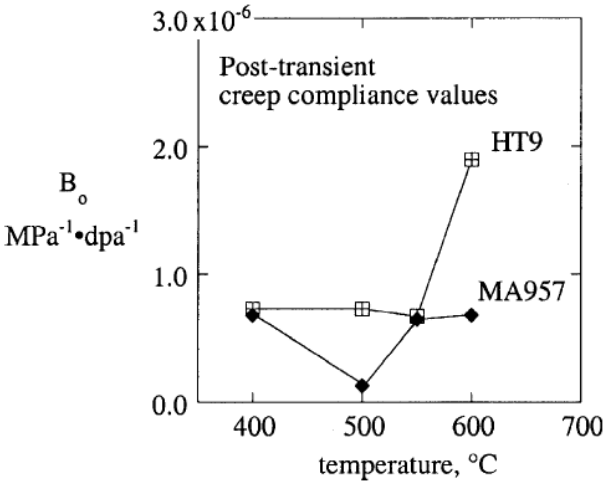

Figure 2-7. Creep compliance in MA957 and HT-9 as a function of irradiation temperatures [53].

Available irradiation creep data, most for F/M steels, are highly scattered [54]. Although it is difficult to deduce any useful information for composition optimization due to variability of the materials' production history, experiment conditions, and even data interpretation, one general guideline can be deduced. One key aspect is radiation induced defect supersaturation that leads to great enhancement of diffusion controlled processes. Thus dislocation climb by absorption of point defects, which is a key mechanism in many models of irradiation creep, is enhanced.

2.2.3 Hardening and Embrittlement

Hardening of metallic materials can occur within certain temperature range. It is usually an undesirable phenomena. In BCC Fe alloys, hardening is usually caused by pinning dislocation or slowing dislocation movements via defect-dislocation interactions. A variety of defects can make dislocation movement more difficult, such as some defect clusters, defect-impurity complex, dislocation loops, dislocation networks, voids, bubbles, and precipitates. Hardness of materials is generally correlated to yield strength [55]. For BCC Fe alloys, irradiation hardening induced embrittlement could be a serious problem.

One drawback of ferritic alloys is a tendency to become brittle and loss of ductility after irradiation at low temperatures, in contrast to austenitic steels [56]. Ductility of materials can be measured in several ways, one of which is fracture toughness. Fracture toughness is a critical mechanical property of a material that quantitatively describes the material's ability to absorb energy and resist fracture. Ferritic alloys usually exhibited good fracture toughness and is likely to experience ductile fracture. Irradiation at low temperature regions ($T < 0.3T_m$) may reduce the deformation sustained before yield stress reaches fracture stress of materials. Under this case, brittle fracture is likely to develop.

Effects of hardening and loss of ductility usually quickly become saturated at relatively low damage levels (a few dpa), depending on irradiation temperature [57], [58]. With irradiation temperature increases, more radiation damage can be tolerated before it develops to saturation. At higher temperatures, radiation-induced hardening is significantly reduced. In a high-dpa, high-temperature case, the reduction of fracture toughness is more likely to be due to other embrittlement mechanisms, such as void and/or bubble formation, precipitates, and any mechanisms that weaken grain boundaries or interfaces, since hardening does not contribute significantly [59].

2.3 Neutron-Ion Correlation Studies

2.3.1 Earlier Studies (1970s-1990s)

The concept of using ion accelerator to simulate fast neutron induced damage is pioneered and demonstrated by Nelson, Mazey and Hudson at Harwell in the United Kingdom [60]. Since void formation was observed in stainless steels in the late 1960s [61], it has been a major concern for fast neutron reactor applications. The higher damage rate in a fast reactor core environment could cause significant dimensional instability in those materials within a few years of service. Their work in 1970 explored the effectiveness of several ion irradiation experimental parameters, such as ion energies, ion species, and helium injection to producing void swelling. Although historical studies regarding void swelling may not necessarily be applicable to our current microstructural features, it is still helpful and interesting to conduct a brief survey of earlier neutron ion correlations achievements in this section.

Before the unit of displacements per atom (dpa) was introduced, the radiation dose on materials was usually quantified by the fluence in units of number of incident particles per unit area, such as neutrons/cm^2. The first problem for neutron ion correlation study is how to correlate damage introduced by ions with that by neutrons. Kulcinski et al. explored the validity of using the total number of displaced atoms as a first order approximation [62].

Systematic investigations in the United States of applying ion irradiation as an accelerated techniques to study radiation effects can be traced back 1970s. During that period, the majority of studies comparing neutron and ion irradiation focused on the void swelling behaviors in austenitic stainless steel systems. Several programs in the United States, such as the Liquid Metal Fast Breeder Reactor (LMFBR) program and Energy Research and Development Administration (ERDA) program, produced a good amount of studies on intercorrelations among ion (including electron) and neutron irradiation experiments. The early work from these research programs was summarized in a series of papers published in the proceedings of the workshop on correlation of neutron and

charged particle damage [63]. Another recent review of this topic using data from this period can be found in a paper by Garner et al. [22].

One of the most detailed and fundamentally oriented studies was produced by the Alloy Development Intercorrelation Program (ADIP), and a summary of experiments can be found in a report by Garner et al. from 1984 [64]. The program employed a well characterized, simple ternary model alloy Fe-15Cr-25Ni, with low impurities for correlation experiments. Multiple national laboratories and institutes participated in the study via irradiation experiments and post-irradiation characterizations. Several charged particle species, namely electrons, protons and nickel ions at various energies, were applied in ion irradiation experiments. The Phase I of the program compared void swelling behavior across different ion irradiation parameters, such as ion species, ion energy, irradiation temperature, and damage rate, as shown in Table 2-1. Since it is not the scope of this dissertation to discuss the difference among different ion species, the electron and proton data will not be surveyed.

Table 2-1. Experimental details of ADIP Phase I Experiment [64]. Only results from Ni ion irradiations were surveyed. Note that all specimens were injected by ~6 appm helium. AI-Atomic International; HEDL-Hanford Engineering Development Laboratory; NRL-Naval Research Laboratory; W-ARD-Westinghouse Advanced Reactors Division; HVEM-High-Voltage Electron Microscope.

Laboratory	Particle	Displacement Rate (dpa/sec)	Data Extraction Technique
AI	0.75 MeV p^+	2×10^{-4} (nominal)	1.5 – 3.7 μm TEM, sectioning
GE	5.0 MeV Ni^+	2×10^{-2}*	TEM, section at peak dose
HEDL	1.0 MeV e^-	2.1×10^{-3} (40 barn)	Uniform displacement profile, HVEM stereomicroscopy
NRL	2.8 MeV Ni^+	2.0×10^{-2}*	TEM, section at peak dose
W-ARD	3.5 MeV Ni^+	5×10^{-3}*	HVEM full-range stereomicroscopy

* Measured at peak displacement rate.
† Six appm He uniformly implanted in all specimens.

Shown in Figure 2-8 reproduced from reference [64], it is clear that the void swelling is not identical among results from three different laboratories. In fact, the differences in onset of swelling can be as large as 48 dpa when irradiated at 750°C and are around 15 dpa at other irradiation temperatures. On the other hand, similar evolution trends can be observed. The swelling evolution consists of an incubation stage with various lengths and a steady state swelling stage with similar rate. The authors concluded that such discrepancies in incubation stage cannot be simply explained by different data extraction techniques or irradiation dose rates. Other experimental details, such as sectioning, electrochemical polishing and initial dislocation structures may affect the measured incubation period. The experiment results suggest that incubation stage is quite sensitive to irradiation temperature. Void swelling results from neutron irradiated Fe-15Cr-25Ni specimens to $2.2\text{-}2.7\times10^{22}$ n/cm^2 (E > 0.1 MeV) are shown in Figure 2-9. But neutron fluence is not yet high enough to produce meaningful swelling comparisons. Several important concepts have been proposed or reinforced with studies in conducted by ADIP. The temperature shift concept, for example, has been tested for charged particle irradiations. The preliminary neutron data suggested that there may be a shift in peak swelling temperature due to a dose rate effect.

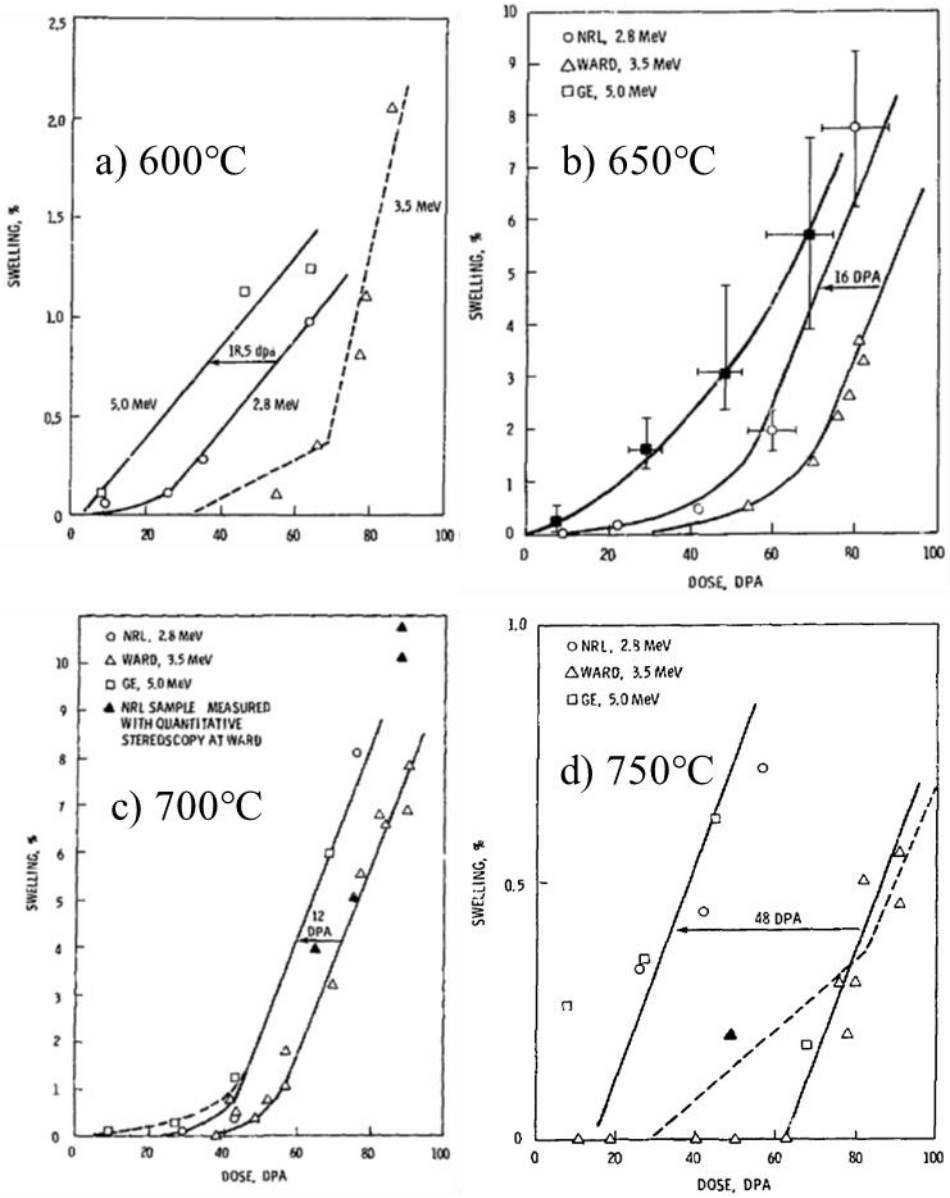

Figure 2-8. Void swelling in Fe-15Cr-25Ni irradiated by 2.8 MeV (NRL), 3.5 MeV (W-ARD) and 5.0 MeV (GE) Ni ions at various temperatures [64].

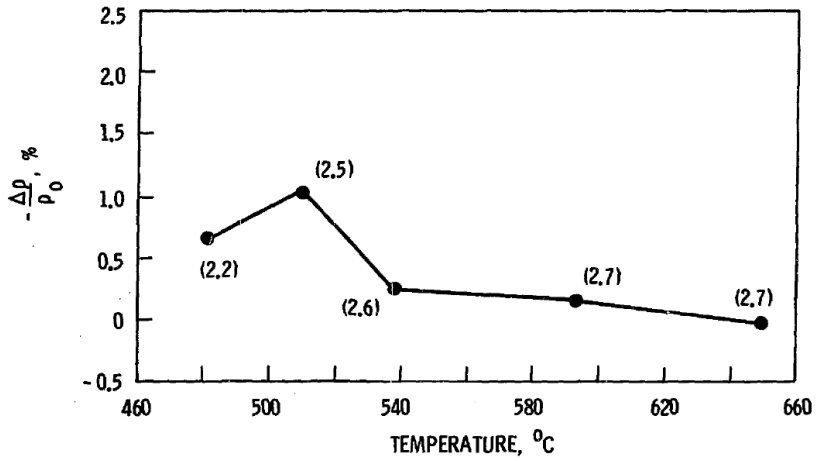

Figure 2-9. Neutron induced density changes in ADIP Phase I alloy [64]. The number in parentheses represent the neutron fluence in units of 10^{22} n/cm^2 (E > 0.1 MeV).

Fe-Cr-Ni model alloys irradiated by neutrons to higher fluences in EBR-II are shown in Figure 2-10 [65]. The graph shows that the steady-state swelling rate is ~1%/dpa regardless of composition difference or irradiation temperatures. This rate is much larger than swelling reported in Ni ion irradiated material (Figure 2-8). The swelling rate calculation can be affected by a variety of factors, especially the data extraction method. Depth control in the sectioning method is quite difficult and inaccurate. Stereographic transmission electron microscope (TEM) examination is generally more accurate and representative. Johnston et al. [66-70] performed stereographic TEM measurements for swelling and provided an empirical correlation between a simple step height measurement and void swelling. The swelling data produced in such way are shown in Figure 2-11. The resulting steady-state swelling rates are close to ~1%/dpa as observed in neutron irradiated cases.

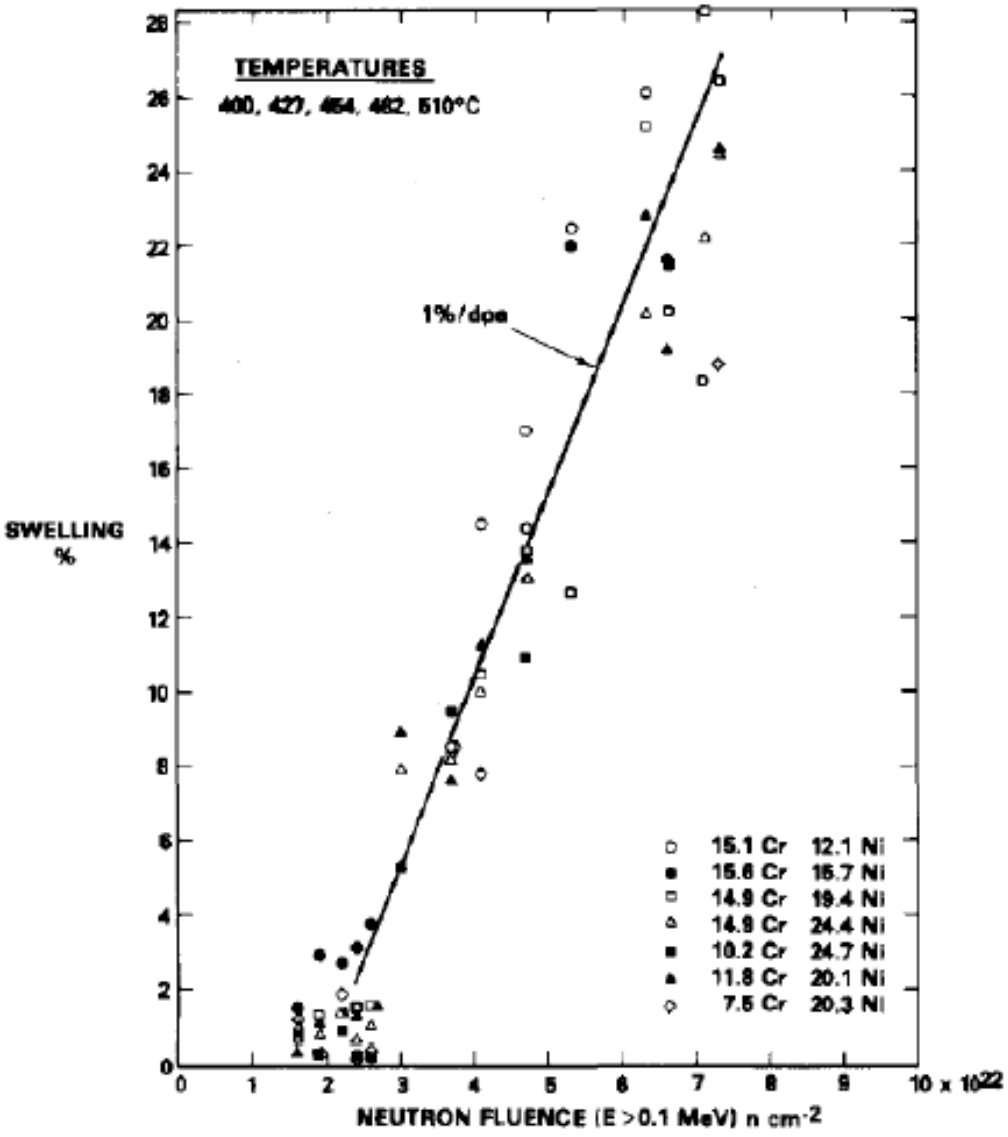

Figure 2-10. Swelling data in Fe-Cr-Ni model alloys irradiated by neutrons in EBR-II fast reactor [65].

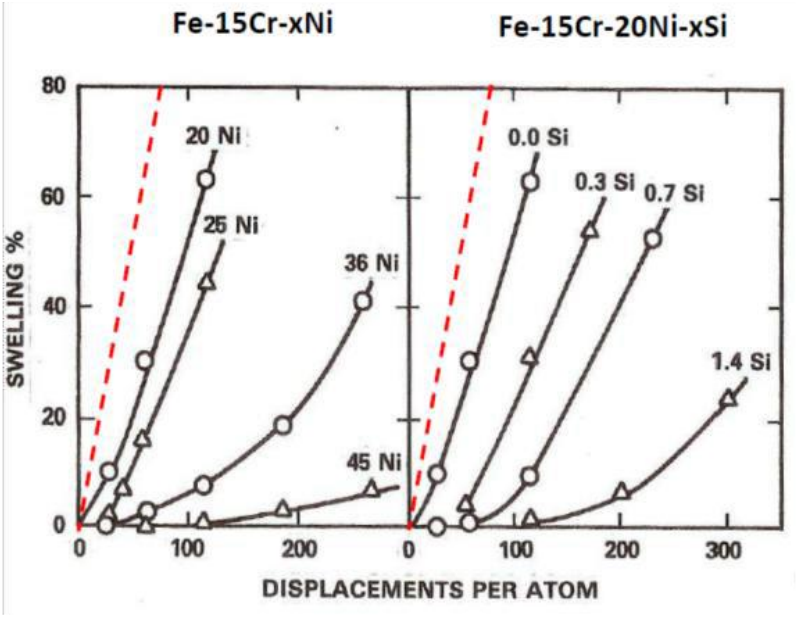

Figure 2-11. Ion-induced swelling of Fe-Cr-Ni model alloys with variable composition. The dotted red line indicate 1%/dpa swelling. Note that the transient regime from incubation varies with composition [68].

Another example of the effectiveness of ion irradiation in simulating neutron induced void swelling was produced by Bullough et al. [71]. The research developed a new sink strength model for a straight dislocation with long-range field interactions with point defects and implemented it in conjunction with sink strengths for other common defect types in irradiated metals. The void swelling was then calculated under the framework of a rate theory model. Electron and heavy-ion irradiation experiments in M316 SS were employed for parameter calibration of the model and a prediction was made for neutron irradiated materials. The model yielded satisfactory agreement with experimentally measured void swelling in neutron irradiated M316 SS specimens. One important thing pointed out by the paper is that ion irradiation based simulation based experiments can be useful in providing parameters for physical based models for neutron irradiated materials.

Besides neutron ion correlation for fast reactor relevant conditions, several studies regarding the fusion reactor environment were conducted during that time [72-

75]. They will not be surveyed here due to the complications that comes with the effects of helium on microstructural evolution. A good review of using ion irradiation to simulate neutron damage for fusion related environment is available in Abromeit [76].

Although there were noticeable progresses in knowledges regarding neutron ion correlation in the early years, recent advances in characterization and computation techniques, especially recognizing neutron-atypical variables as briefly mentioned in section 2.1.3, reveal that some of those experimental procedures may be problematic and perceptions of that time may not be correct. For example, some recent ion range calculations using the Stopping Range of Ions in Matter (SRIM) [77] indicate that early works may underestimate Ni ion ranges significantly; cross-sectional examinations of ion irradiated specimens reveal that injected interstitials significantly suppress void swelling [24, 78] while a fair amount of early day study was taking examination in regions that might be affected by injected interstitials [67, 79].

2.3.2 Recent Progress

Publications directly investigated ion and neutron irradiation correlations to high damage levels are rare, even though there are a number of separate studies of ion or neutron irradiations to high doses individually. Unlike the earlier studies which focused on void swelling behaviors, most recent studies covers a wider range of microstructural features, including dislocation structures, voids, precipitates and second phases, and radiation-induced segregation (RIS). Another difference from the past is that a fair amount of recent studies are in the BCC ferritic alloys rather than focused on austenitic steels. We have noticed correlation studies were conducted even on vanadium alloys [80]. The intercorrelation investigations concerning other aspects of radiation effects on materials, such as mechanical properties [81, 82] and irradiation assisted stress corrosion cracking [83, 84], are also gaining attentions [85].

One neutron ion correlation study that is relevant to our research topic was reported by Was et al. in 2014 [86]. The study investigates a full range of microstructural features, from dislocations and precipitates to void swelling, in neutron or ion irradiated

ferritic-martensitic alloy HT-9 to damage doses beyond ~100 dpa. They studied an HT-9 fuel bundle duct (ACO-3) that was used in Fast Flux Test Facility (FFTF) and was irradiated to a cumulative 155 dpa at average temperature of 443°C. An archive sample of the same heat of HT-9 was used for ion irradiation, so that variabilities in materials are eliminated. The specimen was irradiated by 5 MeV self-ions at 460°C with 1 appm helium pre-implantation to 188 dpa. The ion irradiation temperature was determined according to the previously envisioned "temperature shift" concept and calculated by rate theory models. The microstructures of both materials were examined by TEM and APT.

The size distributions of voids, characterized by TEM, in ion or neutron irradiated HT-9 is shown in Figure 2-12. Both ion and neutron induced voids sizes follow similar distributions, except that a small fraction of larger ones (>60 nm) in neutron irradiated specimens. Figure 2-13 shows the quantitative comparison for dislocation loops, voids and G-phases. These features are not identical in size or number density. For example volume fractions can be off by a factor of ~2-3, as shown in Figure 2-13a). It is not surprising that void swelling is larger in the ion irradiated specimen given a higher dose was accumulated. Based on other void swelling studies in HT-9 [87, 88], this level of damage is probably still within the incubation or transient regime of void swelling. Thus such difference is not unexpected since incubation regime of void swelling is very sensitive to experimental technique or parameters [3, 27, 63]. Regarding size and density shown in Figure 2-13b), large discrepancies have been observed for dislocation loops and G-phases while void size and density ratios are comparable. Despite the differences in absolute values, we cannot ignore the evidence that ion irradiation did a reasonably good job in recreating similar microstructural features in ferritic-martensitic alloys under similar irradiation temperatures to high doses. Besides many neutron-atypical variable effects in ion irradiation, we cannot ignore another layer of complexity: that in-reactor irradiation usually includes multiple rounds of irradiation that involves complicated thermal and neutron flux history.

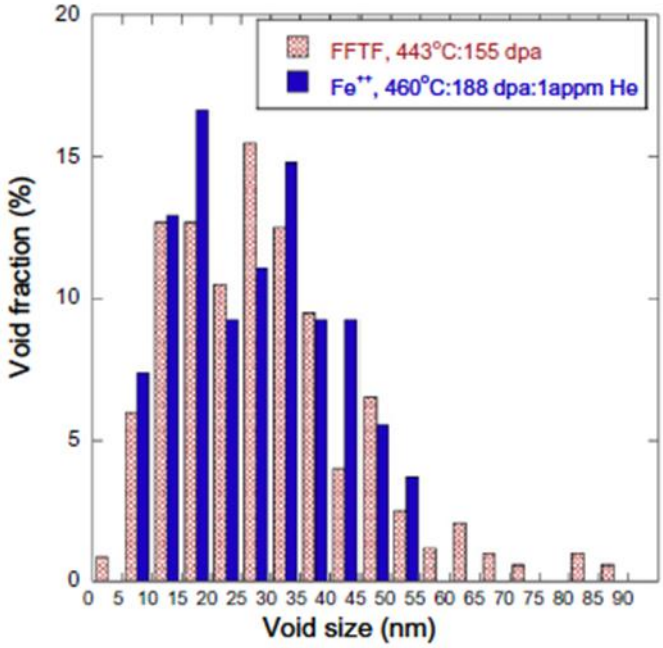

Figure 2-12. Comparison of void size distribution observed in neutron or ion irradiated HT-9 [86].

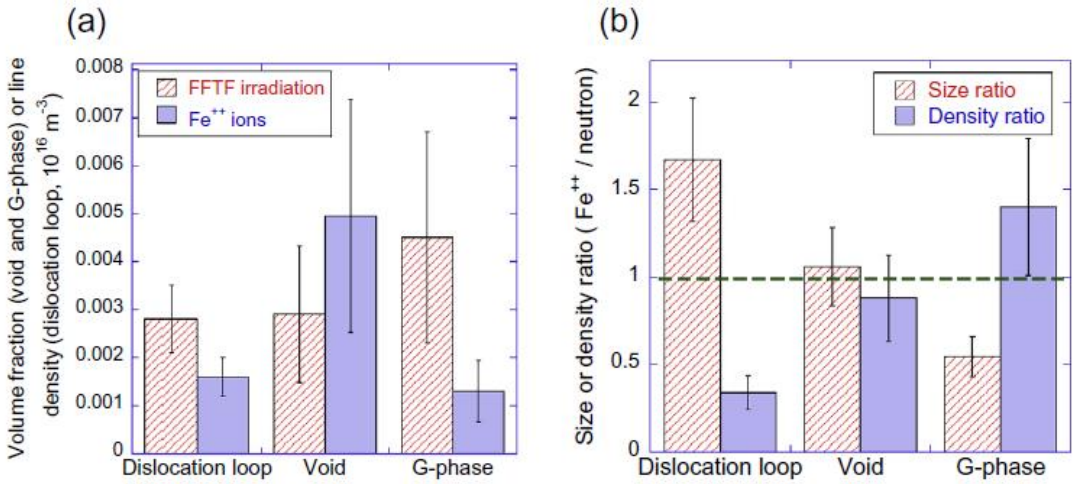

Figure 2-13. Comparison of a) volume fraction and b) size and density ratios of voids, G-phases and dislocation loops after irradiation [86].

Pareige et al. [89] investigated the segregation and solute clustering behaviors of Si, P, Ni and Cr in two Fe-Cr model alloy (Fe-9Cr and Fe-12Cr) irradiated by ion or neutrons. The specimens were ion irradiated by Fe^{+} ions of 0.5, 2 and 5 MeV at 100-420°C to 0.5 dpa in order to produce a quasi-constant damage profile in the irradiated region. Neutron irradiation was performed at the BR2 reactor to 0.6 dpa at 300°C. Solute clusters and segregations were characterized by using APT.

Two types of precipitates, CrSiPNi clusters and α′ (Cr-enriched) clusters, were observed in two neutron irradiated alloys, while only CrSiPNi clusters were found in corresponding ion irradiated specimens. In the Fe-9Cr alloy, the clusters developed to similar size and number density, while in Fe-12Cr alloy, ion irradiation produced larger cluster sizes, as shown in Table 2-2. The calculated solute enrichment is shown in Table 2-3. All elemental enrichments are quite different between the ion and neutron irradiated two alloys, except phosphorus (P). The absence of α′ was attributed to that Cr atoms having insufficient time to form α′ during the short period of ion irradiation. The study shows that in the low dose transient regime, some microstructural features can be recreated while others may not be, due to transient regime's sensitivity to experimental parameters.

Table 2-2. CrSiPNi clusters size and number density comparison among neutron and ion irradiated Fe-9Cr and Fe-12Cr [89].

	Fe–9at.%Cr		Fe–12at.%Cr	
	300 °C		300 °C	
	Ion irradiation 0.5 dpa	Neutron irradiation 0.6 dpa	Ion irradiation 0.5 dpa	Neutron irradiation 0.6 dpa
ND (10^{23} m^{-3})	2.8 ± 0.6	2.4 ± 0.5	3.3 ± 0.6	1.1 ± 0.7
Radius (nm)	1.5 ± 0.3	1.65 ± 0.2	1.3 ± 0.3	1.6 ± 0.2

Table 2-3. Solute enrichment ($\Delta C_i = C_i - C_i^{matrix}$) in clusters after ion or neutron irradiation at 300°C [89].

Alloy	Fe	Cr	Si	P	Ni
Ions					
Fe–9%Cr	Bal.	5.8 ± 1.6	2.0 ± 0.7	2.4 ± 0.6	0.4 ± 0.4
Fe–12%Cr	Bal.	2.7 ± 1.3	1.3 ± 0.4	3.5 ± 0.7	0.3 ± 0.2
Neutrons					
Fe–9%Cr	Bal.	6.7 ± 1.3	6.6 ± 0.8	2.2 ± 0.5	1.3 ± 0.4
Fe–12%Cr	Bal.	16.0 ± 2.4	7.8 ± 1.5	3.3 ± 1.0	1.2 ± 0.6

Neutron-ion correlation investigations in the ODS alloys are even rarer due to limited availability of high dose neutron irradiated materials. Ribis et al. [90] recently conducted a comparative study on the stability of nano-sized oxide particles in ODS alloys irradiated by neutrons or ions to above 50 dpa. Neutron irradiation was performed on commercial MA957 cladding tubes at the Phenix fast reactor in France to 50 dpa at 412°C and to 75 dpa at 430°C. An Fe-14Cr-1W-0.3Ti-0.3Y_2O_3 alloy, developed at CEA/SRMA, was used for ion beam irradiation to 75 and 150 peak dpa at 500 ˚C at the CEA-JANNUS Saclay facility using 500 keV Fe^+ ions. Microstructural examination was carried out by TEM.

The size and density of nanometer size oxide particles in specimens before and after irradiation are listed in Table 2-4. It shows that initial conditions of oxide particles are quite different between unirradiated MA957 and unirradiated Fe-14Cr ODS alloy specimens. Both ion and neutron irradiation were found to induce oxide particles coarsening while slightly reducing number density in specimens. The author attributed the coarsening to radiation-induced Ostwald ripening. One characteristic feature of Ostwald ripening is the linear relationship between particle volumes and time.

Table 2-4. Size and density of nano-sized oxide particles measured by TEM [90].

Dose (dpa)/irradiation time	Diameter (nm)	Density (m^{-3})
0 (Fe-14Cr-1W-0.3Ti-0.3Y_2O_3)	1.1 (±0.5)	2.9×10^{23}
75/1.1 × 10^5 s (Ion)	4.5 (±0.2)	10^{23}
150/2.3 × 10^5 s (Ion)	5.6 (±0.2)	1.2×10^{22}

Dose (dpa)/irradiation time	Diameter (nm)	Density (m^{-3})
0 (MA957)	2 (±0.5)	5.4×10^{22}
50/3.8 × 10^8 s (Ref. 6) (Neutron)	2.2 (±0.5)	4.7×10^{22}
75/5.7 × 10^8 s (Neutron)	2.5 (±0.5)	4.5×10^{22}

Figure 2-14 plots the cube of the diameter of oxide particles against damage dose in the materials. The good linear fits for both irradiations further support the Ostwald ripening mechanism being the key factor during irradiation. The growth rate can be calculated from the slope of these fitted lines. The result shows that nano-oxide particles experience more rapid growth kinetics during ion irradiation than neutron irradiation. This phenomenon is not unexpected for Ostwald ripening mechanism since the growth kinetics is proportional to solute diffusivity, which is approximately proportional to damage rate, as shown in the equation inset in the figure.

This study exhibited the potential for using ion irradiation as a simulation of experiments by demonstrating particles growth that follows Ostwald ripening mechanism, even though experimental conditions were not ideal for such intercorrelation studies, i.e., the materials are different, initial oxide particle populations are different, and ion irradiation dose and temperature are different. It is interesting that in some other neutron irradiated ODS alloy experiments conducted at similar conditions, oxide particles were observed to experience significant ballistic dissolution and re-precipitation

effects within this temperature range while the coarsening of nano oxide particles occurred at higher in-reactor irradiation temperatures above ~500°C [91]. Such discrepancies maybe due to different variabilities in materials or other unknown factors that need to be investigated further.

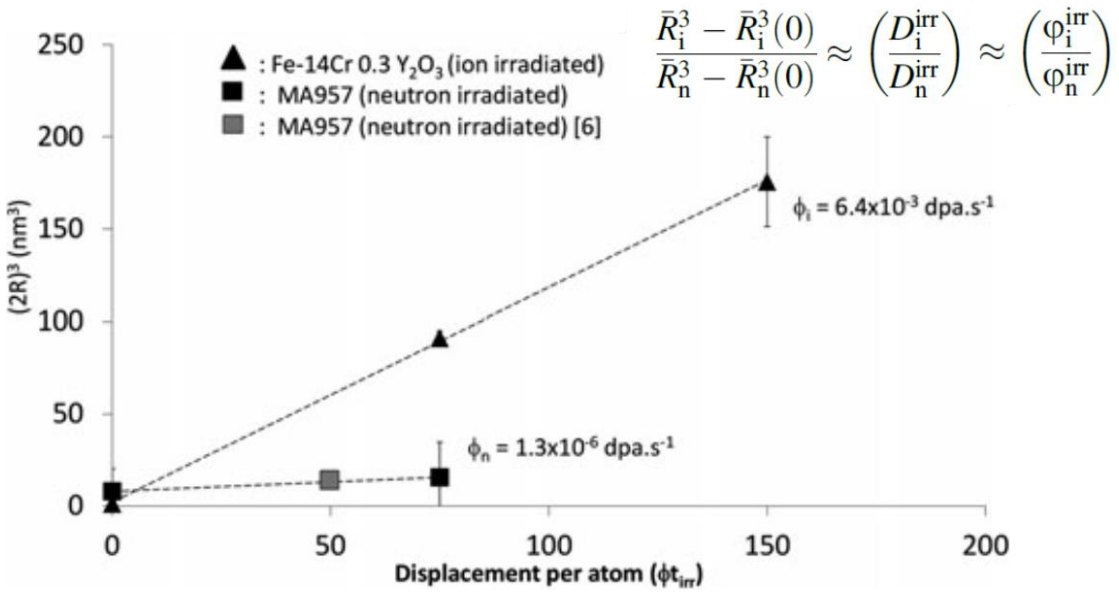

Figure 2-14. Cube of the oxide particle diameters vs. damage dose for both neutron and ion irradiation [90]. The inset equation is the characteristic growth kinetics for Ostwald ripening.

Another recent correlation irradiation study on a 9Cr ODS alloy using proton beam was reported by Swenson and Wharry [92]. A model Fe-9Cr ODS alloy was irradiated to 3 dpa at 500˚C by neutrons or protons, which enabled a direct comparison of microstructural evolutions, such as dislocation structures, voids, and oxide particles. Both TEM and APT were employed for characterization.

Table 2-5 shows the microstructures characterized by TEM for unirradiated and irradiated specimens. Generally good agreement in microstructural evolution between proton and neutron irradiated specimens have been found: there are slight increases in

grain sizes and carbide number density; dislocation lines remain almost unchanged; isolated voids are present in both specimens, but the overall swelling low in both; and dislocation loops developed are comparable in size and size distribution, but their number density is much higher after proton irradiation.

Table 2-5. TEM measured microstructural evolution in unirradiated, proton irradiated and neutron irradiated Fe-9Cr ODS alloy [92].

Feature	Measurement	As-received	Proton-irradiated (3 dpa, 500 °C)	Neutron-irradiated (3 dpa, 500 °C)
Grains/Laths	# of grains measured	104	104	104
	Effective diameter ($\times 10^{-6}$ m)	0.23 ± 0.12	0.31 ± 0.11	0.31 ± 0.09
Dislocation lines	# of measurements	17	46	39
	Density ($\times 10^{14}$ m^{-2})	19.1 ± 3.8	17.6 ± 5.3	18.5 ± 4.8
Carbide Precipitates	# of carbides measured	36	51	68
	Effective diameter ($\times 10^{-6}$ m)	0.11 ± 0.07	0.07 ± 0.03	0.10 ± 0.06
	Density ($\times 10^{20}$ m^{-3})	0.20	0.46	0.47
Voids	# of voids measured	0	8	22
	Diameter ($\times 10^{-9}$ m)	–	4.00 ± 1.51	3.64 ± 1.14
	Density ($\times 10^{21}$ m^{-3})	–	0.34 ± 0.44	0.24 ± 0.12
Dislocation loops	# of loops measured	0	688	182
	Diameter ($\times 10^{-9}$ m)	–	8.4 ± 1.7	8.9 ± 2.0
	Density ($\times 10^{21}$ m^{-3})	–	10.2 ± 8.0	2.7 ± 0.7

APT characterization was applied, mostly focused on analyzing yttrim titanium oxygen (YTiO) nano-oxide particle evolution, as shown in Table 2-6. The radiation stability of the oxide particles was found to be noticeably different. The YTiO particles remained stable under proton irradiation but exhibited decreases in size, number density, and volume fraction under neutron irradiation. The chemistry and composition of oxide particles underwent similar trend in evolution. The fractions of three major constituents – yttrium (Y), titanium (Ti) and oxygen (O) – inside clusters are nearly unchanged in proton irradiated specimens, while a fair amount of them are dispersed into the matrix after neutron irradiation. Atomic ratio between Y and Ti inside clusters was increased significantly in neutron irradiated specimens but remained similar in ion irradiated one. The authors attributed the observed discrepancies in oxide particle evolution to the damage rate effects on solute diffusion and different efficiency of incident particles in ballistic dissolution.

This study indicates that proton irradiation can reproduce the loop microstructures, even if the dpa rate is orders-of-magnitude different. The applicability of ion simulation experiments in reproducing microstructures is suggested to be dependent on the types of mechanisms they follow. Some mechanisms, such as recombination-driven ones, are not as sensitive to dose rate difference as others, such as diffusion-driven processes, are. The low damage dose in the study adds some complexities in accessing long-term microstructure evolution since the transient regime is known to be sensitive to many variables. The evolution of oxide particles in ODS alloys in current literatures varies greatly and no simple trend can be summarized from them [90, 92].

Table 2-6. APT measured microstructural evolution in unirradiated, proton irradiated and neutron irradiated Fe-9Cr ODS alloy [92].

Oxide nanoclusters	As-received	Proton-irradiated (3 dpa, 500 °C)	Neutron-irradiated (3 dpa, 500 °C)
# of clusters measured, ΣN_c	486	964	335
Analysis Volume, V_T (nm^3)	856,053	1,722,204	816,586
Average Diameter, D_G (nm)	5.96	4.77	3.41
Standard deviation for D_G	±3.10	±1.91	±1.69
Std. dev. of the mean for D_G	±0.14	±0.06	±0.09
Density, N_{nc} (x 10^{21} m^{-3})	568	560	435
Volume fraction, f_v	5.2%	5.1%	2.4%
Species, % in clusters, f_{cl}^i			
Y	74.0%	81.3%	52.1%
Ti	71.4%	65.5%	24.0%
O	66.2%	67.7%	32.3%
Cr[a]	6.2%	7.3%	3.4%
Si	7.1%	11.1%	8.3%
Mn	5.9%	6.8%	6.0%
Ni	8.1%	16.8%	8.3%
C[a]	10.6%	13.5%	4.5%
W[a]	5.1%	3.2%	1.8%
Y:Ti	0.54 ± 0.33	0.53 ± 0.26	0.97 ± 0.81
(Y + Ti):O	1.16 ± 0.22	1.15 ± 0.31	1.22 ± 0.46

[a] Does not include species clustering in carbide precipitates.

2.4 Oxide Dispersion Strengthened (ODS) Alloy

The development of oxide dispersion strengthened alloys can be traced back to 1970s which was then targeted for high temperature applications such as gas turbine. The excellent thermal stability of common oxide dispersions has greatly extended maximum service temperatures where alloys still maintain reasonably good strength.

With oxide dispersions stabilize grain boundaries and pin dislocation movements, high temperature creep strength of ODS alloys is also significantly enhanced.

ODS ferritic alloy is one specific class of these materials. Typical current ODS ferritic alloys employ Y and Ti-containing oxides as dispersions in the matrix. Common fabrication route of ODS includes mechanical alloying of alloy powders and oxide intermetallic powders, hot-extrusion to consolidate alloyed powders, followed by hot-rolling, heat treatment and final machining [93].

2.4.1 ODS Alloys for Nuclear Applications

ODS ferritic alloys have been a promising candidate for nuclear applications during the development and testing of Sodium-cooled Fast Reactors (SFR), due to their excellent high temperature mechanical properties and potential excellent radiation tolerance. The dispersion of nanometer-scale thermally stable oxide particles in the matrix not only improves tensile strength and creep resistance but also leads to enhanced radiation damage tolerance by providing additional sinks for defects recombination [17, 94, 95]. ODS alloys are designed to be potentially use as fuel cladding tubes. Multiple processing optimization efforts have been taken for tube fabrications [96-98].

Experimental data are limited in the high neutron dose regime (>~100 dpa) for ODS alloys. A couple of existing studies are from FFTF [44, 91, 99, 100], JOYO [101] and Phenix [102] on multiple ODS alloy MA957 specimens. Toloczko et al. examined MA957 irradiated at 400 to 750°C to 40-110 dpa in FFTF. The results have demonstrated excellent resistance to irradiation creep and to void swelling to high dose levels below 600°C irradiation temperatures [44, 100]. Bailey et al. recently examined oxide particles in these MA957 by atom probe tomography (APT) and reported that the oxides were stable when irradiated at 550-670 °C [91]. In MA957 specimens irradiated at ~500 and 700°C to ~100 dpa in JOYO, Yamashita et al. found that oxide particles were still effectively pinning dislocations even though their population was reduced by a half while their sizes increased slightly [101]. Ribis et al. observed a slightly lower density but no distinguishable changes of size of oxide particles in MA957 irradiated at

412°C to 50 dpa and at 430°C to 75 dpa in Phenix, compared with unirradiated specimens [102].

2.4.2 Structure and Composition of YTiO Dispersion

Although YTiO oxide particles in ODS alloy are well-known as a key contributor to excellent high temperature properties, there are still debates about their microstructures and compositions in ferritic ODS alloys. Analysis of oxide particles is quite difficult due to their ultra-fine sizes. A variety of crystal structures and stoichiometry have been reported in the past decades [103-108].

Crystal structure of YTiO dispersions in ODS alloys are commonly reported to be $Y_2Ti_2O_7$ cubic or Y_2TiO_5 orthorhombic. Wu et al. employed HRTEM to investigate nano-oxides in both thin foil MA957 specimens and oxide particles extracted from the same heat of material by acid. Crystal structures correspond to both $Y_2Ti_2O_7$ and Y_2TiO_5 have been observed among oxide particles whose diameters were less than 10 nm [108]. EDS results from their study shows that stoichiometry of oxide particles are in good agreement with corresponding crystal structures. Among analyzed particles, crystal structure of some oxides does not match any known YTiO crystal structures. One potential complication in the analysis is that whether extracted nano-oxides are representative for those embedded in Fe matrix. Some concerns have been expressed that nanoparticles at that size could be sensitive to environmental effects. Brandes et al. examined 14YWT using HRSTEM and found embedded oxide particles morphology is consistent with truncated rhombic structure but they cannot be identified as any known structures, such as $Y_2Ti_2O_7$, Y_2TiO_5 or Y_2O_3 [107]. Hirata et al. investigated an YTiO cluster of ~2 nm in an extremely thin region using STEM and reported that it was a NaCl type crystal structure [106]. The crystal structure was inferred by comparing experimental STEM images with simulated STEM images of crystal structures that were generated from molecular dynamics modeling. Sakasegawa et al. found that chemical compositions of oxide particles were correlated with their sizes, as plotted in Figure 2-15. Other crystal structural characterization techniques, such as XRD and SANS,

suggested that a mixture of stoichiometric and non-stoichiometric oxide particles were present in ODS alloys [104, 109].

Chemical composition of YTiO particle in ODS alloys measured by APT is usually highly non-stoichiometric. The Y/Ti ratio is typical within the range of 0.2-0.5 while the (Y+Ti)/O ratio is >1 [91, 107, 110-112]. Similar Y/Ti ratio has also been reported in EDS analysis presented in Hirata et al.'s study [106]. Although different from many TEM-based characterizations, majority of APT studies are self-consistent. Some may attribute this discrepancy to artifacts in APT. However, a recent study by Williams et al. compared composition of oxide particles in ODS with bulk Y_2O_3 and suggested that the discrepancy cannot be simply dismissed in this argument [110].

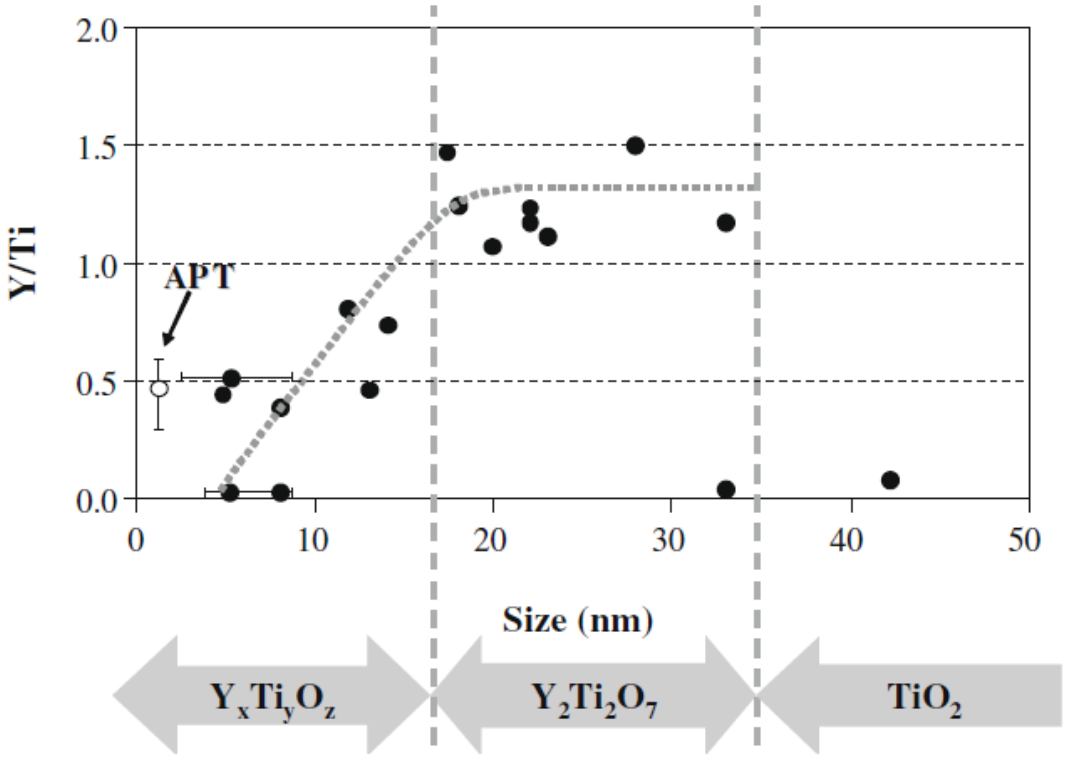

Figure 2-15. Correlation between chemical composition and oxide particle sizes [105].

2.5 Atom Probe Tomography (APT)

Atom probe tomography (APT) is a powerful technique to characterize chemical distribution in three dimension to the sub-nanometer scale in materials. APT exploits the principle of field ion evaporation where surface atoms are removed successively. APT specimen is usually fabricated into needle shape and immersed to a standing DC electrostatic field. Upon the ionization of surface atoms, which can be induced by either high voltage or laser, they are accelerated by electric field towards local electrode and away from specimen. Signals of some accelerated ions are then collected by using a 2D spatial sensitive detector. The mass-to-charge ratio can be calculated by precisely control over evaporation, which makes APT isotope sensitive. A schematics of how APT works is shown in Figure 2-16.

In early generations of APT instruments, field evaporation was induced by electric field pulsing. Since the introduction of laser assisted field evaporation technique, which enables analysis of low/non-conductive materials, and many other advancements in instrumentation in recent decades, APT has become popular rapidly in many field of materials science. Due to the small size of microstructural features, namely oxide particles, alpha-prime and radiation-induced segregation (RIS) at grain boundaries in nanostructured ferritic alloys, quantitative analysis using high resolution transmission electron microscopy (HRTEM) is difficult. That makes APT a great complementary tool for obtaining those microstructural and chemical information.

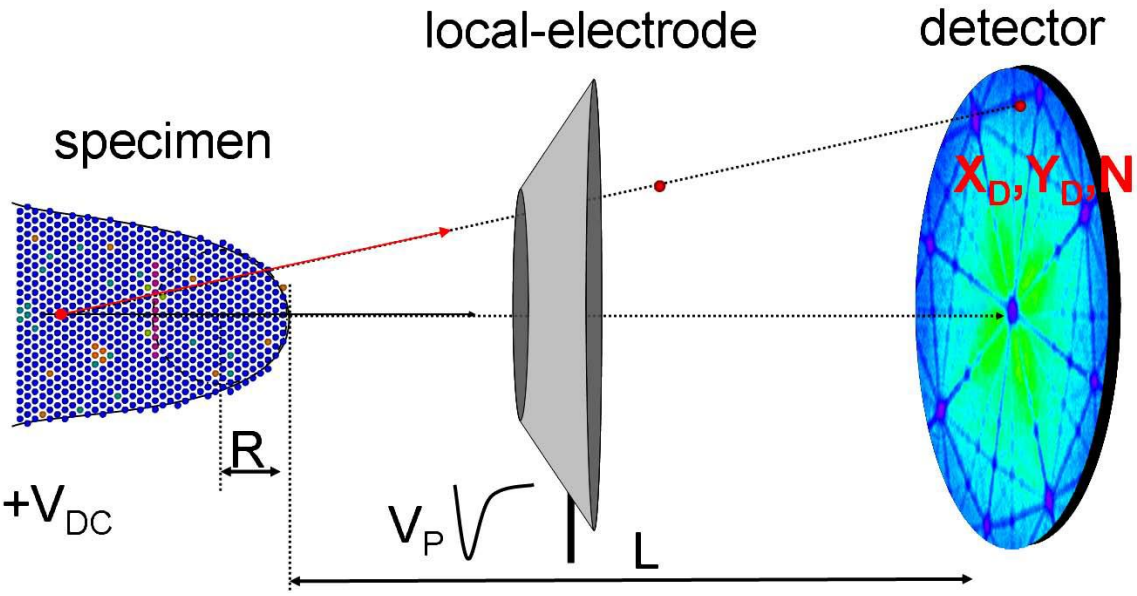

Figure 2-16. Schematic view of the local electrode atom probe, X_D, Y_D are the coordinates of the impact of the ion on the position sensitive detector, N refers to the position of atom within the sequence of detected atoms [113].

2.5.1 Pulsed Field Evaporation

The electric field at surface of APT needle specimen surface can be expressed as:

$$F = \frac{V}{k_f R} \tag{2.4}$$

where F is the induced electric field, V is applied voltage, R is the curvature of APT needle apex and k_f is the field factor. When the applied voltage is high and specimen curvature is small, electric field near apex can be strong enough to cause polarization, pull surface atoms away and eventually induce ionization. A brief overview of proposed field evaporation theories can be found in reference [114]. The exact mechanisms involved in field evaporation is still unclear. It is commonly assumed that ionization and desorption of atoms occurs by overcoming an energy barrier via thermal activation. The probability of field evaporation can be written as:

$$P_{evap} \propto \exp\left(-\frac{Q(F)}{k_B T}\right) \tag{2.5}$$

where *Q(F)* is the energy barrier dependent on the electric field *F*. *T* is temperature and k_B is Boltzmann constant. In general, the larger the field *F*, the smaller the energy barrier. To keep a fixed probability of field evaporation, there are infinite number of combinations between *Q(F)* and *T*. Thus, two different modes can be applied to induce the same field evaporation rate: the voltage (field) pulsing mode and the laser (thermal) pulsing mode, as shown in schematics in Figure 2-17.

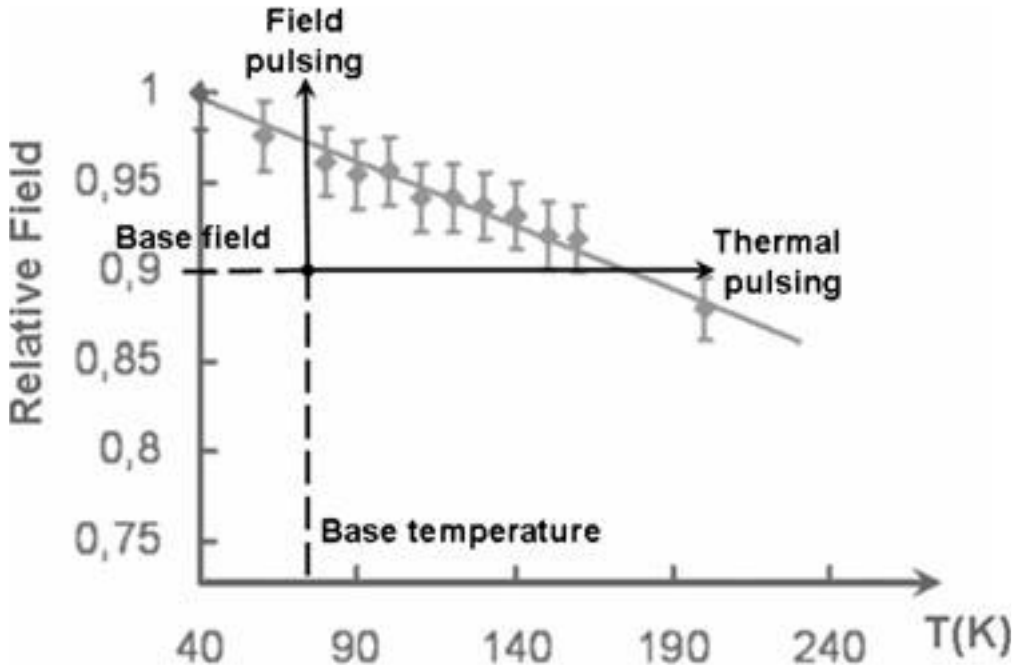

Figure 2-17. Schematics view of pulsing modes [114]. The relative field is the ratio between a field and the field needed to bring energy barrier to zero.

2.5.2 Principles of Tomographic Reconstruction

Tomographic reconstruction of data into three dimensional space with sub-nanometer resolution is probably what makes APT powerful compared to traditional microscopy where information is gathered in 2D projection. The sequence number, spatial coordinates (X_D, Y_D) on detector, and time-of-flight of each collected ions are

recorded in APT. A reconstruction model that specifies methods to calculate ions positions is then applied. In general, the z coordinate (depth) of an ion is calculated based on evaporation order of sequence and spatial coordinate (x, y) is calculated based on signal position in the detector. The mass-to-charge ratio of ion is calculated using time-of-flight principle and the identity of ion is determined by matching user-defined mass ranges in mass spectrum. However, tomographic reconstruction for APT is rather complex and there is no "correct" or "perfect" reconstruction model [113, 115-117].

In general, current reconstruction model employs a reverse projection method that project detected ion back to a series of curvature surfaces. A schematics for a general reconstruction approach is illustrated in Figure 2-18. The first assumption is that apex surface of APT needle is part of a sphere with radius of R. Usually R is too small to be accurately measured when fabricating specimens in FIB. It is then usually deduced from equation (2.4) with user-defined field factor k_f. The applied voltage V can be taken from experimental conditions recorded by instrument. The evaporation field F in equation (2.4) is typically taken as a constant value for a given material and can be determined from modeling of field evaporations. Image compression factor, ξ, controls the position of point P, which is the center point of reverse projection.

The depth coordinate of ion for reconstruction is deduced from ion evaporation sequence. It is usually assumed that ions are removed one by one and layer by layer and only those on the apex tip are removed. As ions evaporated, the specimen surface become farther away from detector. Thus the depth coordinate of new ion can be written as a function of previous ion's coordinate:

$$z_{tip}^{i+1} = z_{tip}^{i} + dz \tag{2.6}$$

where z is depth coordinate, i is ion sequence number and dz is depth increment. The depth increment is related to analyzed volume:

$$dz = \frac{n_{evap}\Omega}{\eta w_v(z)} \tag{2.7}$$

where n_{evap} is number of evaporated atoms, η is detect efficiency, Ω is average atomic volume and $w_v(z)$ is a function describing change of analyzed volume of specimen with respect to depth.

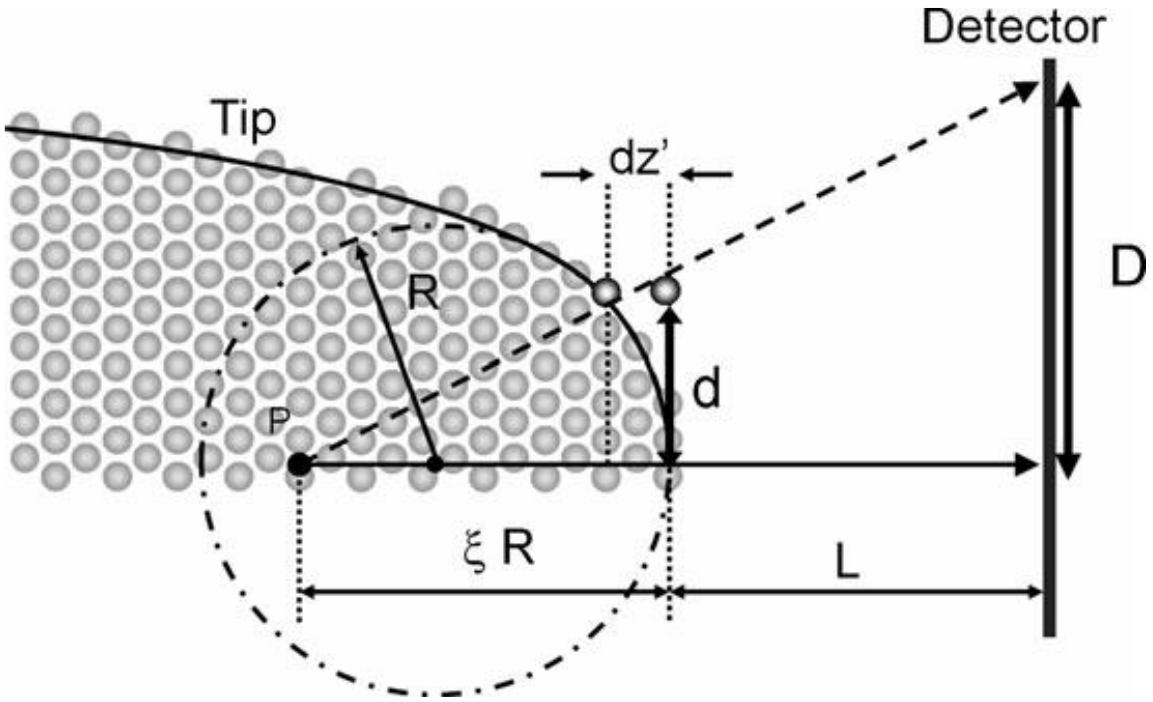

Figure 2-18. Schematics for reconstruction approach following Bas et al. protocol [116].

Note that although changes in field factor, k_f, or image compression factor, ξ, lead to noticeable changes in the shape of reconstructed volumes, all current model abides the conservation of analyzed volume. A demonstration of reconstruction parameter's effect on reconstructed data is shown in Figure 2-19. Although more advanced reconstruction models are progressing, the image compressing factor and field factor are still difficult to determine and they could be specimen-specific. Several reconstruction calibration techniques have been proposed during the past decade. For example, the crystallographic features can be used to calibration both k_f and ξ by

matching reconstructed inter-planar distance with theoretical values; the initial and final curvature radius of APT specimen can be observed by TEM or SEM so that geometry for analyzed volume can be roughly determined.

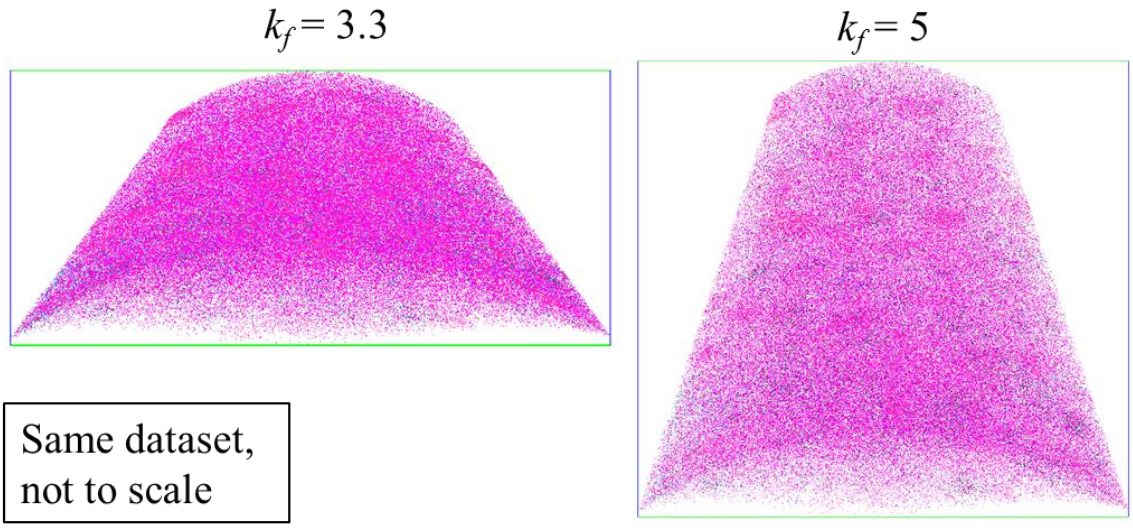

Figure 2-19. A demonstration of reconstruction parameter effects on shape of reconstructed volume for the same dataset.

Although APT has provided many great insights via enabling visualization of 3D chemical distributions in material, it shall not be forgot that successful reconstruction relies on a variety of assumptions in the reconstruction models. There are cases where simple point-projection model may fail, such as in thin film layered structures if evaporation fields are very different from layer to layer. Another intrinsic limitation is the radial evolution can sometimes become ambiguous, e.g. the APT specimens' apex curvature may be fitted with multiple radius, or too irregular to be properly fitted. Reconstruction procedures assume field evaporation is uniform throughout APT specimen, which is likely true for pure elements but may not hold for complex materials. One notorious reconstruction artifact is the trajectory aberration where local ion positions are heavily distorted due to different evaporation field across interfaces [118-

121]. Tomographic reconstruction is still advancing in the APT community. Several reconstruction based on other principles have been proposed and tested recently. For example, Peterson and Ringer developed an algorithm to correlate geometry of APT tip using electron tomography to guide APT reconstruction [122]. Vurpillot et al. tested an alternative method to stack field desorption map layer-by-layer for reconstruction instead of using point-projection model [123].

3 EXPERIMENTAL

3.1 Materials: ODS Alloy MA957

The target material in this study is an ODS alloy, MA957, that came from comprehensive irradiation tests decades ago in the U.S. Liquid Metal Fast Breeder Reactor (LMFBR) Program. MA957 purchased from International Nickel Company (INCO) were fabricated into pressurized tubes for creep study and were then irradiated at FFTF in the Materials Open Test Assembly (MOTA). The detailed fabrication procedures can be found in several U.S. Department of Energy reports [96, 97]. A brief description of differences in fabrication procedures is listed in Table 3-1. The nominal composition of MA957 is Fe-14Cr-1Ti-3Mo-0.25Y_2O_3. Table 3-2 listed bulk compositions of selected heats. It can be seen that those two are almost identical in terms of chemical compositions.

Table 3-1. Fabrication and heat treatments of MA957 selected for this study.

Heats	DBB0111 (EV), DBB0122 (TX)
Fabrication	EV: Drawn bar, followed by gun drilling to final dimensions. TX: Same but drilled and tube drawing.
Final Heat Treat	760°C/30 min/AC

Table 3-2. Bulk composition (wt%) of unirradiated MA957.

Alloy	Tube ID	Heat	Cr	Ni	Mn	Mo	Si	C	V	Ti	Y_2O_3
MA957	EV	DBB0111	13.8	0.13	0.05	0.31	0.05	0.014	--	1.05	0.22
MA957	TX	DBB0122	14.2	0.10	0.06	0.31	0.03	0.014	--	1.03	0.22

Figure 3-1 shows a photo of a pressurized tube and specimens cut from it. From each tube, a ring tensile specimen, two dog-bone tensile specimens, four TEM disk size 3 mm specimens, and several 1.0 mm by 0.5 mm by 0.5 mm sample coupons (not shown here) were extracted. Microstructures examined by scanning electron microscopy (SEM) are shown in Figure 3-2. Grain structures of MA957 show a large degree of anisotropy, elongated along the axial direction, due to hot extrusion processing during materials fabrication.

Figure 3-1. Photo of pressurized tubes and specimens cut from it.

These heats of MA957 have been investigated to some extend previously. MA957 EV tubes irradiated by neutron from 412-750°C were initially investigated for creep and swelling by Toloczko et al. [44, 53]. Microstructures of some of neutron irradiated TEM disks were reported in reference [96]. Characterization of oxide particles

has been reported by Bailey et al. using APT [91] and by Edward et al. using TEM [124]. An ion irradiation study that focused on void swelling in MA957 EV heat has been published by Toloczko et al. [45].

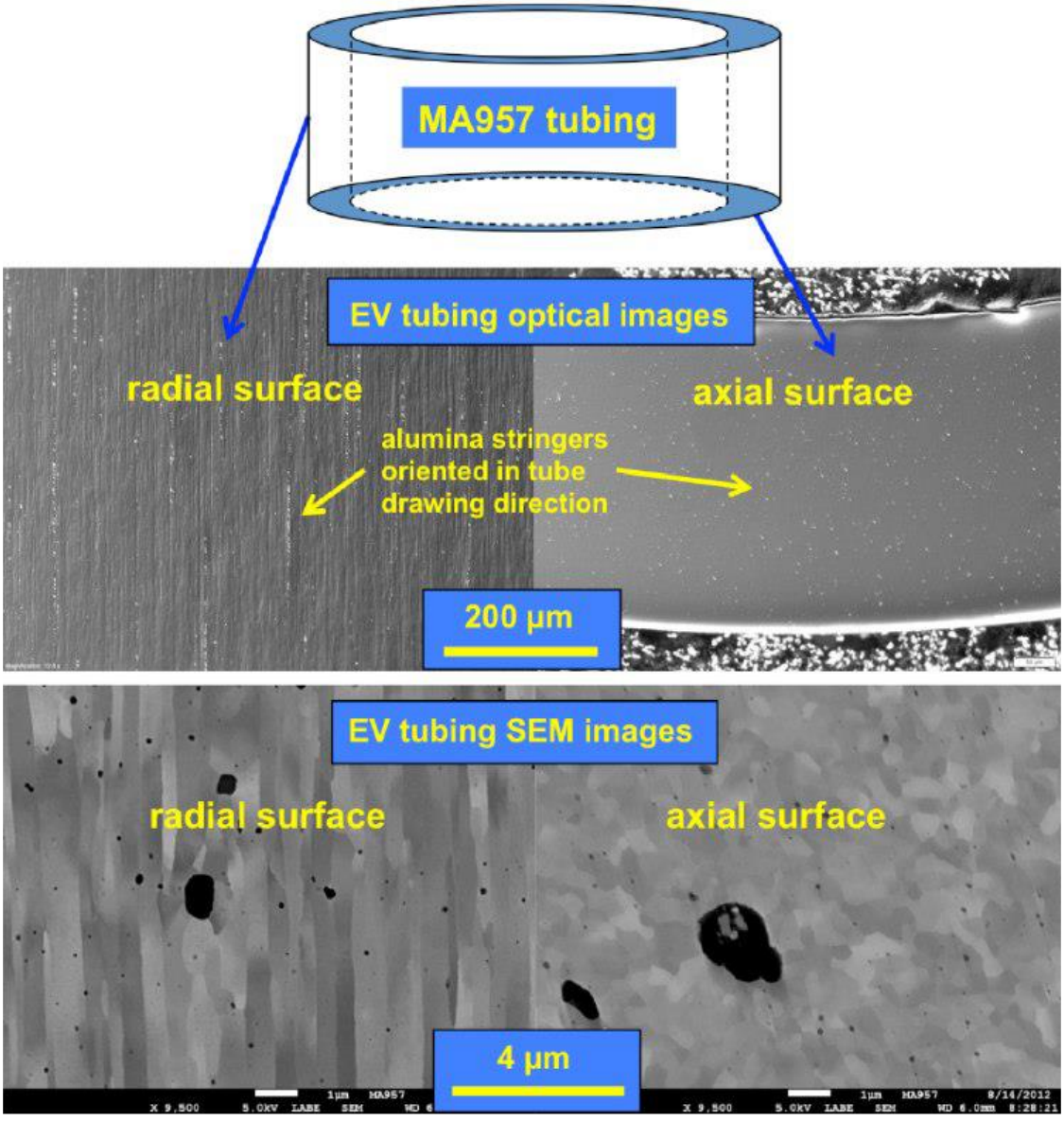

Figure 3-2. Optical and SEM images of grain structures of MA957 under radial or axial orientations.

3.2 Neutron Irradiation Experiments

MA957 pressurized tubes were neutron irradiated in FFTF/MOTA. One powerful aspect of MOTA is that it is designed to carry-out irradiation experiments for materials. Specimen temperature was closely monitored and controlled to minimize temperature uncertainty associated with in-reactor testing [125]. Pressurized tubes of two heats MA957 (DBB0111 (EV) and DBB0112 (TX)) that were irradiated to 43-113 dpa at 385-550° C are selected for microstructural characterization to investigate neutron irradiation effects. The detail neutron irradiation conditions are shown in Table 3.3.

Table 3-3. Neutron irradiation conditions of pressurized tube.

Tube	Creep Stress (MPa)	Dose (dpa)	Temp (°C)
TX	0	43	385
EV	60	109	412
TX	0	48	495
EV	60	113	550

3.3 Ion Irradiation Experiments

3.3.1 Specimen Preparation

3 mm TEM disk size specimens were cut from archive DBB0111 (EV) MA957 pressurized tubes. To make better thermal contact with hot stage, curved TEM disks were mechanically grinded to flat surface on both side of the specimen. The convex side was mechanical polished and then electro-chemical polished using jet polisher with chemical mixture of 90% ethanol and 10% perchloric acid. A DC voltage at 60V was applied between specimen and electrode. Electro-chemical polishing was performed to remove surface hardening layer, caused by mechanically polishing, since it was not representative of the bulk material.

3.3.2 Irradiation Conditions

Polished TEM disks were then clamped on hot stage and loaded in a Van de Graff accelerator at Kharkov Institute of Physics and Technology (KIPT). The target was then irradiated by at 1.8 MeV chromium ions and specimen temperature was closely monitored by thermal couple. Ion irradiation conditions are listed in Table 3-4. The ion irradiation damage and injected ion profiles are calculated by SRIM [77] in Kinchin-Pease mode with displacement threshold energy of 40 eV as suggested by Stoller et al. [10]. Calculated results are presented in Figure 3-3. Ion irradiation not only sputters atoms on the surface of target material but also injects a considerable amount of atoms into the material, which could potentially alter the SRIM-calculated profiles. This effect has been evaluated in by Wang et al. [30] using an iterative mathematical treatment. The result shows that the effective dose profile is shifted slightly toward the surface for 1.8 MeV ion irradiation. Microstructural characterization by TEM for MA957 has been reported previously [126, 127].

This study focused on experimental results for specimens irradiated at 100 dpa, so that they can be compared with results from neutron irradiated specimens. Oxide particle sizes of 500 dpa datasets will be used as an experimental reference to assess ballistic dissolution effect to be compared with theoretical calculation in section 5. The void swelling study in this material matrix has been published elsewhere by Toloczko et al. [45].

Table 3-4. Ion irradiation conditions for MA957 specimens. Note that only 100 dpa specimens were presented in details for this study.

400°C 100 dpa				400°C 500 dpa
420°C 100 dpa				420°C 500 dpa
450°C 100 dpa	450°C 200 dpa	450°C 300 dpa	450°C 400 dpa	450°C 500 dpa
500°C 100 dpa				500°C 500 dpa

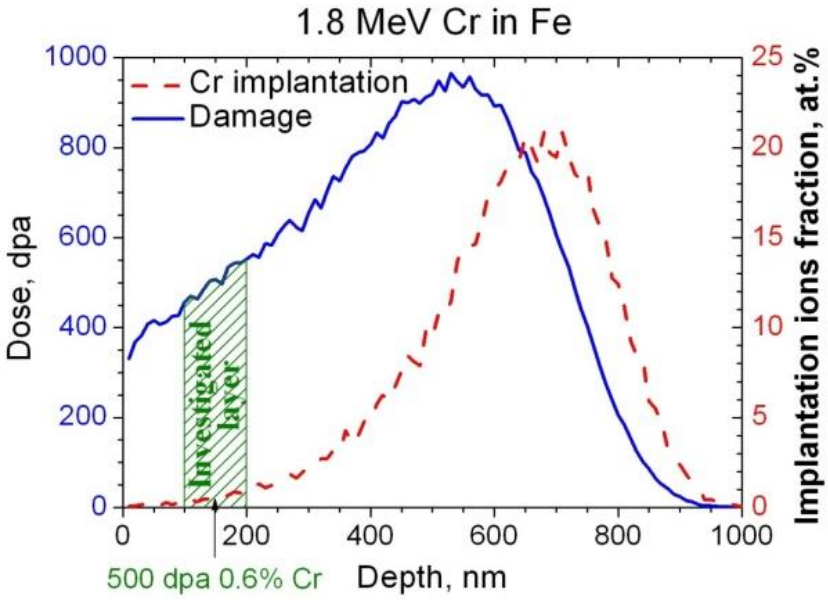

Figure 3-3. SRIM calculated damage and injected ions profiles using Kinchin-Pease mode for 1.8 MeV Cr.

3.4 Atom Probe Tomography

3.4.1 Specimen Preparation

APT needle specimens were fabricated via lifting out from the pressurized tube specimens, mounting on micro-post array, and annular milling by using FEI Quanta Dual-Beam focused ion beam (FIB). Before lift-out, a protective layer of platinum was firstly deposited on the surface of the specimen. Sections around each edge of the protected area were milled to forming a wedge-shaped bar. The sample was then attached to a probe tip with Pt, cut from the rest of material, and lifted out using an Omniprobe. The lifted wedge was then cut and weld to a silicon micro-post on silicon coupon. The mounted material was annular milled from the top, forming a sharp tip with an end radius of ~100 nm. All finished tips were subjected to a final mill at a low energy (a few keV) in order to remove the gallium-contaminated layer from the surface of the tip. The detail descriptions about APT needle fabrication procedures can be found in Thompson et al. and Miller et al. [128, 129].

As mentioned in previous section for materials, several 1.0 mm by 0.5 mm by 0.5 mm sample coupons were EDMed from those tubes and APT specimens were lifted out from them. For ion irradiated MA957, APT needle specimens were pulled from irradiated TEM disk specimens. All APT needle specimens for neutron irradiated MA957 were fabricated at University of California Berkeley and all needle specimens from ion irradiated MA957 were prepared at PNNL in similar procedures [130].

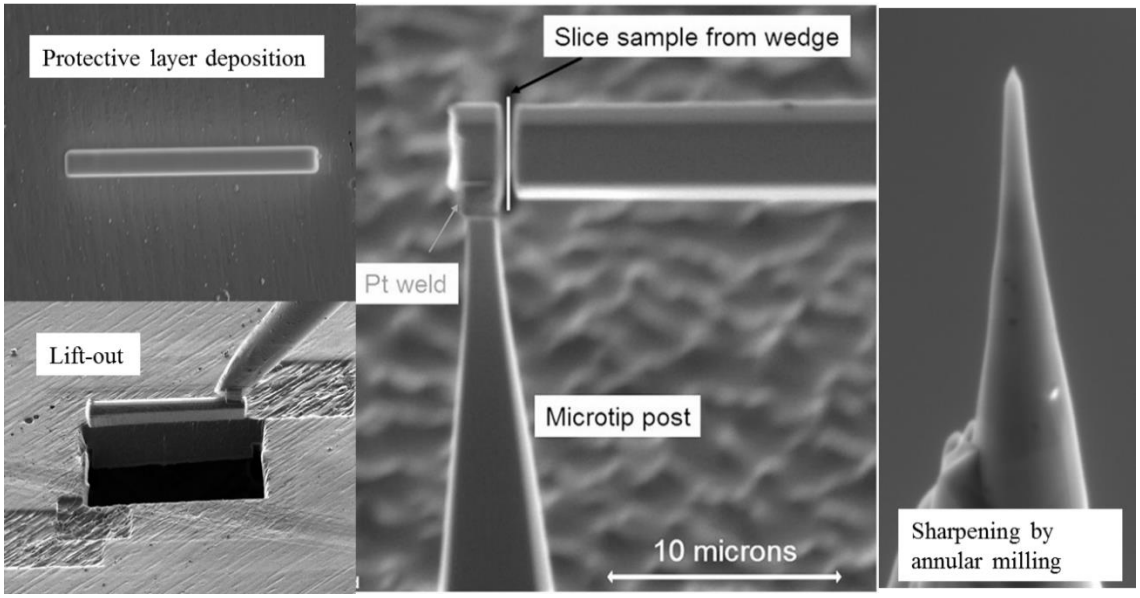

Figure 3-4. Typical process for making APT specimens. From left to right are lift-out, staging on to a silicon post, and sharpening. Note that slicing sample from wedge was taken from reference [129]. All other images are from our own data.

3.4.2 Experimental Conditions and Specimen Matrix

APT analysis was carried-out using a CAMECA Local Electrode Atom Probe (LEAP) 4000X HR at Environmental Molecular Science Laboratory (EMSL) at Pacific Northwest National Laboratory (PNNL). Both high-voltage (HV) pulsing or laser pulsing modes were used for data collection. Due to historical reasons, all datasets of neutron irradiated specimens were collected using HV pulsing mode and all datasets of ion irradiated specimens were collected using Laser pulsing mode. Typical operation parameters are: repetition rate of 200-250 kHz, evaporation rate of 0.3-0.5%, specimen temperature of 40-60 K, and pulse fraction of 20% for high-voltage pulsing mode or laser energy of 40-60 pJ for laser pulsing mode. Obtained datasets were reconstructed from the datasets using the Integrated Visualization and Analysis Software (IVAS) version 3.6.12. Because APT only provides information on a very small volume of material (~60×60×100 nm), multiple APT tips were prepared and analyzed for each

specimen to generate data with good statistics. The number of APT tips examined per material and irradiation condition is summarized in Table 3-5 and Table 3-6.

Table 3-5. APT specimen matrix for neutron irradiated MA957.

Temp (°C)	Dose	Tube	No. of APT Tips	Total Ions Collected (million)	Volume ($\times 10^6$ nm^3)
385	43	TX	9	25	0.79
412	109	EV	8	33	1.06
495	48	TX	7	16	0.49
550	113	EV	7	33	1.07

Table 3-6. APT specimen matrix for ion irradiated MA957.

Temp (˚C)	DPA	Tube	No. of APT Tips	Total Ions Collected (million)	Volume ($\times 10^6$ nm^3)
400	100	EV	9	143	4.57
	500		4	39	0.93
420	100		6	65	2.07
	500		8	58	1.84
450	100		6	47	1.65
	300		3	25	0.78
	500		3	22	0.70
500	100		8	75	2.39
	500		4	10	0.33

3.4.3 Data Analysis and Interpretation

Data analysis and interpretation are non-trivial for APT. In this study, iso-concentration surface approach was used for precipitate identification and analysis [131]. Iso-concentration surface is a computed 2D contour surface on which the sum of ion concentrations equals a user-defined value. The region inside a closed surface can be considered as a potential precipitate and region outside can be regarded as the matrix.

The concentration threshold is usually determined by using dominant ion species in those precipitates or clusters, e.g. Cr for alpha-prime, Y, YO, TiO for oxide particles.

Examples of an ion map and iso-concentration surfaces for YTiO oxide particles are shown in Figure 3-5a) and b). Note that all particle sizes are measured in terms of radius, which are converted from iso-concentration enclosed volumes by assuming a spherical geometry. Number density of clusters is calculated by dividing *effective total number, N_{eff},* by *total analysis volume, V*. Some clusters are only partially included in the analyzed volume, and they are counted as contributing partially (half) to the effective total number of clusters. That is, $N_{eff}=N_{enclosed} + 0.5\times N_{partial}$. Cluster size distributions are calculated using only fully enclosed clusters. Choice of cluster identification directly affects measured results of physical quantities for precipitates in APT datasets. The iso-concentration surface method was applied due to its simplicity and good consistency. Proximity histograms (proxigrams) are radial concentration profiles calculated based on iso-concentration surfaces. It is useful to estimate composition of iso-concentration defined clusters. An example of proxigram is shown in Figure 3-5c).

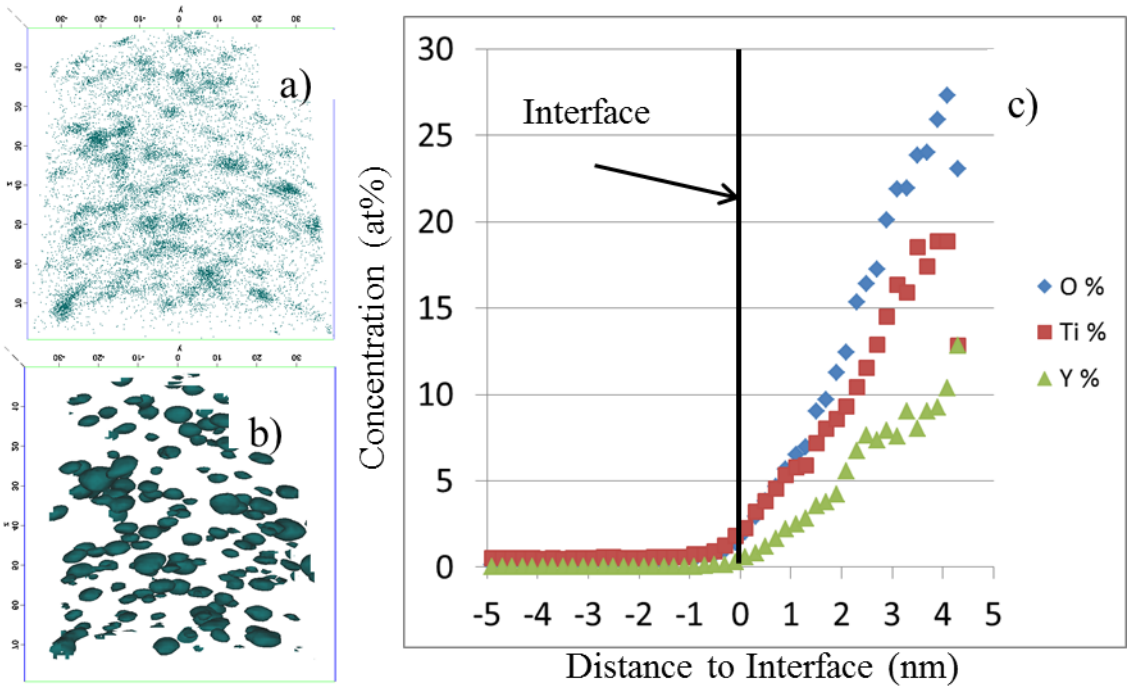

Figure 3-5. Examples of ion map, a), iso-concentration surface, b), and proximity histogram (proxigram), c). The YTiO number density for this particular dataset is 4.4×10^{17} cm^{-3}, volume fraction is ~2.2%.

Table 3-7 lists APT measured composition for unirradiated MA957 and compared with bulk composition. It can be seen that those values are quite close to each other, even though analysis volume in APT is small. Vanadium has been detected in MA957 while it is not reported in nominal composition. Both Ti and Y concentrations are lower than measured in bulk. It can be attributed to the small APT analysis volume where large but low density particles containing Ti, Y and O are difficult to be picked up.

GB chemistry was analyzed using 1D concentration profiles with fixed bin width along the direction that perpendicular to the GB plane. The measured concentration is usually expressed as ionic% or atomic%. The ionic percentage treats each species of identified ions, single or molecular, as an individual constituent and calculates their corresponding proportions in total number of ions; the atomic percentage breaks

molecular ions into corresponding numbers of atoms and calculates atomic proportions for each element type. In our system, values using these two units are usually close for major metallic ion species, but could be significantly different for elements like oxygen that heavily participate in molecular ions formation. Most GB chemistry results were presented in the unit of at%. Ionic% was used for TiO, Ti and Y due to strong correlation of TiO and Y with the presence of Y, Ti and O enriched particles. Simply decomposing TiO into Ti and O atoms did not properly represent oxide particles' behavior with respect to GBs.

Table 3-7. Comparison of APT-measured composition with nominal values in EV and TX MA957.

Alloy	Tube ID	Method	Cr	Ni	Mn	Mo	Si	C	V	Ti	Y	O
MA957	EV	By APT	14.31	0.16	0.05	0.30	0.05	0.01	0.04	0.48	0.08	0.11
MA957	EV	Nominal	13.8	0.13	0.05	0.31	0.05	0.014	---	1.05	0.17	0.05
MA957	TX	By APT	14.50	0.16	0.07	0.33	0.04	0.01	0.05	0.68	0.09	0.09
MA957	TX	Nominal	14.2	0.10	0.07	0.31	0.03	0.014	---	1.03	0.17	0.05

4 EXPERIMENTAL RESULTS

4.1 Evolution of YTiO Particles

4.1.1 Unirradiated MA957

Before going deeper into comparison between neutron and ion irradiated MA957 results, a baseline must be established for APT results for YTiO particles obtained via high-voltage (HV) pulsing and laser pulsing. Because the tasks for microstructural characterizations of neutron or ion irradiated MA957 are independent at the beginning, portions of neutron data had been obtained under HV pulsing mode and some ion data had been obtain in the laser mode. Data collections for each task were continued as in the original mode after the neutron-ion comparison objective was setup to fully utilize resources. Although consistency was maintained within each data series, the differences between measured quantities must be evaluated for comparison across neutron or ion irradiated material data sets.

Ion maps for ions that are major constituents of YTiO particles (Ti, O, TiO, Y and YO) are shown below in Figure 4-1. The presented data set was obtained from the same APT needle (within the same grain) to minimize grain-to-grain variabilities. Data collection was first performed under HV pulsing and then switched to laser pulsing. APT analysis on other needles followed the same approach. TiO and Y ion maps made in HV and laser modes are visually similar. But O and YO maps exhibited noticeable differences: oxygen ions are less diffuse and YO population is significantly lower in HV pulsing mode than laser pulsing mode. The oxygen-rich region at the very top of HV pulsing data is likely from oxidation.

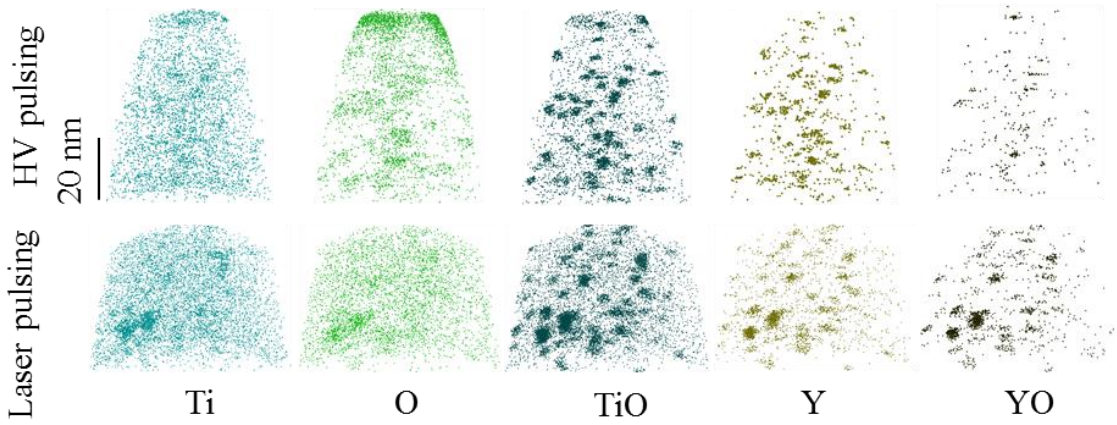

Figure 4-1. Ion maps of several elements of interests for datasets collected under HV pulsing and laser pulsing mode in one unirradiated MA957 needle.

A demonstration of the iso-concentration surface method is presented in Figure 4-2 for unirradiated MA957. The defined oxide clusters are overall in generally good agreement with cluster identification in ion maps using human visual inspection. As we can see, some very small clusters may not be detected with this method. The size, number density, and volume fraction for this dataset are listed on the right of Figure 4-2, and they are typical values detected in unirradiated specimens.

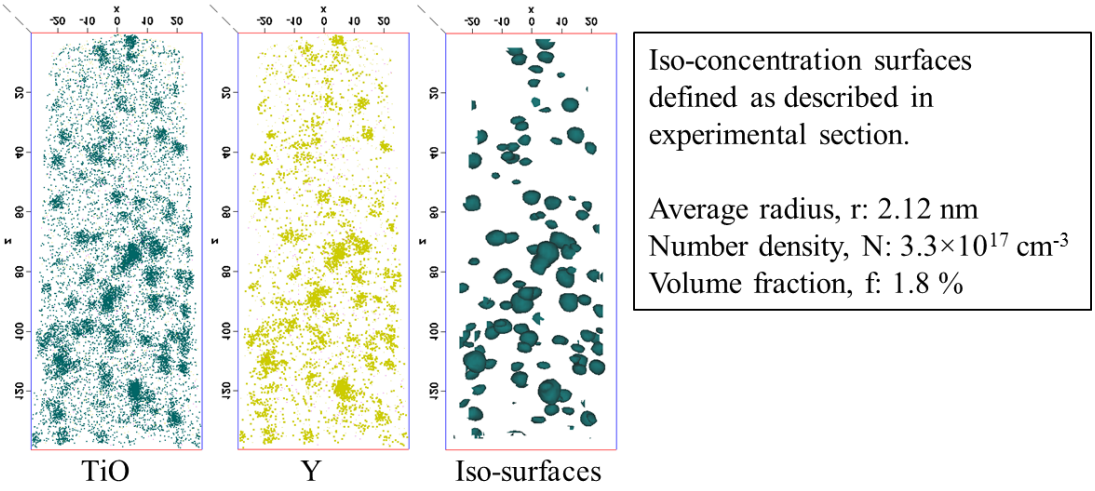

Figure 4-2. An example of cluster identification using the iso-concentration method and statistics for oxide particles obtained using this method.

HV mode vs. Laser mode

As mentioned before, HV mode was used to collect neutron irradiated specimen data and laser mode was applied for ion irradiated specimens for historical reasons. The differences between the two operation modes can be many; however, only effects on oxide particle measurements and its potential solution will be discussed in this section. A systematic comparison of the effects of laser and HV operation modes on MA957 will be published in future study. To establish a baseline, multiple APT needles from the same unirradiated specimens (EV series) were fabricated and data were collected using either HV or laser operation mode.

The size distribution for unirradiated EV MA957 obtained via HV and laser modes is shown in Figure 4-3, in which systematic differences can be seen. Number density distribution are listed in Table 4-1 for YTiO particles and show similar results for data produced in HV and laser modes. On average, clusters defined using from HV mode datasets show smaller mean values than those obtained using laser mode. The size distribution in HV mode dataset is also slightly more symmetrical than that in Laser mode, in which a small fraction of large particles composes a long distribution tail.

Table 4-1. Comparison of number densities measured in unirradiated MA957 (EV) by APT using laser or HV modes.

Number Density of YTiO (cm^{-3}) in an APT Tip	Number of Tips in Each Range	
	HV Mode	Laser Mode
$< 1\times10^{17}$	1	0
1×10^{17} to 3×10^{17}	5	6
3×10^{17} to 5×10^{17}	3	3
$> 5\times10^{17}$	0	0

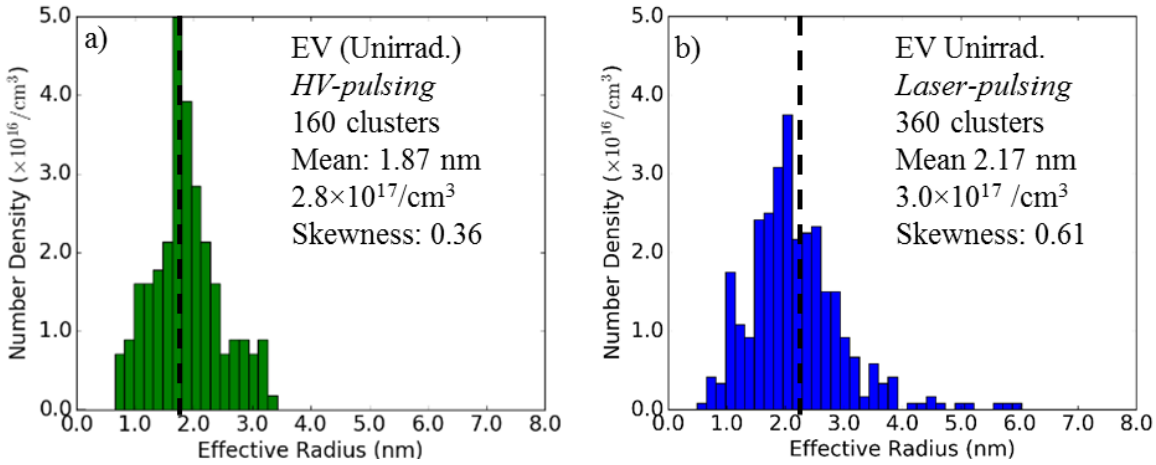

Figure 4-3. Cluster size distributions of YTiO in dataset collected via HV pulsing and laser pulsing in unirradiated EV MA957.

Whether two distributions are the same can be tested using a Kolmogorov-Smirnov (K-S) test. The K-S test is a statistical test that determines whether the null hypothesis, which is that two distributions were drawn from the same parent distribution, can be rejected. The K-S test implemented in the SciPy package returns a K-S statistics value and a confidence p-value. In general, if the K-S statistics value is large and p-value is small, the null hypothesis is rejected. The K-S test results for data from HV and laser modes are shown in Figure 4-4a). It can be seen that cluster size distributions obtained from HV and laser modes are statistically different. This systematic difference can be corrected if the sizes are normalized to the average values, as shown in Figure 4-4b). K-

S test result suggests that we cannot rule out the possibility that normalized size distributions are sub-distributions from the same parent.

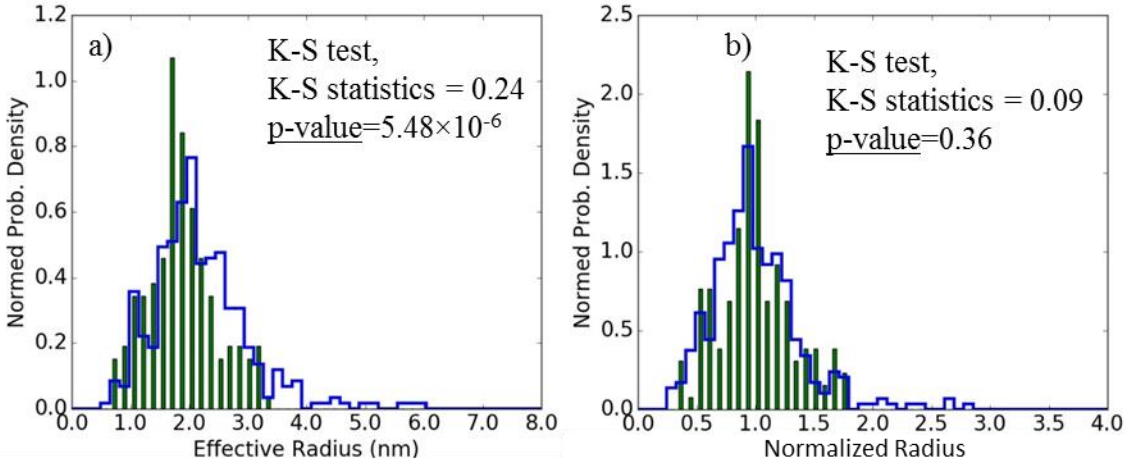

Figure 4-4. Size distribution K-S test results a) before and b) after normalization to mean particle radius in both HV (green bars) and laser (blue outline) modes.

The explanation for the systematic differences may be two-fold: first, an underestimation of yttrium in HV mode would lead to a smaller radius if the same concentration criterion is used for constructing an iso-concentration surface; second, a higher effective evaporation field in HV mode would reduce the trajectory aberration of elements [110]. Figure 4-5 shows that both measured overall yttrium and oxygen concentrations in the entire tip and measured yttrium percentages inside clusters are higher in the laser-pulsing mode than in HV mode. This result indicates potential loss of yttrium when operated under HV pulsing mode.

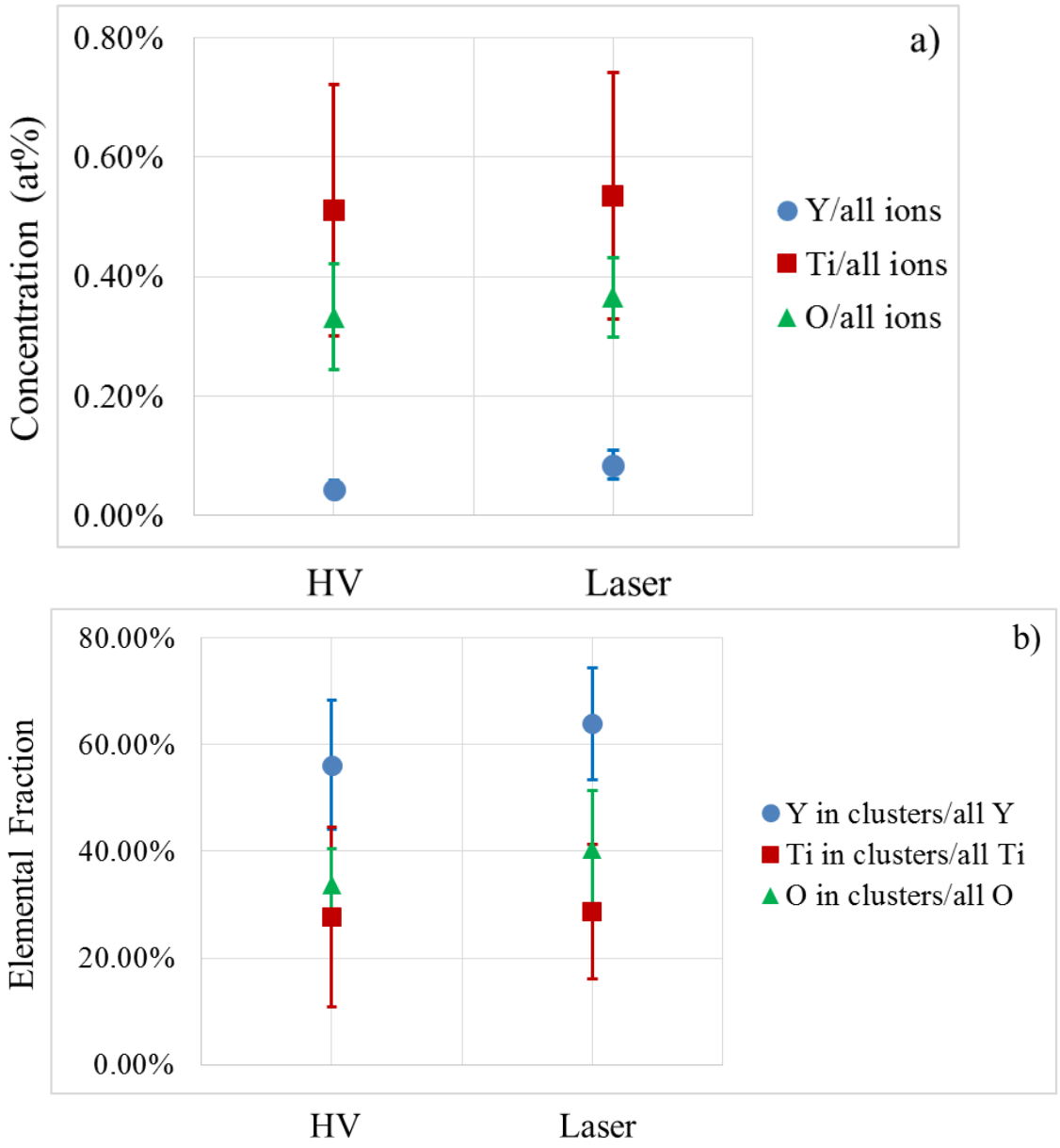

Figure 4-5. Comparison of results obtained with laser and HV modes: a) concentrations of Y, TiO and O with respect to all ions and b) percentage of Y in clusters with respect to all ions of the same species in the tip.

Heat TX vs. Heat EV

The size distributions of YTiO oxide particles in unirradiated TX and EV MA957 are shown in Figure 4-6. Oxide particles in both materials follow comparable but not identical size distributions, with most of them falling within 0.5 to 3.5 nm and the average sizes are 1.79 and 1.87 nm for TX and EV, respectively. Both distributions are in the bell-curve shape with very similar mean values, although the distributions are not identical. The number densities of oxide particles are 2.6×10^{17} /cm^3 for TX and 2.8×10^{17} /cm^3 for EV. All TX data will be colored magenta and all EV data will be colored dark green in the following results. Size distributions and number densities were obtained from a total of nine APT tips for TX and eight APT tips for EV MA957.

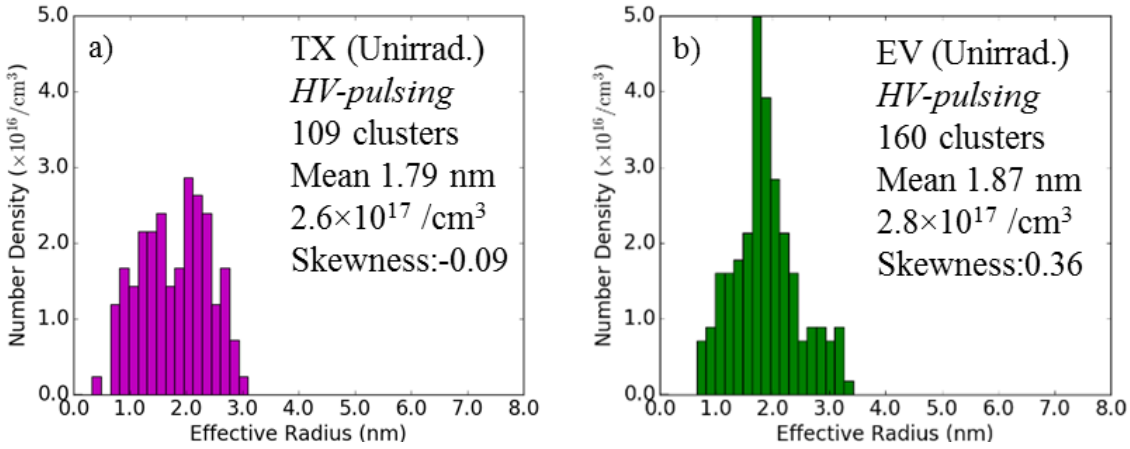

Figure 4-6. YTiO oxide particle size distributions for unirradiated MA957: a) TX; b) EV. Note that the y-axis represents number density of particles with corresponding sizes. The YTiO clusters are defined at a 2 ionic% iso-concentration surface for the sum of Y, YO and TiO. Particle size is measured in radius.

4.1.2 Neutron Irradiated MA957

Typical ion maps of Ti, O, TiO, Y and YO in neutron irradiated MA957 are shown in Figure 4-7. The numbers of detected oxide particles are distinctly different based on irradiation temperature regime. High number densities of YTiO particles are

observed after 385 and 412°C irradiation, while irradiation at 495 and 550°C changes number density a little. Ti ions, although slightly enriched in oxide particles, do not appear strongly associated with oxide particles visually due to interference of relatively high solution concentration.

Figure 4-8 shows the size distributions of YTiO particles in both TX and EV MA957 specimens after neutron irradiation. Compared with the unirradiated specimens in Figure 4-6, it is clear that neutron irradiation altered oxide distributions in specimens. At lower temperatures, 385°C for TX (Figure 4-8a) and 412 °C for EV (Figure 4-8c), both distributions skew positively (toward smaller sizes); while at higher temperatures, 495°C for TX and 550 °C for EV, particles grow larger, as shown in Figure 4-8b and d. Concurrent with increasing sizes, the number densities of YTiO particles dropped at higher temperatures. A higher proportion of small size particles is consistent with irradiation induced recoil dissolution. Since TX specimens were irradiated to 43-48 dpa, we could expect that oxide particles would continue evolving and the differences between TX and EV might diminish if higher doses were achieved. Even under different doses, size distributions are comparable in specimens irradiated at similar irradiation temperatures, as shown in Figure 4-8a and c. However, YTiO number density is higher in the sample irradiated to 109 dpa than that in material irradiated to only 43 dpa.

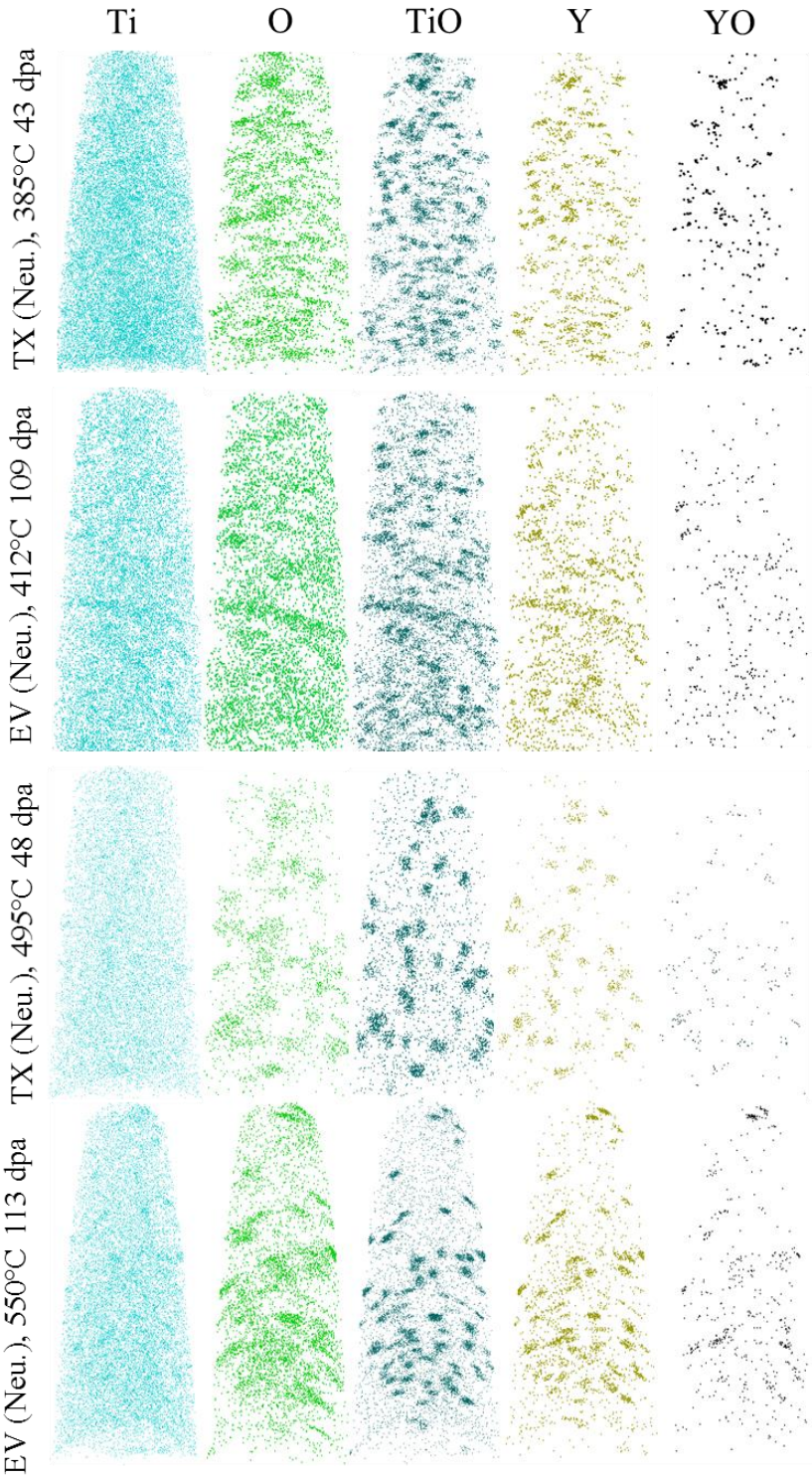

Figure 4-7. Typical ion maps (Ti, O, TiO, Y and YO) for elements of interest in neutron irradiated MA957.

Irradiation temperature is a key factor that affects precipitate evolution. Figure 4-9 plots average sizes and number densities of YTiO particles in neutron irradiated materials. The average sizes of oxide particles can be clearly categorized into two groups when compared with values in unirradiated material: those who shrink at temperatures ~400°C and those that coarsen above ~495°C. Interpolating from current data, the transition temperature from shrinking to coarsening seems to fall within 450-500°C. All specimens irradiated below 550°C exhibited increasing populations of YTiO particles to some extent. As noted previously, neutron dose differences may or may not change the current trend in plots. For example, the size of oxide particles may be further reduced and number density may be increased correspondingly at 385°C.

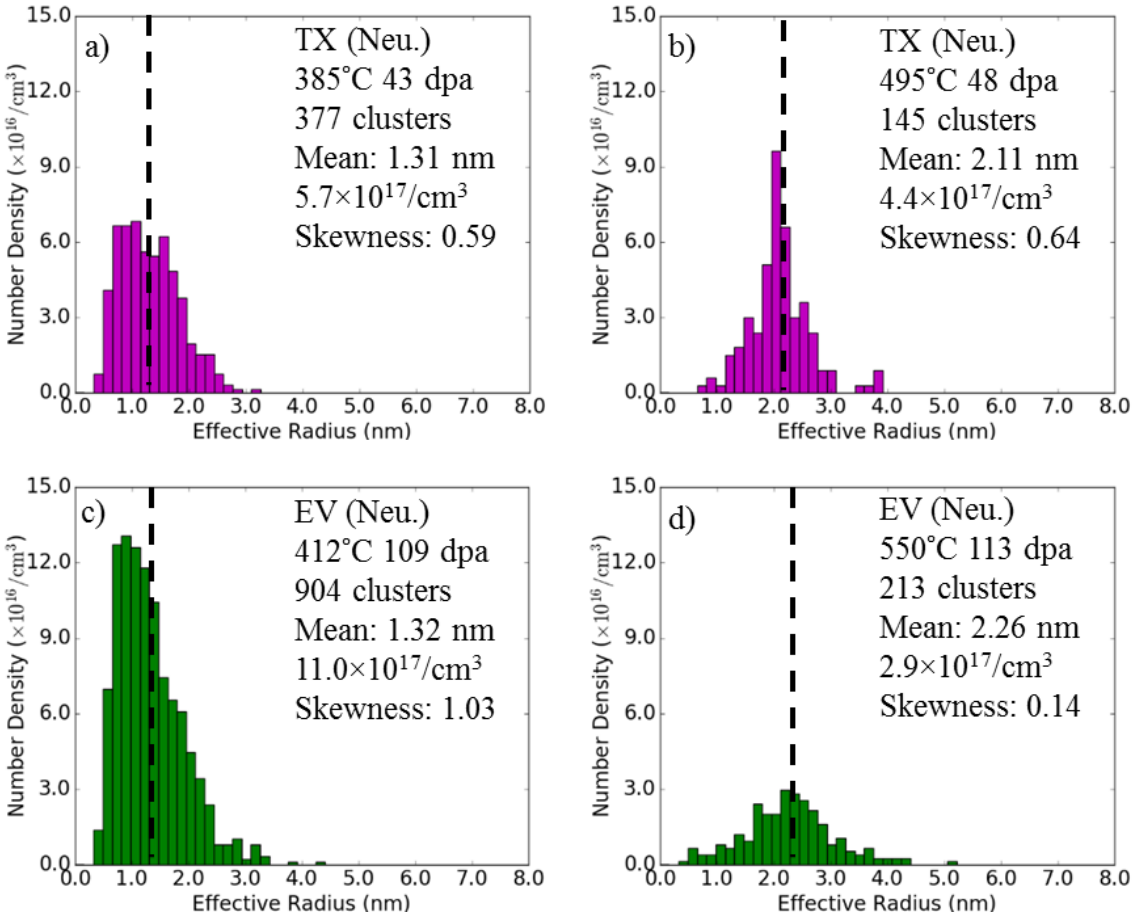

Figure 4-8. Size distributions of YTiO particles in neutron irradiated TX and EV materials.

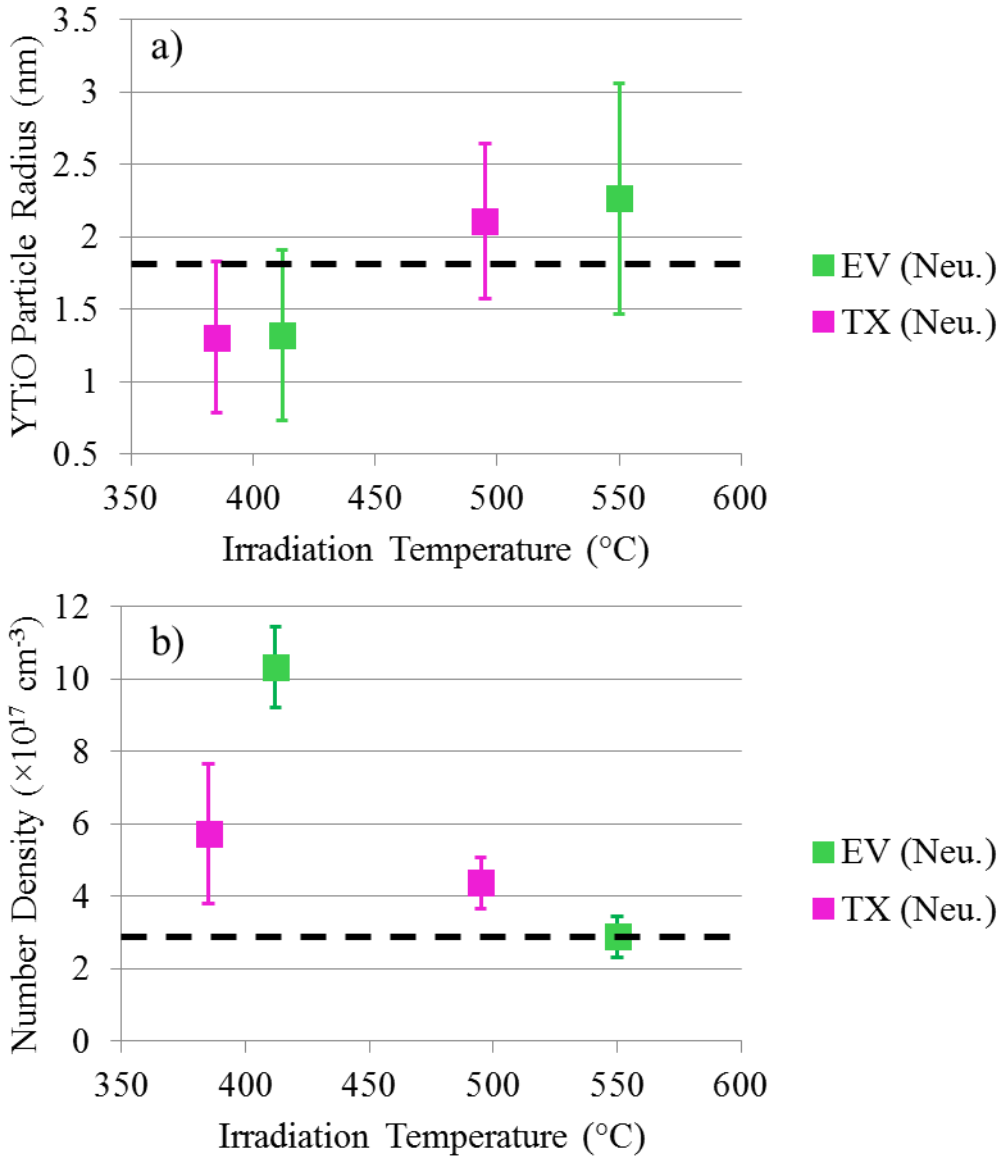

Figure 4-9. Comparisons of a) particle sizes and b) number densities with respect to irradiation temperatures in neutron irradiated material. Black dotted lines in both figures indicate values in unirradiated material.

4.1.3 Ion Irradiated MA957

Typical ion maps of Ti, O, TiO, Y and YO in MA957 irradiated by Cr ions to 100 dpa are shown in Figure 4-10. Morphologies of YTiO particles are distinctly

different depending on irradiation temperature. Nano-oxide interfaces appears quite blurry and lost its sharpness in MA957 irradiated at 400°C. This phenomenon is alleviated at 420 and 450°C, where contrast between clusters and matrix is stronger. Number density of particles also is higher at those temperatures. In addition to common fine particles, several extra-large (radius > 5nm) precipitates consisting of Y, Ti and O also exist in the analysis volume. This type of particles has been observed multiple times in datasets collected by laser mode but are much less frequent in HV mode.

The size distributions of YTiO clusters in unirradiated specimens and in specimens irradiated with Cr ions at 400, 420, 450, and 500°C are shown in Figure 4-11. The size distribution in unirradiated specimen, shown in Figure 4-11a, follows a bell-curve-like distribution with a mean radius of ~2.17 nm and standard deviation of ~0.83 nm. Several large oxide particles (5-10 nm), as have also been observed in some reconstructed datasets, are scattered in the distribution tail. In Figure 4-11b, mean sizes of oxide particles clearly shrank to 1.70 nm in specimens after irradiation at 400°C to 100 dpa. As irradiation temperature rises from 420 to 500°C, the size distributions become more similar to that in unirradiated materials, as shown in Figure 4-11c, d and e.

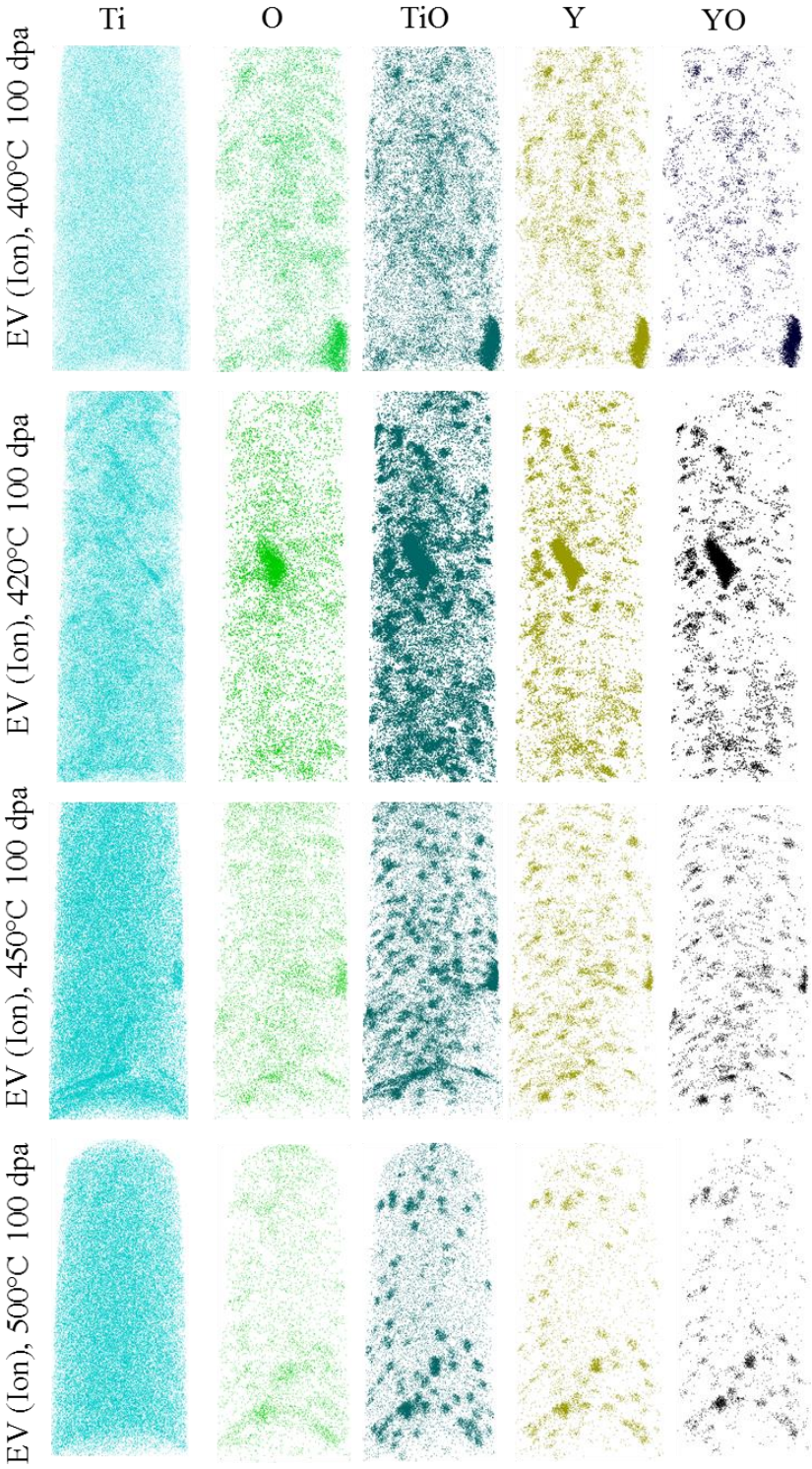

Figure 4-10. Typical ion maps (Ti, O, TiO, Y and YO) for elements of interest in MA957 ion irradiated to 100 dpa.

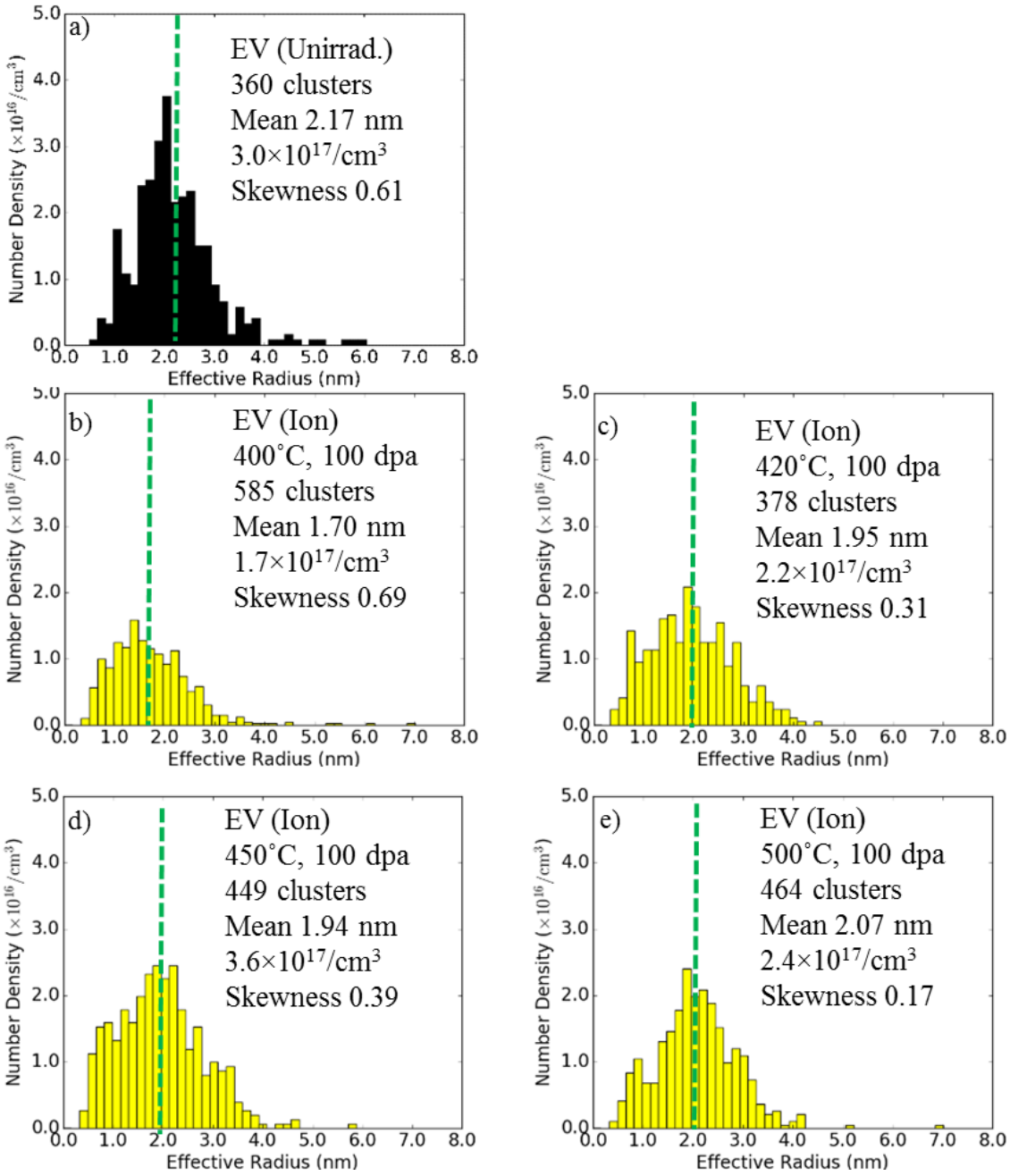

Figure 4-11. Size distribution (in radius) of YTiO clusters in unirradiated and ion irradiated MA957. Histograms are colored based on dpa: unirradiated-black, 100 dpa-yellow. Iso-concentration surface for clusters are defined as 2 ionic% for the sum of TiO, Y, and YO ions.

Average sizes and number densities are presented in Figure 4-12. The mean sizes of observed oxide particles are reduced after ion irradiation at all temperatures compared to unirradiated specimens. As irradiation temperature rises, mean particle sizes increase from 1.70 nm to 2.07 nm for 100 dpa specimens. Two competing mechanisms are considered responsible for the behavior of oxide particles sizes under irradiation: ballistic dissolution and diffusion-driven re-combination/re-precipitation [90]. Significant shrinkage of oxide precipitates observed at 400 and 420°C suggests that ballistic dissolution is dominant at lower irradiation temperatures, where diffusivities of oxide constituents in oxide particles are low. At higher temperatures where oxide solute atoms have higher mobility, back diffusion from solution to particles become stronger. As can be expected, there may exist an equilibrium size for an irradiation temperature where ballistic dissolution and re-combination/re-precipitation are balanced.

The number density of oxide particles exhibited a different trend from that of mean particle sizes. Instead of almost monotonically increasing, number densities follow a quadratic-like curve, with a peak located at around 450°C, as shown in Figure 4-12b. In 100 dpa specimens, number densities of YTiO clusters are noticeably reduced when irradiated at 400, 420 and 500°C. Particle number density is usually associated with the nucleation and growth process. A decline in number density suggests that either particles are being dissolved faster than new particles can nucleate and grow or there are some unrecognized effects hindering new particle nucleation and growth past critical sizes.

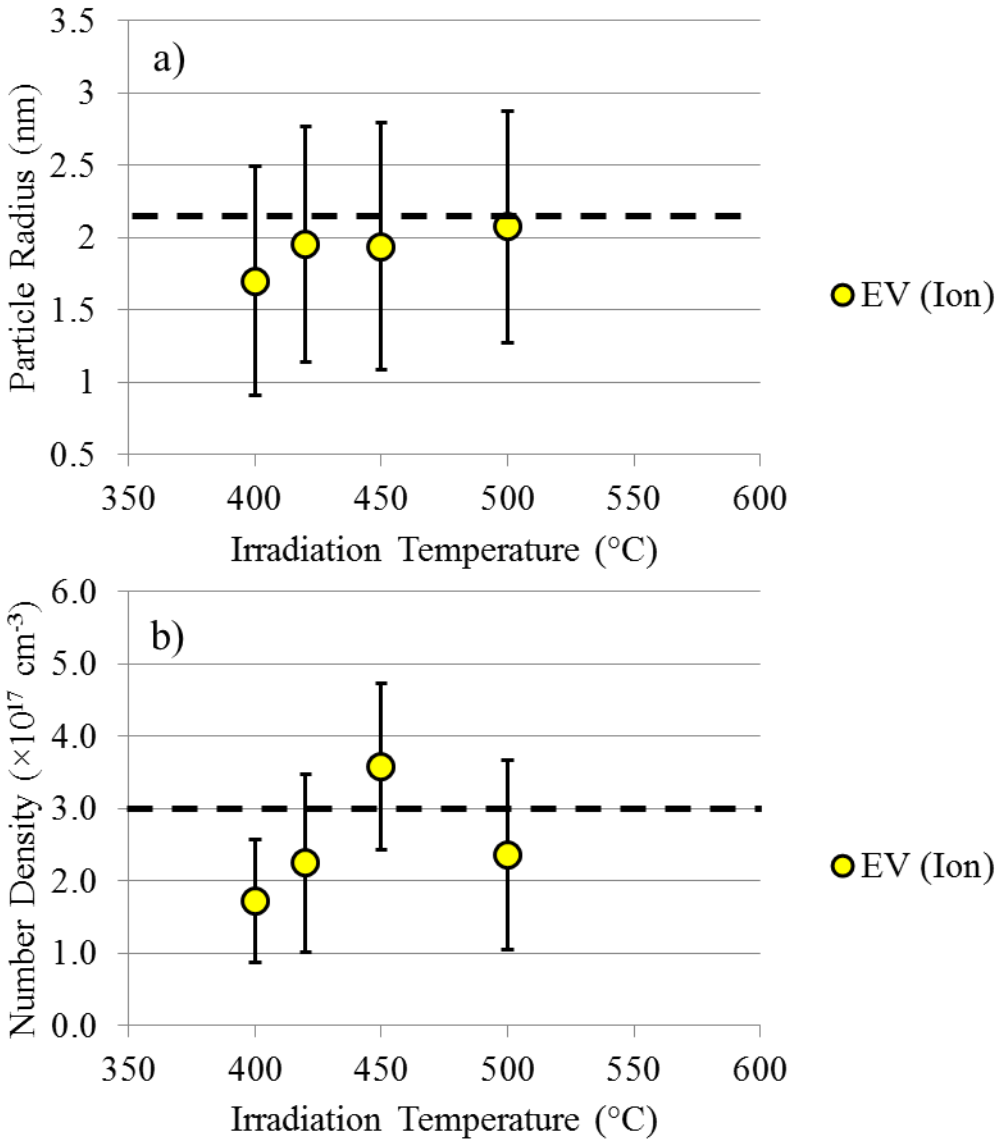

Figure 4-12. Comparison of statistical characteristics of YTiO particles in MA957 before (indicated by black dashed lines) and after ion irradiation as a function of temperature.

4.1.4 Effects of Neutron vs. Ion Irradiation on YTiO Oxide Particles

For a comparison of neutron vs. ion irradiation of YTiO particles, Figure 4-13 shows their normalized mean sizes and normalized number densities at various

irradiation conditions. It was demonstrated in section 4.1.1 that in order to compare precipitate data collected using HV and laser mode, precipitate size need to be normalized. All normalizations have been carried out based on values for unirradiated condition obtained from the corresponding heat specimens and APT operation mode. A good agreement was observed for particle size evolution. Both average sizes and evolving trends with irradiation temperatures are very similar between neutron and ion irradiated oxide particles. Unlike in neutron irradiated MA957, oxide particles in ion irradiated specimens never exhibited coarsening behavior within the current temperature range. Without ion irradiation data at corresponding higher irradiation temperature, we cannot be certain whether responses to ion and neutron irradiation would be different at higher temperatures.

Number densities of YTiO dispersoids are drastically different between neutron and ion irradiation specimens. At lower irradiation temperature, the population of oxide particles increased 2-3 fold for neutron irradiation while it decreased to 50%-60% in ion irradiated specimens. Oxide particle number density in MA957 ion irradiated at 450°C, which is the peak value, is only slightly higher than in unirradiated specimens. In specimens neutron irradiated at higher irradiation temperatures, oxide particle population drops noticeably. Although number density curves share a similar shape for neutron and ion irradiation, it is uncertain whether this is just a coincidence or a phenomenon governed by physics. The uncertainty lies in the lower dose data at 385°C that may or may not have a higher number density of YTiO particles than at 412°C if irradiated to higher doses. Again, it would be most beneficial to investigate temperature effects if ion irradiation data at 550°C could be produced.

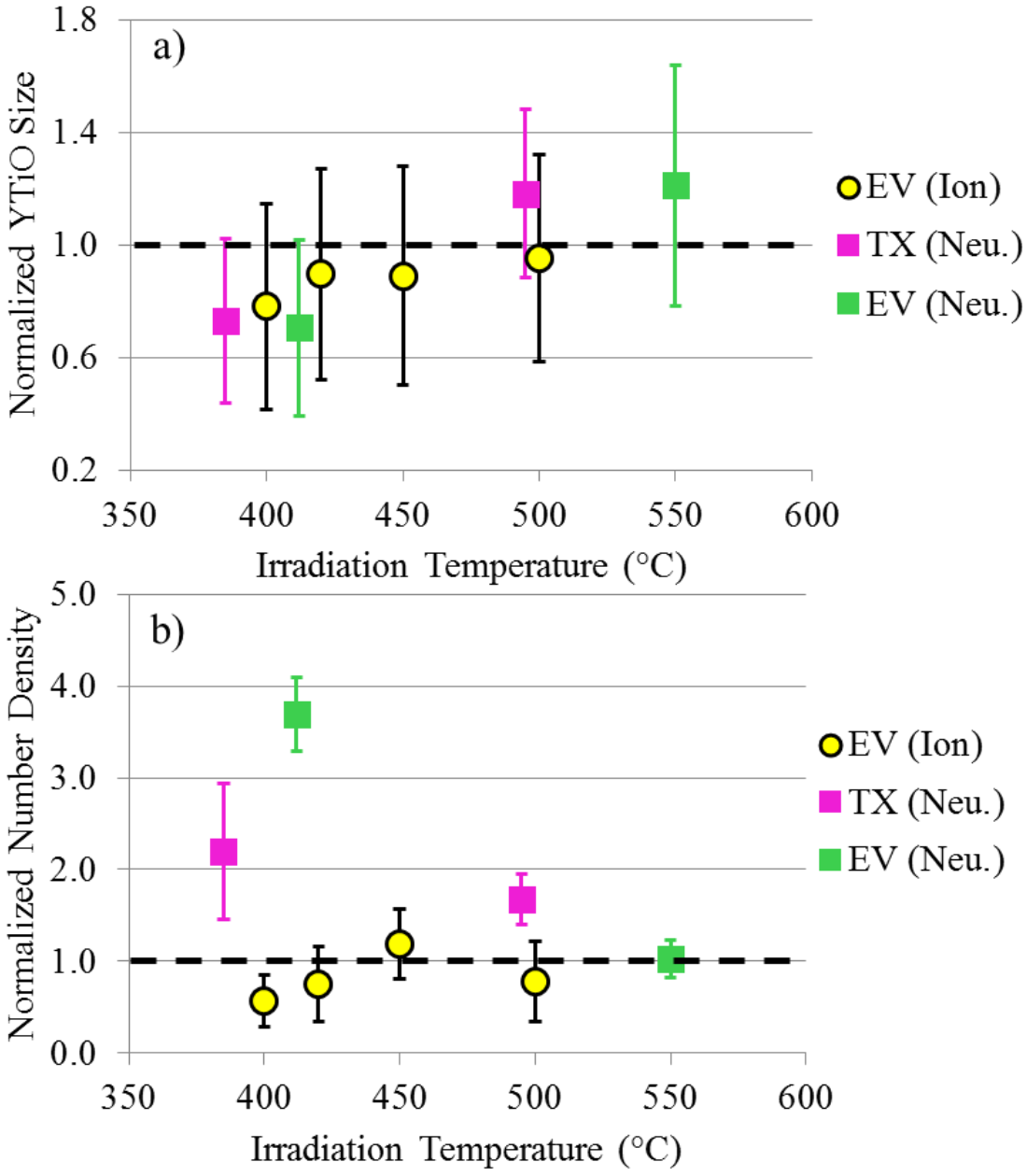

Figure 4-13. Comparison of normalized YTiO sizes and number densities in MA957 irradiated by neutrons or ions.

The preliminary compositional analysis for the YTiO particles is shown in Figure 4-14. Figure 4-14a and b plotted the fractions of Y, Ti and O inside defined YTiO

clusters with respect to all Y, Ti and O ions in entire APT tips. The dashed lines mark corresponding values measured in the unirradiated counterparts. These fractions for all three elements generally increase with irradiation temperatures for both ion and neutron irradiation. The trends are consistent with the observed average cluster sizes, which is as expected since all oxide particles are defined by a 2 ionic% concentration threshold of Y, TiO, and YO. Unlike cluster sizes that could surpass average values in unirradiated specimens when irradiated at higher temperatures, fractions of Y, Ti, and O atoms inside clusters do not exceed their corresponding values in unirradiated specimens. This could be explained by a change of lattice parameters or other impurity atoms being mixed in clusters. Figure 4-14c and d show the ratios between Y and Ti and between (Y+Ti) and O inside clusters. A significant increase in Y/Ti ratio is apparent in MA957 ion irradiated at 400°C. At higher irradiation temperature, Y:Ti ratios are approaching values in unirradiated specimens. For ion irradiation, the lowered (Y+Ti):O ratio could be attributed to the loss of Ti to the matrix at lower irradiation temperature. In neutron irradiated specimens, there are only small changes in Y/Ti. One explanation for the higher Y:Ti ratio is the higher displacement energy of Y than Ti due to higher bonding strength so that Y loss only happens at higher temperatures [132]. Whether or not temperature effect upon displacement energy of Y could be this strong is still unclear to us. It is more probable to us that some other unrecognized effects in ion irradiation may be responsible for the change of Y:Ti ratio in YTiO clusters.

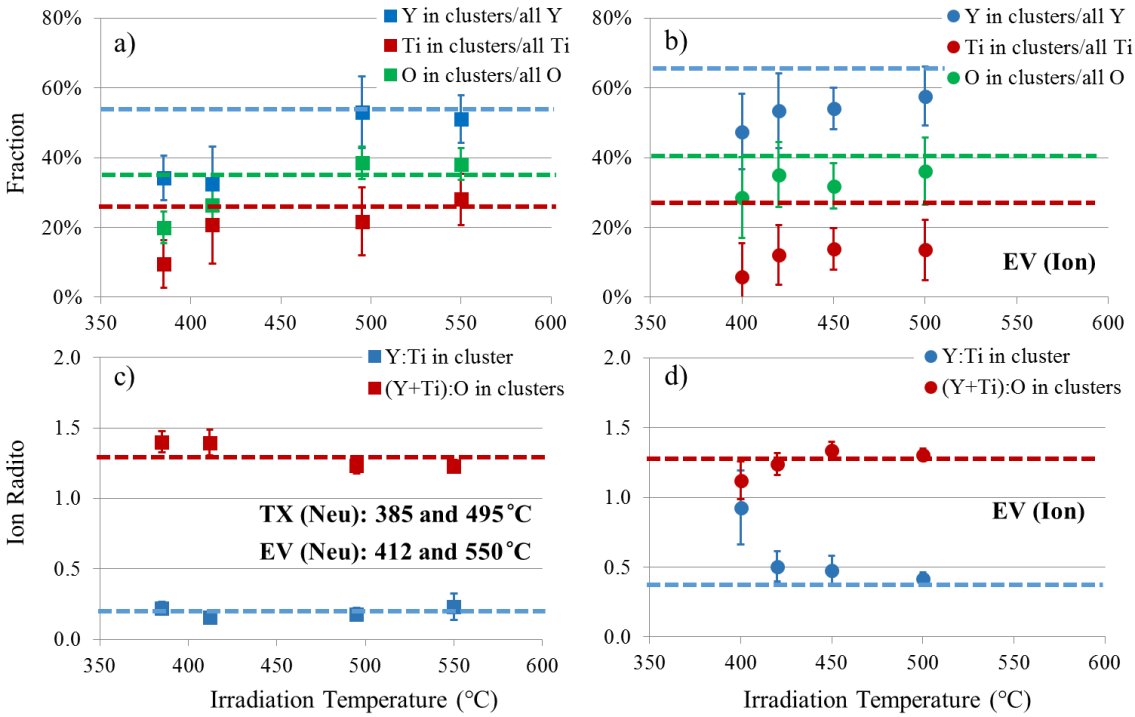

Figure 4-14. Compositional analysis of YTiO clusters in ion and neutron irradiated MA957: a) and b) the fraction of Y, Ti and O in clusters with respect to all Y, Ti and O in entire tips; c) and d) the ratio of Y to TiO inside clusters and in the entire APT tips. The dashed lines are corresponding values in uniradicated specimens.

4.2 Evolution of Alpha-Prime

4.2.1 Neutron Irradiated MA957

Formation of α′/Cr-enriched precipitates was observed in all APT tips from materials that were irradiated at temperatures below 495°C. Typical morphologies of alpha-prime are shown in Figure 4-15. It can be seen that when irradiation temperature rises from 385 to 412°C, their shapes become more irregular and sometimes appears to be interconnected. No alpha-prime was visually observed in analysis volume at irradiation temperatures above 495°C. It has been confirmed using nearest neighbor analysis using IVAS (not shown here).

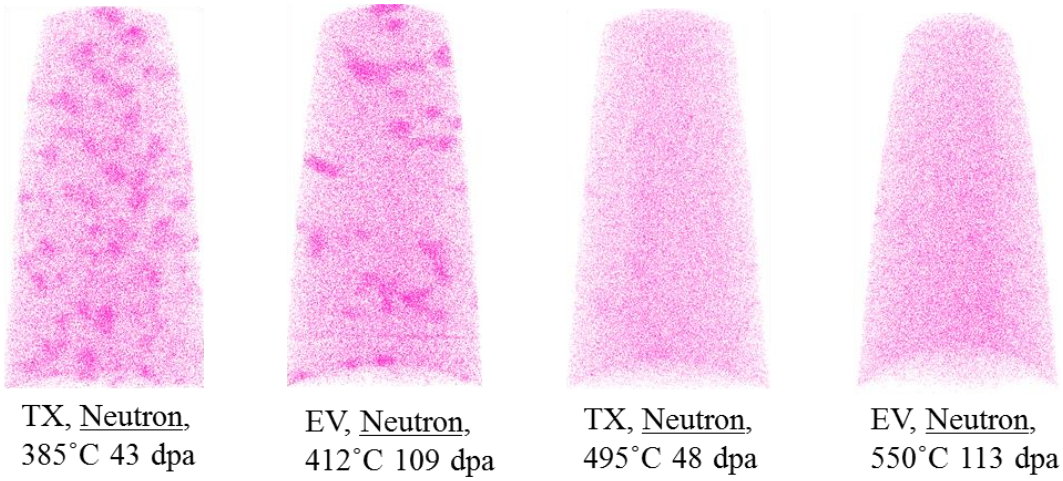

Figure 4-15. Typical ion maps of Chromium for neutron irradiated MA957.

Figure 4-16a and b show size distributions of α′ in TX (irradiated at 385°C) and in EV (irradiated at 412°C) MA957. The distribution is obviously broader and shifted towards larger values at 412 than at 385°C. At 385°C, α′ is higher in population but smaller in sizes compared to 412°C irradiation. Both size distributions are relatively symmetric; however it is obvious that a higher portion of very large precipitates is present at 412°C.

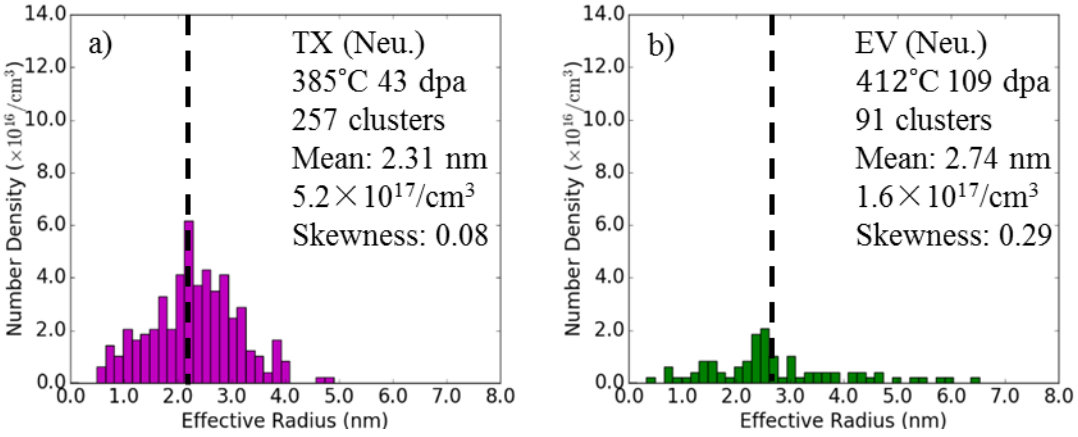

Figure 4-16. Alpha-prime size distributions in specimens irradiated at 385°C and 412°C.

As shown in Figure 4-17a and b, α′ coarsened and the population declined when irradiation temperature rose from 385 to 412°C. No α′ was observed, at least none in the APT analyzed volume, for specimens irradiated at 495 and 550°C. The absence of Cr-enriched precipitates at higher temperatures could be attributed to the increasing Cr solubility, which makes Cr precipitates unfavorable in these conditions. Our experimental results suggest that for MA957 (14 wt% Cr), the solubility limit is likely in temperature range between 420 and 500°C.

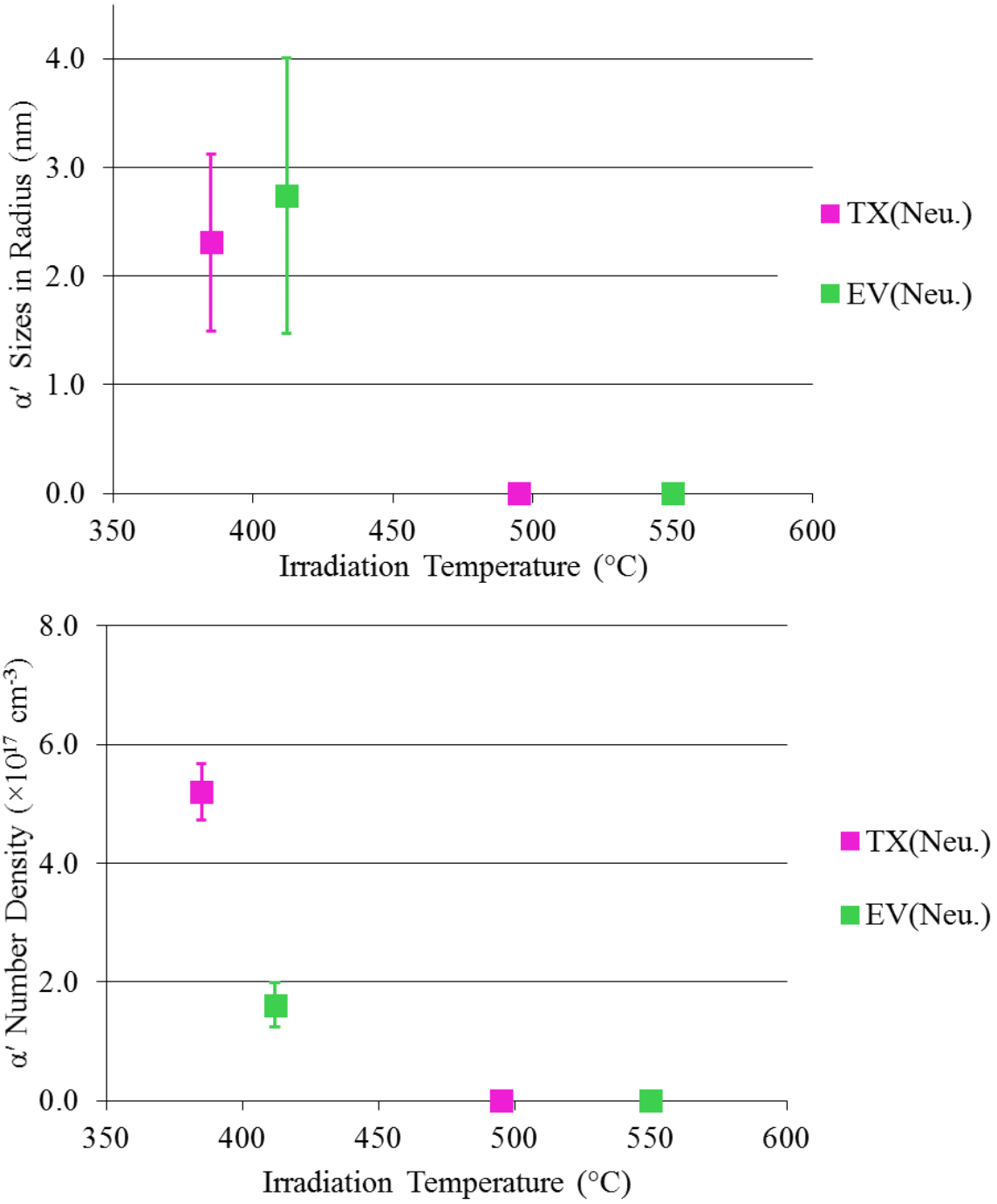

Figure 4-17. Size statistics for α′ in neutron irradiated MA957 as a function of irradiation temperature: a) mean size; b) number density.

4.2.2 Ion Irradiated MA957

Formation of α′ (Cr-enriched fully coherent precipitates) was observed in ion irradiated MA957 at temperatures up to and including 450°C. Alpha-primes particles are almost uniformly distributed in specimens irradiated at 400°C. As irradiation temperature increasing, the population of these precipitates decreases and they become more isolated. Visual inspection and iso-concentration surfaces suggest that no α′ exists in the analysis volume for MA957 irradiated at 500°C.

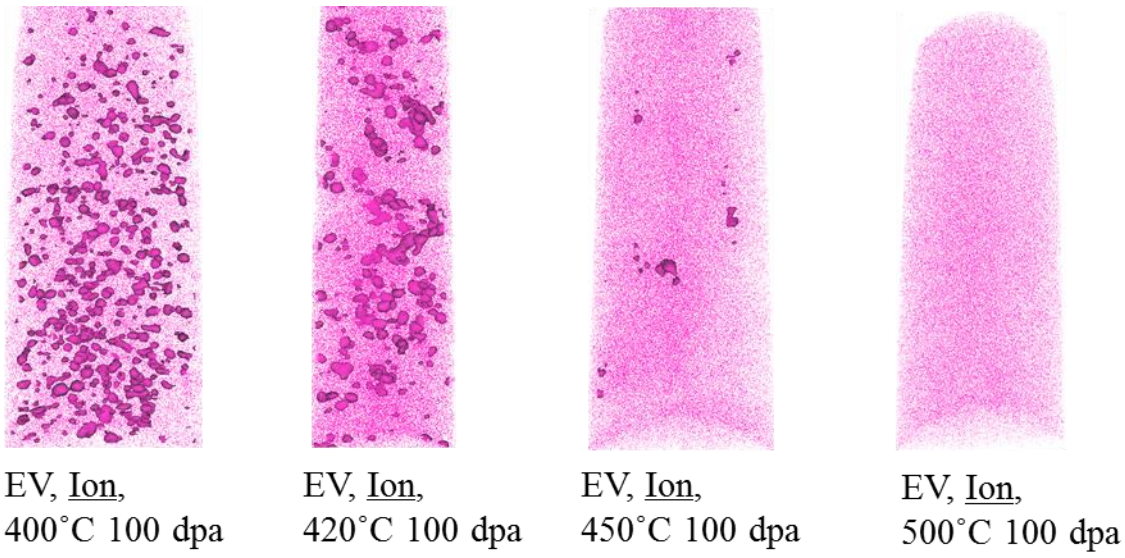

Figure 4-18. Typical Cr ion maps for ion irradiated MA957. Iso-concentration surfaces of Cr at 25 at% are included for better visualization of Cr-rich regions.

Unlike in neutron irradiated specimens, Cr enrichment in ion irradiated specimens is less clearly defined due to smaller average sizes. To confirm clusters defined by iso-concentration surface, nearest neighbor distributions (solid lines) are plotted for 400, 450 and 500°C specimen datasets in comparison to those in randomly distributed Cr (dashed lines), as plotted in Figure 4-19. When Cr clusters are present, the probability of finding another Cr at a shorter distance than in a random distribution

increased. Thus at a given small search radius, more Cr neighbors can be detected. More Cr precipitates in clusters means a higher portion of the nearest neighbor distribution can be detected at lower values. As the Figure 4-19 demonstrates, Cr clusters exist at 450°C even though there is a slight skew towards zero. But for 500°C, overlap of the experimental and randomized distributions suggests Cr is likely to be distributed randomly rather than clustered.

Figure 4-20 shows α′ size distributions measured in APT reconstructed datasets. A dominant population of small clusters can be seen in specimens irradiated at 400°C. Size distribution is then broadened for MA957 irradiated at 420°C accompanied by a drop in number density. At 450°C, alpha prime sizes are again reduced together with a much lower population. All size distributions of α′ are left-skewed instead of symmetrically bell shaped.

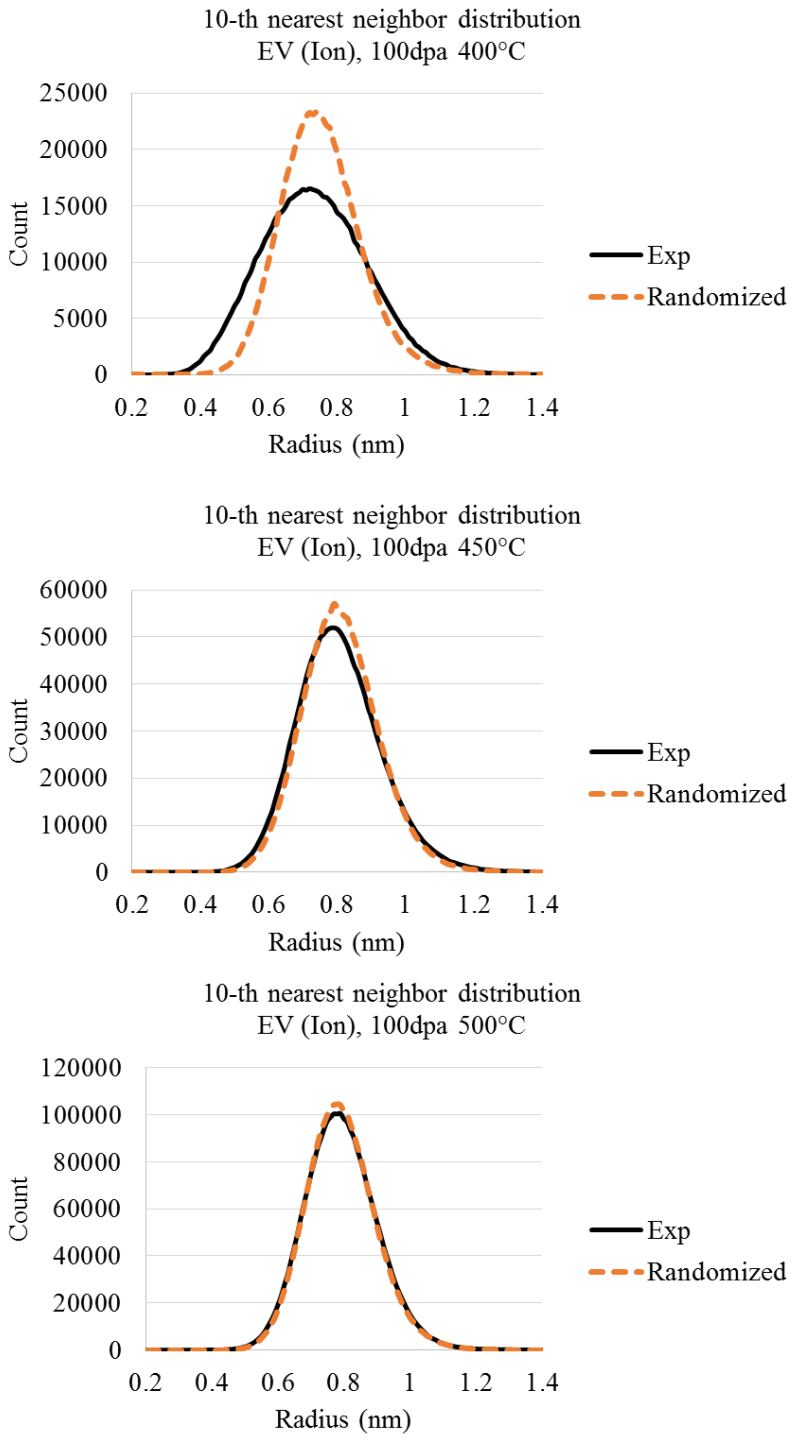

Figure 4-19. 10th nearest neighbor distribution calculated for Cr in ion irradiated MA957. The dashed curves represent distributions calculated from a randomized dataset where Cr can be assumed to be randomly distributed.

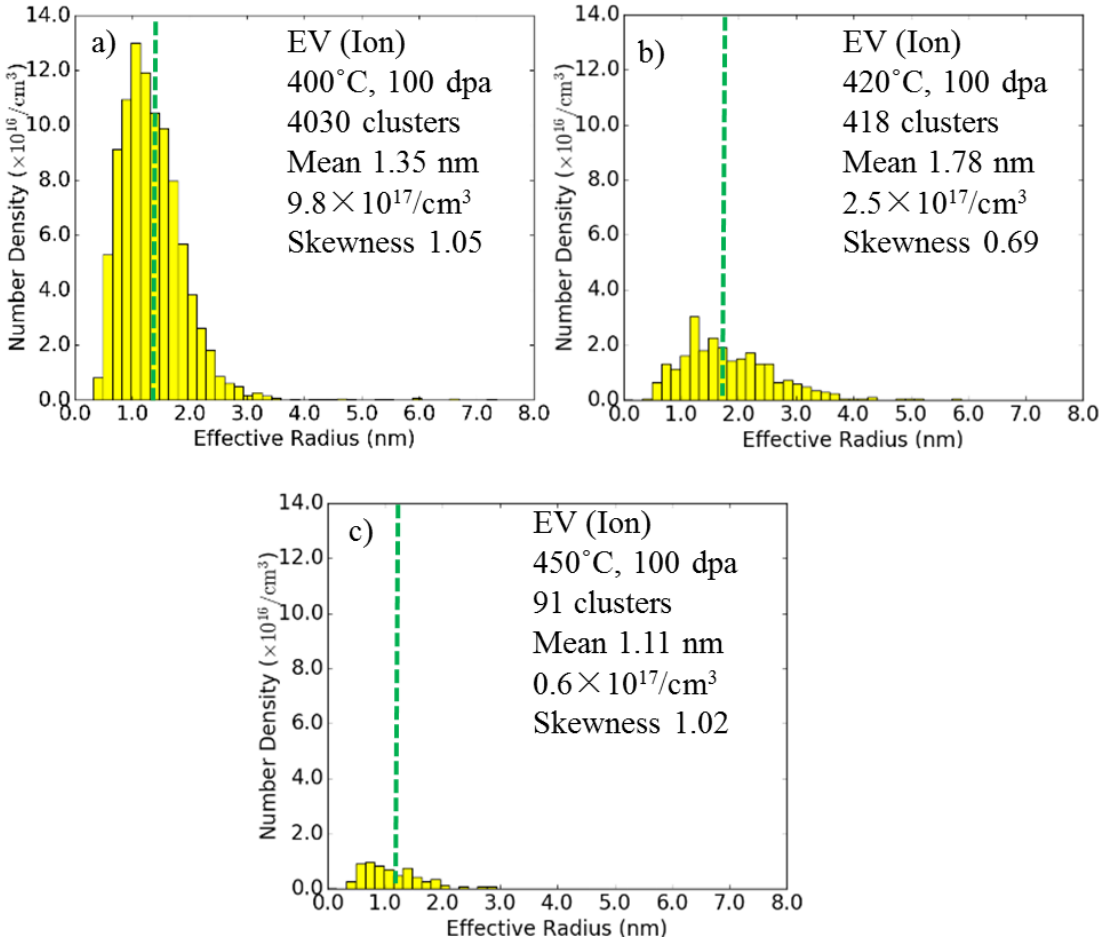

Figure 4-20. Size distributions of α′ in specimens after ion irradiation. Iso-concentration surfaces for clusters are defined as 25 at% for Cr ions.

Figure 4-21 presents the α′ statistics. Although the average size had a non-monotonic response with irradiation temperature (peak size observed at 420°C), the number density monotonically decreases as irradiation temperature increased from 400°C to 450°C. Only a few α′ clusters were found in specimens irradiated at 450°C, and no α′ was observed for specimens irradiated at 500°C, at least none in the APT analyzed volume. The absence of Cr-enriched precipitates at higher temperatures could be attributed to the increasing Cr solubility. Our experimental results suggest that for MA957 (14 wt% Cr), the solubility limit for 14 wt% Cr is likely in the temperature range between 450 and 500°C, which agrees with other reports on neutron irradiated or

thermally aged 14Cr alloys [133-136]. The excellent agreement with neutron irradiated materials suggests a minimal temperature shift for this microstructural feature.

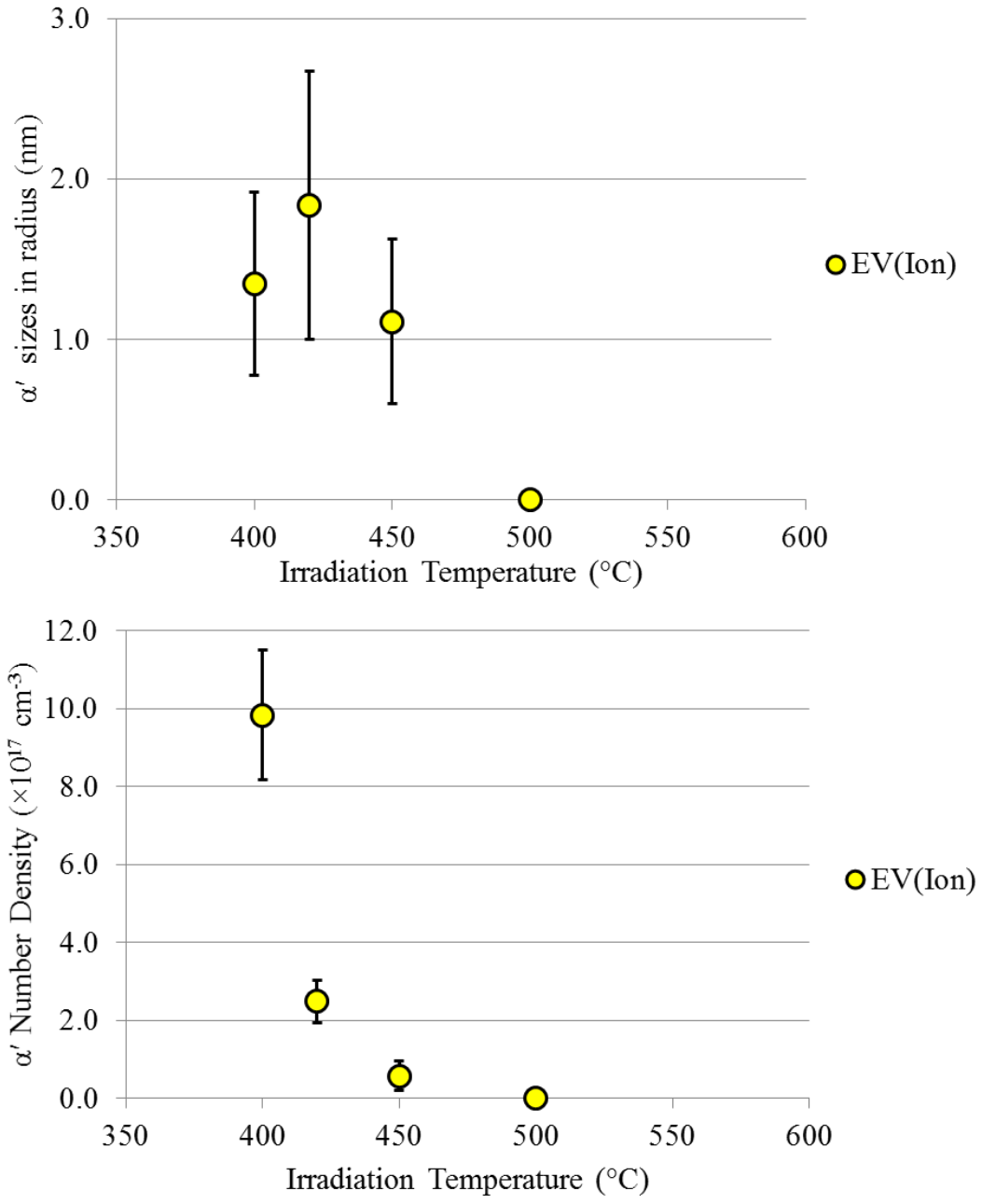

Figure 4-21. Mean size (radius) and number density of α′ as a function of irradiation temperature for specimens ion irradiated to 100 dpa.

4.2.3 Effects of Neutron vs. Ion Irradiation on Alpha-Prime

Comparisons of mean particle sizes and number densities of α′ in MA957 irradiated by neutrons or ions are displayed in Figure 4-22. Evolution trends of both mean size and population are in good agreement for neutron and ion irradiated specimens. Both neutron and ion irradiation results suggest that the critical temperature for the solubility limit of Cr in MA957 is located between 420 and 500°C. Noticeable differences can be observed as well. First is the smaller size of Cr precipitates after ion irradiation. At similar irradiation temperatures, α′ number densities in ion irradiated specimens are higher than those after neutron irradiation. Since there is no alpha prime in unirradiated specimens, the nucleation process probably plays quite an important role in controlling final precipitate number density and size.

The volume fractions of α′ in neutron and ion irradiated specimens are shown in Figure 4-23. Volume fractions in both neutron and ion irradiated specimens decrease almost linearly at comparable rates from a few percent to zero above 450°C. Interestingly, the two curves could almost overlap if the neutron irradiation one were shifted to lower temperature or vice versa. This observation is contrary to the traditional "temperature shift" argument, which states that in order to produce similar microstructures, a higher irradiation temperature should be imposed to compensate for the increased damage rate. If we assume that the Cr remaining in solution is at its solubility limit at corresponding temperatures, the volume fraction data suggest that the solubility limit is higher under ion irradiation than neutron irradiation at similar temperatures, since less Cr precipitates from the matrix.

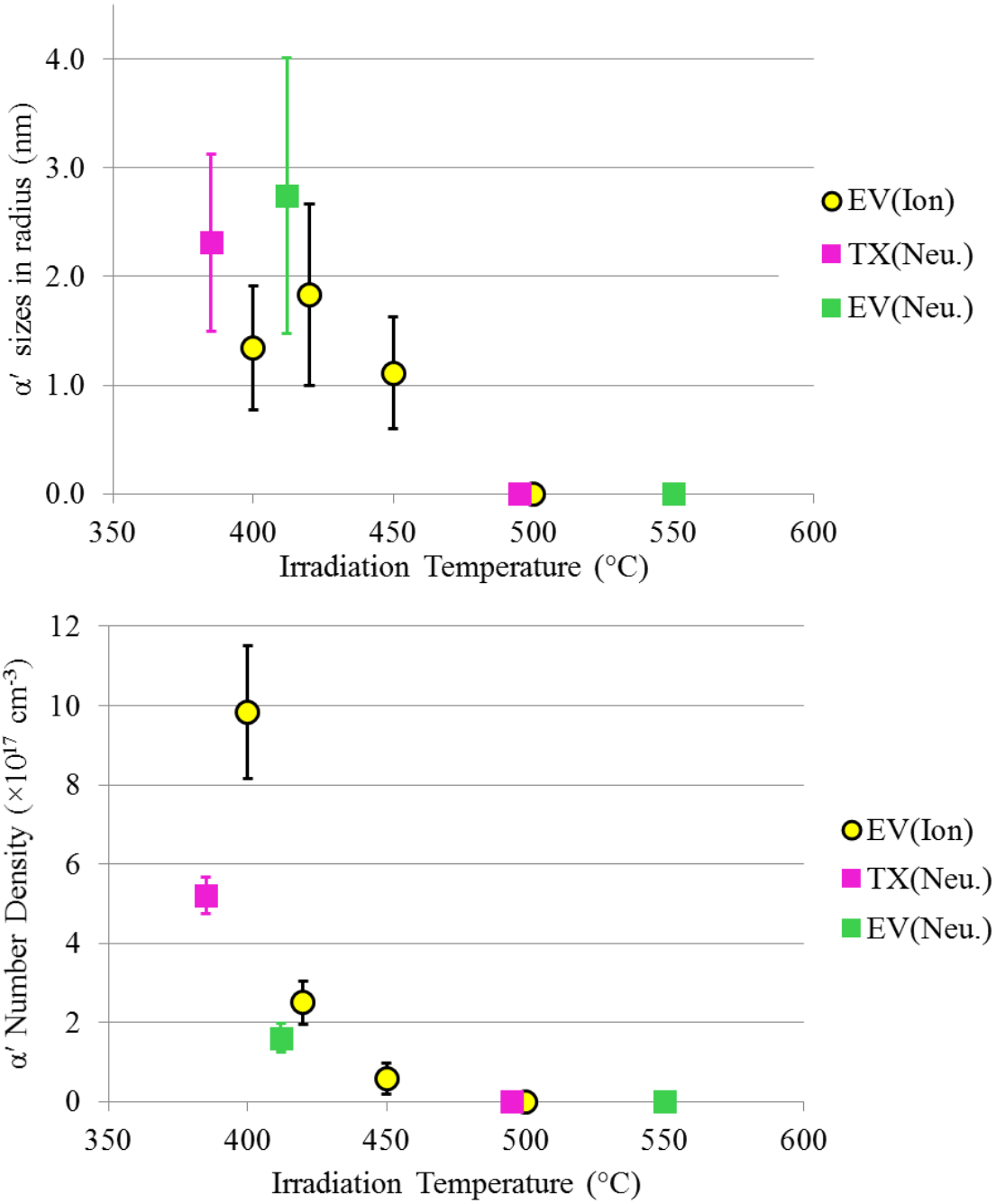

Figure 4-22. Mean size (radius) and number density of α′ as a function of irradiation temperature for MA957 irradiated by neutrons or ions.

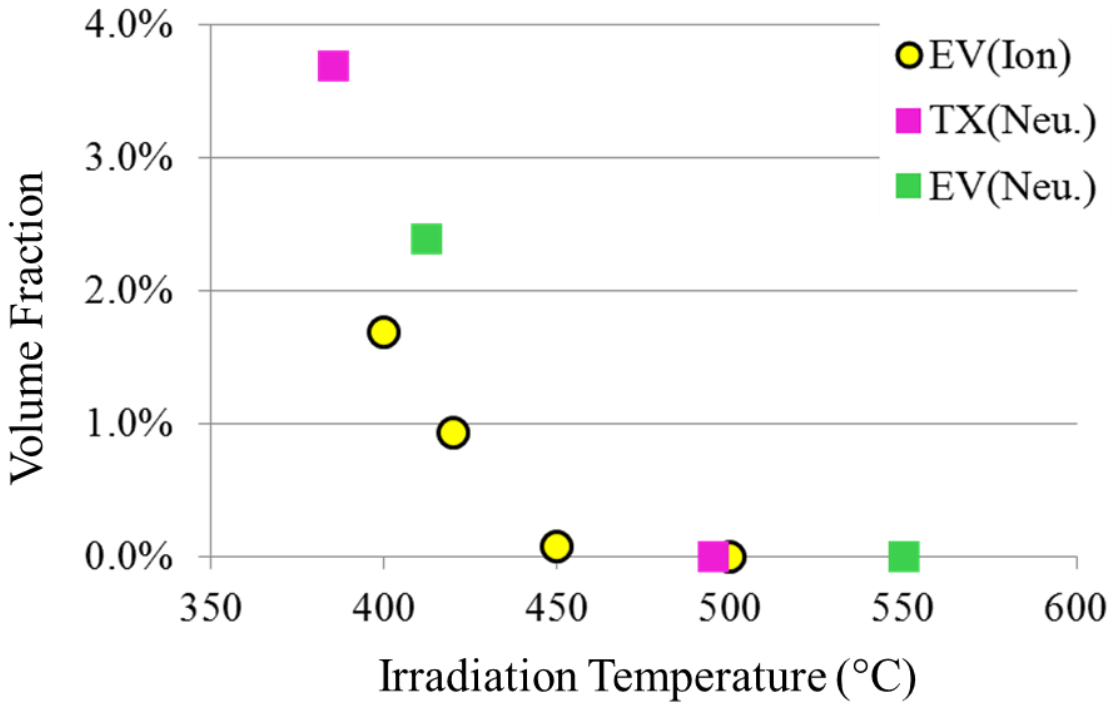

Figure 4-23. Volume fraction of α′ in neutron and ion irradiated MA957.

Figure 4-24 shows radial Cr concentration profiles in the vicinity of α′ clusters in MA957. Each proxigram is calculated from a typical dataset from irradiated MA957 and represents the average radial concentration profiles near all α′ clusters. In neutron irradiated specimens, where particle sizes are larger, Cr concentration toward the center of a precipitate on average goes to ~70-80 at%, while in ion irradiated specimens it is ~50-60 at%. In all proxigrams, a Cr concentration gradient is present from the defined interface to the center of precipitates, in contrast to a sharp interface. The saturation of Cr concentration at the center of precipitates is only observed in MA957 neutron irradiated to 109 dpa at 412°C. The maximum Cr concentration at center of precipitates seems strongly associated with average alpha prime sizes. To find out whether the maximum Cr concentration was a result of different irradiation type or from a size effect, we selected two particles each, one small and one large, from neutron or ion irradiated specimens. As shown in proxigrams in Figure 4-25, the measured maximum Cr

concentration of α′ clusters is indeed associated with measured precipitate size rather than an effect of different radiation conditions. The maximum Cr concentration inside a ~2 nm radius α′ is ~70 at% in both neutron and ion irradiated specimens, while it is ~50 at% for ~1 nm size clusters. These results suggest that alpha prime compositions produced by neutron and ion irradiations are similar for clusters of similar sizes. However, whether the association of composition with size is a true physical phenomenon or an artifact of APT is difficult to determine.

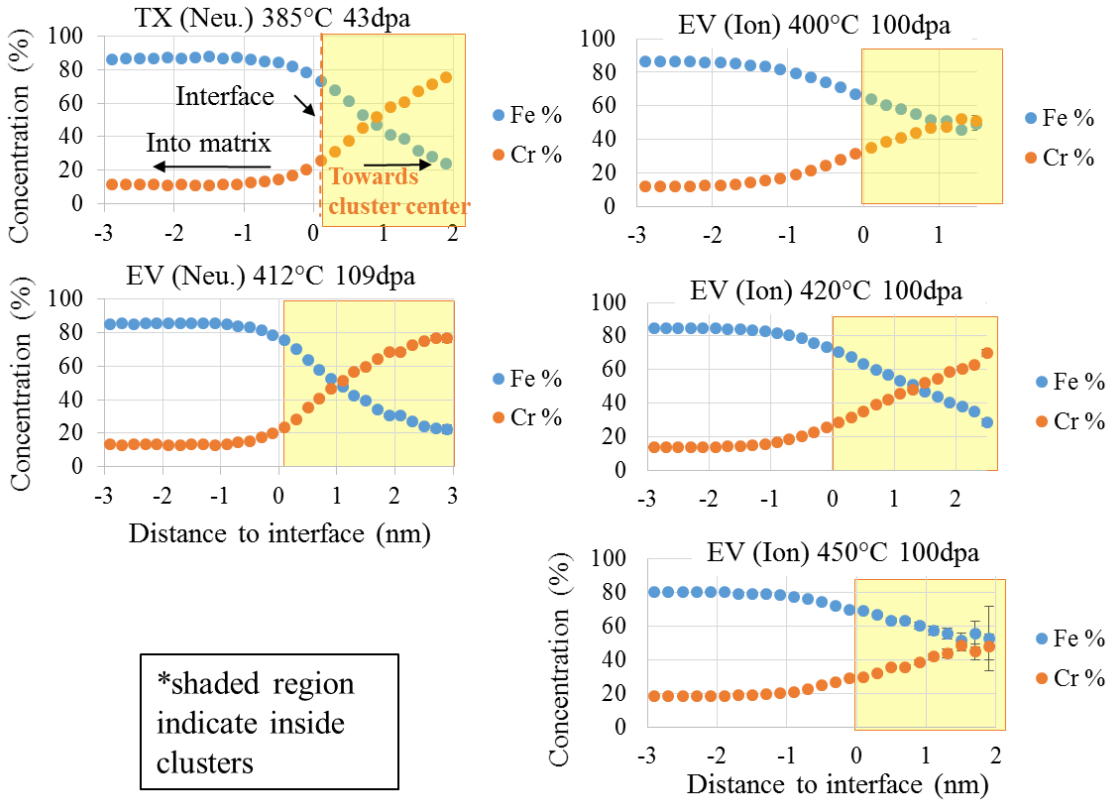

Figure 4-24. Proxigrams for α′ clusters in MA957 under various irradiation conditions.

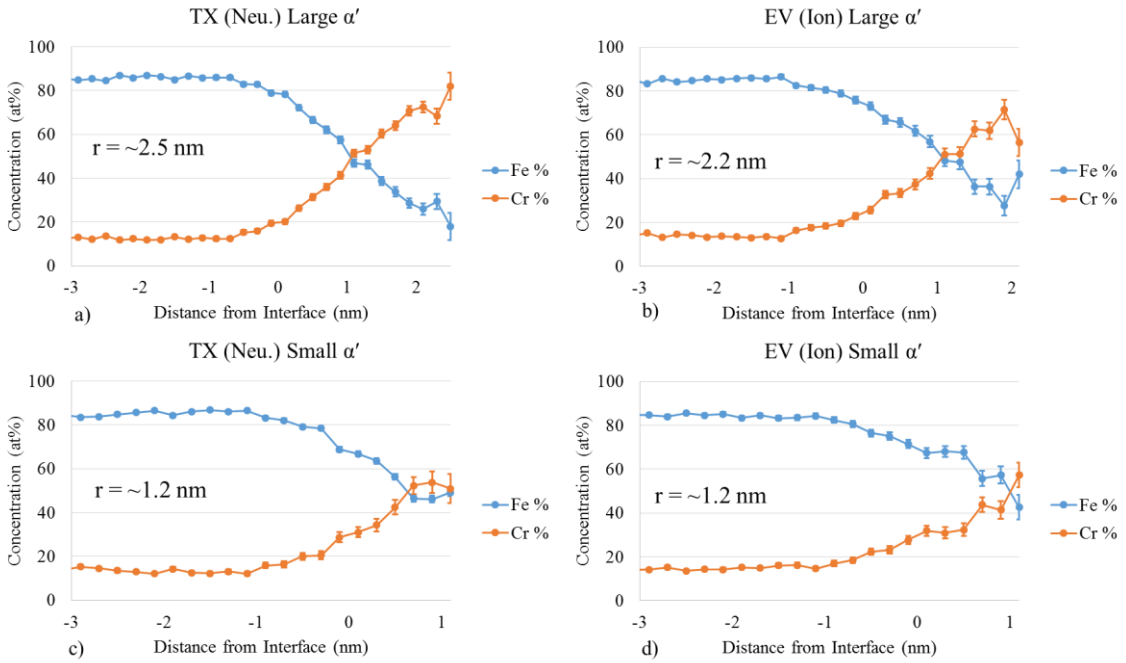

Figure 4-25. Comparison of proxigrams from small and large α′ between neutron and ion irradiated MA957. TX (Neu.) was irradiated at 385°C to 43 dpa; EV (Ion) was irradiated at 420°C to 100 dpa.

4.3 Grain Boundary Chemistry

4.3.1 Unirradiated MA957

The grain boundary chemistry in unirradiated MA957 was examined. Figure 4-26a shows reconstructed APT needles for chromium (Cr), titanium oxide (TiO), titanium (Ti) and silicon (Si) ions. These ion maps were generated with a selected viewing angle so that GB can be displayed on edge for visualization and analysis. It can be seen that Cr, Ti and Si segregated to GB but not TiO. TiO is a common molecular ion species that is mostly associated with TiO-rich particles in APT analysis. For this study, it is usually found in YTiO particles. Only a few oxide particles were seen located on grain boundaries for all three analyzed grain boundaries in unirradiated specimens. 1D concentration profiles along the direction perpendicular to the GB plane are shown in Figure 4-26b and c. These profiles were calculated inside a user-defined cubic volume

region of interest along an axis that is perpendicular to the grain boundary plane. On the grain boundary, chromium is enriched to ~18 at%, and titanium concentration increased to ~3 at% compared to ~0.5 at% in the matrix. One simple way to identify and locate grain boundaries in ion maps is via visualization of certain elements that are known to tend to segregate at GBs. For ferritic steels, silicon can be one choice of such ions. The position of the GB is estimated to be at ~10 nm and is marked in all figures. A small peak of TiO at ~9 nm near the GB, has also been detected. It can be attributed to the presence of several YTiO particles near the grain boundary. Although yttrium should be associated with YTiO particles, it is usually got underestimated in APT analysis running in HV pulsing mode [110]. The detectable yttrium is so low that it is difficult to distinguish it from the background in Figure 4-26c.

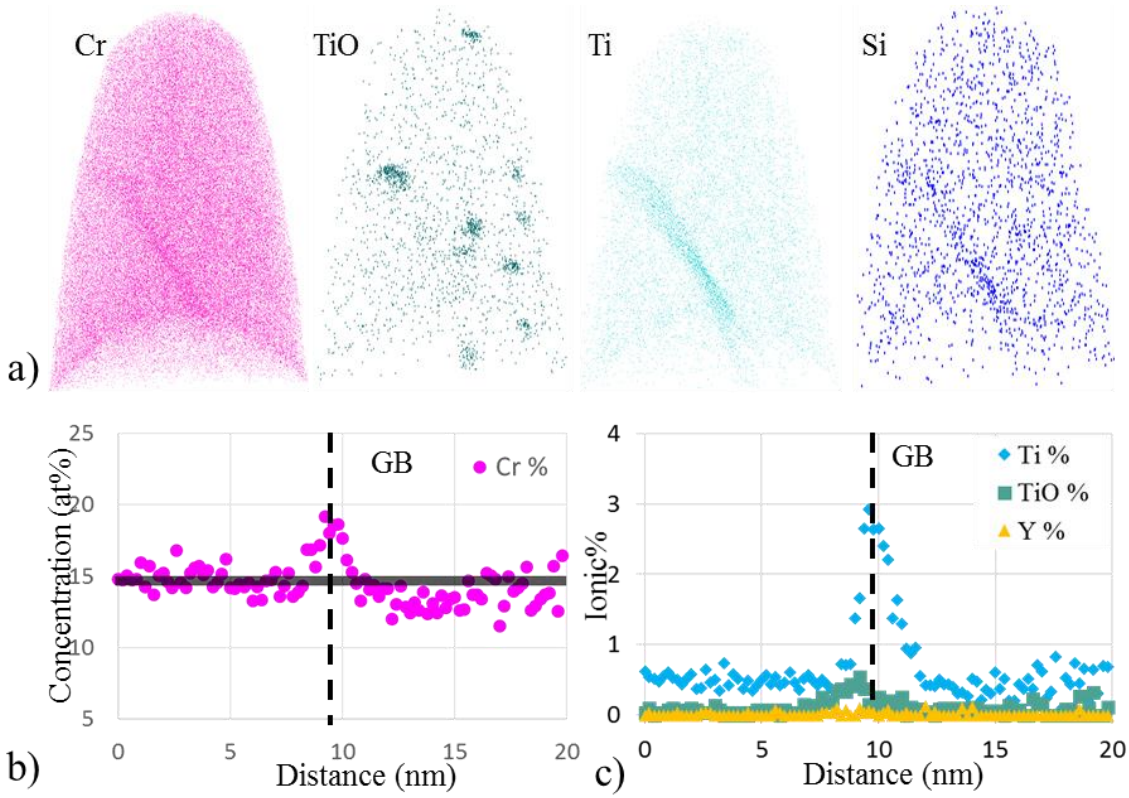

Figure 4-26. Grain boundary chemistry in unirradiated MA957: a) APT ion maps for Cr, TiO, Ti and Si (note that TiO is a molecular ion species usually associated with particles containing Ti and O); b) and c) measured one-dimensional concentration profiles in directions perpendicular to the GB. The dark gray bar in b) indicates Cr concentration in the matrix.

4.3.2 Neutron Irradiated MA957

Figure 4-27 shows a series of reconstructed ion maps of Cr, TiO, Ti and Si for specimens irradiated by neutrons at various temperatures. It can be seen that Si segregated to the GB plane at all irradiation temperatures and Ti did the same. The chromium ion maps are not as clear due to the formation of Cr-enriched second phases at 385 and 412°C, which pulls Cr from the matrix into precipitates. Cr is enriched on the GBs in the specimens irradiated at 495 and 550°C. In this report, the segregation of an element is determined by comparing elemental concentration with matrix concentration in unirradiated materials. Under this criterion, Cr exhibits mixed enrichment/depletion in

APT datasets. Another apparent difference from unirradiated materials is that TiO shows significant enrichment at grain boundaries at irradiation temperatures below 550°C, which suggests re-precipitation of TiO-rich particles at grain boundaries after neutron irradiation. Even at 550°C, there are probably more oxide particles at GBs than in unirradiated materials. More detailed analysis to determine number of oxide particles per unit GB area is needed, as well as their compositions, for a better understanding of this response to radiation.

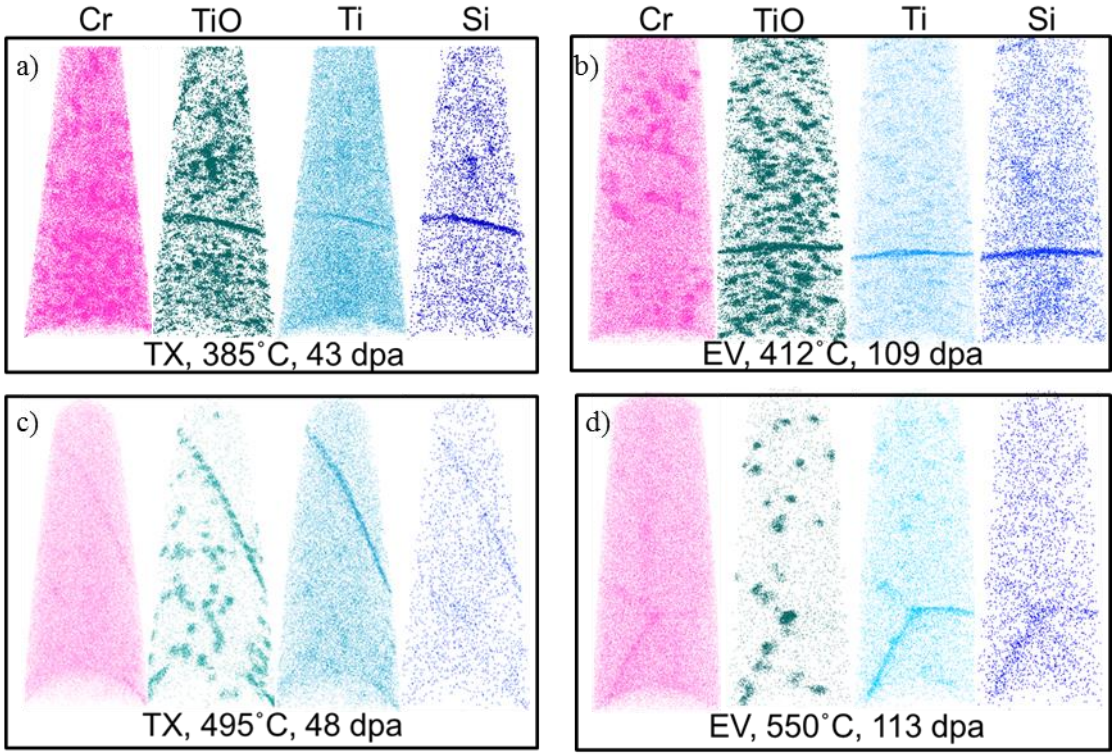

Figure 4-27. Ion maps for chromium, titanium oxide, titanium and silicon for various specimens neutron irradiated at different temperatures. Note that for 412°C, Cr was depleted in some APT datasets and enriched in others (only one type is shown here).

1D concentration profiles for elements of interest, Cr, Ti, TiO and Y along directions perpendicular to GB planes are shown in Figure 4-28 and Figure 4-29. As irradiation temperature increased from 385 to 550°C, chromium underwent transition from depletion to enrichment at grain boundaries. Determination of such transition temperature is complicated by the formation of α′ during the irradiation. Further complicating the analysis, several datasets at 412°C (not shown here) exhibited Cr enrichment at the grain boundaries. For specimens irradiated at 385°C, Cr is clearly depleted at the GBs. The asymmetrical 1D concentration profile observed in Figure 4-28a may be attributed to the migration of grain boundary. The enrichment of Y and TiO ions on GBs at 385 and 412°C is consistent with our visual observation that a noticeable population of TiO-rich particles re-precipitates on grain boundaries during neutron irradiation. Such preferential precipitation is greatly reduced as irradiation temperature increases to 550°C.

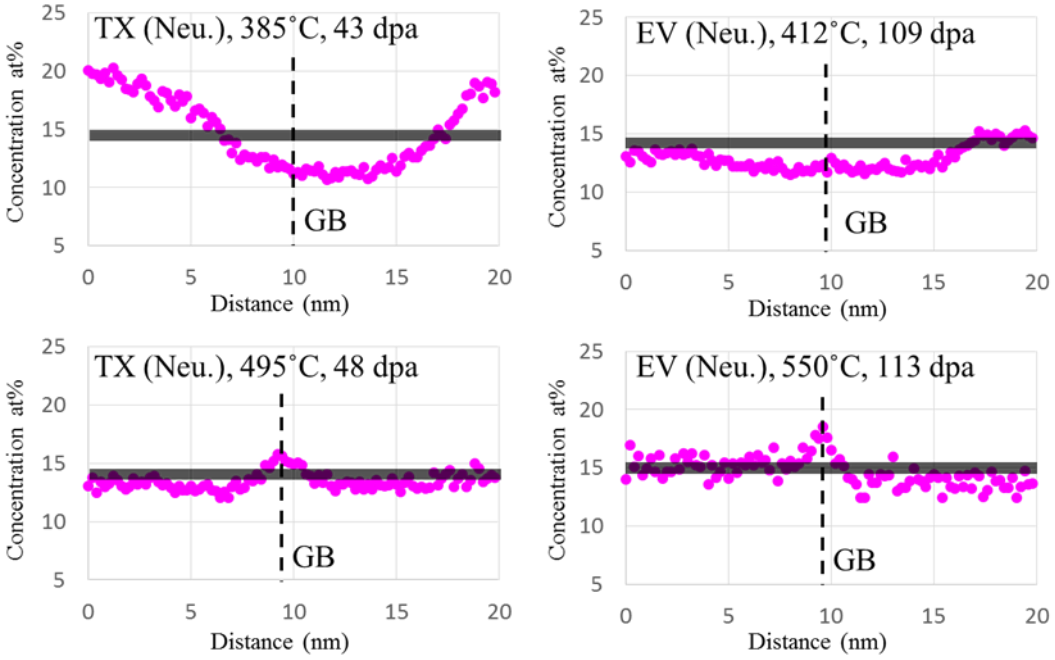

Figure 4-28. 1D concentration profiles of Chromium along directions perpendicular to grain boundary in specimens irradiated by neutrons at different temperatures. Note that for 412°C, Cr maybe enriched or depleted in various datasets.

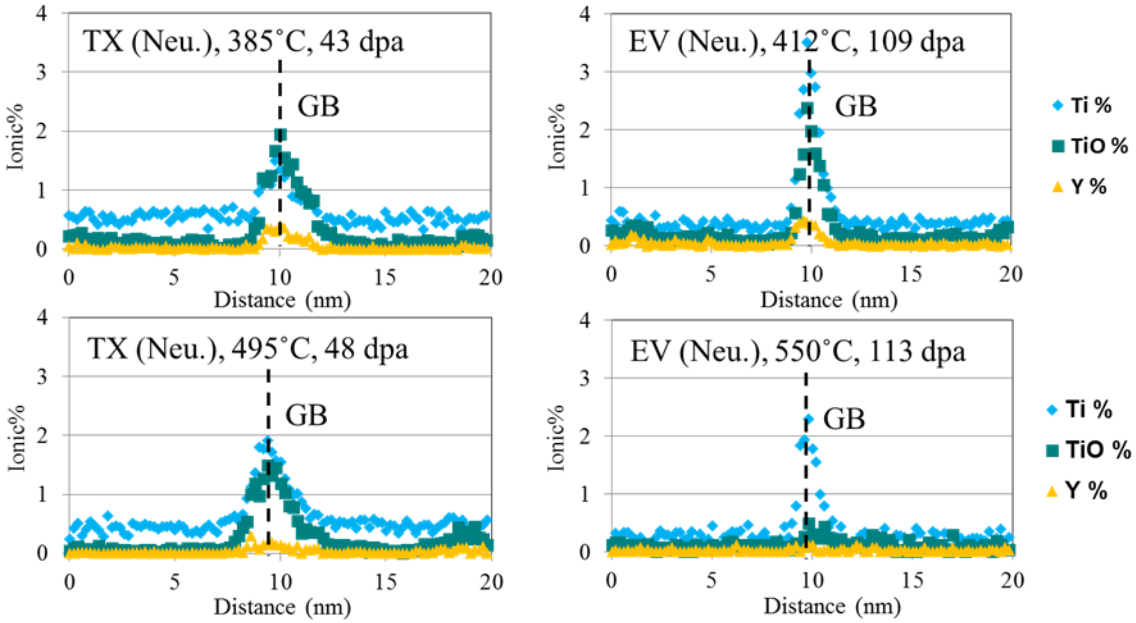

Figure 4-29. 1D concentration profiles of TiO, Ti, and Y along directions perpendicular to grain boundary in specimens irradiated by neutron at different temperatures.

4.3.3 Ion Irradiated MA957

Ion maps of Cr, TiO, Ti and Si for specimens ion irradiated to 100 dpa at various temperatures are presented in Figure 4-30. It can be seen that similar to neutron irradiation, Si segregated on GBs at all irradiation temperatures below 500°C. The chromium ion maps, on the other hand, shows depletion on the grain boundaries in almost all specimens at every tested temperatures. An apparent difference from unirradiated materials is that TiO ions are significantly enriched at GBs at irradiation temperatures around 450-500°C. This suggests that either TiO-containing particles were ballistically dissolved and then re-precipitated to GBs, or GBs migrated and were pinned by high density oxide dispersoids during irradiation. At 500°C, a region near GB boundary that is depleted of oxide particles is clearly visible, however this feature is not symmetrical. It could be attributed to grain boundary migration during irradiation or effects from special grain orientation relationships.

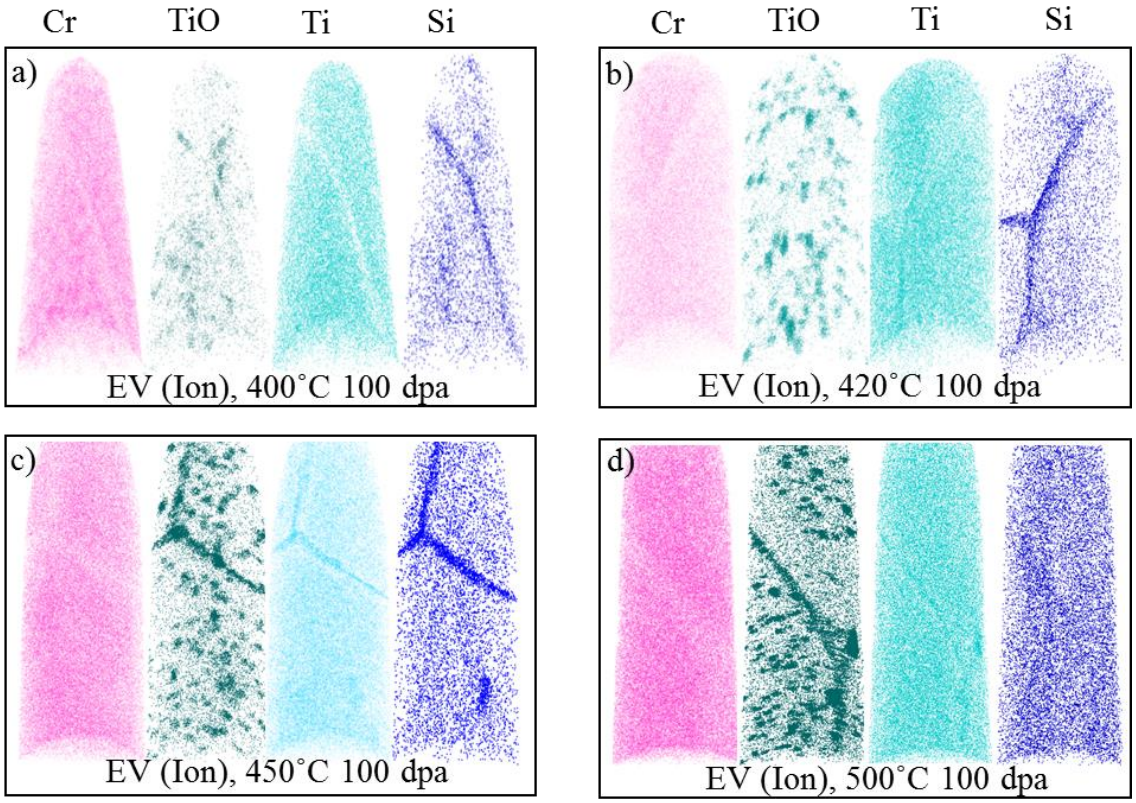

Figure 4-30. Ion maps for chromium, titanium oxide, titanium and silicon for various specimens irradiated to 100 dpa at different temperatures by Cr ion. The aspect ratios for reconstructed datasets were adjusted to fit the figure.

1D concentration profiles near grain boundaries for Cr along directions perpendicular to GB planes are shown in Figure 4-31. As irradiation temperature increases from 400 to 500°C, the magnitude of Cr depletion on grain boundaries is reduced by a few atomic percent for specimens irradiated to 100 dpa. In two datasets (not shown here) for 100 dpa 500°C specimens, Cr is enriched to at similar level to that in unirradiated specimens. Other than those, Cr in all other specimens exhibited depletion at grain boundaries, regardless of whether α′ was formed. Similar mixed depletion/enrichment behavior has been reported in a model 12Cr ODS alloy irradiated by self-ions at 500°C using both APT and TEM [137]. Such complex grain boundary chemistry in ferritic alloys is not fully understood yet. The asymmetrical 1D

concentration profile observed in Figure 4-31d may be attributed to the migration of grain boundary. Si is strongly segregated to GBs at lower irradiation temperature but its concentration is reduced at higher temperatures (not shown in figures).

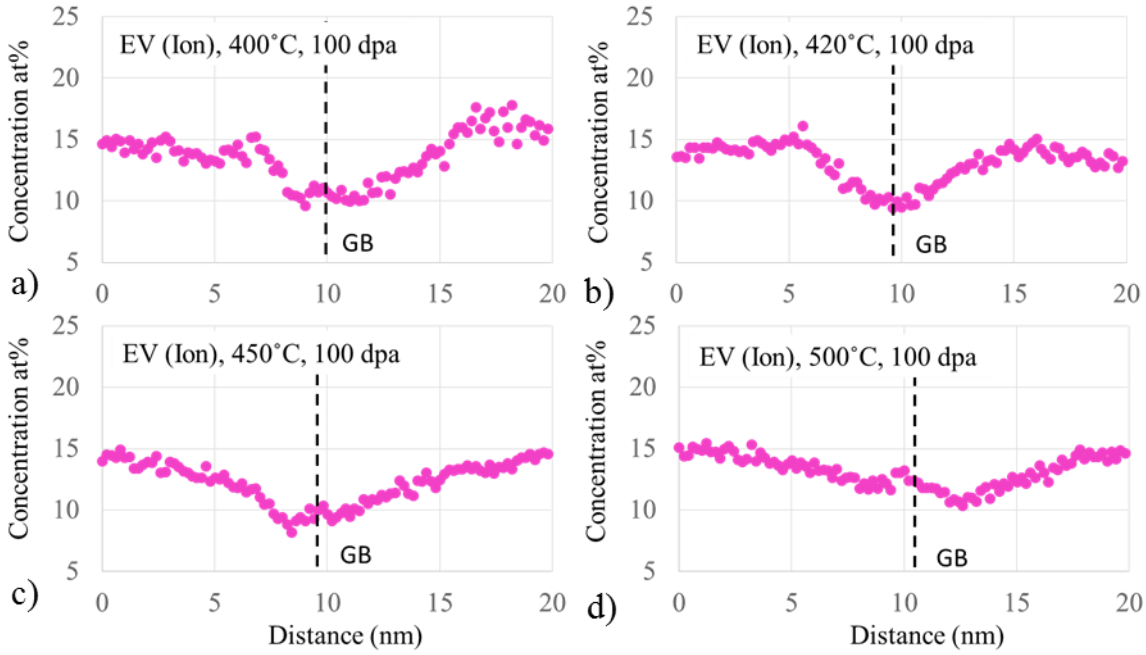

Figure 4-31. 1D concentration profiles of Cr along directions perpendicular to GBs in specimens ion irradiated to 100 dpa.

Figure 4-32 displays the 1D concentration profile of Ti, TiO, and Y. Because TiO ions are strongly associated with TiO-containing particles, current GB chemistry results indicate that either those particles had been formed on grain boundaries or grain boundaries migrated and were pinned by oxide particles at 450°C. Considering the GBs are enriched with Ti, O and Y, it is likely these particles are fine precipitates of YTiO oxides.

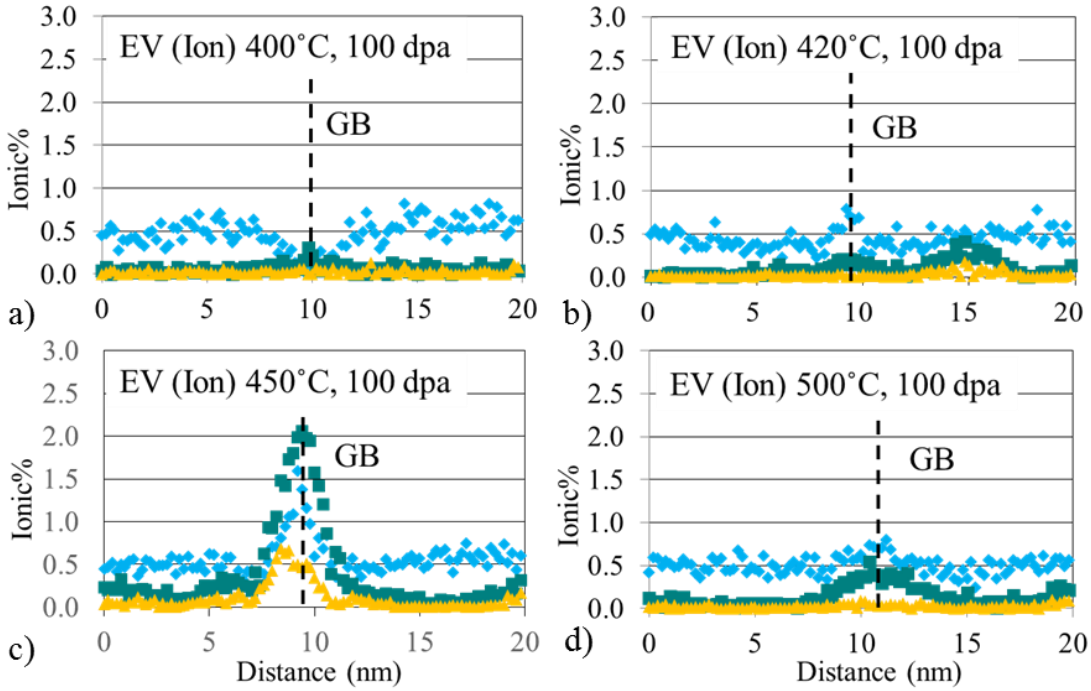

Figure 4-32. 1D concentration profiles of TiO (dark green), Ti (cyan) and Y (yellow) along directions perpendicular to grain boundary in ion irradiated specimens to 100 dpa at various temperatures.

4.3.4 Comparison of GB Chemistry between Neutron and Ion Irradiation

The grain boundary chemistry results are summarized in Table 4-2 and Table 4-3 and can be compared. In general, the evolution trends of elemental segregations, such as Cr, TiO and Si, agree for GBs in MA957 irradiated by neutrons or ions. However, the GB chemistry may not be the same at similar irradiation temperatures for neutron and ion irradiated specimens. Caution must be taken even though a clear trend has been observed in Table 4-2 for neutron irradiated MA957, since it is drawn from a limited number of GBs. Table 4-3 summarizes GB chemistry for ion irradiated specimens. A few limitations regarding GB chemistry ion-irradiated materials. First, ion irradiation only penetrated to a depth of ~1 μm, which means that for this materials, only one or two grains will be affected. Second, combined with the high diffusivity of typical random grain boundaries, it is probably easy for the unirradiated portions of a GB to affect what

is happening along the irradiated portion of a GB. Thus, ion irradiations are not ideal, but still interesting for comparison. In addition, the GB chemistry is likely affected by GB angle and varies from grain to grain, which makes systematic study using APT especially difficult.

Table 4-2. Summary of radiation induced segregation (RIS) at GBs for several elements of interest in MA957 irradiated by neutrons. "+", "0" and "-" mean enrichment, no change/not sure, and depletion, respectively.

Temperature (˚C)	Dose (dpa)	# GB's Examined	Cr	Ni	Si	Y	Ti	TiO
-	Unirrad.	3	+	0/+	+	0/+	+	0/+
385	43	1	-	+	+	+	+	+
412	109	15	-/+	+	+	+	+	+
495	48	1	+	+	+	+	+	+
550	113	4	+	0/+	+	0/+	+	+

Table 4-3. Summary of RIS at GBs for MA957 irradiated by ions. . "+", "0" and "-" mean enrichment, no change/not sure, and depletion, respectively.

Temperature (˚C)	Dose (dpa)	# GB's Examined	Cr	Ni	Si	Y	Ti	TiO
-	Unirrad.	3	+	0/+	+	0/+	+	0/+
400	100	4	-	+	+	0/+	-	0/+
420		4	-	+	+	0/+	-/+	0/+
450		7	-	+	+	0/+	-/+	+
500		3	-/+	+	+	0/+	+	+

5 THEORETICAL CALCULATIONS BASED ON RATE THEORY MODELS

5.1 Defect Balance and Radiation Enhanced Diffusion

5.1.1 Defect Balance Equations

One direct consequence of irradiation in the microstructure is the creation of point defects and defect clusters. Some of them are able to freely migrate. Diffusion kinetics of solute atoms is altered and subsequent microstructural evolution is affected. To the first order of approximation, only point defects will be considered in the following analysis. Point defect concentration is a dynamic balance between defect production and annihilation as described by the following equations:

$$\begin{aligned}\frac{dC_v}{dt} &= K_0 - K_{iv}C_iC_v - K_{vs}C_sC_v + L_v \\ \frac{dC_i}{dt} &= K_0 - K_{iv}C_iC_v - K_{is}C_sC_i + L_i\end{aligned} \tag{5.1a}$$

where C_v and C_i are vacancy and interstitial concentration, L_v *and* L_i are thermal emission of vacancies and interstitials, which can be related to equilibrium defect concentration; K_0 is defect production rate; K_{iv}, K_{vs}, and K_{is} are reaction rate coefficients between interstitial and vacancy, vacancy and sink, and interstitial and sink, respectively. The thermal emission term must satisfy following conditions:

$$\begin{aligned}0 &= -K_{iv}C_i^{eq}C_v^{eq} - K_{vs}C_sC_v^{eq} + L_v \\ 0 &= -K_{iv}C_i^{eq}C_v^{eq} - K_{is}C_sC_v^{eq} + L_i\end{aligned} \tag{5.1b}$$

where C_v^{eq} and C_i^{eq} are vacancy and interstitial concentrations at thermal equilibrium, respectively.

The defect concentrations are represented by a mean field, but in reality, they may not be uniform due to damage cascades and local defect sinks. A systematic review of the deficiencies of the defect balance equation can be found in Was [8]. Normally in the low and intermediate irradiation temperature regimes, the equilibrium defect

concentrations are negligible. For BCC iron, the thermally activated interstitials concentration can be neglected to even higher temperatures.

The defect reaction rate constant can be expressed by:

$$K_{iv} = 4\pi r_{iv}\left(D_i + D_v\right)/\Omega \tag{5.2}$$

$$K_{vs} = 4\pi r_{vs} D_v / \Omega \tag{5.3}$$

$$K_{is} = 4\pi r_{is} D_i / \Omega \tag{5.4}$$

where r_{iv}, r_{vs} and r_{is} are interaction distance for interstitial-vacancy, vacancy-sink and interstitial-sink, respectively; D_i and D_v are diffusion coefficients for interstitial and vacancy, respectively; Ω is atomic volume in BCC Fe. Assuming a vacancy mechanism for diffusion, the radiation enhanced diffusion coefficient will then be described by:

$$D_a^{rad} = f_v D_v C_v = \frac{C_v}{C_v^{eq}} D_a^{eq} \tag{5.5}$$

where f_v is correlation coefficient. Both parts in equation (5.5) can be used for estimating radiation enhanced diffusion effects.

5.1.2 Sink Strength Calculations

In real materials, multiple defect sinks can co-exist. To more conveniently account for their contribution to the sink strength, defect reaction rate coefficients are used:

$$\begin{aligned} K_{jX} C_X C_j &= (4\pi r_{js} C_s / \Omega) D_j C_j = (\sum_X k_{jX}^2) D_j C_j \\ K_{iv} C_i C_v &= \left(4\pi r_{iv} / \Omega\right)\left(D_i + D_v\right) C_i C_v = k_{iv}^2 \left(D_i + D_v\right) C_i C_v \end{aligned} \tag{5.6}$$

where j represents defect type, i.e., vacancy (v) or interstitial (i); X is the sink type, such as dislocation (d), grain boundary (gb), precipitate (ppt) and void (V); k_{jX}^2 is the sink strength of sink X with respect to defect j. The total sink strength in a material is then defined as the sum the strengths of all individual sinks.

Sink strengths can be estimated in different models. In this research several most widely used ones will be adopted. The dislocation sink strength in reaction rate-controlled process can be described as [138]:

$$k_{vd}^2 = z_{vd} l_d C_d \qquad (5.7)$$
$$k_{id}^2 = z_{id} l_d C_d$$

where l_d is the length of dislocation lines per unit volume, C_d is the number density of dislocation lines, and dislocation capture efficiencies z_{vd} and z_{id} are related to capture sites per unit length of dislocation line (they are not equal in BCC Fe). Grain boundary sink strength for both vacancies and interstitials can be expressed as [139]:

$$k_{gb}^2 = \begin{cases} 6k/d, & kd \to \infty \\ 60/d^2, & kd \to 0 \end{cases} \qquad (5.8)$$

where d is average grain diameter, k^2 is the sink strength of other microstructural features (usually ~10^{10}-10^{11} cm^{-2}). Considering precipitates as infinite sink, their strength can be described as [42, 140]:

$$k_{ppt}^2 = 4\pi r_{ppt} C_{ppt} \qquad (5.9)$$

where r_{ppt} and C_{ppt} are average radius and number density of precipitates, respectively. For coherent precipitates, the case is more complicated. It has been considered that the interface of coherent particles cannot absorb an unlimited number of point defects and the defect influx must be equal among vacancies and interstitials. Solving such a problem is complicated and materials system dependent. For simplicity, the upper bound sink strength of this type of precipitate, which is the same as the sink strength of the incoherent ones, is chosen for the following calculations.

Unirradiated MA957

Since this study heavily relied on APT characterization, limited information on microstructural features like dislocations and grain sizes is available. These parameters for sink strength calculation are listed in Table 5-1. The dislocation density in unirradiated MA957 was found to be ~1×10^{11} cm^{-2} [141]. However, a series of

fabrication processes were performed to make the materials studied here into final tubing geometry and the dislocation density is likely to be higher level by as much as one order of magnitude. In reality dislocation lines were a considered biased sink for interstitials, but an accurate value for such bias is not well known. Such a biased sink is thought to be vital for void swelling to occur. In this calculation, the bias is set according to a study by Stoller et al. [142]. Past investigations on this particular materials before irradiation showed that grains are elongated, with ~0.5 μm width and ~5 μm length on average [96]. If we assume a spherical grain with the same average grain volume, the grain diameter would be ~1.34 μm. Two types of precipitates, YTiO particles and α′ (Cr-rich), are included in sink strength calculation. They are likely to produce noticeable effects due to their high number density and small sizes.

Table 5-1. Parameters for sink strength calculation in unirradiated MA957.

Parameter	Value	Reference
Dislocation density (cm^{-2})	1.0×10^{11}	[108]
Dislocation capture efficiency, z_{id}, z_{vd}	1.02, 1.0	[138]
GB diameter (cm)	1.34×10^{-4}	[96]
Oxide particle size (cm)	1.87×10^{-7}	This study
Oxide particle density (cm^{-3})	2.8×10^{17}	This study

The calculated sink strengths for unirradiated MA957 specimens are listed in Table 5-2 below. Under the above parameter assumptions, it can be seen that the grain boundary contribution to overall sink strength is only ~5%, while nanometer-sized oxide particles contribute the majority and dislocation structures provide a fair amount. However, as pointed out in parameter selection, the large uncertainty in dislocation density could mean its strength is as much as an order of magnitude higher (upper

bound), which would drastically alter the relative sink strength among current microstructure features.

Table 5-2. Calculated sink strengths for microstructure features in unirradiated MA957.

	k_{iX}^2		k_{vX}^2	
	Value ($\times 10^{11}$ cm^{-2})	Relative Contribution (%)	Value ($\times 10^{11}$ cm^{-2})	Relative Contribution (%)
Dislocation	1.02	12.77	1.00	12.55
Grain boundary	0.39	4.88	0.39	4.89
Oxide particles	6.58	82.35	6.58	82.56
α′	0.0	0.0	0.0	0.0
Total	7.99	-	7.97	-

Neutron Irradiated MA957

Figure 5-1 is a stacked column plot of sink strength (exact numbers are listed in Table 5-3) calculated according to the above formulas. The result shows that the majority of sink strength is provided by nanoscale precipitates: oxide particles and α' clusters. The combined sink strengths decrease almost monotonically with respect to irradiation temperature under the examined conditions. Even though there are noticeable changes in the population of nanoscale precipitates, sink strengths are comparable at all irradiation temperatures; the largest difference is between 385 and 550°C specimens. Contribution of both dislocations and GBs are relatively small. The grain structures are fairly stable according to TEM characterization, so grain size was set to a constant. Due to lack of dislocation density data, a constant value (the same as in unirradiated specimens) is assumed. This should be a reasonable approximation because 1) the relative contribution from dislocations is small; 2) the variation is limited to within an order of magnitude according to studies of ODS ferritic alloys [143]; 3) the dislocation

density is probably increased at lower irradiation temperatures and decreased at higher temperatures, which follows the general trend for calculated total sink strength.

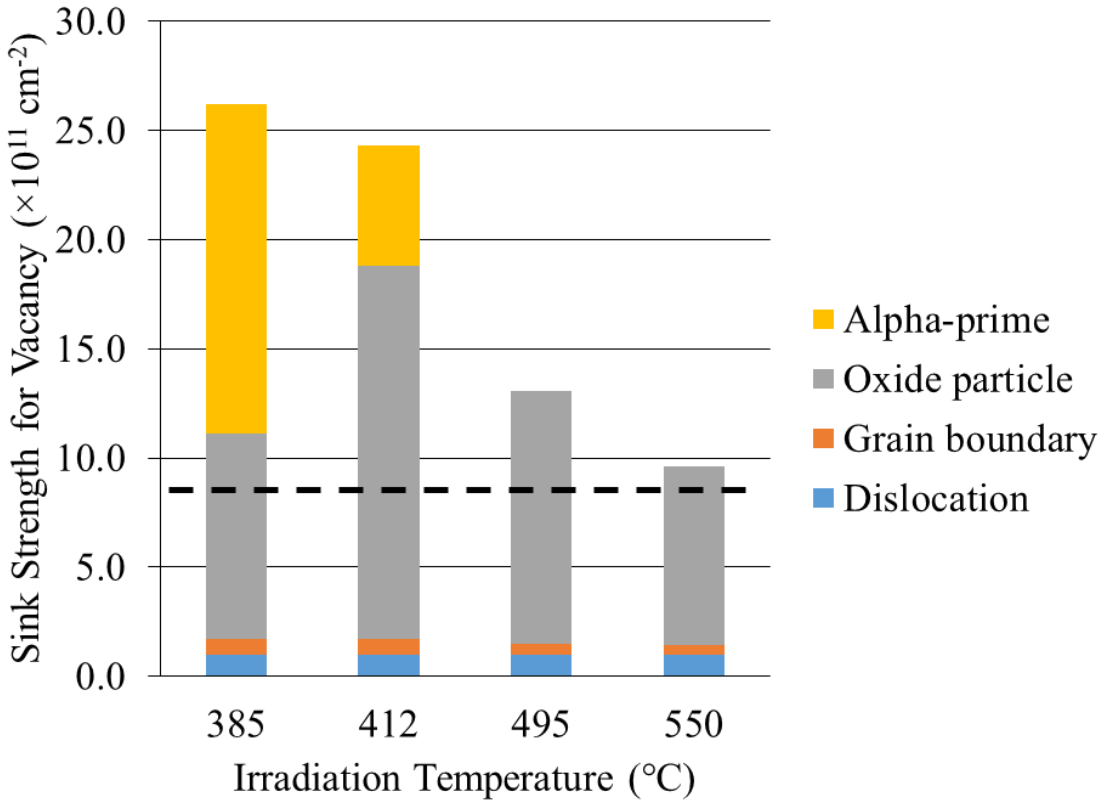

Figure 5-1. Stacked column plot of calculated combined sink strength for vacancies (k_{vX}^2) in neutron irradiated MA957 at different temperatures. The dashed line indicates sink strength in unirradiated materials. Note that sink strengths for interstitials are not plotted since there are only minor differences (~0.02×10^{11} cm^{-2}) due to defect bias from dislocations.

Table 5-3. Calculated total sink strength values for vacancies (k_{vX}^2) in neutron irradiated MA957 at different temperatures.

	Irradiation Temperature	385°C	412°C	495°C	550°C
Sink Strength ($\times 10^{11}$ cm^{-2})	Dislocation	1.00	1.00	1.00	1.00
	Grain boundary	0.715	0.689	0.502	0.429
	Oxide particle	9.39	17.1	11.6	8.20
	α′	15.1	5.55	0.00	0.00
	Total	26.2	24.3	13.1	9.63

Ion Irradiated MA957

Under the same assumptions as used in calculations for neutron irradiated specimens, sink strength was calculated for materials ion irradiated to 100 dpa, as plotted in Figure 5-2 and listed in Table 5-4. The results are similar to what we have observed in neutron irradiated specimens, where precipitates are dominant in providing sink strengths. Combined sink strength also decreases as irradiation temperature rises. The highest sink strength of oxide particles is found at 450°C, while that for neutron irradiated specimens was located at 412°C. Although sink strength differences can be varied by as large as a factor of ~3 under those conditions, all of them can still be considered high sink strength materials. No obvious grain structure changes have been observed and dislocations were not characterized.

Table 5-4. Calculated total sink strength values for vacancies (k_{vX}^2) in ion irradiated MA957 at different temperatures.

	Irradiation Temperature	400°C	420°C	450°C	500°C
Sink Strength ($\times 10^{11}$ cm^{-2})	Dislocation	1.00	1.00	1.00	1.00
	Grain boundary	0.654	0.495	0.463	0.378
	Oxide particle	3.68	5.49	8.70	6.12
	α′	16.7	5.74	0.996	0.00
	Total	22.0	12.7	11.2	7.50

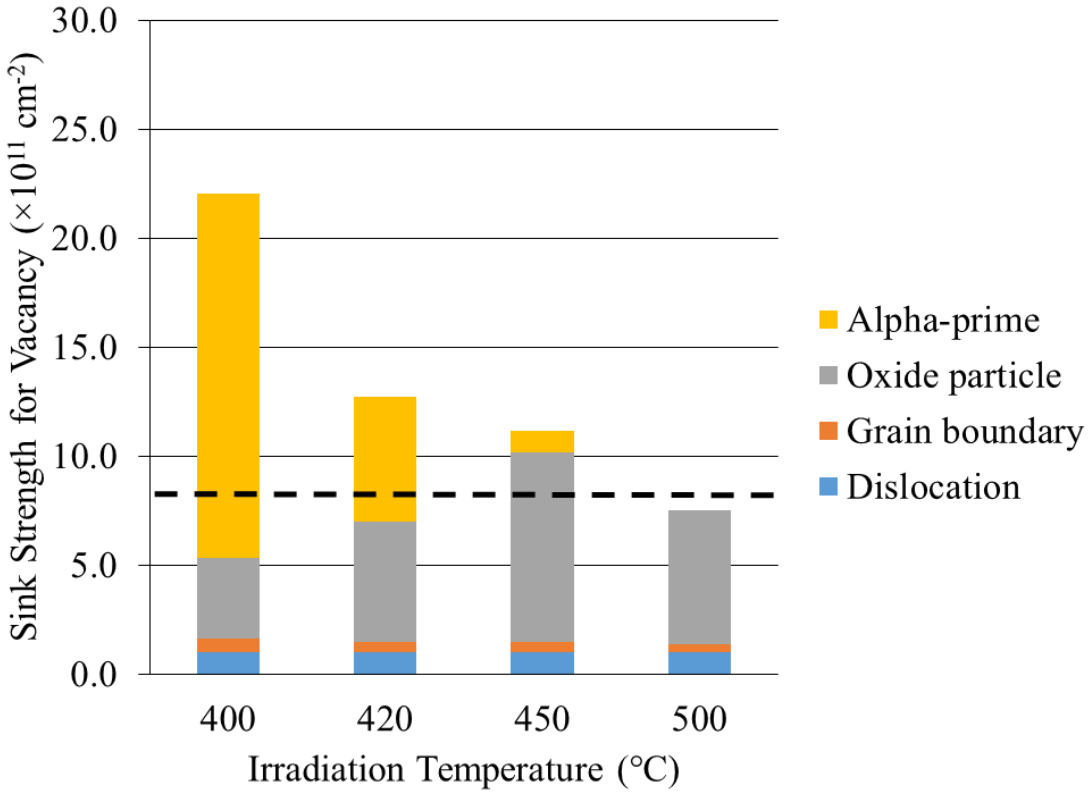

Figure 5-2. Stacked column plot of calculated combined sink strength for vacancies (k_{vX}^2) in ion irradiated MA957 at different temperatures. The dashed line indicates sink strength in unirradiated materials. Note that sink strengths for interstitials are not plotted since dislocation bias for interstitials is small in these scenarios (~0.02×10^{11} cm^{-2}).

5.1.3 Defect Concentration and Radiation Enhanced Diffusion

The defect balance equation (5.1a) can be rewritten with sink strength representations in the following form, since interstitial concentration at thermal equilibrium can be neglected within the temperature of interest:

$$\begin{aligned}\frac{dC_v}{dt} &= K_0 - k_{iv}^2(D_i + D_v)C_iC_v - \left(\sum_X k_{vX}^2\right)D_vC_v + L_v \\ \frac{dC_i}{dt} &= K_0 - k_{iv}^2(D_i + D_v)C_iC_v - \left(\sum_X k_{iX}^2\right)D_iC_i\end{aligned} \tag{5.10}$$

The parameters for solving these equations are listed in Table 5-5 below. The irradiation temperature and damage rate are selected to match the experimental conditions. Sink strengths are directly adopted from calculations in the previous section. There are many sets of parameters from various studies for parameters related to point defect diffusion related parameters [144-148]. The migration energy of a mono-vacancy in BCC Fe is considered to be within the range from ~0.5 to 0.8 eV, and ab initio modeling, molecular dynamics and experimental data generally agree [24, 145, 149]. As for interstitials, values in the range from 0.1 to 0.4 eV have been reported [147, 148, 150], depending on the simulation method. For self-consistency, a set of parameters from Mendelev, et al was used [147], since both vacancy and interstitial diffusion coefficients were calculated under the same framework and the vacancy results were in good agreement with experimental works. In addition to the uncertainties in migration energy in BCC Fe, it has been reported that the migration energy could be affected by the presence of solute atoms [151], which makes the case even more complicated. The recombination radius is treated as sum of the vacancy interaction radius and the interstitial interaction radius by Stoller et al. [142].

Table 5-5. Parameters used for solving defect balance equation.

Parameter	Value
Boltzmann Constant, k_B (eV/K)	8.617×10^{-5}
Lattice parameter, a_0 (cm)	2.876×10^{-8}
Atomic volume, Ω (cm^3)	1.189×10^{-23}
Irradiation Temperature, T (°C)	385-550
Damage rate, K_0 (dpa/s)	1×10^{-6} or 1×10^{-2}
Sink strength, k_{iX}^2 or k_{vX}^2 (cm^{-2})	$7.97\text{-}26\times10^{11}$
Vacancy diffusion coefficient pre-exponential factor, D_v^0 (cm^2/s)	7.87×10^{-3}
Vacancy migration energy, E_m^v (eV)	0.6
Vacancy formation free energy, G_f^v (eV)	See text
Interstitial diffusion coefficient pre-exponential factor, D_i^0 (cm^2/s)	5.34×10^{-4}
Interstitial migration energy, E_m^i(eV)	0.15
Interstitial formation free energy, G_f^i (eV)	See text
Recombination radius, r_{iv} (cm)	4.466×10^{-8}

The vacancy and interstitial concentration at thermal equilibrium can be calculated by the Arrhenius equation:

$$C_j = \exp\left(-\frac{G_j^f}{k_B T}\right), j = i, v \tag{5.11}$$

where G_j^f is the defect formation enthalpy, k_B is Boltzmann constant, T is temperature. Usually the defect formation energy is used as an approximation and assumed to be temperature independent. Since interpolated free energies are available in Mendelev et

al. [147], from which diffusion parameters are taken, the interpolation equation is adopted in this study:

$$G_j^f = g_0 + g_1 T + g_2 T^2 + g_3 T^3 \tag{5.12}$$

where g_0, g_1, g_2, and g_3 are parameters, as listed in Table 5-6.

Table 5-6. Coefficients for interpolating free energy of point defect formation [147].

Defect	g_0 (eV)	g_1 (eV)	g_2 (eV)	g_3 (eV)
Vacancy	1.724	-1.20×10^{-4}	-2.79×10^{-8}	-5.93×10^{-11}
Interstitial	3.530	-1.57×10^{-3}	4.94×10^{-7}	-4.51×10^{-11}

Defect Concentration

Analytical Solutions for Steady State

The defect balance equation has been relatively well studied for transient behaviors under several typical scenarios as well as steady state solutions. A systematic review can be found in Was [8], chapter 5. Since formation of interstitials in BCC Fe is not energetically favorable within temperature range of interest, its equilibrium contribution is set to zero for convenience. Then the steady state solutions for vacancy and interstitial concentrations can be written as equation (5.13) and (5.14), respectively:

$$C_v^{ss} = -\left[\frac{K_{is}C_s}{2K_{iv}} - \frac{C_v^{eq}}{2}\right] + \left[\left(\frac{K_0 K_{is}}{K_{iv}K_{vs}} + \frac{K_{is}C_s C_v^{eq}}{K_{iv}}\right) + \left(\frac{K_{is}C_s}{2K_{iv}} - \frac{C_v^{eq}}{2}\right)^2\right]^{1/2} \tag{5.13}$$

$$C_i^{ss} = \frac{K_{vs}}{K_{is}}\left(C_v - C_v^{eq}\right) \tag{5.14}$$

The reaction rate coefficients can be computed from sink strengths as described in equations (5.6), (5.7) and (5.8).

The time required to reach the onset of steady state is approximated by:

$$t^{ss} = \frac{1}{K_{vs}C_s} \tag{5.15}$$

Figure 5-3 shows the estimated time to reach steady state using sink strengths obtained for unirradiated and irradiated MA957. The data suggests that a steady state defect concentration can be reached in a time on the order of 10^{-6} s within the range of irradiation temperatures studied here. The defect concentrations converge to steady state faster at higher temperatures due to increasing defect mobility. It can be seen that steady state defect balance can be established almost instantaneously in MA957 at all stages in this study.

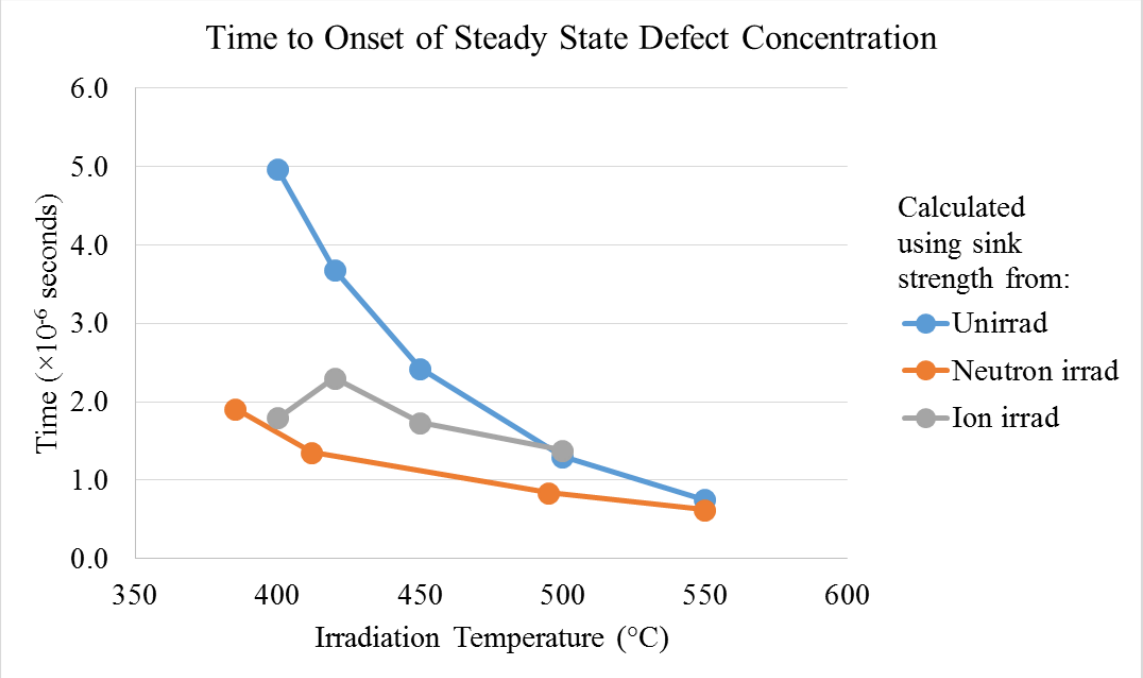

Figure 5-3. Time required to reach steady state defect concentration estimated by analytical approximations according to equation (5.15).

Defect concentration at steady state at thermal equilibrium and under neutron irradiation (damage rate $K_0=10^{-6}$ dpa/s) are plotted in Figure 5-4 on logarithmic scale. The steady state defect concentration directly links to sink strengths. Using sink

strengths obtained from unirradiated and neutron irradiated microstructures results in qualitatively similar steady state values. At lower irradiated temperatures (< 500°C), it is clear that both vacancy and interstitial concentrations are elevated by irradiation compared to unirradiated case. Above 500°C, the thermal emission of vacancies quickly becomes dominant. Thermally generated interstitials still play a minor part at those temperatures and the total interstitial concentration slightly decreases due to higher defect mobility promoting defect annihilations.

Figure 5-5 shows steady state defect concentrations calculated at thermal equilibrium and under ion irradiation (damage rate 10^{-2} dpa/s) on logarithmic scale. Unlike the neutron irradiation cases, both vacancy and interstitial concentrations are dominated by irradiation-induced defects while thermally generated defects are negligible at all temperatures. Both vacancy and interstitial concentrations slightly decrease at higher irradiation temperatures due to higher mobility. Since sink strengths in ion irradiated specimens are qualitatively similar to those in unirradiated specimens, there are only slight differences in steady state defect balance concentrations.

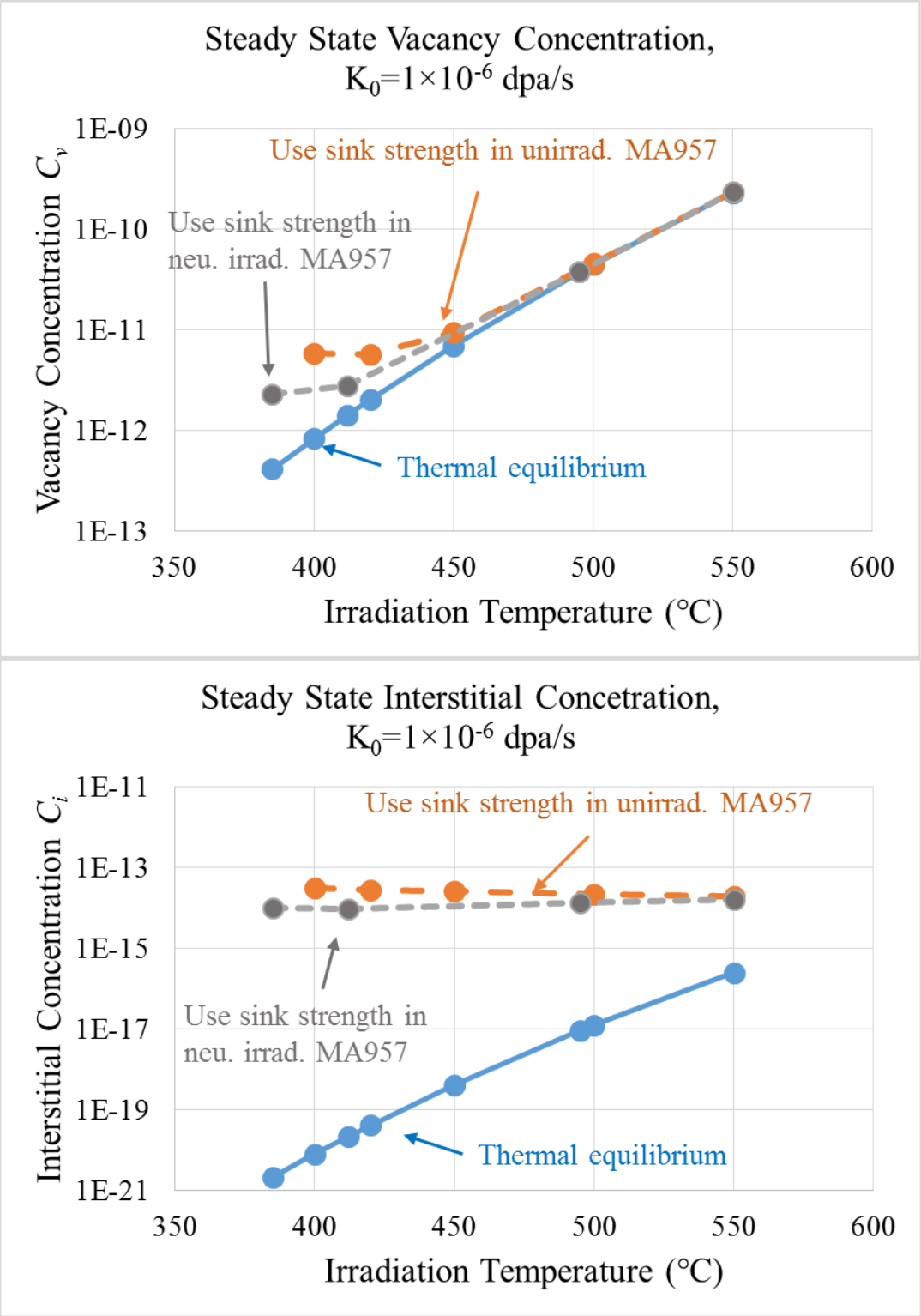

Figure 5-4. Steady state defect concentration at thermal equilibrium and under neutron irradiation (damage rate 10^{-6} dpa/s).

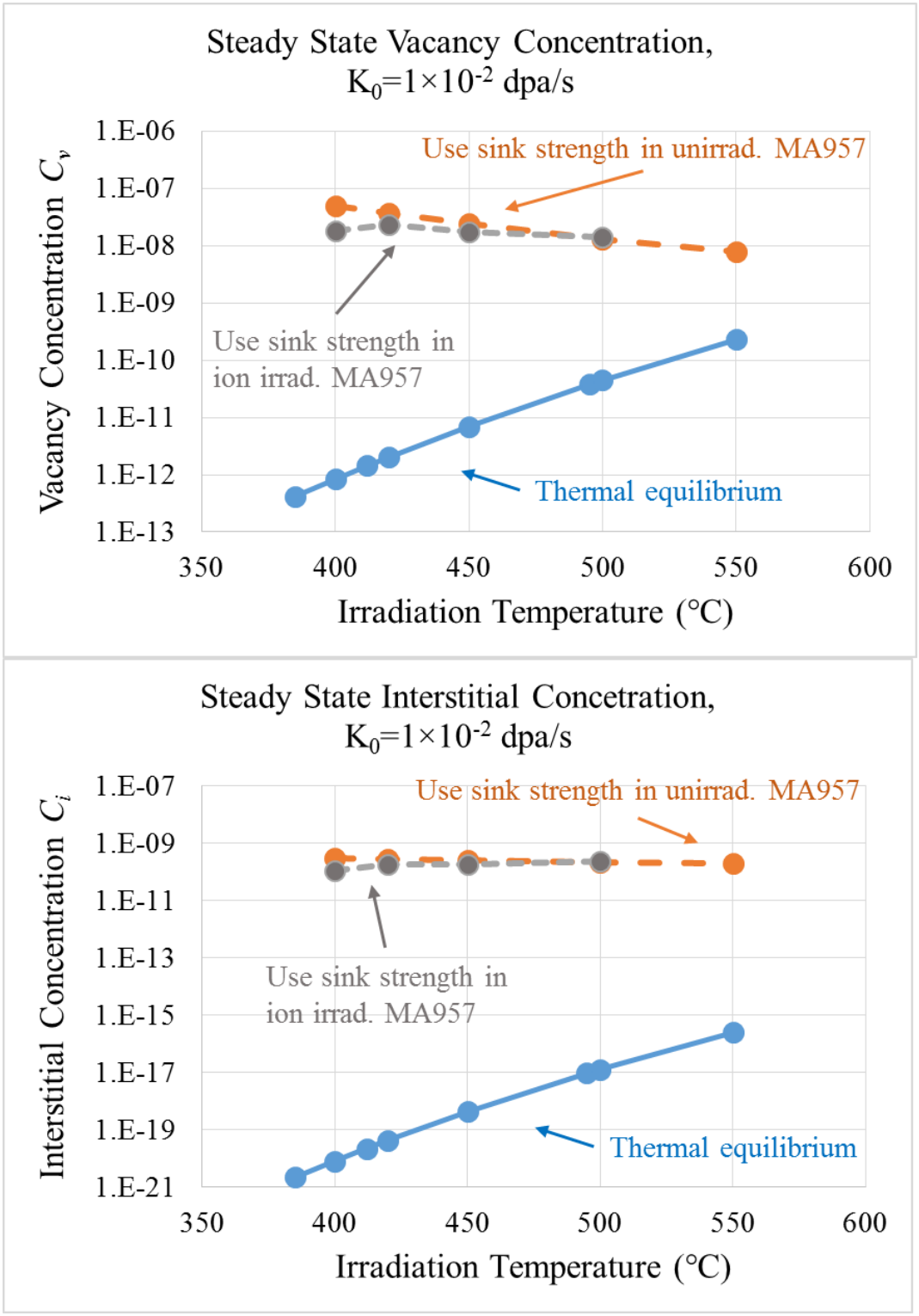

Figure 5-5. Steady state defect concentration at thermal equilibrium and under ion irradiation (damage rate 10^{-2} dpa/s).

Numerical Solutions for Transient Behavior

Solving the time dependence of defect balance equations analytically for transient behavior is nontrivial; however, numerical methods can be applied to solve them relatively easily. Figure 5-6 shows the numerical solutions to transient behavior of vacancy concentration evolution under several scenarios. The first set of cases are neutron irradiation conditions where the damage rate is 10^{-6} dpa/s. Two material conditions, represented by two sink strengths, are considered for transient behavior of vacancies: the sink strength obtained from unirradiated MA957 is used to represent the initial stage of irradiation where no significant microstructural features occurred yet; and the sink strength from correspondingly irradiated MA957 is used to represent the fully developed or developing microstructures near the end of irradiation. The results can be grouped into two categories based on irradiation temperatures. At low irradiation temperature, vacancies slowly accumulate below 10^{-12} dpa due to defect production by irradiation. The vacancy accumulation rate then slightly accelerates due to the contribution of sinks to interaction with interstitials. The steady state is then reached around roughly 10^{-11} dpa (~10^{-5} s), depending on the sink strength from microstructural features. At high irradiation temperatures, as has been shown in the previous steady state analysis, thermally generated vacancies are dominant so that there is no obvious defect accumulation. The most noticeable difference in ion irradiation is the strong vacancy accumulation, which occurred at all temperatures, preceding a steady state due to a higher damage rate (10^{-2} dpa/s). The sink strengths obtained for different materials also directly affect both steady state and transient vacancy concentration. Higher irradiation temperature increases defect mobility, which results in a slight reduction in steady state defect concentration and slightly shorter time to reach steady state, as has been discussed in steady state analysis.

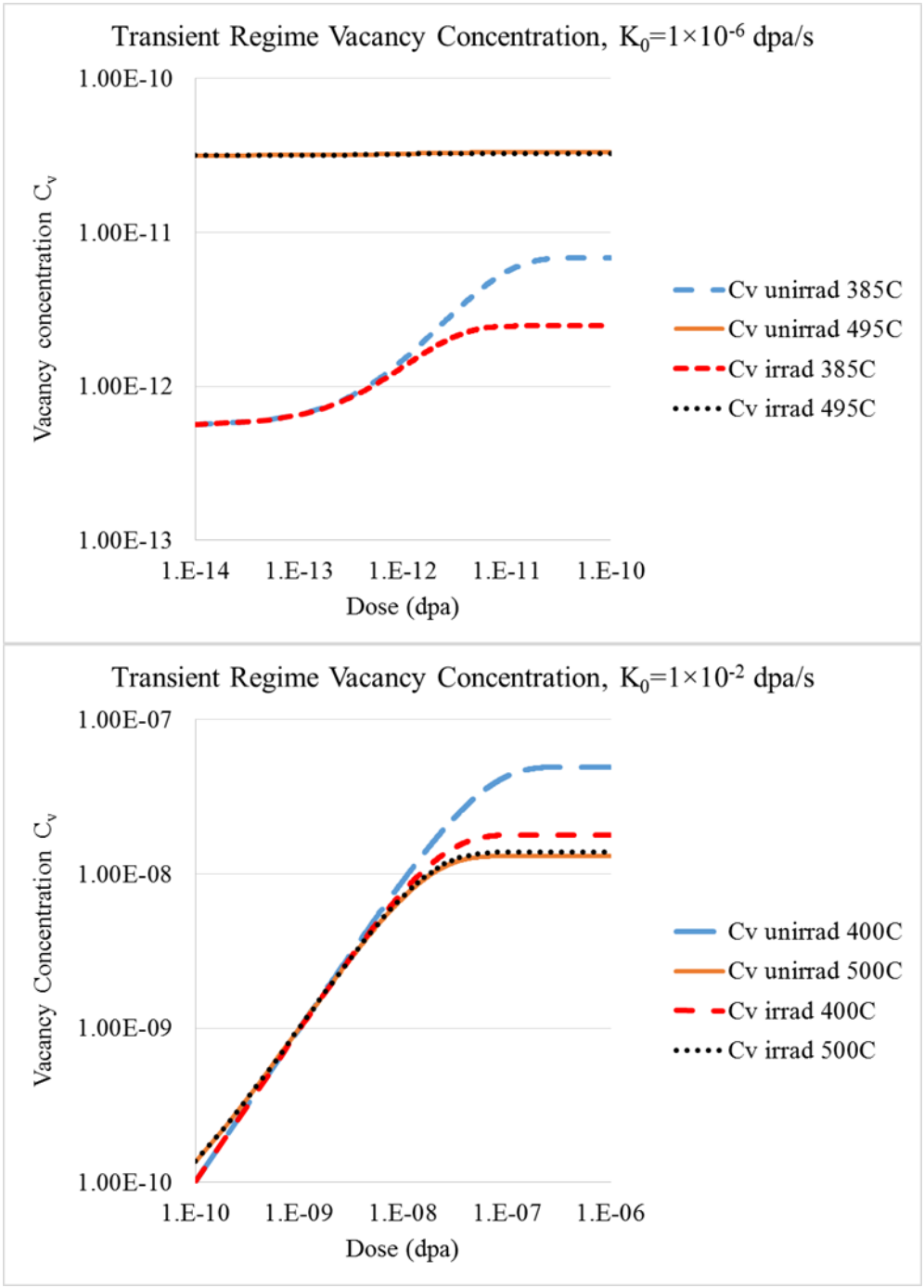

Figure 5-6. Transient behavior of vacancy concentration in neutron and ion irradiated specimens when irradiation begins (using sink strength from unirradiated MA957) and ends (using sink strength from correspondingly irradiated MA957). Note that the total length of time is the same for these calculations. The difference in total dose is due to differences in dose rate.

Radiation Enhanced Diffusion (RED)

The microstructural features of interest for neutron-ion comparison in this study are YTiO oxide particle, Cr-rich α', and changes in grain boundary chemistry. Thus Y, Ti, O and Cr solute atoms are the focus of our concern. Oxygen is a known to diffuse rapidly via interstitial mechanism in BCC Fe [152]. Radiation usually has a less significant impact on this class of solute atoms. Although thermally most solute atoms diffuse via vacancy mechanism due to high formation energy of interstitials [153], we cannot simply ignore their contributions under irradiation conditions, where an interstitial defect of solute with concentration an order of magnitude higher can be introduced, as previously demonstrated in Figure 5-4 and 5-5. Thus considering diffusion coefficients for Y, Ti and Cr should include both vacancy and interstitialcy mechanisms [145].

The irradiation enhanced diffusion can be written as:

$$D_{solute}^{rad} = \frac{C_v}{C_v^{eq}} D_{solute,v}^{thermal} + D_{solute,i}^{0} C_{solute,i} \tag{5.16}$$

where D_{solute}^{rad} is the radiation enhanced diffusivity of solute atoms; $D_{solute,v}^{thermal}$ is the diffusivity of solute via vacancy mechanism under thermal equilibrium; $D_{solute,i}^{0}$ is the diffusion coefficient for solute to diffuse via interstitialcy mechanism; and $C_{solute,i}$ is the interstitial concentration of solute atoms. The first term and second term correspond to vacancy and interstitialcy mechanisms, respectively.

Vacancy Mechanism

The relative enhancement of vacancy concentration is plotted in Figure 5-7 using a steady state defect concentration obtained for unirradiated MA957. It can be directly linked to enhanced diffusivity through equation (5.16). The results should be similar to those using sink strengths from irradiated microstructures based on the similarities observed in Figure 5-4 and 5-5. Solute diffusivities are greatly enhanced below 450°C under neutron irradiation, while orders of magnitude greater enhancement is estimated for ion irradiation at all temperatures. Note that although defect concentration increases

at lower irradiation temperatures, the effective diffusivities of solute or matrix atoms are either decreasing or approaching a steady state due to lower attempted jump frequencies at those temperatures.

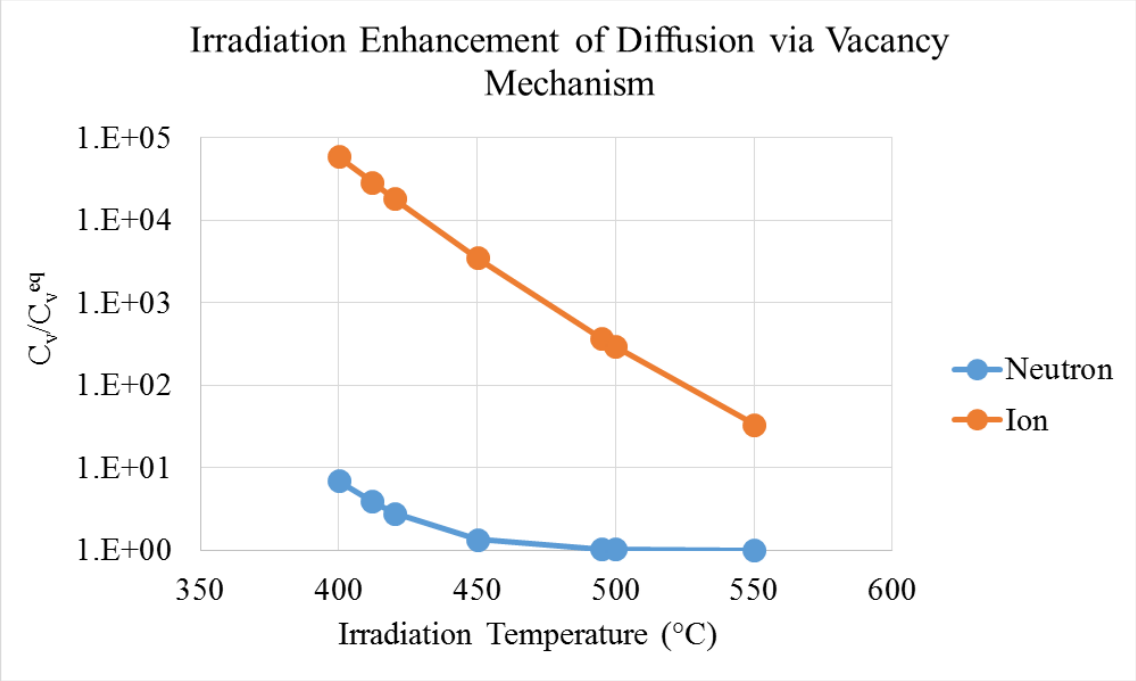

Figure 5-7. Relative enhancements of vacancy concentration under neutron (damage rate 10^{-6} dpa/s) and ion irradiation (damage rate 10^{-2} dpa/s) at various temperatures.

The diffusion coefficients for Y, Ti, and Cr from experimental measurements are shown in Table 5-7. As has been mentioned, the main mechanism for solute diffusion in BCC Fe under thermal equilibrium is via vacancy mechanism, so these parameters will be used as $D_{solute,v}^{thermal}$ in equation (5.16). The calculated diffusion coefficients for these solute atoms under thermal equilibrium and under irradiation-induced enhancement are shown in Figure 5-8. As expected from previous defect balance equation results, strong enhancements have been observed for lower irradiation temperatures under neutron irradiation and for all irradiation temperatures under ion irradiation. At higher

temperature and under lower dose rate, there is little enhancement from irradiation. At high dose rate, the temperature influence (slope with respect to temperatures) on diffusivity of solutes becomes lower since irradiation-enhanced diffusion is dominant.

Table 5-7. Diffusion parameters from experimental measurements.

Elements	Pre-exponential factor, D_0 (cm^2/s)	Activation energy, Q (eV)	Reference
Y	1×10^{-1}	3.10	[154]
Ti	2.1×10^{3}	3.04	[155]
Cr	6.4×10^{-1}	2.40	[149]

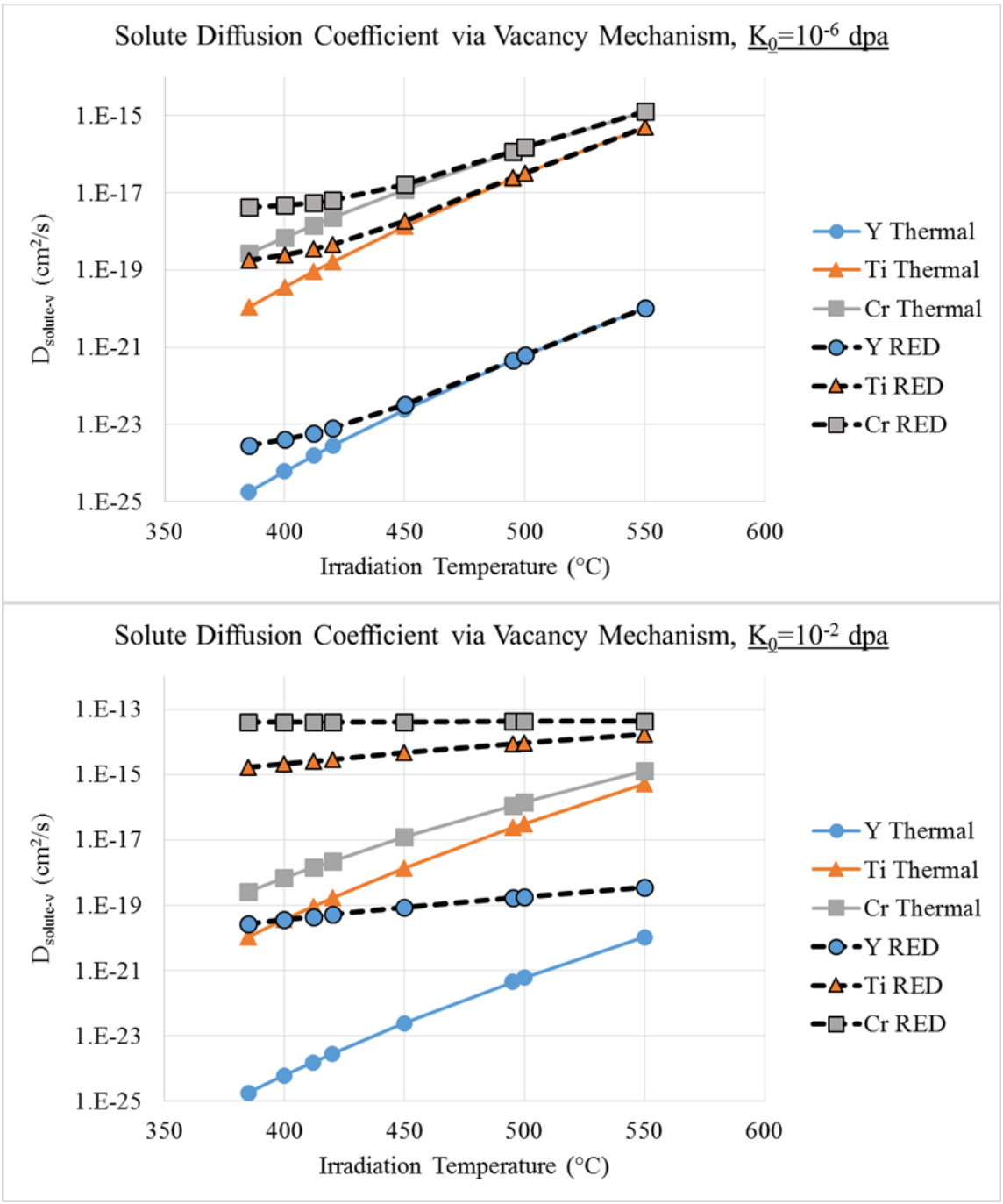

Figure 5-8. Thermal equilibrium and irradiation enhanced vacancy-mediated diffusion coefficients for solute atoms Y, Ti and Cr subjected to two damage rates.

Interstitialcy Mechanism

Interstitial diffusion coefficients for solute atoms like Y, Ti and Cr are extremely difficult to measure experimentally. Especially for Y and Ti, even computational diffusion data are limited for parameter selection. Table 5-8 lists the best parameters we could find for this work. The energy barriers for Y and Ti are calculated assuming the dumb-bells are mainly Fe-Y or Fe-Ti due to relatively low concentration of Y and Ti [156]. The pre-exponential factor and migration energy for Cr are available from reference [144]. Due to lack of interstitial attempt jump frequency for Y and Ti, we assumed it to be similar to that of a Cr interstitial, which is on the same order of magnitude as Fe self-interstitials. The interstitial concentration of solute atoms produced by irradiation, $C_{solute,i}$, is then assumed to be a fraction of the steady state defect concentration and is proportional to the corresponding atomic concentration in the bulk material. The calculated diffusivity coefficients for interstitialcy mechanism are shown in Figure 5-9. The data suggest that for Cr and Ti, diffusivity via interstitialcy mechanism is several orders of magnitude lower than that via vacancy mechanism. As for Y, the interstitialcy mechanism is more dominant at lower irradiation temperatures and is comparable with the vacancy mechanism even above 500°C.

Table 5-8. Diffusion parameters used for interstitialcy mechanism calculation.

Parameters	Values	Reference
Interstitial migration energy, Y (eV)	0.21	[156]
Interstitial migration energy, Ti (eV)	0.24	[156]
Interstitial migration energy, Cr (eV)	0.26	[144]
Interstitial pre-exponential factor, Y (cm^2/s)	9.02×10^{-4}	No data; assuming the same jump frequency as Cr
Interstitial pre-exponential factor, Ti (cm^2/s)		
Interstitial pre-exponential factor, Cr (cm^2/s)	9.02×10^{-4}	[144]

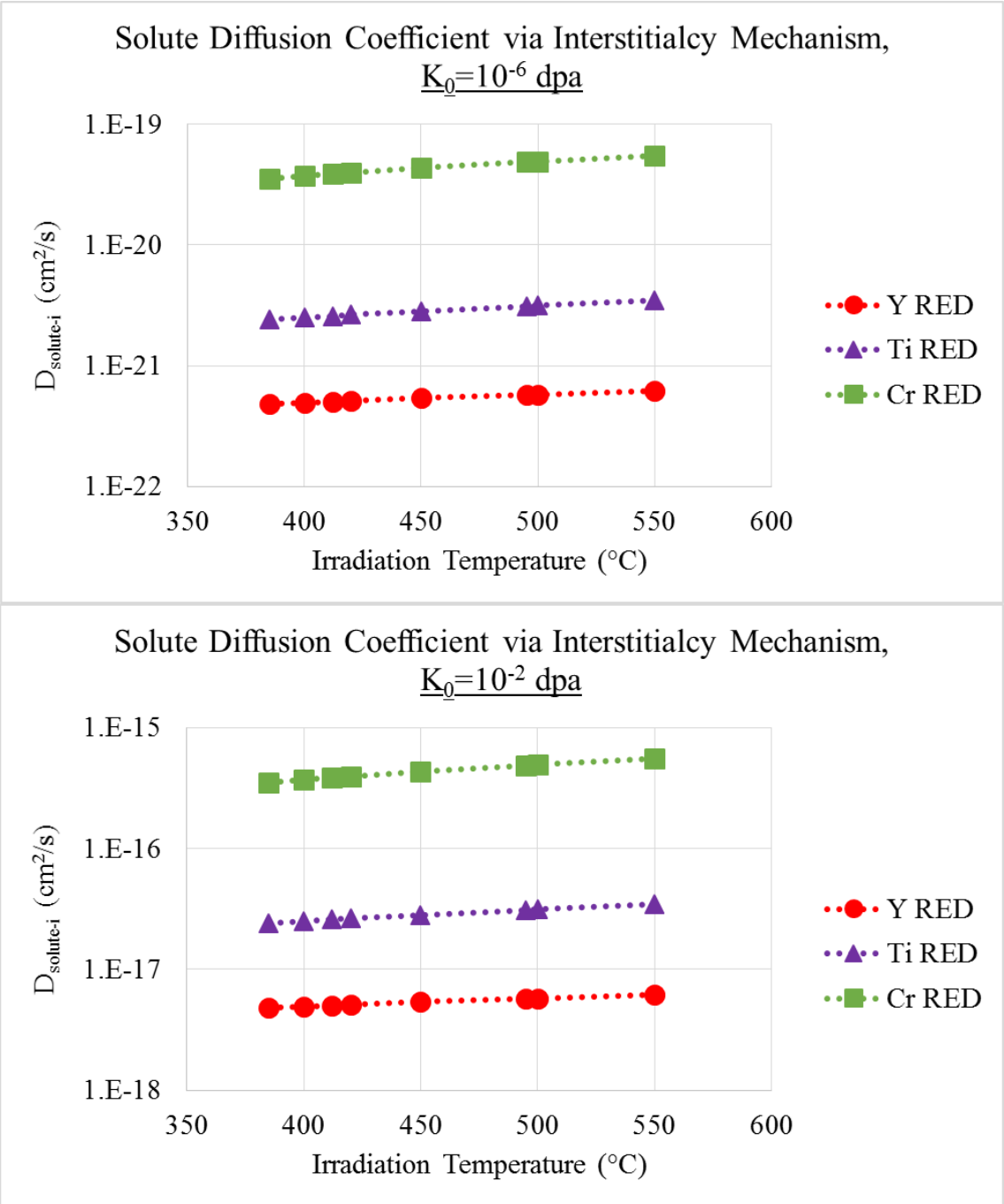

Figure 5-9. Irradiation enhanced diffusion coefficients for solute atoms Y, Ti and Cr via interstitial mechanism subjected to two damage rates.

To summarize, irradiations could enhance solute diffusivity by orders of magnitude depending on temperature, dose rate, and sink strength. Irradiation enhanced diffusion via vacancy and interstitialcy mechanisms are calculated and compared among solutes and irradiation conditions. Even though interstitial concentration produced by irradiation is an order of magnitude higher than that at thermal equilibrium, its contribution to the total diffusivity is negligible for Ti and Cr atoms. As for Y, the calculated interstitialcy diffusivity is much higher than the diffusivity mediated by vacancy mechanism at irradiation temperatures below 500°C. However, it might be an overestimated by our assumption for interstitial Y production. In reality, Y is mostly concentrated in YTiO particles so that makes the production of Y interstitials may not be as high as directly proportional to their atomic concentration in the bulk. Considering the overestimation, the interstitial diffusivity could be much lower. Since we have observed Y segregation to grain boundaries at lower irradiation temperature, it is reasonable to say that interstitialcy mechanism should not be ignored [91]. Further investigations will be conducted using diffusivities for Y with and without considering interstitialcy mechanism.

5.2 Phase Stability under Irradiation

Precipitates and second phases are a vital part of microstructural features that link to mechanical properties. Irradiation is known to have profound effects on those phases, such as inducing their formation when it would otherwise not feasible under pure thermal equilibrium, or causing dissolution of otherwise thermodynamically stable phases. Several mechanisms have been identified as governing their behaviors. Recoil dissolution [157-161], also called ballistic dissolution or atom mixing, causes disordering of phases and ejects atoms into the matrix. This process drastically accelerates the exchange of atoms between distinct phases and matrix around interfaces. Depending on the irradiation temperature, it could lead to amorphization or shrinking of those phases. The excessive solute elements in the matrix could lead to nucleation of new phases or enhanced coarsening rate of pre-existing phases [38, 162]. In addition, the

irradiation induced local enrichment or depletion of solute atoms, such as in a binary solid solution system, could also alter phase stability if the solubility limit is crossed [38].

In this chapter, we are trying to understand what causes the differences and similarities observed in our results by theoretically and quantitatively analyzing several experimental factors, such as damage dose rate and irradiation temperature effects using models based upon rate theory. Analysis results will be provided based upon each models.

5.2.1 Nelson, Hudson, Mazey Model

A simple yet very useful model is the NHM model for precipitate evolution under irradiation proposed by Nelson, Hudson and Mazey in 1972 [157]. The model was developed to include two competing effects: radiation induced dissolution of solutes and radiation enhanced solute back diffusion for re-deposition. Assuming all precipitates are spherical, of the same size, r_p, and subjected to irradiation with damage rate K_0 dpa/s, the volume change caused by recoil dissolution can be expressed by:

$$\frac{dV}{dt} = -4\pi r_p^2 \varphi K_0 \tag{5.17}$$

where V is the average volume of precipitate, φ is a rate coefficient for solute dissolution per dpa. The growth rate caused by solute diffusion flux is simply defined by [163]:

$$\frac{dV}{dt} = \frac{3DC_s r_p}{C_p} \tag{5.18}$$

where C_s and C_p are solute concentrations in the matrix and precipitate, respectively, and D is the radiation enhanced diffusivity of solute atoms. This re-precipitation term is a simplification of the Gibbs-Thomson formula by assuming a perfect interface sink where solute solubility at the interface is zero [164]. Due to the conservation of mass, those two concentrations must satisfy the following equation:

$$C = \frac{4}{3}\pi r_p^3 N C_p q + C_s$$
$$q = \frac{n V_m^{Matrix}}{V_m^{ppt}} \tag{5.19}$$

where N is the number density of precipitates, C is the total concentration of solute, and q is the molar volume ratio between matrix and precipitates. q is a term we added here to address differences in molar volumes which are negligible in the original formula for a solid-solution system. Since the nature of this equation is the conservation of mass, the total amount of solute in precipitates must be calculated with this correction if its molar volume is noticeably different from that of the matrix. V_m is the molar volume of major matrix elements or precipitates, n is related to the stoichiometry of the element of interest in the precipitate. The net change in size in terms of radius is the sum of the effects of dissolution and coarsening:

$$\frac{dr_p}{dt} = -\varphi K_0 + \frac{3DC_s}{4\pi r_p C_p} \tag{5.20}$$

The equation is more convenient when expressed as radius change since that is the quantity that most experimental studies reported. Note that although equation (5.4) forbids the size $r_p = 0$, the original form in terms of volume has no such constraint. Since it is only a trivial case and not of interest for our investigation, this expression will not affect fine precipitate size for future calculations and analysis. A schematic for the NHM model is shown in Figure 5-10. Combining equation (5.19) and (5.20) yields:

$$\frac{dr_p}{dt} = -\varphi K_0 + \frac{3DC}{4\pi r_p C_p} - qDr_p^2 N \tag{5.21}$$

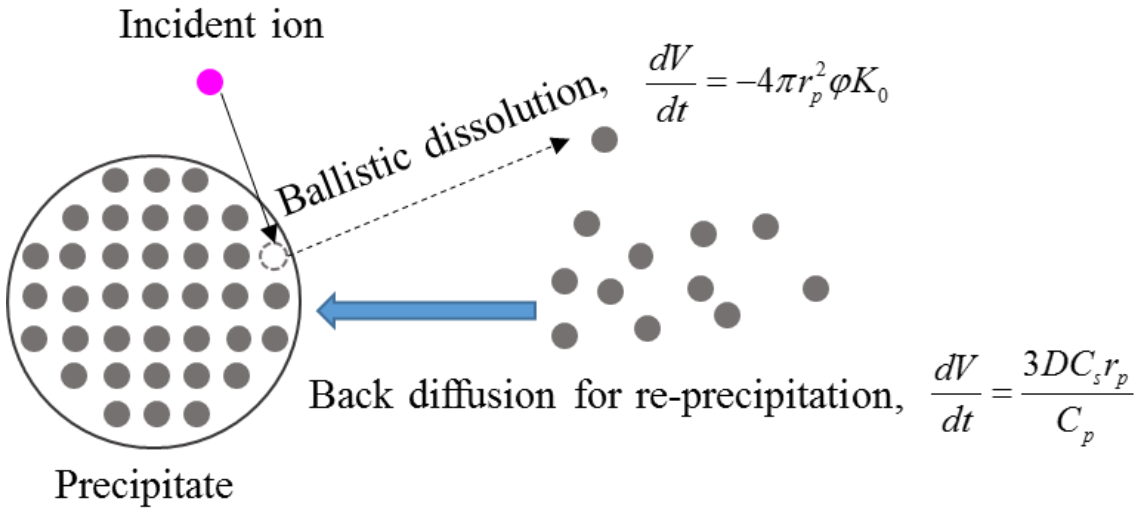

Figure 5-10. Schematic for the NHM model that illustrates ballistic dissolution and re-precipitation processes.

Steady State Analysis

The steady state solution can be easily obtained for equation (5.21):

$$\left[\frac{\frac{3C}{4\pi C_p} - qr_p^3 N}{r_p}\right] = \frac{\varphi K_0}{D} \tag{5.22}$$

where C is the solute concentration measured in the bulk material and N is the number density of the precipitate. On the left-hand side are steady state particle size and number density, and on the right hand-side are dissolution rate coefficient and terms that relate to experimental conditions such as temperature and dose rate. This ratio can be related to defect concentration and sink strengths:

$$\frac{D}{K_0} = \frac{D^v_{solute} C_v + D^i_{solute} \frac{K_{vs}}{K_{is}} \left(C_v - C_v^{eq}\right)}{K_0} \propto \frac{D^* C_v}{K_0} \approx \frac{D^*}{K_{vs} C_s} \tag{5.23}$$

where D^* is the combined diffusivity terms. The last term is an approximation in which equilibrium vacancy concentration is negligible and the defect annihilation at sinks is

more dominant than defect recombination. Equation (5.23) clearly shows that, in principle, there exists a temperature region where dose rate does not significantly affect steady state particle sizes.

As we can see from equation (5.22), the particle size also relies on their steady state number density, which cannot be solved from this equation. For analysis purposes, we could use experimentally measured density as input, and then compared the estimated steady state size and chemistry with experimental values.

Based on radiation enhanced diffusivity calculations, plots of D/K_0 versus irradiation temperature are shown in Figure 5-11 using sink strengths from unirradiated microstructures and in Figure 5-12 using sink strengths from irradiated microstructures. Diffusivities for Y atoms with and without considering interstitialcy mechanism are quite different in absolute values. Due to lack of accurate interstitialcy diffusion parameters, the current calculation only suggests that it could potentially be a significant factor, and more work needs to be done to provide evidence. Both figures yield similar trends for D/K_0 against temperature. We can see that at irradiation temperatures below 450°C, D/K_0 is very similar for neutron and ion irradiation, no matter which diffusion mechanism is considered. This is in good agreement with equation (5.23). The similarity even extends to 500°C if the interstitialcy mechanism contribution is considered for Yttrium. Above 500°C, thermally generated vacancies take a dominant role in neutron irradiation conditions and diffusion occurs primarily by via vacancy mechanism. For ion irradiation conditions, irradiation enhanced diffusivity is dominant at all temperatures due to a higher defect generation rate. The bottom graphs in Figure 5-11 and Figure 5-12 show similar behavior for Ti and Cr. Only the vacancy mechanism is considered, since it is orders of magnitude higher than the interstitialcy mechanism at all temperatures.

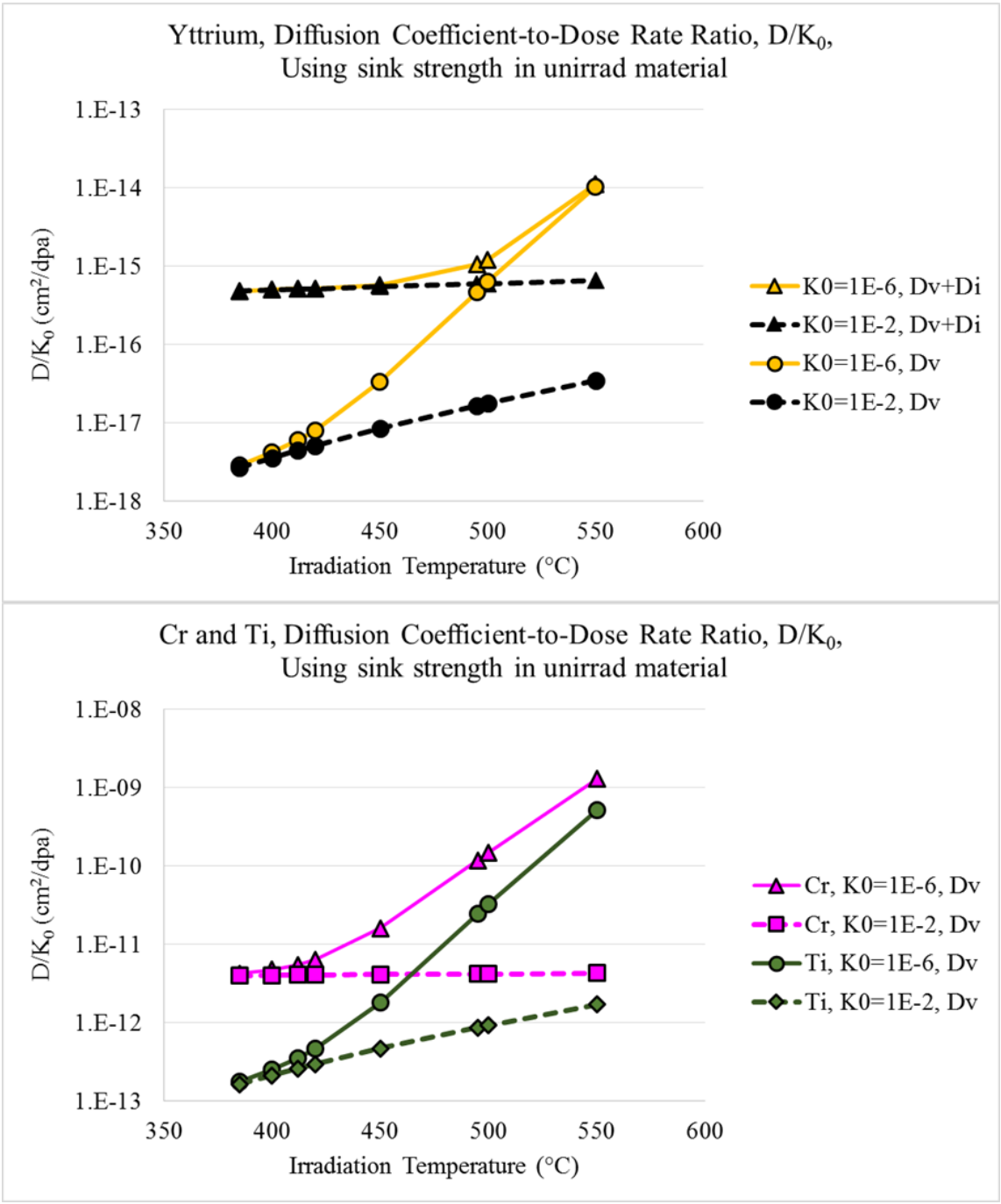

Figure 5-11. *D/K₀* plotted as a function of irradiation temperature using sink strengths in unirradiated microstructures. Diffusion via interstitialcy mechanism is included and compared with diffusion via vacancy mechanism only for Yttrium. Only the vacancy mechanism is considered for Titanium and Chromium because the diffusivity of vacancies is much higher than those via interstitialcy mechanism.

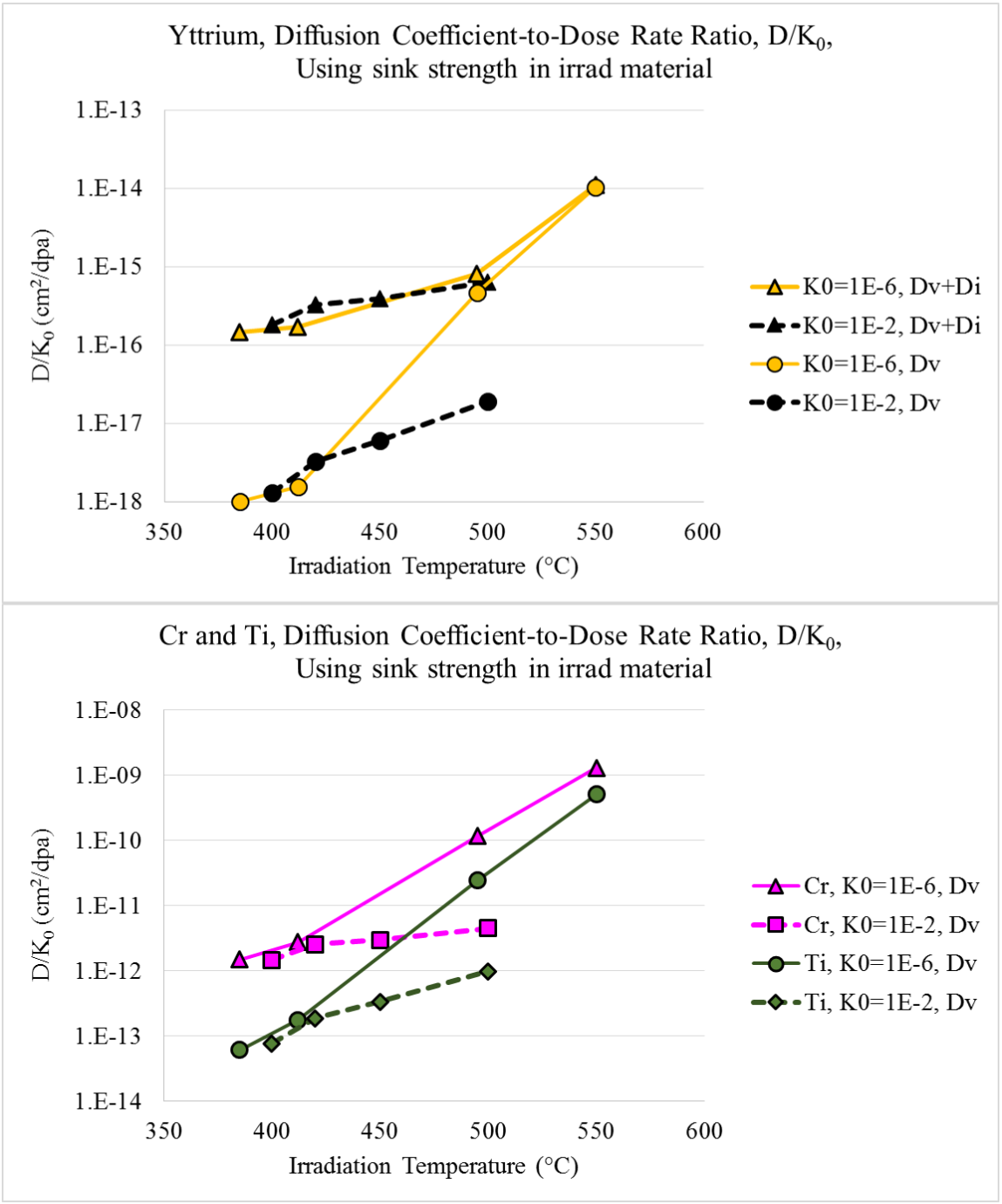

Figure 5-12. *D/K₀* plotted as a function of irradiation temperature for Yttrium with and without consideration of diffusion via interstitialcy mechanism, and for Titanium and Chromium via vacancy mechanism only, using sink strengths in irradiated microstructures.

YTiO Dissolution Rate and Re-precipitation Rate

Dividing each term in equation (5.21) by damage rate K_0, we obtain the precipitate size change rate per dpa:

$$\frac{dr_p}{K_0 dt} = -\varphi + \left(\frac{3C}{4\pi r_p C_p} - q r_p^2 N \right) \frac{D}{K_0} \tag{5.24}$$

It can be seen that in the temperature regime where D/K_0 is very similar for neutron and ion irradiation (< 450-500°C in our conditions), re-precipitation and dissolution rates can be almost independent of dose rate and temperature.

Dissolution Rate Calculated by SRIM

One way to roughly estimate dissolution rate of YTiO precipitates is via a target mixing calculation in SRIM. For simplification, a 4 nm layer, roughly the average diameter of oxide particles, of $Y_2Ti_2O_7$ was embedded between two 30 nm BCC Fe layers. A 1.8 MeV Cr ion was used as the incident ion and threshold displacement energies for Y, Ti and O were taken from *ab initio* molecular dynamics calculation in Xiao et al. [165]. Other parameters for the Fe layer were setup following suggestions in Stoller et al. [10]. A full damage cascade model was performed to produce recoil distributions from target mixing. Note that this is a rough calculation only intended to gain an order of magnitude estimate of ion beam mixing effects of YTiO particles. In reality, target mixing is more complicated, since the energy of incident ions that reach oxide particles is not a single value but is spread across an energy spectrum that relates to depth; there are also other secondary effects such as curvature of particles and sub-cascades.

The recoil distribution of Yttrium under 0.5 dpa damage is shown in Figure 5-13. The recoil distribution of Titanium is quite similar to that of Y and is not shown here. The recoil distribution calculated by SRIM shows a different solute spatial distribution compared to the NHM model, in which uniform recoil distribution is assumed. It can be seen that the majority of recoil atoms rest within ~5 nm of the interface and a tiny portion of recoils have been displaced beyond 10 nm. Considering that the YTiO

precipitate density in unirradiated material is ~3×10^{17} cm^{-3}, the average distance between centers of precipitates is evaluated to be ~18.2 nm. Although a small fraction of recoils could potentially be displaced past the middle point between precipitates, we need to emphasize that recoil distribution in the NHM model is a rough estimation.

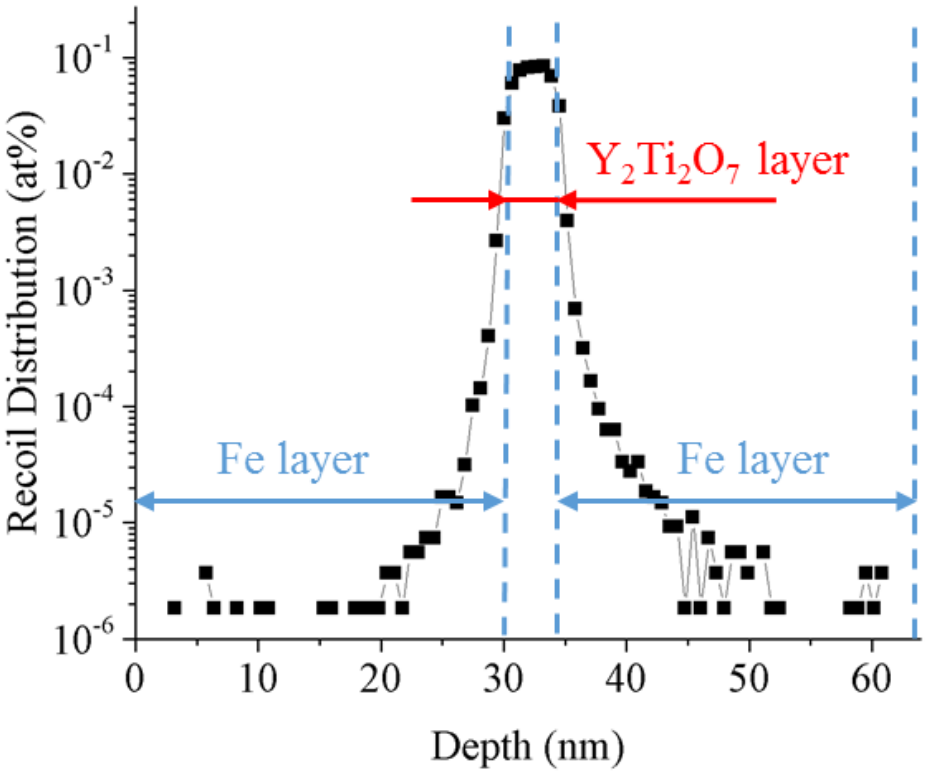

Figure 5-13. Recoil distribution of Yttrium under ion fluence of 1×10^{15} ions/cm^2, which is roughly equivalent to 0.5 dpa at 150 nm depth, where our analysis took place. The total number of recoils was converted to atomic percentage assuming BCC Fe atomic density was not changed for dilute concentration of solutes.

Figure 5-14 shows recoil distribution from interface into solution and a fitting curve that uses an exponential function. The recoil distribution can then be converted to thickness reduction per dpa by:

$$\frac{dr_{1D}}{K_0 dt} = \int_{\text{interface}}^{\infty} xR(C_s)\frac{\rho_{Fe}}{\rho_{YTiO}}dr \tag{5.25}$$

where x is stoichiometric correction, R is recoil distribution, ρ is atomic density, and r is distance from the interface. Since Ti is displaced at similar rate to Y and assuming O, being a fast diffuser, always maintains stoichiometric balance, x is then ~5.5, which means that on average, a total of 5.5 atoms were displaced in $Y_2Ti_2O_7$ per 1 Y displacement. In this case, the thickness reduction rate in a 1D $Y_2Ti_2O_7$ layer, $dr_{1D}/(K_0 dt)$, is evaluated to be 3.9×10^{-8} cm/dpa. Note that this value is at best an approximation for dissolution rate. The real dissolution rate could be much different due to interface energy, curvature, and a variety of complicated factors. However, currently there is no way to incorporate those effects in SRIM.

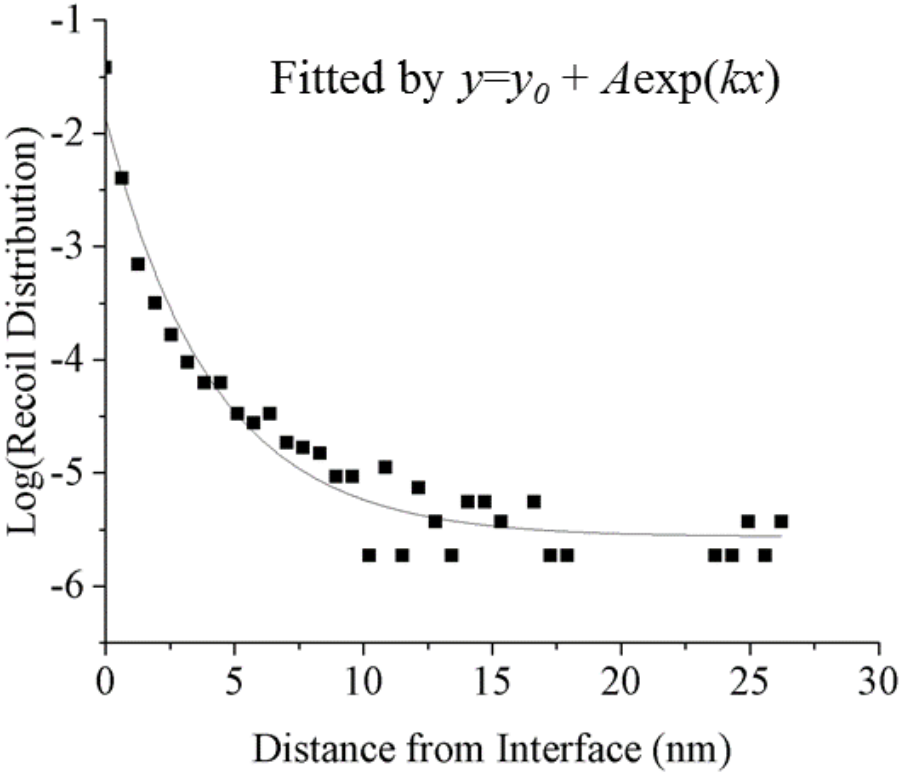

Figure 5-14. Fitting recoil distribution from YTiO layer interface into solution subjected to ion fluence 1×10^{15} ions/cm^2.

YTiO Size Change Rates from Experiments

Figure 5-15 shows average sizes of YTiO precipitate under ion or neutron irradiation to different doses. For ion irradiation conditions, particle size change rate per dpa, dr/K_0dt, decreases as irradiation temperature increases from 400 to 500°C. With particle size approaching a steady state value at higher doses, slopes of curves are gradually diminishing. Similar trends have also been observed for neutron irradiation conditions at 385 and 412°C. Unlike ion irradiated specimens, precipitate coarsening, $dr/(K_0dt) > 0$, occurred for nano-oxides when irradiated at 495 and 550°C by neutrons. In general, the relationship of precipitate size to dose and temperature is in good qualitative agreement with equation (5.24). However, quantifications of dissolution rate coefficients and re-precipitation rates from experimental data in the following sections suggest that more complexities maybe involved.

Another way to gain dissolution rate is through deduction by subtracting the calculated re-precipitation rate in the NHM model from experimentally measured particle size reduction rate. Nano-oxide size change rates, $dr/(K_0dt)$, can be roughly estimated by slopes according to Figure 5-15. We need to emphasize that this is at best an approximation to estimate dissolution rate due to limited data points. Clearly these nano-oxide particles experienced a rapid reduction in size, ~1-5×10^{-10} cm/dpa, below 100 dpa, and a slower decrease in size, ~1-8×10^{-11} cm/dpa, between 100 to 500 dpa. Note that all data between 100 and 500 dpa are quite similar, on the order of ~5-8×10^{-11} cm/dpa, except in specimens irradiated at 450°C. That different behavior needs further investigation; however, we suspect it may be linked to stronger void swelling at this temperature [45]. Similar calculations are carried out for neutron irradiated materials. At 385 and 412°C, YTiO particles are shrinking at rates ~5-11×10^{-10} cm/dpa, but coarsening at rates ~3-7×10^{-10} cm/dpa when irradiated at 495 and 550°C. Estimated particle size change rate per dpa, dr/K_0dt, excluding coarsening, is plotted in Figure 5-16.

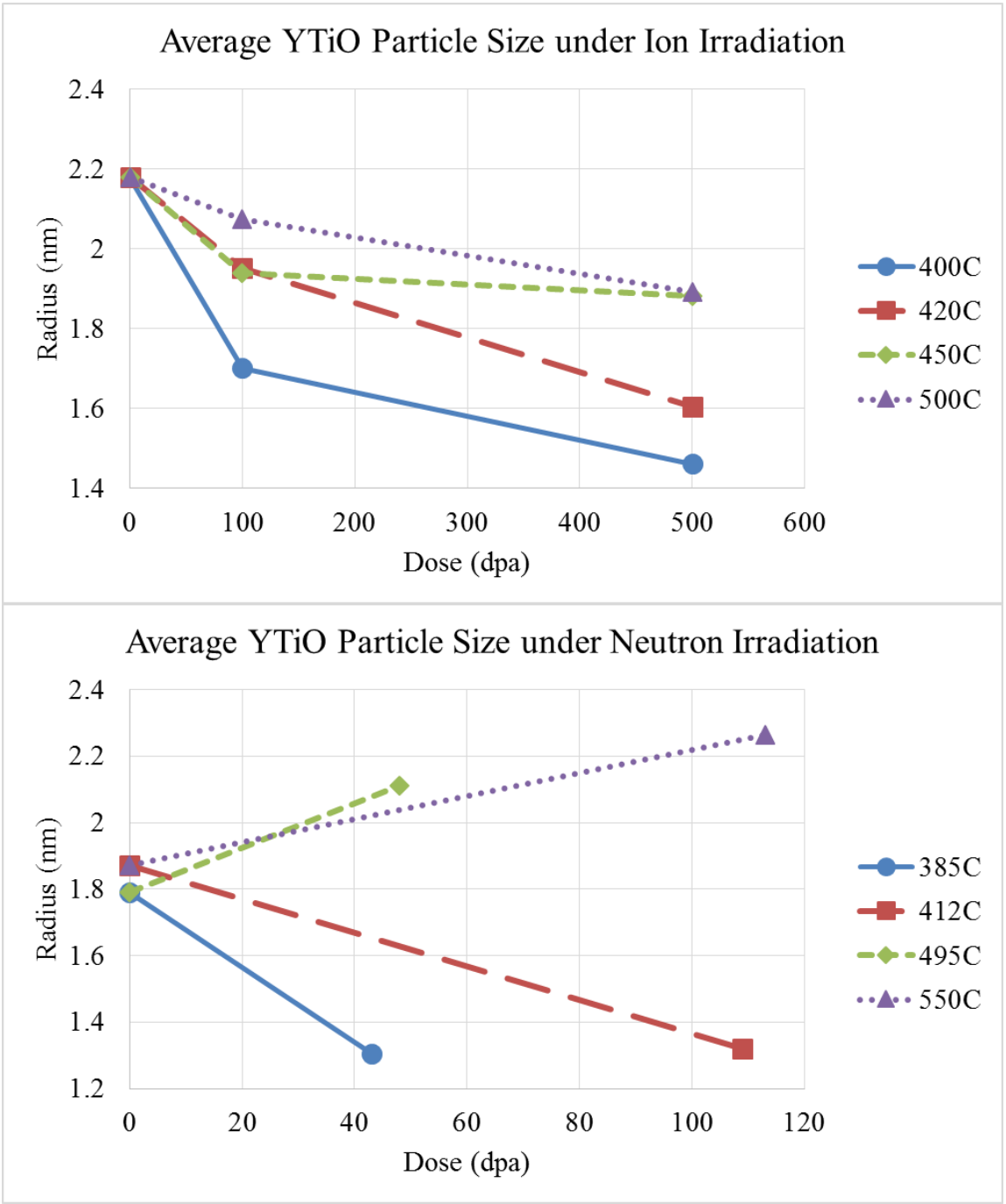

Figure 5-15. YTiO precipitate average sizes as a function of dose at various temperatures after ion or neutron irradiation.

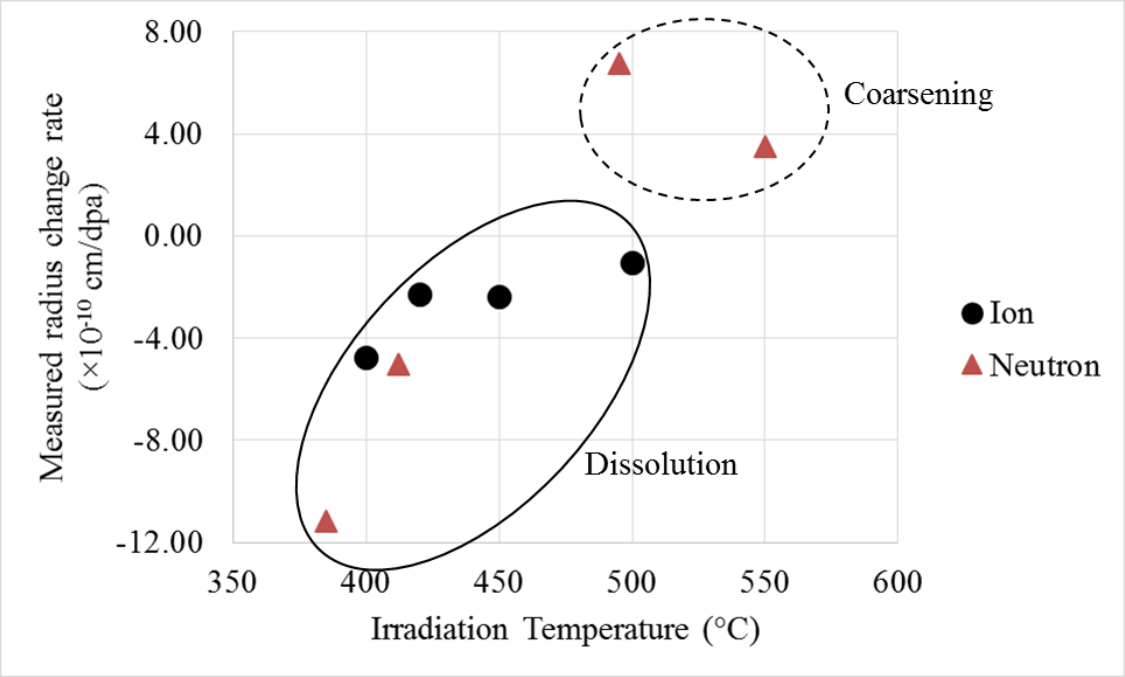

Figure 5-16. YTiO precipitate size change rate per dpa for ion and neutron irradiation conditions below 500°C.

Estimated particle size change rates, $dr/(K_0 dt)$, based on ion irradiation data, are plotted in Figure 5-17. It can be seen that at different cumulative dose ranges, the particle size changes per dpa can be different by orders of magnitude. The large fluctuation around 450°C maybe due to interference of void swellings, as previously mentions. However further investigation is needed.

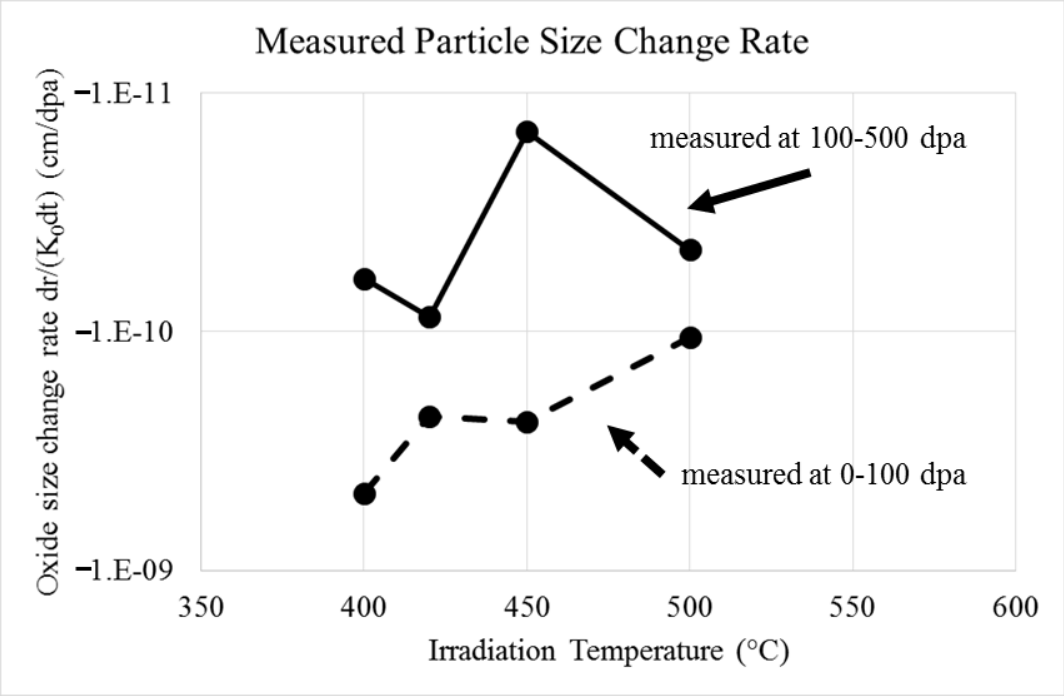

Figure 5-17. Measured particle size change per dpa at different dose regimes.

Re-precipitation Rate

For simple a solid solution system, equation (5.24) works well, but it may be inadequate for multicomponent precipitates. For example, assuming Y is the rate-controlling element, the corresponding re-precipitation rate needs to be corrected by some factor since other elements are almost re-precipitating at the same time. The corrected equation can be written as follow:

$$\frac{dr_p}{K_0 dt} = -\varphi + \left(\frac{3C}{4\pi r_p C_p} - q r_p^2 N \right) \frac{xD}{K_0} \tag{5.26}$$

where *x* is stoichiometric correction, 5.5, since re-deposition of every Y atom is accompanied by 1 Ti atom and 3.5 O atoms, assuming their diffusion is much faster to keep precipitate stoichiometry unchanged. However, as our experimental data on YTiO particle composition has shown, this argument does not hold in specimens ion irradiated at 400°C.

Typical nano-oxide related parameters for quantification are listed here: the radius is 1.0-2.0×10^{-7} cm, the number density is 1.0-6.0×10^{17} cm^{-3}, C and C_p are 0.08 and 18.2 at%, respectively, for all specimens, and q is 0.1838 assuming the precipitate is $Y_2Ti_2O_7$ and the matrix is BCC Fe. D/K_0 is determined as discussed previously in the steady state analysis section. Since oxygen is an interstitial species that usually diffuses orders of magnitude faster than common vacancy mediated solute diffusion [166], only Y and Ti will be covered for rate calculations.

The re-precipitation rates for Y and Ti can be evaluated using the second term in equation (5.26). The results are plotted in Figure 5-18. The re-precipitation rates, if Y is the rate controlling element, are calculated to be 7-18×10^{-12} cm/dpa for ion irradiation conditions. Both vacancy and interstitialcy mechanisms are assumed to be non-negligible. If titanium is the rate-controlling element in re-precipitation process, the re-precipitation rate is evaluated to be 3-28×10^{-9} cm/dpa for ion irradiation conditions. Compared with measured YTiO particle size change rates, re-precipitation rates calculated based on diffusivity of Y are too small to counter the effect of ballistic dissolution. On the other hand, re-precipitation rates based on Ti are too large.

Two major issues arise during our quantification efforts: calculated re-precipitation rates are significantly deviate from measured values, and the observed strong temperature dependence of particle size change rate, dr/K_0dt, does not match well with relative weak temperature dependence of D/K_0 for solute Y. Since ballistic dissolution can be considered an athermal process within the temperature range of our interests, dissolution rate per dpa, φ, is likely to be invariant with irradiation temperature. The discrepancy suggests that the current re-precipitation rate and its temperature dependence may be underestimated. Many factors may be responsible: diffusivity of solute may be higher than expected, since there is limited experimental data; diffusivity may be governed by other complicated mechanisms; other factors like solute drag, segregation or other effects may become important; the local solute concentration near precipitates is underestimated, since all solutes are assumed to be uniformly distributed in solution during dissolution in the NHM model; YTiO growth

kinetics is more complicated than estimated by the expression in the NHM model, etc. Most assumptions are difficult to examine due to lack of critical kinetic and thermodynamic parameters. Within current theoretical framework of a simple dissolution-re-precipitation model, arguments about local solute concentration profiles have been tested in later sections.

In brief summary, the rate-controlling element is likely to be Y rather than Ti or O assuming simple diffusion controlled growth kinetics. However, the re-precipitation rate based on current diffusivity of Y is too small to counter the ballistic dissolution effect. Since Yttrium diffusivity from Hin et al. [152] was extracted by fitting YTiO growth using a classical nucleation and growth model and no other direct experimental data are available, the uncertainty of this value is unknown. It is difficult to justify whether the NHM model is adequate for quantification of irradiation stability of YTiO particles. Another possible scenario is that a larger fraction of displaced Y atoms are in the configuration of Fe-Y dumbbells than expected so that its effective diffusivity is higher. Such effects need detailed analysis and knowledge about energies for multiple configurations, both of which are beyond the scope of this dissertation.

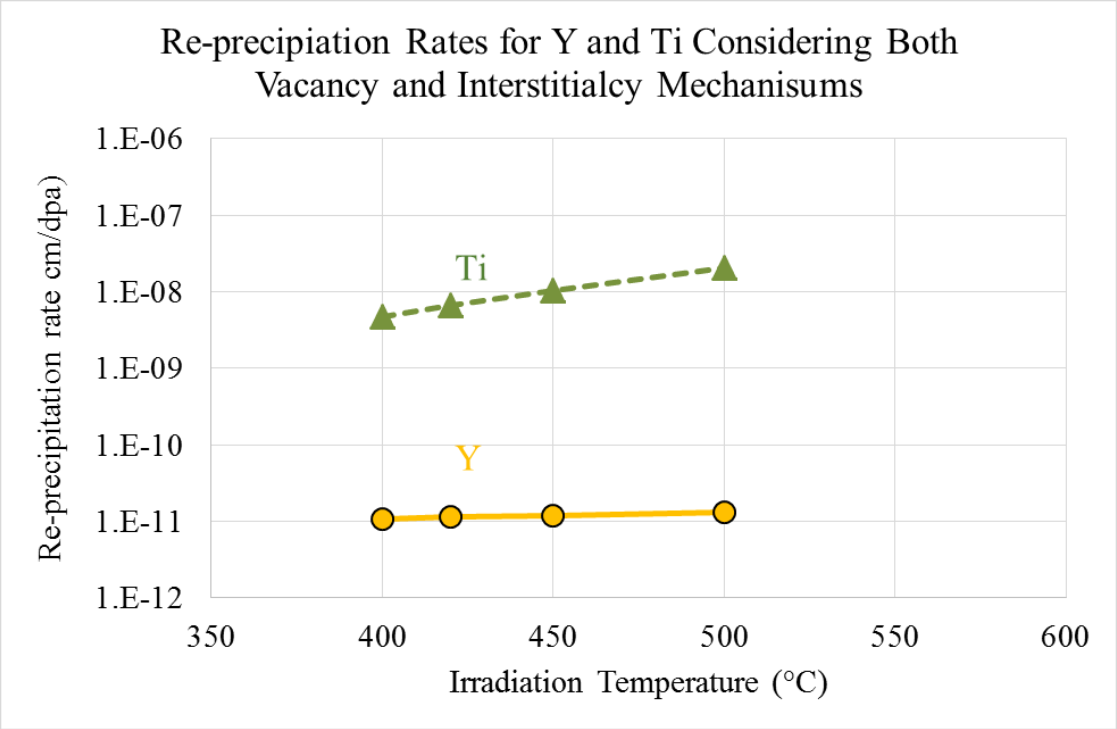

Figure 5-18. Calculated re-precipitation rates based on Y and Ti diffusivity using sink strengths in unirradiated material.

Time Dependent YTiO Precipitate Sizes

In the previous section we showed that measured size change rate for oxide particles are one or two orders of magnitude higher than the re-precipitation term calculated based on Y in this material system under ion irradiation conditions. An upper bound of average size shrinkage of YTiO particles can be roughly estimated by neglecting the re-precipitation term in equation (5.24):

$$\frac{dr_p}{K_0 dt} \approx -\varphi \tag{5.27}$$

A simple extrapolation can be made to estimate the average radius evolution of YTiO particles. Taking MA957 irradiated by ions at 400°C to 500 dpa as an example, where the dissolution rate coefficient is roughly estimated to be ~4×10^{-11} cm/dpa if re-precipitation term is ignored. The steady state size calculated by equation (5.22) then is

on the order of 10^{-2} nm, which is unrealistically small. It suggest that under these assumptions, YTiO oxide particles have not reached steady state and are still transient. Nevertheless, before this system reaching steady state, it would take an additional ~1630 dpa to further reduce the average radius by ~0.6 nm. Even if a higher dissolution rate, 4×10^{-10} cm/dpa, is applied, roughly 156 dpa will be needed to cause size shrinkage of the same amount, as shown in Figure 5-19.

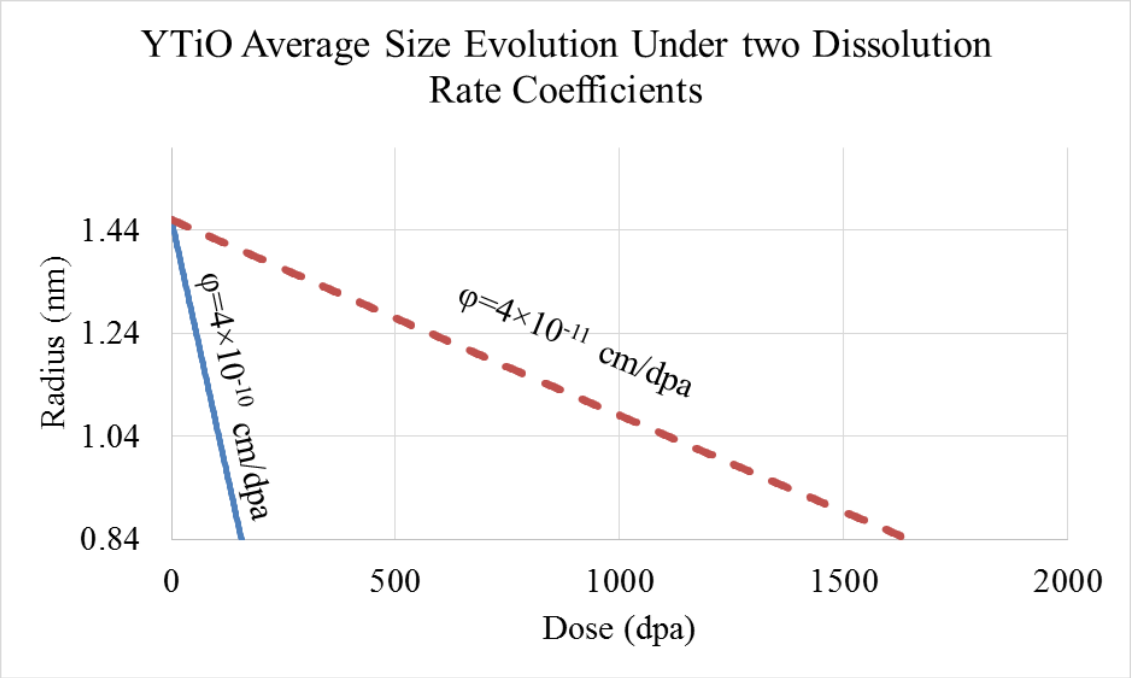

Figure 5-19. YTiO size evolution as a function of dose under two dissolution rate coefficients.

Alpha-Prime Stability

It is generally considered that α′ formation is accelerated by irradiation. Generally, irradiation induced precipitate forms and reaches steady state early during irradiation at dose level of a few or tens of dpa. The simple NHM model may not be adequate to fully address evolution of α′, especially without consideration of nucleation

and thermodynamics, but it would still be interesting to estimate re-precipitation and dissolution rates at α′ formation temperatures.

The solute re-precipitation term (the second term in equation (5.24)) is estimated to be on the order of 10^{-7} cm/dpa, taking parameters from specimens irradiated at 400°C to 100 dpa, where C=~10%, C_p=~80%, r_p=1.3 nm, q=~1.0, N=9.8×10^{17} cm^3, and D/K_0=1.5×10^{-12} cm^2/dpa. Due to the high diffusivity of Cr, the time required to reach steady state is usually much shorter than that for slow diffusing solutes. A demonstration for α′ under two dissolution rate coefficients is shown in Figure 5-20, both of which reach steady state fairly quickly, within a few dpa.

However, rather large differences have been observed in between specimens ion irradiated to 100 and 500 dpa at 400 and 420°C, as listed in Table 5-10. Variations in size and density with dose at such high dose levels cannot be explained within the current model and further investigation is needed.

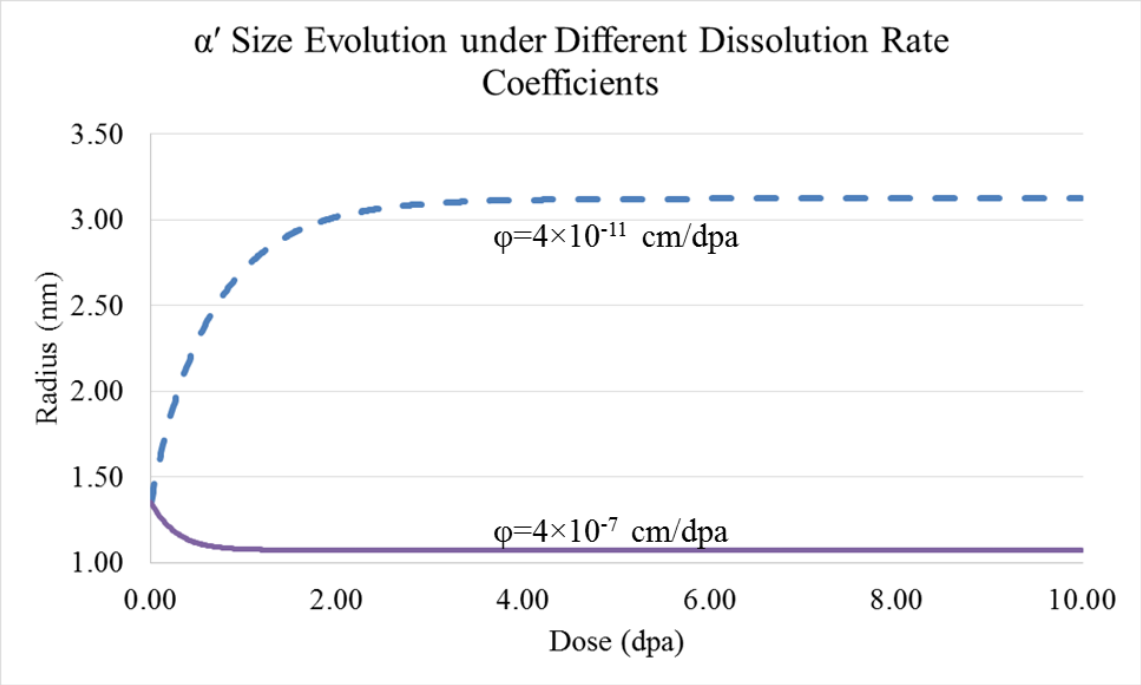

Figure 5-20. Alpha-prime size evolution as a function of dose under two dissolution rate coefficients.

Table 5-10. Alpha-prime size and density in MA957 ion irradiated to 100 and 500 dpa.

	400°C		420°C	
Dose (dpa)	r_p (nm)	N (/cm^3)	r_p (nm)	N (/cm^3)
100	1.35	9.8×10^{17}	1.84	2.5×10^{17}
500	1.67	7.1×10^{17}	1.74	6.7×10^{17}

5.2.2 Cell Models

The NHM model is a simple yet effective method to describe precipitate stability under irradiation. One problem based on previous analysis suggests that even though the re-precipitation term in the NHM model takes the upper limit of the Gibbs-Thomson effect by assuming zero solute solubility at precipitate-matrix interfaces, the re-precipitation value is still too low. This could be attributed to a variety of possible reasons such as simplification by not considering effects from solute drag, solute segregation, etc. Another possibility, as we have briefly mentioned before, could be that solute concentration near an interface is underestimated since all solutes are assumed to be uniformly dissolved in solution by ballistic effects in that model. To obtain information on the solute concentration profile, we need a slightly more detailed model than the NHM.

Several cell models were developed by Brailsford, Wilkes, and Frost and Russell in the 1980s and 1990s [159, 167, 168] based on the master diffusion equation:

$$\frac{\partial C}{dt} = D\nabla^2 C + G(r) \tag{5.28}$$

where D is the diffusivity of solute, C is solute concentration, and $G(r)$ is a source term that relates to the ballistic dissolution rate by irradiation. The boundary conditions for this equation are set to $C|_{r=rp} = C_r$ and $dC/dr|_{r=L} = 0$ similar to those suggested in two papers by Frost and Russell [168, 169], where r_p is precipitate size, L is cell size, and C_r is solubility of solute at the precipitate-matrix interface.

The major difference among these cell models lies in their definitions of the source term, as shown in Figure 5-21. In the Wilkes model [160], solute atoms are assumed to be distributed uniformly in solution by irradiation induced dissolution, which is essentially the same as is hypothesized in the NHM model. In the Brailsford model [167], the dissolved solute atoms are distributed in a thin shell around the precipitates. The Frost and Russell model, a more realistic solute distribution, in which solute is most abundant in the proximity of precipitates and approaches zero at distances greater than the recoil radius:

$$G(r) = \frac{\Theta}{4rR}\left[r_p^2 - \left(r - R\right)^2 \right] \tag{5.29}$$

Note that $\Theta \neq \varphi$, which is the dissolution rate coefficient in terms of radius per dpa in the NHM model. One problem with this source term is that R must be smaller than $2r_p$; otherwise G will become negative. The constraint is purely artificial due to its formulation.

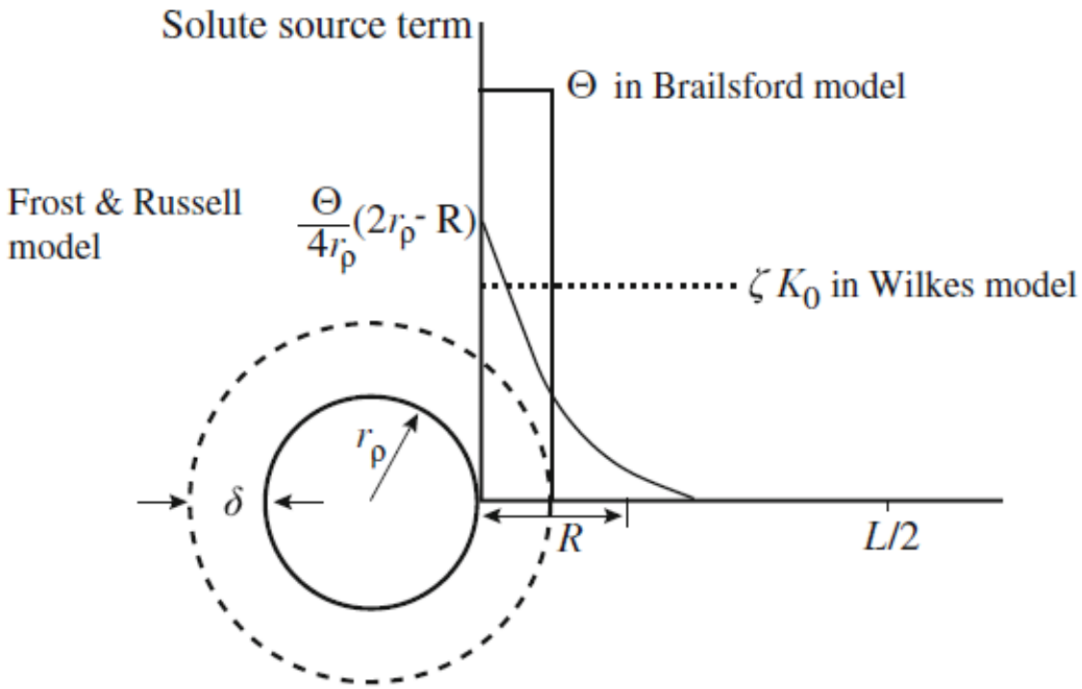

Figure 5-21. Source terms for irradiation induced dissolution of solute from precipitate in various models. The term r_p is the precipitate radius, L is the precipitate spacing, R is the recoil radius in the Frost and Russell model [168, 169], Θ is the dissolution induced rate of precipitate volume change, and δ is the shell about r_p in the Brailsford model [167]. This image was obtained from Was [8].

Supposedly, Θ is the volume dissolution rate per second. However, when Frost and Russell implemented equation (5.29), which is originally from reference [170], the lower integration limit was altered to r_p instead of R-r_p as in the original form. As a result, the integration over equation (5.29) in the Frost and Russell model depends on recoil distance R rather than only being proportional to precipitate volume. Due to this change, the dissolution rate coefficient per unit volume precipitate Θ′ in the Frost and Russell model is proportional to the originally defined value Θ by a factor that depends on R and r_p for mass conservation. Integration results for the original function (5.30a) and for the Frost and Russell model (5.30b) are listed below:

$$\int_{R-r_p}^{R+r_p} G(r)\times 4\pi r^2 dr = \frac{4}{3}\pi r_p^3\Theta \tag{5.30a}$$

$$\int_{r_p}^{R+r_p} G'(r)\times 4\pi r^2 dr = \left(-\frac{R^3}{12}+Rr_p^2\right)\pi\Theta' \tag{5.30b}$$

Assuming the dissolution rate in terms of volume is the same as in the NHM model, we obtained:

$$\begin{aligned}&\left(-\frac{R^3}{12}+Rr_p^2\right)\pi\Theta' = \frac{4}{3}\pi r_p^3\Theta = 4\pi r_p^2\varphi K_0\\ &\Theta'' = \Theta'\times\frac{N_A}{V_m^{ppt}}\times\frac{C_p}{\rho_{Fe}}\end{aligned} \tag{5.31}$$

where Θ″ is the dissolution rate expressed in solute concentration in solution, N_A is Avogadro's number, V_m is molar volume of precipitates, C_p is solute concentration in precipitate, and ρ_{Fe} is atomic density of matrix BCC Fe.

Steady State Analysis

The steady state solute distribution solution can be written as obtained by Frost and Russell [168]:

$$\triangle C(r) = \frac{\Theta'}{48RD}\left[r^3 - r_p^3 - 4R\left(r^2 - r_p^2\right) - 6\left(r_p^2 - R^2\right)\left(r - r_p\right) - \left(3r_p - R\right)\left(r_p + R\right)^3\right]\left(\frac{1}{r} - \frac{1}{r_p}\right) \tag{5.32}$$

where Θ′/D is proportional to K_0/D. The maximum solute concentration is proportional to the damage rate and the square of the recoil distance R, and is inversely proportional to the solute diffusivity and precipitate size r_p.

The solute concentration change, ΔC(r), is shown in Figure 5-22 as a demonstration. For the conditions selected for calculation, steady state solute concentrations are found to be similar for neutron and ion irradiation due to similar K_0/D values as discussed in the NHM model. As we can immediately notice, the steady state concentration solution enhancements are much higher than the solubility limit for Y at ~385-400°C [171]. This is because no nucleation mechanism is included in the cell

models. The result is qualitatively consistent with our observation of increases in the number density of nano-oxide particles at 385 and 412°C under neutron irradiation. Similar levels of solute elevation are predicted for ion irradiation conditions as well. However, experimentally, the number density of oxide particles is observed to either decrease or remain almost unchanged for ion irradiation conditions. We suspect that a high damage rate in ion irradiation may affect solute clusters' ability to reach critical size during nucleation and growth processes. At higher temperatures, steady state solute concentrations are reduced due to increases in solute mobility. This is also qualitatively consistent with the observation of unchanged or lower number density at higher irradiation temperatures.

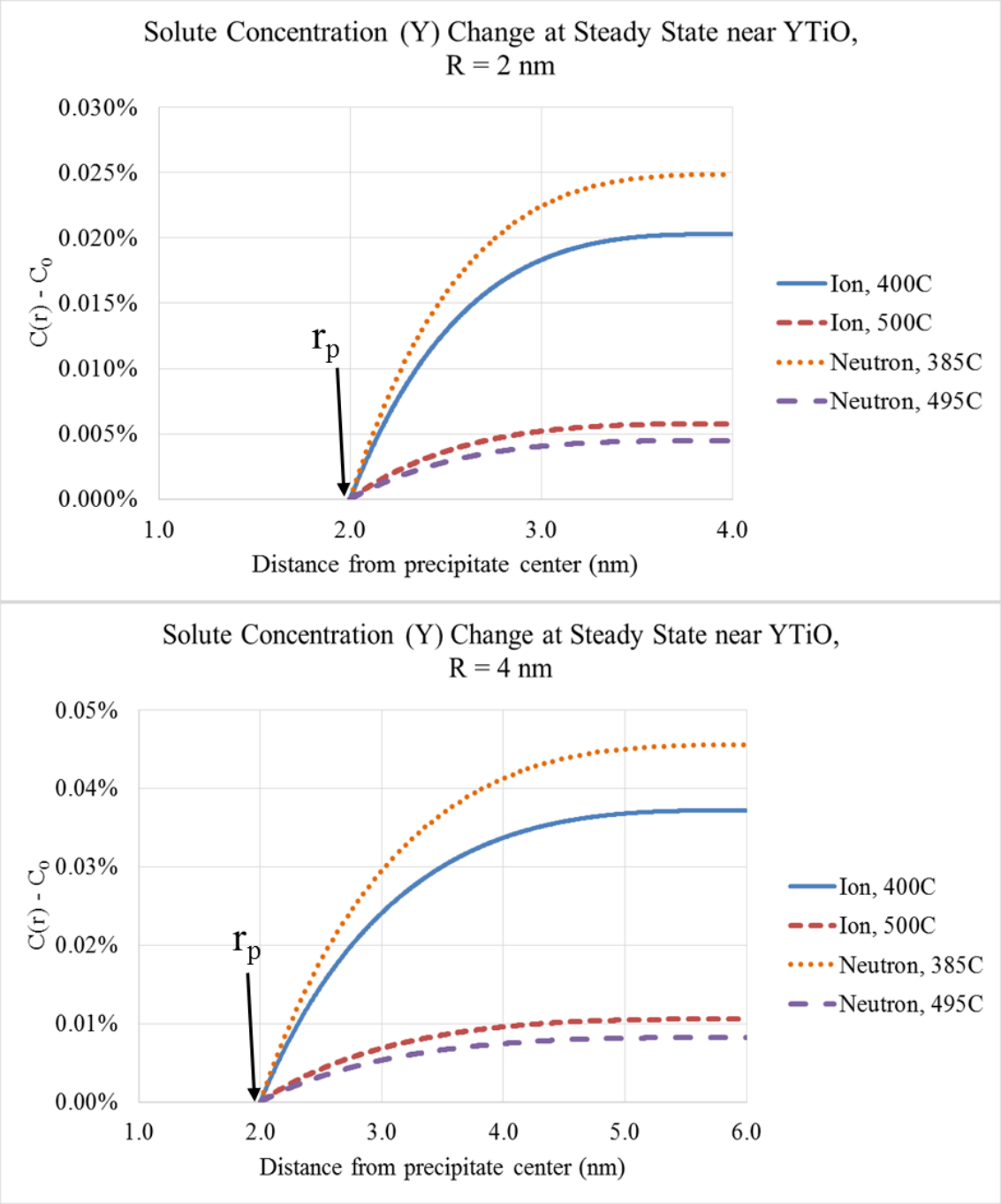

Figure 5-22. Solute concentration (Yttrium) change at steady state calculated according to equation (5.32) for r_p = 2 nm, R = 2 or 4 nm, $K_0 = 10^{-2}$ dpa/s for ion and 10^{-6} dpa/s for neutron, and $\varphi = 4\times10^{-11}$ cm/dpa; D is radiation enhanced diffusivity considering both vacancy and interstitialcy mechanisms, and C_0 is thermal equilibrium solute concentration in solution.

Steady state is approached when time exposed to irradiation reaches:

$$t \approx \frac{L^3}{8Dr_p} \tag{5.33}$$

where L is the inter-particle distance. Considering that YTiO particle number density is on the order of 3×10^{17} cm^{-3}, the average inter-particle distance is then L = ~18 nm. Thus the characteristic time for Y in YTiO to reach steady state is $t \approx 2.4\times10^{10}$ s ≈ 771 years for $K_0 = 10^{-6}$ and is $t \approx 2.4\times10^{6}$ s ≈ 28 days for $K_0 = 10^{-2}$ at ~385°C. At a higher temperature 550°C, reaching steady state requires $t \approx 3.3\times10^{8}$ s ≈ 10 years for $K_0 = 10^{-6}$ and is $t \approx 3.3\times10^{4}$ s ≈ 0.387 days for $K_0 = 10^{-2}$. The estimated durations to reach steady state suggest that YTiO particle evolution is still within the transient regime at lower irradiation temperatures but maybe achievable at higher ones.

Similar analysis can also be applied to α′. Due to large variations in experimental data, there is little point in showing details and comparisons here. In general, according to equation (5.33), the duration to reach steady state for Cr can be estimated to be $t \approx 3.0\times10^{6}$ s ≈ 35 days for $K_0 = 10^{-6}$ and is $t \approx 3.3\times10^{2}$ s for $K_0 = 10^{-2}$, which are much more rapid than those for Y. Maximum solute concentration enhancement, based on equation (5.32) is expected to be around one order of magnitude higher than for Y to a level of ~1.4 at% since $(C/C_p)_{Cr}/(C/C_p)_Y \approx 34$.

Cell models are based on the same physical processes as considered in the NHM model and include further improvements to include spatial variation of solutes. In general, they are good for probing solute concentration and can reach similar conclusions to those of the NHM model does for particle stability with respect to irradiation conditions, like temperature and dose rate. Technically, it is more appropriate to analyze YTiO particles using transient solutions. Ideally, these results would be coupled with a nucleation mechanism for estimating solute supersaturation and nucleation processes. However, due to limited time available, this effort is not included in this dissertation but will likely to be part of future work.

Numerical Solutions

Before numerical solutions are presented, we first need to re-examine the source term. As has been mentioned previously, the source term expressed in equation (5.29) is artificially constrained. To explore solutions in a wider parameter space, the source term is replaced by the exponential fitting function described in Figure 5-14 with corresponding parameters. The dissolution rate is then matched by the scaling integration of the function to an equivalent amount of solutes as calculated by the NHM model's dissolution rate coefficient φ. Note that although the current source term may be a good approximation for ion irradiation, it cannot guarantee effectiveness for neutron irradiation, where the recoil energy spectrum is different. In general, recoil energy is higher in neutron irradiation and as a result, recoil atoms are expected to travel farther than values estimated using 1.8 MeV Cr ions. However knowing the recoil distribution under neutron irradiation requires calculation of a recoil energy spectrum, which is non-trivial. For simplicity and demonstration purposes, the same form of source term is used for neutron irradiation conditions.

Another uncertainty in this calculation is the solubility limit of solute atoms at the precipitate-matrix interface, C_r, which is related to the equilibrium solute limit of solute at a flat interface through interface energy and curvature [164]. However, the solute limit at a flat interface is also unknown due to lack of experimental data. Two extreme cases, $C_r = 0$ and $C_r = C_s$, are tested in numerical solutions. It is more likely that the solubility limit at the interface, C_r, is smaller than the equilibrium solute concentration in solution. Only under such circumstances does the observed size refining and coarsening make sense, since $C_r = C_s$ forbids coarsening to occur. Parameters like r_p and L are adopted from experimental measurements, and D values are calculated as described in section 5.1.3. The master diffusion equation is then solved by finite difference method with 100 central-space elements and a forward time-stepping scheme.

Figure 5-23 demonstrates effects of dissolution rate φ and interface solubility limit C_r on solute concentration profiles to 100 dpa at 400°C. As expected, higher φ leads to accumulation of solute atoms near interfaces, which results in elevated solute

concentration in nearby regions. The higher solute concentration gradient near the interface for Y is not surprising due to its low mobility. It suggests that for YTiO particles, the re-precipitation term in the NHM model is underestimated if the dissolution rate is large, as we previously suspected. The upper graph in Figure 5-23 illustrates three possible cases for solute concentration evolution with different diffusivity/dissolution rate ratios: when back-diffusion is dominant, precipitates would undergo a coarsening processes similar to that in thermal aging conditions; with dissolution rate increase, more solute will be displaced into solution but new particles may not immediately form before reaching the solubility limit; in a higher dissolution rate regime, solute is supersaturated in solution and new particles are likely to nucleate and grow. Boundary condition C_r also has a direct effect on this elevation, as demonstrated in the lower graph in Figure 5-23. With $C_r = C_s$, we can see that effectively only dissolution is possible under irradiation due to lack of a coarsening driving force. Thus in the following part only the $C_r = 0$ boundary condition will be applied.

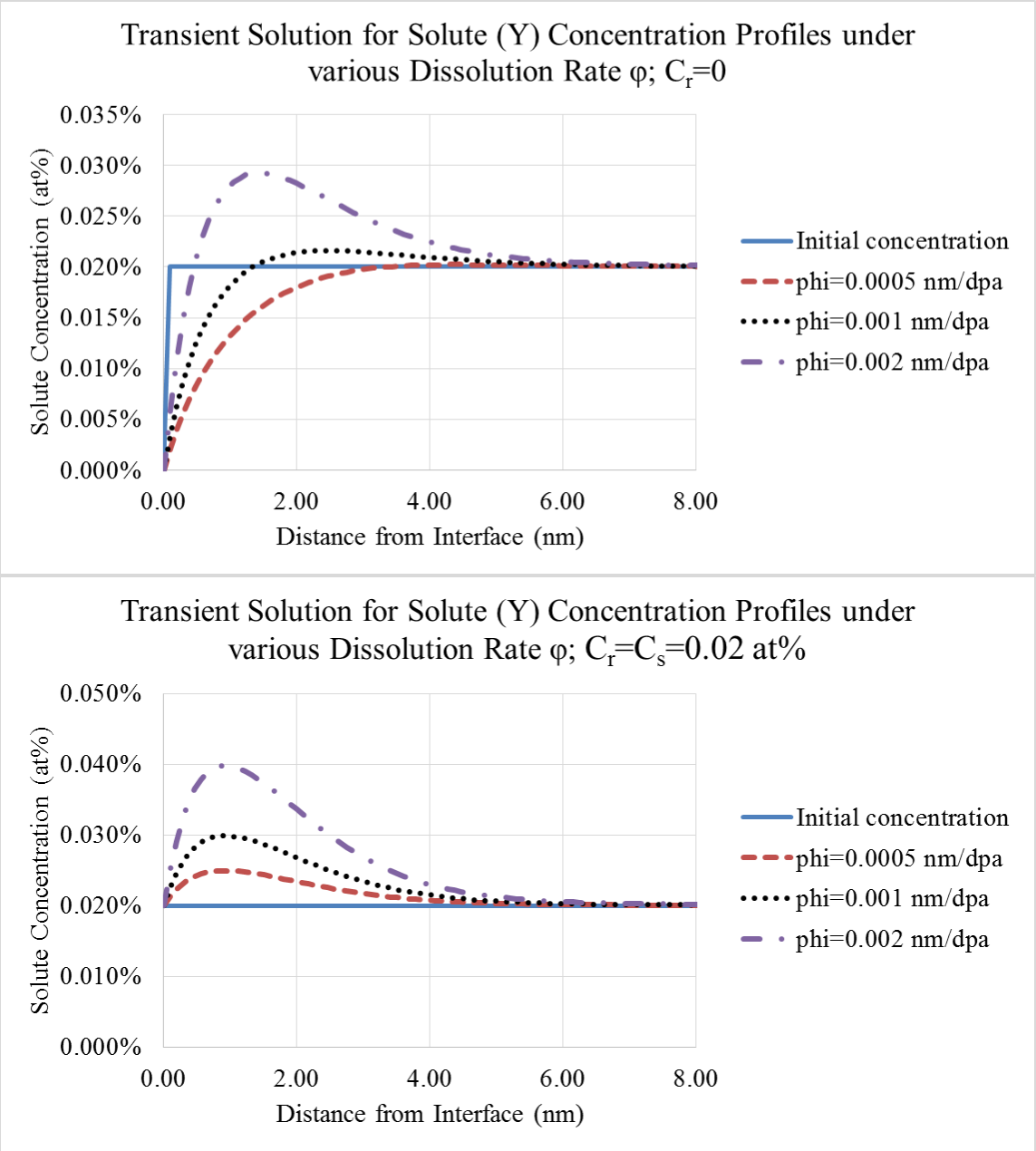

Figure 5-23. Effects of dissolution rate φ and boundary condition C_r on solute (Y) concentration profiles to 100 dpa. Other parameters are r_p=1.7 nm, L=22.4 nm, and D=1.8×10^{-4} nm^2/s, which correspond to microstructure ion irradiated at 400°C to 100 dpa.

Figure 5-24 shows effects of irradiation temperature and accumulated dose on Yttrium concentration profiles. At 400°C more solute piles up near the interface due to low mobility, while at higher temperatures a depleted zone of solute is predicted. Continuing irradiation drives solute distribution towards steady state. This result is in good agreement with general observations for YTiO precipitates. The analysis suggests that under the current assumption of Y mobility, it is likely that irradiation only introduces local perturbations to these solute atoms rather than inducing long-range diffusion.

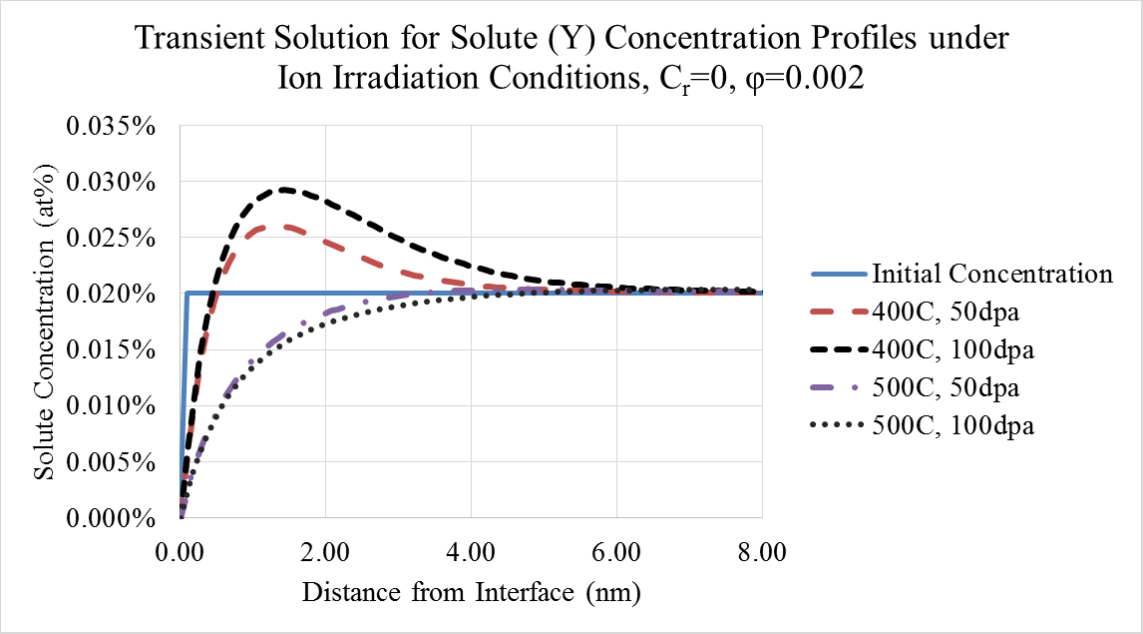

Figure 5-24. Temperature and dose effects on solute concentration profiles at ion irradiation relevant conditions. Precipitate size, cell size, and diffusivities are setup using experimental data and calculated radiation enhanced diffusion.

Solute distributions under neutron irradiation conditions calculated using a cell model are shown in Figure 5-25. Two types of source terms have been tested. Solute concentration profiles are quite similar to those obtained for ion irradiation at similar

temperatures when the same source term is applied. However, switching to a uniform source term significantly alters solute profiles even though the amount of dissolved atoms is conserved. This behavior is as expected, since the farther recoils are displaced, the more difficult is re-precipitation through back-diffusion.

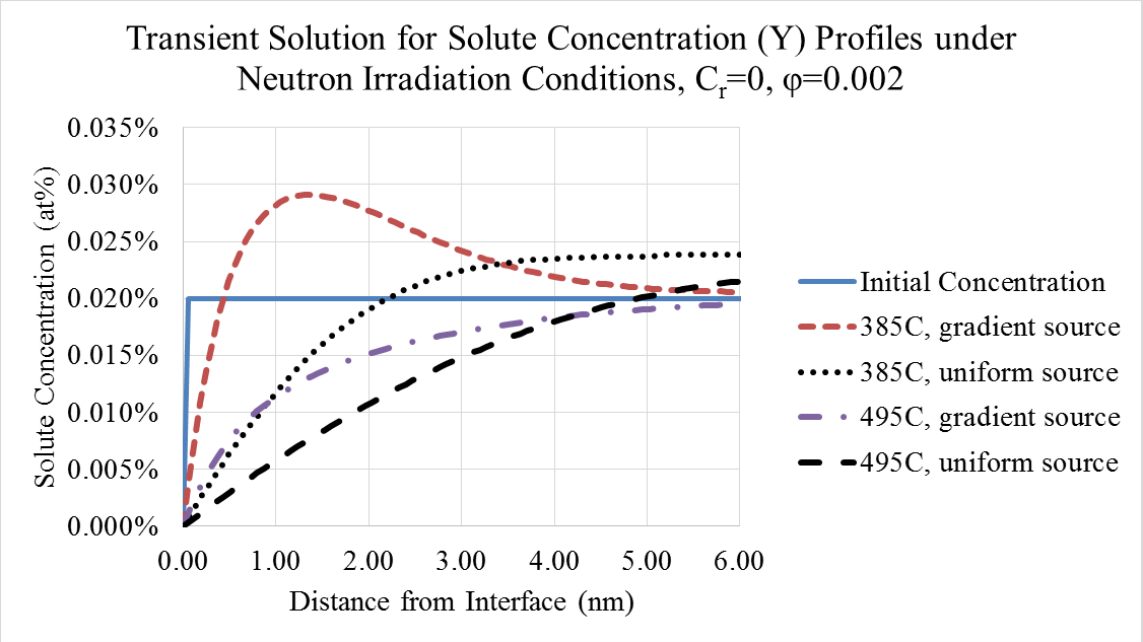

Figure 5-25. Comparison of source term effects on solute concentration profiles for Yttrium under neutron irradiation conditions to 100 dpa. "Gradient" means the same type source term is used as for ion irradiation, while "uniform" means the recoil distribution is assumed to be uniform in the simulation cell. Mass is conserved by ascertaining integrations of solutes equal to the dissolved amount. Precipitate size, cell size, and diffusivities are set up using experimental data and calculated radiation enhanced diffusion.

As mentioned in the steady state analysis section, one major disadvantage is lack of a nucleation mechanism in the Frost and Russell cell model. This is especially true for the lower irradiation temperature regime in our study (< 450-500°C), when the cell model predicted the solute concentration to be higher than the solubility limit. Since nucleation of YTiO particles is commonly attributed to a homogeneous nucleation

mechanism [154], nucleation of new particles is highly likely to happen following supersaturation of solutes. Such prediction is qualitatively in good agreement with the observed enhanced precipitate number density for neutron irradiation cases. However, it cannot explain a slightly reduced or unchanged number density in ion irradiation. Due to limited knowledge of the nucleation process under irradiation, it is difficult for us to address such behavior. But as mentioned previously, we suspect a high damage rate may hinder growth of nuclei to above critical sizes.

6 DISCUSSION

As presented in experimental result section, microstructural features of interest produced by ion irradiation are similar to those in neutron irradiated specimens in many ways: such as the development of YTiO particle sizes, and α′ cluster sizes and number densities with irradiation temperature. Multiple distinct differences were also observed, e.g. grain boundary chemistry. Such complicated scenarios suggest that a simple correlation is hardly adequate. Instead, detailed analysis and discussions are needed in order to establish neutron-ion correlations. In this section, observed similarities and differences of YTiO particles, α′, and grain boundary chemistry are qualitatively or semi-quantitatively analyzed. At last, the validity of correlations between microstructural responses to neutron and ion irradiation are discussed based on both experimental results and theoretical calculations.

6.1 Correlations of YTiO Particles

6.1.1 Sizes, Size Distributions and Number Density

As has been shown in section 4, ion irradiation can successfully reproduce some aspects of oxide particles' responses in MA957 similar to those after neutron irradiation. For example, average size of oxide particles are found to be in good agreement between neutron and ion irradiated specimens.

Figure 6-1 plotted guide lines that were linearly fitted to each group of datasets. First of all, guide lines for TX and EV MA957 irradiated by neutrons are almost parallel to each other. Since TX specimens were irradiated to about half dose of EV specimens, it is reasonable to assume that average size of oxide particles at 385°C will continue to decrease if irradiated to higher dose, indicated by the arrow. The fate of oxide particle size at 495°C is difficult to predict, since this temperature is about the critical point where thermally-generated vacancy become dominant, as has been shown in section

5.2.1. Thus decreasing or increasing in average sizes are both possible, which depends on the magnitude of the dissolution rate and the re-precipitation rate. Considering this, particle size evolution in neutron irradiated data is self-consistent.

Experimental data for oxide particle size evolution in this study qualitatively agree for ion and neutron irradiated specimens below 500°C, considering error bars and other possible complications. For ion irradiations, the guide line fitted to YTiO particle sizes in specimen irradiated by ions has a smaller slope compared to those in specimens irradiated by neutrons. Below the critical temperature, ~500°C, where vacancy at thermal equilibrium is dominant in neutron irradiation condition, average sizes of oxide particles in ion irradiated specimens would be more similar to those in MA957 irradiated by neutrons. In addition, due to nucleation of new oxide particles, results of post-irradiation measurements in neutron irradiated specimens are a combination of newly formed and pre-existing particles. The average particle size is likely to be smaller if new particles did not rapidly grow to steady state. In specimens irradiated by ions, particle sizes are less affected by newly formed particles during irradiation, since YTiO particle number densities are either decreased or unchanged, which could be an indication that nucleation of new YTiO particles are hindered or suppressed under those conditions. More ion irradiation data at higher irradiation temperatures are needed to determine if coarsening of oxide particles observed in neutron irradiated specimens can be reproduced.

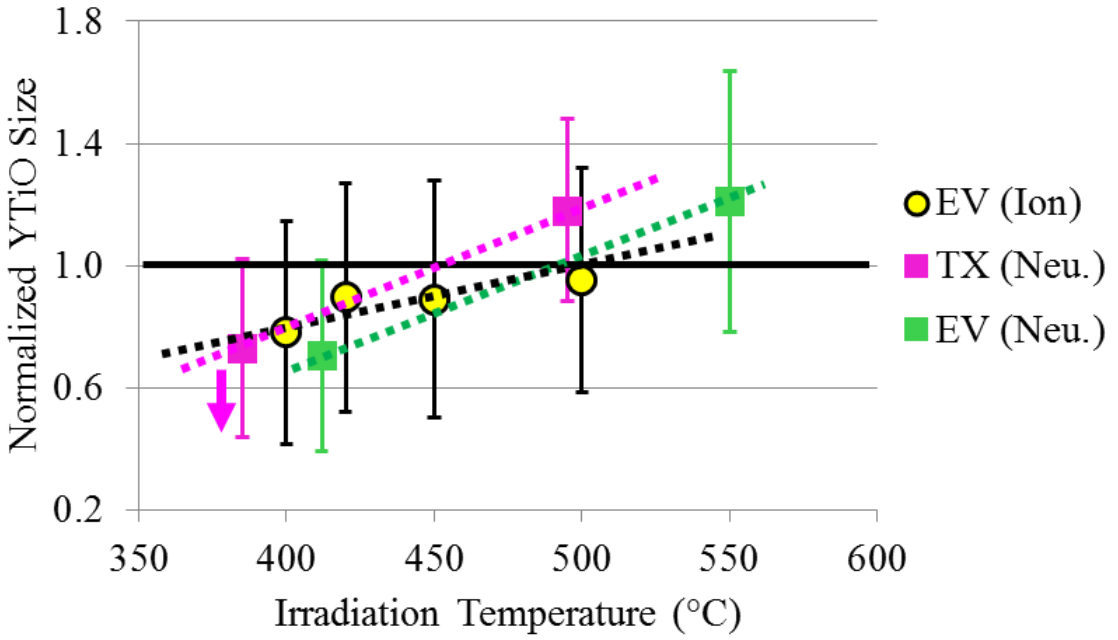

Figure 6-1. Normalized sizes of YTiO particle evolutions with respect to irradiation temperatures. The dotted lines are estimated trend lines to guide eyes.

Although particle size evolution trend with respect to irradiation temperature are in good agreement for specimens irradiated by neutrons and ions, they are not identical. Figure 6-2 compares size distributions of YTiO particles between specimens irradiated by neutrons and ions at temperatures below 500°C. The size distributions in neutron irradiated specimens have higher portions that correspond to small oxide particles, compared to those in specimens after ion irradiation. The result is consistent with the observation that neutron irradiated specimens have a higher number density of particles. The growth of newly formed particles was likely to follow inverse Ostwald ripening mechanism.

The number density of YTiO particles is the largest observed discrepancy between neutron and ion irradiated specimens. A comparison of number density is presented in Figure 4-13. Understanding this phenomenon would have required knowledge of YTiO particle nucleation under irradiation environment. In conventional nucleation theory where irradiation is absent, the nucleation rate is generally considered

as proportional to solute diffusivity and the number of available nucleation sites [154, 172]. Apparently, this is the opposite of our observation, in which solute atoms under ion irradiation have higher diffusivities but lower number densities of oxide particles were observed compared with those in specimens after neutron irradiation. Due to the complications of nucleation process, only a few theories were developed during the past decades that taking irradiation condition into consideration. Maydet and Russell [37, 173] proposed a nucleation theory for incoherent precipitates. According to their theory, irradiation promote oversize solute precipitate in which vacancy excess is needed, while destabilize undersized solute precipitate. This theory's prediction does not agree with our observations. Without a clear mechanism, here we propose several possible explanations. Since dose rate is one of largest difference in experimental variables, we are tempted to believe that nucleation process is affected by dose rate. It either somehow increases the solubility of Y or Ti in BCC iron, or damage cascade events destroy nuclei much faster than it could grow to reach critical sizes. For the first explanation, some recent *ab initio* modeling works have found that binding energy of Y-vacancy is high [153, 174], which suggests that vacancy could help to stabilize Y. Nevertheless, we have little evidences to support either explanations.

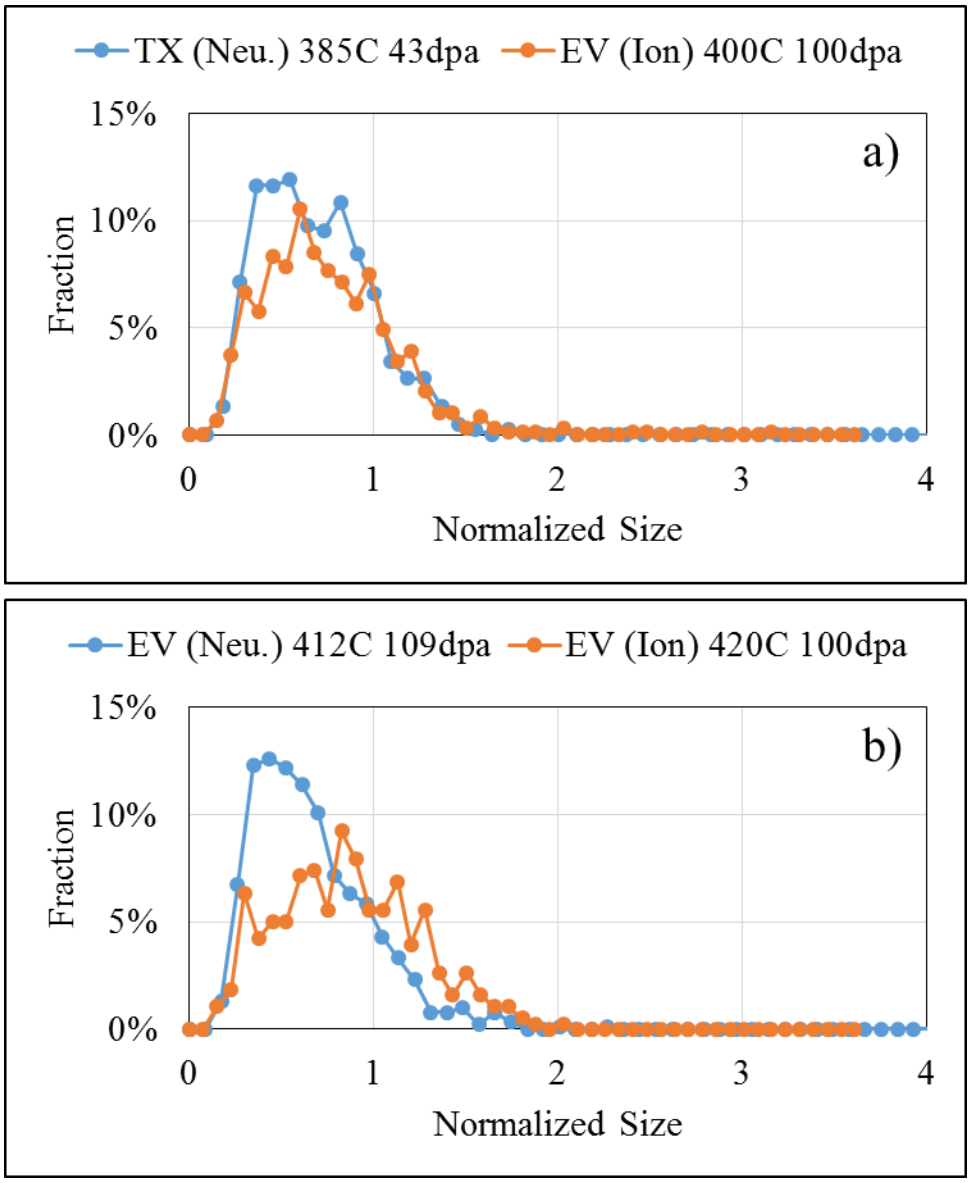

Figure 6-2. Size distributions of YTiO particles: a) comparison between neutron and ion irradiated specimens at 385 and 400°C; b) comparison between neutron and ion irradiated specimens at 412 and 420°C.

Several experimental results that indicate dose rate could affect nucleation process have been found in literatures. First set of comparison is made among two studies about 14YWT, both of which were made by Oak Ridge National Laboratory (ORNL) and irradiated by 5 MeV Ni at EMSL at PNNL during about same period of

time [175, 176]. The dose rates however, are differed by one order of magnitude. Both studies used APT for oxide particle characterization. These two sets of experiments are probably the closest we could find in open literatures with minimized uncertainties. Since we have access to raw datasets for 14YWT in reference [175], we took our liberty to re-analyze those data using the same iso-concentration surface method as in this research. A brief summary for comparison among those three results are listed below in Table 6-1. It can be seen that size evolution are in roughly good agreement. The number density of YTiO particles, which relates to nucleation, is found to be increased or stable in the lower dose rate. In specimens irradiated at high dose rate, YTiO particle number density decreases within temperature range of 300 to 600°C, which approximately overlaps with that in our experiment. Although the absolute values of number density of YTiO particles depend on method used for analysis, the trend is usually preserved. We would like to caution that there are some uncertainties for comparing these two sets of experiments. One of these uncertainties is whether identical materials were used. It would also be better if raw data can be obtained for reference [176] and apply the same analysis approach as in this research.

Table 6-1. Comparison dose rate effects on oxide particle number density.

Material	Irrad. Temp (°C)	Dose (dpa)	Dose Rate (dpa/s)	Size	Number Density	Reference
14YWT	100-600	50*	$\sim 1\times10^{-3}$	Decrease	Increase ≥ 300°C; Else decrease	Re-analyze [175]
14YWT	100-600	50*	$\sim 1\times10^{-3}$	Decrease ≤ 450°C; Else stable	Stable	[175]
14YWT	300-600	100	$\sim 1.4\times10^{-2}$	Decrease at 300°C; Else stable	Decrease	[176]

*Dose and dose rate are adjusted using Kinchin-Pease mode instead of Full cascade.

Another experimental results about dose rate effects in ODS alloy is an unpublished research by Hyosim Kim and Dr. Lin Shao at Texas A&M University. Self-ion irradiations at two different dose rates, 3.5×10^{-3} dpa/s and 3.5×10^{-4} dpa/s, were conducted upon a F/M 12Cr ODS alloy using 3.5 MeV Fe^{2+} at 475°C to 100 peak dpa. YTiO particles in irradiated specimens were characterized by TEM and results are shown in Table 6-2. Number densities of both high and low dose rate experiments are found to be higher than that those in unirradiated regions. Higher number density of oxide particles were found in specimens irradiated at low dose rate than in those irradiated at high dose rate. The volume fraction of oxide particles is also found to be lower in high dose rate experiment. Although using a different material, results are consistent with 14YWT experiments described in the previous paragraph.

Table 6-2. Sizes and number densities of YTiO particles in ferritic grains in ferritic/martensitic 12Cr ODS alloy irradiated by 3.5 MeV Fe^{2+} at 475°C to 100 peak dpa [Courtesy of Hyosim Kim, from TMS 2017 presentation].

Material	Irradiation Temp (°C)	Dose (dpa)	Dose Rate (dpa/s)	Size	Number Density	Reference
12Cr ODS	475	~70	$\sim3.5\times10^{-3}$	Decrease	$\sim7.5\times10^{17}$ /cm^3	Hyosim, et al. unpublished
12Cr ODS	475	~70	$\sim3.5\times10^{-4}$	Decrease	$\sim4.0\times10^{17}$ /cm^3	

Some opposite experimental results about nucleation of YTiO particles can be found in recent studies as well. Dolph et al. reported that oxide particle density decrease when irradiated at 400°C to 50 dpa at a dose rate of 1×10^{-4} dpa/s with rastering beam mode [177]. Using similar irradiation conditions, Yano et al. observed decreases in both size and number density when irradiated at 500°C in 9Cr ODS alloy [178].

Several theoretical works on nucleation mechanism for irradiation induced incoherent and coherent precipitates have been done around 1980s [37, 38, 173]. The general perception is that higher dose rate would lower effective solubility of solute in

solution and thus promote nucleation. This is, however, opposite to our experiment and several other studies discussed above. A possible explanation for reconciliation of the discrepancy is that there may exit many pre-mature clusters that are below resolution limit and they are difficult to be detected in both APT and TEM. Typical detection rate of APT is ~37% in LEAP instrument used for this study. That means only about a third of atoms are detected and solute clusters of several or tens of solute atoms are likely to be non-detectable or difficult to be detected. As a result, those pre-mature clusters will not be properly identified in our analysis. TEM has even worse resolution for solute clusters of small sizes since they did not generate enough diffraction contrast nor x-ray chemical signatures due to interference of Fe matrix.

In brief, both neutron-ion comparison in this study and ion-ion comparison in literatures found that nucleation process of oxide particles is probably associated with irradiation dose rates. Lowering damage rate in general promotes YTiO particle nucleation than those in high dose rate experiments. Average particle sizes and size distributions are generally less sensitive with dose rate but could potentially be affected as well if newly formed particles are of high number density and have slow growth kinetic.

6.1.2 Volume Fraction

The normalized volume fractions of YTiO particles in neutron or ion irradiated MA957 are presented in Figure 6-3. It is an important characteristics to understand solute elements partitioning. Similar quadratic-like trends can be observed for both neutron and ion irradiated specimens. Volume fractions of oxide particles at all ion irradiation conditions are found to be smaller than unirradiated materials. Since volume fraction is related to number density and particle size, this result is not unexpected. The result is also in good agreement with measured solute elemental partitioning between clusters and solution, as displayed in Figure 4-14. It suggests that extra solute atoms have been introduced in the matrix but new particles are hard to form. Whether it is due to supersaturation or increased solubility by ion irradiation is unknown. In neutron

irradiated specimens, on the other hand, volume fractions of oxide particles are enhanced above 400°C. However, the observed values of volume fraction in neutron irradiated MA957 does not match elemental partitioning analysis in Figure 4-14 if we assume oxide particles' constitutes are Y, Ti, and O only. The discrepancy indicates that either size measurement for oxide particles are overestimated or noticeable amount of impurities have become a part of oxide clusters.

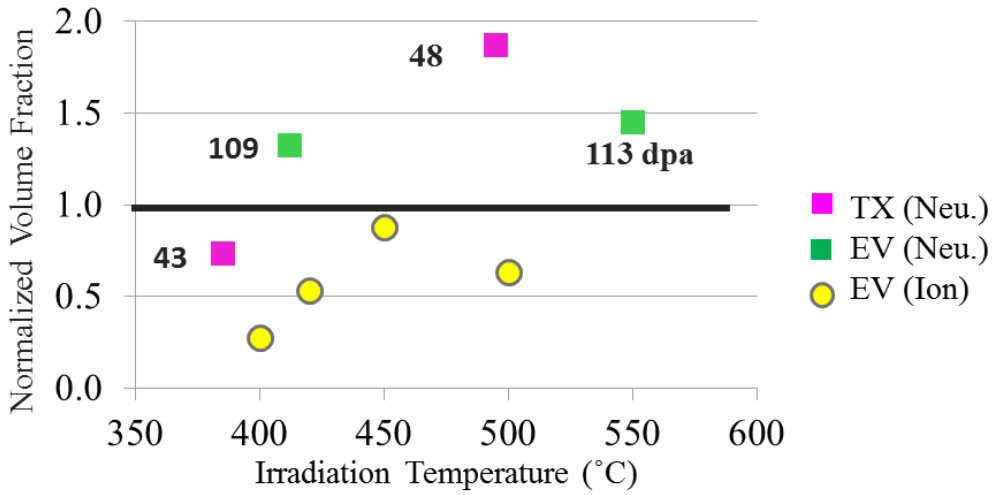

Figure 6-3. Volume fraction of oxide particles compared between neutron and ion irradiated MA957.

Determining the accurate composition in nanometer size precipitate using APT is difficult due to several notorious artefacts, like trajectory aberration and chromatic aberration. For example, trajectory aberration could lead to unphysically high density of matrix Fe ions been detected inside clusters. Thus an alternative analysis method is needed to measure the possible changes. Considering a precipitate composed of only Y, Ti, and O, its size should be directly proportional to the number of ions. That is if precipitate composition stays the same, the interatomic distances among solute atoms

should be nearly invariant. Therefore, a k-th nearest neighbor (kNN) analysis is suitable as such alternative method.

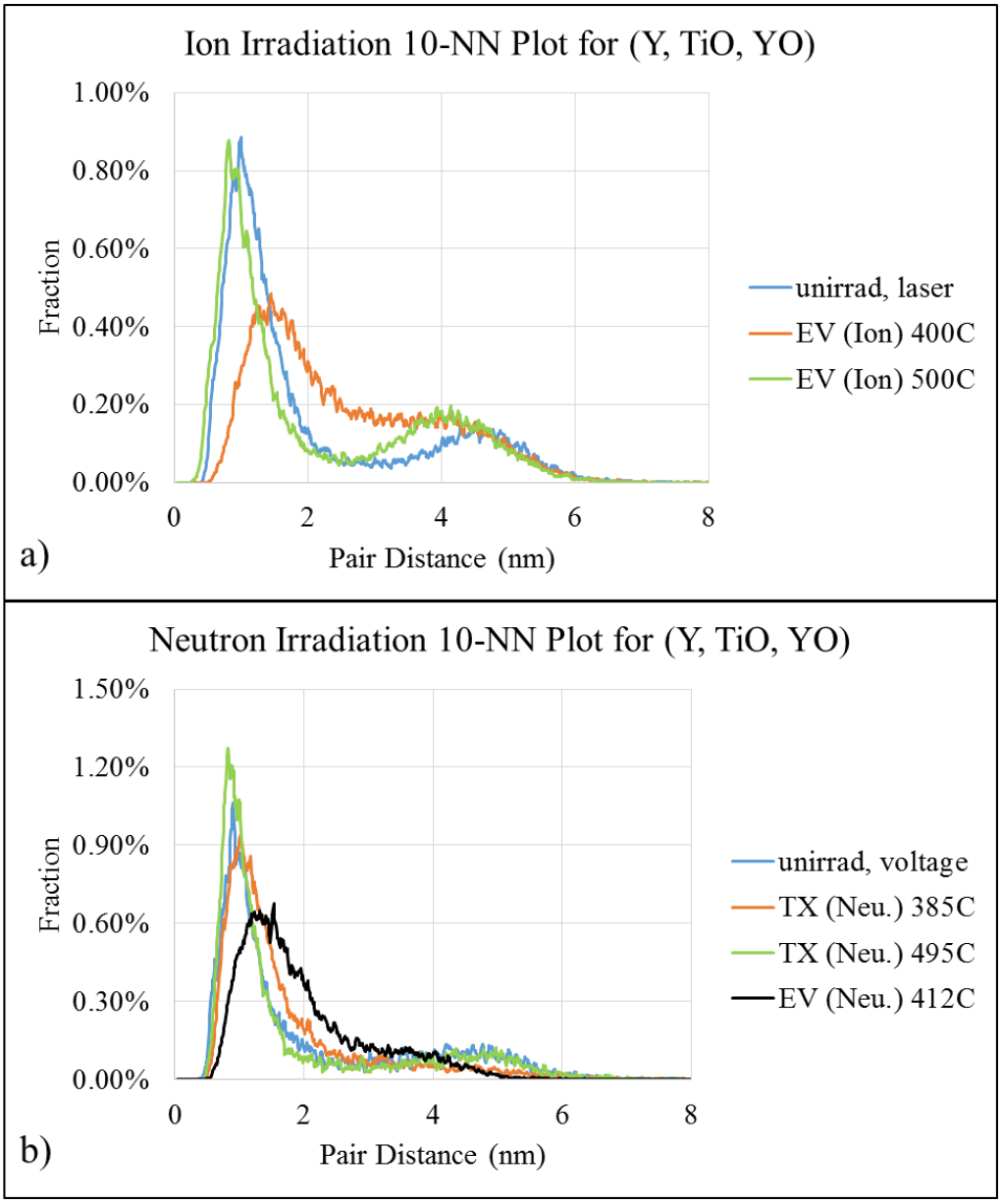

Figure 6-4. 10-th nearest neighbor (10-NN) distributions calculated for (Y, TiO, YO) at various conditions.

In our analysis k is set to 10 to filter out density fluctuation noise in the solution matrix. The 10-th nearest neighbor distribution results are shown in Figure 6-4 for oxide particles in MA957 irradiated by neutrons or ions. In a system where comparable amounts of solute atoms are distributed in clusters and in the matrix, the k-NN distribution of the solutes usually follow a double peak shape. The first peak with smaller distance corresponds to solute atoms partitioning in clusters and the second peak corresponds to solutes dissolved in the solution. Compared with kNN distribution in unirradiated MA957, both neutron and ion irradiations at low temperatures cause the first peak shifting towards larger values. In specimens irradiated at high temperatures, the position of the first peak remained unchanged or decreased slightly. The interpretation of this result can be multitudes. First of all, low temperature irradiation effectively displaced solute atoms from oxide particles into the matrix, as indicated by the grown fraction outside first peak region. At the same time, interatomic distance is increased, indicating that core elements (Y, Ti, O) concentration are lowered and impurities are mixed inside cluster regions. For high temperature ion irradiation, kNN distribution reveal that a noticeable amount of solute were added to the matrix. For high temperature neutron irradiation, slightly larger fraction of solute atoms are found to be fallen under the first peak, which is consistent with observed coarsening. Note that although it seems that the coarsening is contradictory to Figure 4-14 in which fractions of Y, Ti and O inside clusters are relatively stable at high temperatures, close examinations of these specimens found that Ti and O average concentrations in neutron irradiated specimens are slightly higher than those in unirradiated counterparts. Thus, it is reasonable to assume the dissolution of very large particle supplies the coarsening of finer oxide particles under these irradiation conditions.

6.1.3 Chemical Composition

In Figure 4-14 in section 4, results shows that chemical composition of oxide particles in terms of elemental ratios among Y, Ti and O are relatively stable at all irradiation conditions except those in MA957 ion irradiated at 400°C. Thus above

400°C, ion irradiation reproduced oxide particle compositions pretty well. In general (Y+Ti):O ratio remains relative stable [111, 177, 178] after irradiation. The rise of Y:Ti ratio after ion irradiation at 300°C has been observed in reference [176] as well. This phenomenon, the depletion of Ti in oxide particles, is somewhat counterintuitive. Since Ti in general is considered diffuse faster than Y, its back diffusion to oxide particles is expected to be more rapid, as discussed in section 5. The relative increase of Y in oxide particles may be attributed to the threshold displacement energy's temperature dependence [132, 179, 180]. That is Y is easier to be displaced at low temperature than that at high temperature. It is possible that within certain temperature range, a noticeable portion of energy that transferred to Y lattice atom is smaller than threshold displacement energy, E_d. As a result, the number of displacements of Y is reduced. If the number of displacements for other elements, e.g. Ti, remains relatively stable, the chance of Y been ejected from oxide particle is reduced. Since neutron irradiation in general produce PKA with higher energy, displacement disparity of Y may be not as large as in ion irradiation at similar irradiation temperature. Although it is a sound mechanism, quantification of this effect is difficult without prior knowledge about this temperature dependence and the PKA energy spectrum.

Chemical composition of YTiO particles in ODS alloys measured by APT is usually highly non-stoichiometric and much different from those inferred based on crystallographic investigations [175]. TEM investigations using EDS usually generated much different results from APT-based method. Using APT analysis, the typical Y/Ti ratio is in the range of 0.2-0.5 while the (Y+Ti)/O ratio is >1 [91, 107, 110-112]. Similar Y/Ti ratio has also been reported in EDS analysis presented in Hirata et al. [106]. Although different from other measurements, APT studies themselves are quite consistent across a variety of ODS alloys and irradiation experiments. Some may attribute this discrepancy to artifacts in APT. However, a recent study by Williams et al., in which compositions of oxide particles in ODS and of bulk Y_2O_3 were investigated, suggests that it cannot be dismissed easily as artifact [110]. The discrepancy is probably due to difficulties in APT to accurate quantify chemical composition for clusters of only

1-2 nanometers in size buried in BCC Fe matrix. Marquis reported the observation of Cr segregation to oxide particle surfaces and it formed a core-shell structure [181]. In our measurements, no noticeable elemental segregation at the interfaces was detected.

6.1.4 Temperature Shift

The concept of temperature shift was derived based on the rate theory as part of efforts to establish neutron-ion correlation in void swelling [17, 182, 183]. It is a common concept that has been routinely discussed and sometimes used as guidance for designing ion irradiation experiments. Generally speaking, the concept implies that in order to obtain a similar microstructure or microstructural evolution, higher irradiation temperature is needed for higher damage rate experiment to keep defect flux invariant. As we have discussed in previous section, YTiO particle evolution is a complicated matter and a simple temperature shift is not likely to work. However, it still would be interesting to show what it looks like if temperature shift is applied. In this section, we are not trying to evaluate the temperature shift in our experimental data but rather to evaluate whether shifting temperature could make better correlation of microstructural features for neutron and ion irradiated specimens. For simplification, we will not calculate temperature shift by rate theory, instead, the temperature shift is estimated by matching the shape of number density curve.

Figure 6-5a), b) and c) show the average sizes, the number densities and the volume fractions of YTiO particles, respectively, after applying a -38°C shift in temperature. Under the temperature shift assumption, YTiO particle in ion irradiated specimens at 450°C would be roughly correspondent to those in specimens after neutron irradiation at 412°C. Dotted lines are intended to guide eyes only. As expected, the correlation of average sizes is not significant improved, since the slope of size evolution does not change by horizontally shifting curves. The problem for discrepancy in number densities has been discussed in section 6.1.1 and it is not improved by adjusting irradiation temperatures. The difference in volume fraction become even larger after shifting irradiation temperature: the curve peak located at 412°C for ion irradiated

specimens and the peak located at 500°C for specimens irradiated by neutrons. Attempts to adjust irradiation temperature of ion irradiation to “equivalent temperature” in neutron irradiation did not improve correlations between neutron and ion irradiated specimens.

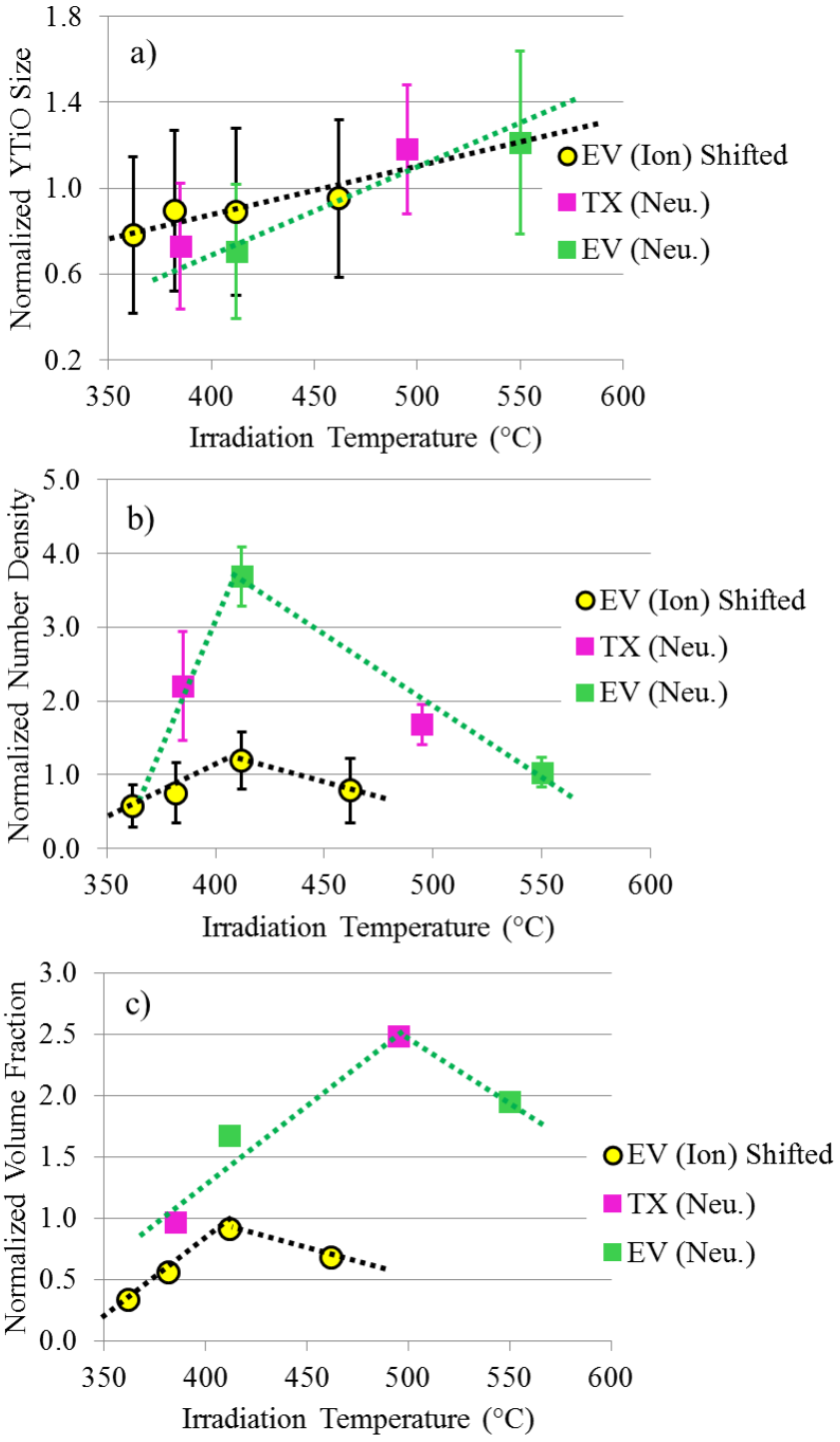

Figure 6-5. The average size, the number density and the volume fraction of oxide particles after shifting ion irradiation temperatures by -38°C. Dotted line are to guide eyes only.

6.1.5 Previous Studies from Literature

In this section, size and number density of oxide particles in neutron or self-ion irradiated ODS alloys from published literatures are briefly summarized and the trends are compared with experimental results in this study. A review paper on this subject has been recently published by Wharry et al. [132]. The review summarized many results from various irradiation conditions. The summarized figure become too convoluted to provide any clear trend. Thus in this section, only self-ion irradiation and fast neutron irradiation to high dose at relevant temperatures are presented. A brief summary of oxide particle results following this guideline are listed in Table 6-3.

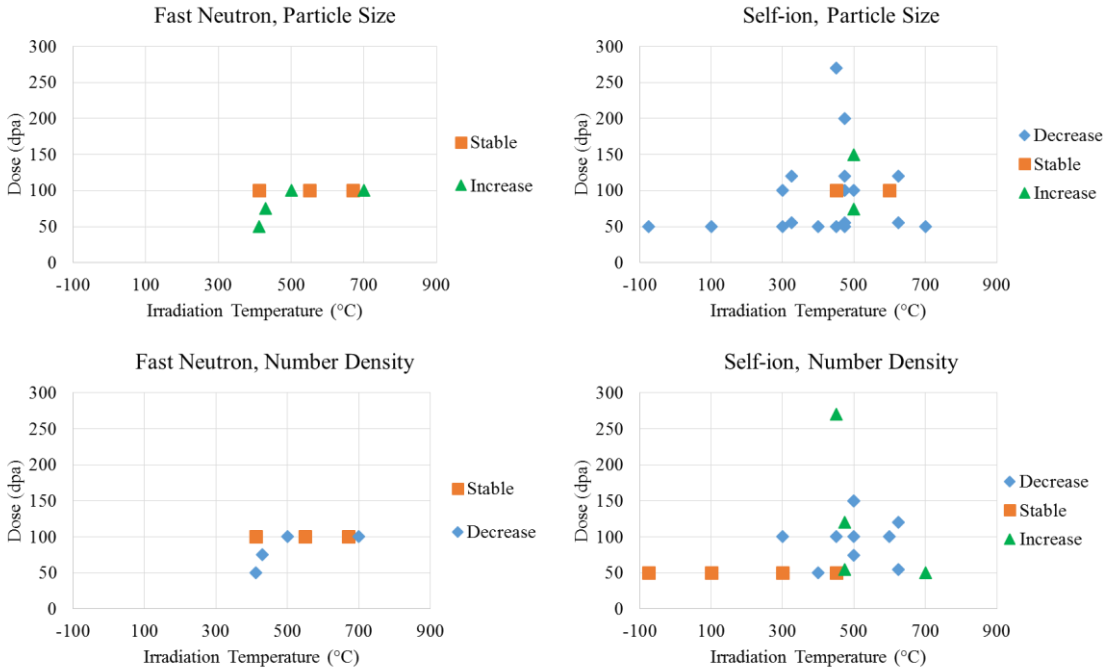

Figure 6-6. Summary of size and number density of oxide particle in ODS alloy irradiated by fast neutron or self-ion from open literatures.

Table 6-3. Summary of previous study on ODS alloys to high dose using self-ion or fast neutron from literatures.

Material	Irrad. Particle	Irrad. Temp (°C)	Dose (dpa)	Dose Rate (dpa/s)	Method	Size	Number Density	Reference
MA957	Fast n	412-670	109-113	~1×10^{-6}	APT	Stable	Stable	[91]
MA957	Fast n	412, 430	50, 75	~1×10^{-6}	TEM	Increase	Decrease	[90, 102]
MA957	Fast n	500, 700	~100	~1×10^{-6}	TEM	Increase	Decrease	[143]
14YWT	Ni^{2+}	-75-600	50*	~1×10^{-3}	APT	Decrease < 600°C	stable	[175]
14YWT	Ni^{2+}	-75-600	50*	~1×10^{-3}	TEM	Increase	Decrease < 600°C, else increase	[175]
14YWT	Ni^{2+}	300-600	100	~1.4×10^{-2}	APT	Decrease at 300°C; Else stable	Decrease	[176]
14YWT	Fe^{2+}	450	270-560	~1.7×10^{-3}	APT, TEM	Decrease	Increase	[111]
12Cr ODS	Fe^{2+}	325-625	55, 120	~1.7×10^{-3}	TEM	Decrease	Decrease at 625°C, Increase at 475°C	[184]
12Cr ODS	Fe^{2+}	475	50-400	~1.7×10^{-3}	TEM	Decrease	N/A	[185]
9Cr ODS	Fe^{2+}	400	50	~1×10^{-4}	APT	Decrease	Decrease	[177]
14YT	Fe^{3+}	700	50	N/A	APT	Decrease	Increase	[186]
18Cr ODS	Fe^{+}	500	74, 150	~6.4×10^{-3}	APT, TEM	Increase (TEM)	Decrease (TEM)	[187]
14Cr ODS	Fe^{+}	500	150	~6.4×10^{-3}	TEM	Increase	Decrease	[90]
9Cr ODS	Fe^{2+}	500	100	~1×10^{-4}	APT	Decrease	Decrease	[178]

Figure 6-6 plotted particle size and number density changes after irradiation from selected literatures. Even for the same ODS alloy MA957 with similar nominal composition and after similar fast neutron irradiation conditions, oxide particle evolutions were reported to be quite different. It suggests that heat treatment history of target material may be very important. For ion irradiation, a majority of experiments found that oxide particle size decreased across wide ranges of temperature and dose.

Their number densities, on the other hand, are reported to be either stable, increased or decreased, where there is no clear trend observed. As has been mentioned before, due to small sizes of oxide particles, characterization methods may have strong influence over results and conclusions. Thus in the near future, development of a standard procedure or commonly agreed method will be much helpful to better understand YTiO particles irradiation responses.

6.2 Correlations of α′

6.2.1 Size, Number Density, Volume Fraction and Temperature Shift

In general, α′ produced in ion irradiated MA957 is well correlated with those in neutron irradiated specimens. First of all, ion irradiation successfully reproduced the formation of α′ in the same temperature range as that in neutron irradiation. The size, number density and volume fraction of α′ are all comparable between neutron and ion irradiated specimens, as shown in Figure 6-7. Dashed lines are plotted for guiding eyes only. The shapes of these curves are also very similar. Ion irradiation, however, did not produced α′ with identical sizes or number densities as those in neutron irradiated specimens. The Cr-rich precipitates α′ after neutron irradiation is generally larger in sizes, lower in number density and higher in volume fraction than those in specimens after ion irradiation. Those differences are very much likely to be real and are not likely to be caused by differences between HV and laser modes in APT. Ion irradiation also successfully reproduced the critical temperature, between 450 and 500°C, for the 14Cr solubility limit in MA957 under irradiation. This is in good agreement with other existing literatures [133, 134].

The higher α′ population in ion irradiation again emphasizes the importance of understanding nucleation mechanism under irradiation in predicting microstructural evolutions. A series of theoretical works on nucleation of under-saturated solid solution have been done by Martin et al. [38, 188, 189]. Although MA957 has much complicated microstructures than simple Fe-Cr binary alloys, it would still be interesting to see if

Martin's theory match experimental data in this study. Martin's nucleation theory predicts that the solvus temperature, which separate solid solution with precipitation in phase diagram, is dose rate dependent. In general, the higher dose rate, the lower the solute solubility for Cr. However, volume fraction of α′ is found to be higher in specimens irradiated by neutrons than that in specimens irradiated by ions. More investigations, both experimental and theoretical investigations will be needed to understand those differences.

Shifting ion irradiation temperature by -10 to -20°C would make both shape of curves for α′ size and number density better aligned, as shown in Figure 6-7. Note that the uncertainty in temperature measurement is about 5-10°C in both neutron and ion irradiation [125]. However, the volume fraction curve would require a positive shift in ion irradiation temperature. Thus simple temperature shift is not adequate for neutron-ion correlation of α′ neither. Since some microstructural features, like α′, may be sensitive to irradiation condition and could reach steady state rapidly, knowing temperature history of analyzed in-reactor specimens is very important.

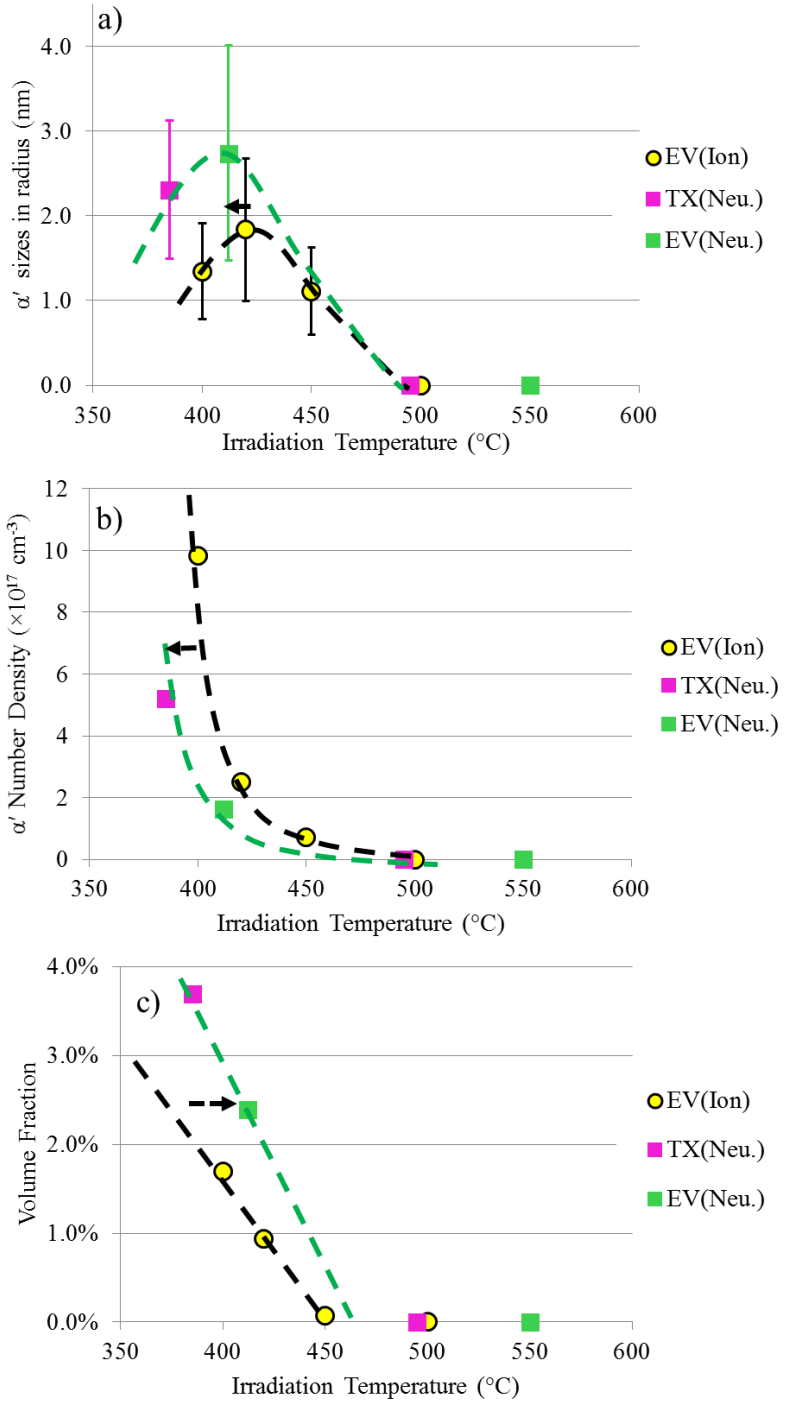

Figure 6-7. The average sizes a), the number density b) and the volume fraction c) of α′ with trend lines to guide eyes. The arrows are place as an estimation that how large ion irradiation temperature needs to be shifted to align curves in specimens irradiated by neutrons and ions.

6.2.2 Composition

The composition of α′ was almost reproduced in ion irradiation, as has been shown in section 4.2.3 results. The observed differences in Cr concentrations of α′ were attributed to the association with cluster size instead of irradiation particle type. As long as two Cr-rich precipitates of similar sizes are compared, the compositions measured by APT are similar between specimens irradiated by neutrons and by ions. However, we cannot tell whether this size dependence originated from APT artifacts or from physical properties of α′, such as interfacial energy.

6.3 Correlations of Grain Boundary Chemistry

Above discussions have shown that self-ion irradiation can reproduce similar microstructural features to those in specimens after neutron irradiation. Self-ion irradiation may have several issues for grain boundary chemistry. First, due to the small penetration depth of self-ion irradiation, only a fraction of grain boundaries may be affected. Combined with the high diffusivity of typical random grain boundaries, the influence of unirradiated portions of a GB and specimen surface upon irradiated portion of a GB are unknown. Thus, self-ion irradiation is far from ideal to study grain boundary chemistry, but it is still interesting for exploration and comparison with specimens irradiated by neutrons.

Grain boundary segregation of Cr are listed in Table 6-4 for neutron and ion irradiated specimens. We observed quite different RIS behaviors between ion and neutron irradiations at similar temperatures and doses. For all irradiation temperatures below 500°C, Cr was depleted at GBs in ion irradiated specimens. After neutron irradiation, Cr segregation transit from depletion to enrichment as temperature increases. To align GB segregation behavior of Cr, a shift in ion irradiation temperature of about -100°C would be required.

Table 6-4. Comparison of grain boundary segregation of Chromium in neutron or ion irradiated MA957.

Neutron		Ion	
Temperature (˚C)	Cr	Temperature (˚C)	Cr
385	-	400	-
412	-/+	420	-
495	+	450	-
550	+	500	-/+

Table 6-5 lists segregations of Y, Ti and TiO ions at GBs, all of which are core constituents of nano-oxide precipitates. Y was observed to enrich at GB at irradiation temperatures below 500°C in specimens irradiated by neutrons and in some ion irradiated specimens. Other ion irradiated specimens show no segregation of Y at GBs. In all neutron irradiation specimens, Ti was observed to be strongly enriched at GBs. Ti was depleted at GBs at low temperatures in ion irradiated specimens. A transient from depletion to enrichment of Ti with increasing irradiation temperatures can be observed. TiO is usually used as a marker for Ti-rich oxide particles. We found a large amount of particles enriched with Ti, O, and sometime with Y decorating GBs at lower irradiation temperature in specimens irradiated by neutrons. The formation of Ti, O-rich particles on GBs was observed at irradiation temperatures above 450°C in specimens irradiated by ions. Similar to Cr segregation, a shift in ion irradiation temperature of about -100°C would be required to align segregation behaviors of Ti and TiO.

Table 6-5. Comparison of grain boundary segregation of Yttrium, Titanium and Titanium Oxide ions in neutron or ion irradiated MA957.

Neutron				Ion			
Temperature (˚C)	Y	Ti	TiO	Temperature (˚C)	Y	Ti	TiO
385	+	+	+	400	0/+	-	0/+
412	+	+	+	420	0/+	-/+	0/+
495	+	+	+	450	0/+	-/+	+
550	0/+	+	+	500	0/+	+	+

Grain boundary segregation in BCC Fe is less studied than that in austenitic steels. A systematic study about RIS in F/M steels was conducted by Wharry et al. in recent years using proton irradiation and modeling with inverse Kirkendall mechanism [190-193]. It is reported that Cr enriches at GBs at low temperatures and then the magnitude of enrichment decreases from 400 to 600°C regardless of dose rate. Cr become depleted at higher irradiation temperatures. The depletion of Cr is usually attributed to that the vacancy flux migration toward grain boundary is larger than interstitial flux [191, 194]. In another study using self-ion irradiation, measured Cr GB segregation was reported to be either enrichment or depletion [137] in the same ion irradiated specimen. In our experiment the case is even more complicated, since Cr segregation at GB is convoluted with α′ formation. Future studies will be needed to better understand current experimental data. Y was observed to be enriched at GB at lower temperatures. The diffusion of Y is likely to be several orders of magnitude slower than Fe self-diffusion. Once Y arrived at GB, it is likely to be trapped. One possible mechanism for Y to reach GB is through interstitialcy mechanism, since irradiation creates higher interstitial population than thermal conditions [156]. We would like to caution that the aforementioned “temperature shift” are just estimated values in order to artificially overlap neutron and ion segregation results without considering its physical meanings.

6.4 Perspectives from Rate Theory Calculations

In section 5, rate theory based calculations have provided many insights for us to better understand similarities and differences in correlations between microstructural features in specimens irradiated by neutrons and by ions. The results suggest that in sink dominant regime for defect annihilation, dose rate does not have a strong effect on phase stability under irradiation. Neutron and ion irradiations correlations are predicted to be good in this regime. At higher irradiation temperatures, thermally generated defects could become dominate when dose rate is low. Above that temperature, dose rate difference needs to be considered. In this section, the calculation will be extended to a wider temperature range and focuses on temperature and dose rate effects on validity of neutron-ion correlations.

6.4.1 Defect Concentration, Enhanced Diffusivity from 100 to 800°C

Since we are extending analysis temperature range to 100-800°C, the assumption that thermally generated interstitials is negligible does not necessarily hold any more at high end of temperatures for low dose rate condition. Analytical solution to steady state at this condition is difficult to write so that numerical solutions are more convenient for calculation. For convenience, target material is assumed to be the same as the unirradiated MA957. All other parameters, such as diffusivity and sink strengths, are directly adopted from section 5. Calculated steady state defect concentrations for two dose rates are shown in Figure 6-8. At low temperatures, irradiation induced defects are higher in concentration due to low defect mobility. With irradiation temperature increase before reaching threshold temperature where thermally generated defect is dominant, defect supersaturation is reduced. After the threshold temperature, thermally generated defects become dominant and defect concentration is increased again. The threshold temperature for this transition for vacancy is around 500°C for low dose rate and is about 700°C for high dose rate. Due to very high dose rate, ion irradiation induced interstitials are dominant within the entire temperature range. As for fast neutron irradiation dose rate, at around 650°C thermal interstitials become the majority.

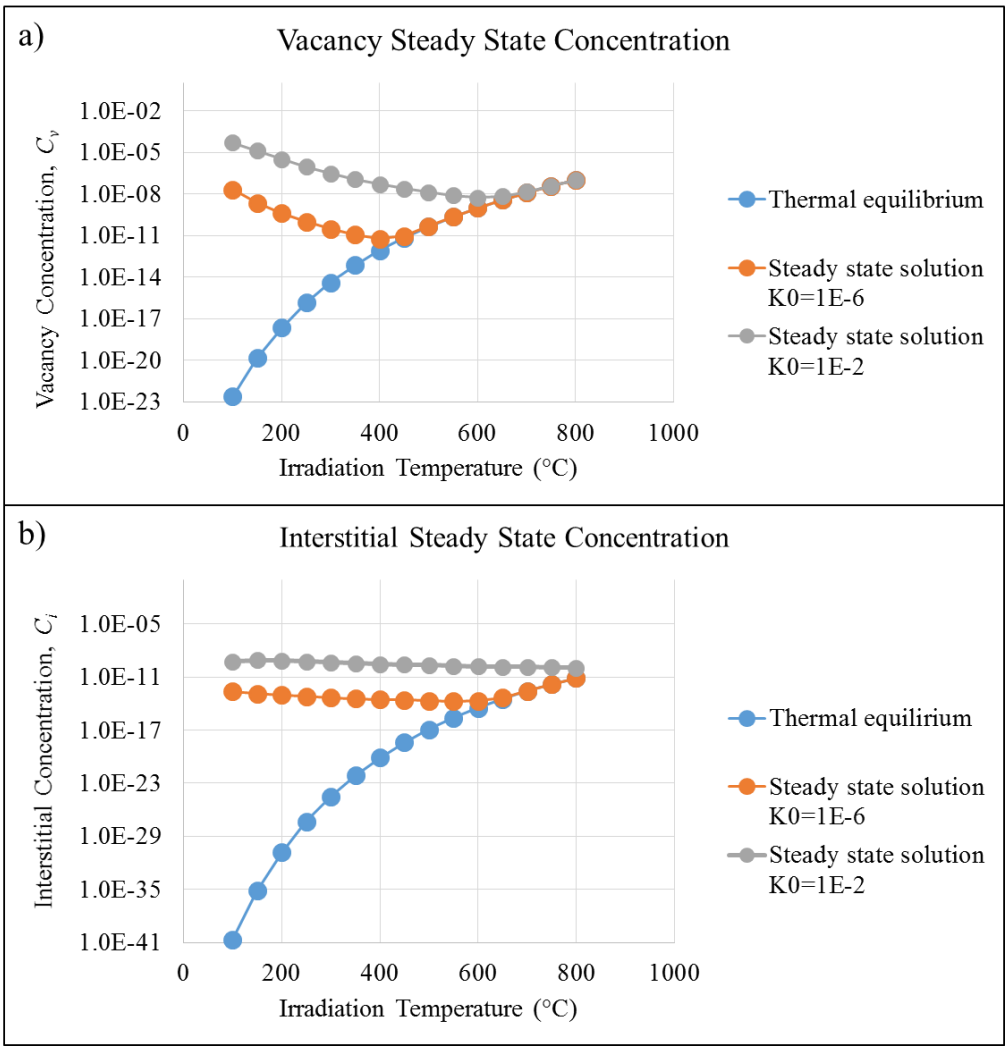

Figure 6-8. Comparison of steady state defect concentrations, a) vacancy and b) interstitial, as calculated in unirradiated MA957 for low dose rate, high dose rate and at thermal equilibrium.

Calculated solute diffusion coefficients via vacancy mechanism under irradiation are shown in Figure 6-9 using the same approach as in section 5.1.3. Since they are proportional to vacancy concentration, there exists a threshold temperatures above which thermal diffusion is dominant. Due to differences in dose rate, this thermal region is not identical between neutron (region I) and ion (region II) irradiation. In irradiation induced defect dominant regions, solute diffusivities are greatly enhanced compared to thermal

diffusion. As expected, higher dose rate yields greater enhancement in solute diffusion. We would like to mention that the choice of vacancy formation energy will have a large impact in the determination of radiation enhanced diffusion coefficients. According to equation (5.16), the enhancement of diffusion via vacancy mechanism is inversely proportion to vacancy concentration at thermal equilibrium, which is directly linked with the vacancy formation energy. For BCC Fe, both 1.6 and 2.2 eV are recommended values [195]. Using 2.2 instead of 1.6 for calculation would increase RED by several orders of magnitude.

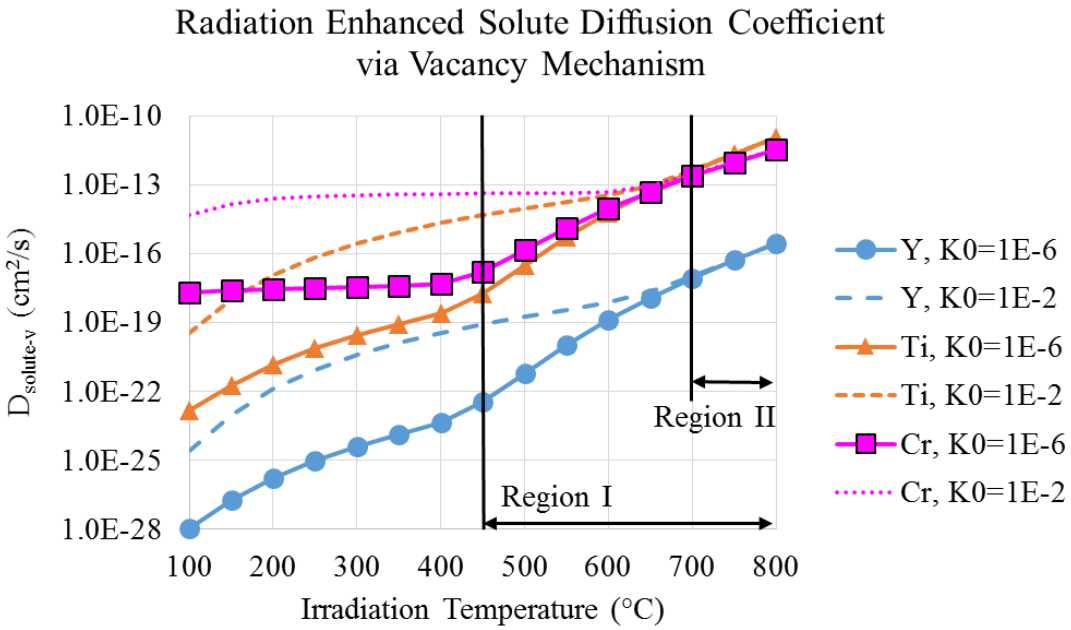

Figure 6-9. Calculated solute diffusion coefficients under low (1×10^{-6} dpa/s) and high (1×10^{-2} dpa/s) dose rates. Region I and Region II are thermal vacancy dominate temperature ranges for low and high dose rate data, respectively.

6.4.2 Ballistic (Cascade) Mixing

In addition to radiation enhanced diffusion, another mechanism, cascade mixing, may not be neglected [12, 196] at low irradiation temperatures. The transfer of energy

from recoiling atoms to its surroundings in the solid lead to an effective random mixing. Thus in a simplified scenario, the damage cascade leads to isotropic mixing of atoms inside, which can be treated as an effective driving force for diffusion. This ballistic mixing diffusion coefficient D_B can be written as:

$$D_B = \frac{1}{6}\lambda^2\varphi \tag{6.1}$$

where λ is the root-mean-square displacement distance of an atom in the collision cascade, φ is damage rate in dpa/s. The magnitude of λ is difficult to be determined accurately. Given that PKAs are probably with kinetic energy not much greater than threshold displacement energy, λ is probably within several times of nearest neighbor distance. For convenience, we will take λ as one lattice distance to 10 times lattice distance. Dose rate φ will be adopted from experiment setting, which are 10^{-2} and 10^{-6} dpa/s for ion and neutron irradiation, respectively. The calculated effective diffusion coefficients induced by ion mixing are listed in Table 6-6. Compared with above calculated radiation enhanced diffusion (RED), we can see that D_B are orders of magnitude high than RED at lower temperatures for Y and Ti. On the other hand, D_B is negligible compared to radiation enhanced diffusion of Cr within the entire temperature range.

Table 6-6. Effective diffusion coefficients D_B induced by ion mixing.

	$\varphi=1\times10^{-2}$ /s	$\varphi=1\times10^{-6}$ /s
$\lambda=a=2.856\times10^{-8}$ cm	1.36×10^{-18} cm^2/s	1.36×10^{-22} cm^2/s
$\lambda=10a=2.856\times10^{-7}$ cm	1.36×10^{-16} cm^2/s	1.36×10^{-20} cm^2/s

Considering ion mixing effect, solute diffusion coefficient under irradiation in equation (5.16) can be modified to:

$$D_{solute}^{rad} = \frac{C_v}{C_v^{eq}} D_{solute,v}^{thermal} + D_{solute,i}^{thermal} C_{solute,i} + D_B \tag{6.2}$$

For convenience and simplicity, we assume only substitutional lattice atoms are affected. The ballistic mixing effects on vacancy and interstitial diffusion should be included in defect balance equations. Considering that ballistic mixing induced diffusion is many orders of magnitude smaller than vacancy and interstitial, above equation is a valid approximation. Comparisons among solute diffusion coefficients of Y and Ti with and without D_B corrections are displayed in Figure 6-10. Since radiation enhanced diffusion for Ti is much larger than D_B above 300°C, ion beam mixing become dominant diffusion mechanism only below that temperature. Interestingly, the diffusion coefficient for Y via vacancy mechanism is so low so that D_B could be dominant over the entire temperature range before thermal vacancy become dominant. However we need to caution that in case interstitialcy mechanism contributes to Y diffusivity under irradiation, as discussed in section 5.1.3, the transition to D_B dominant region would have occurred at lower temperatures. In addition, temperature dependence of oxide particles in our experimental data suggest that at least within 400-500°C region, radiation enhanced diffusivity is either comparable or larger than ion mixing induced diffusion. It is hard to quantify exact contribution from ion mixing to Y diffusivity due to lack of many parameters. Nevertheless current analysis established an effective lower bound for diffusion coefficient of Y, which is much higher than estimated diffusion via vacancy mechanism.

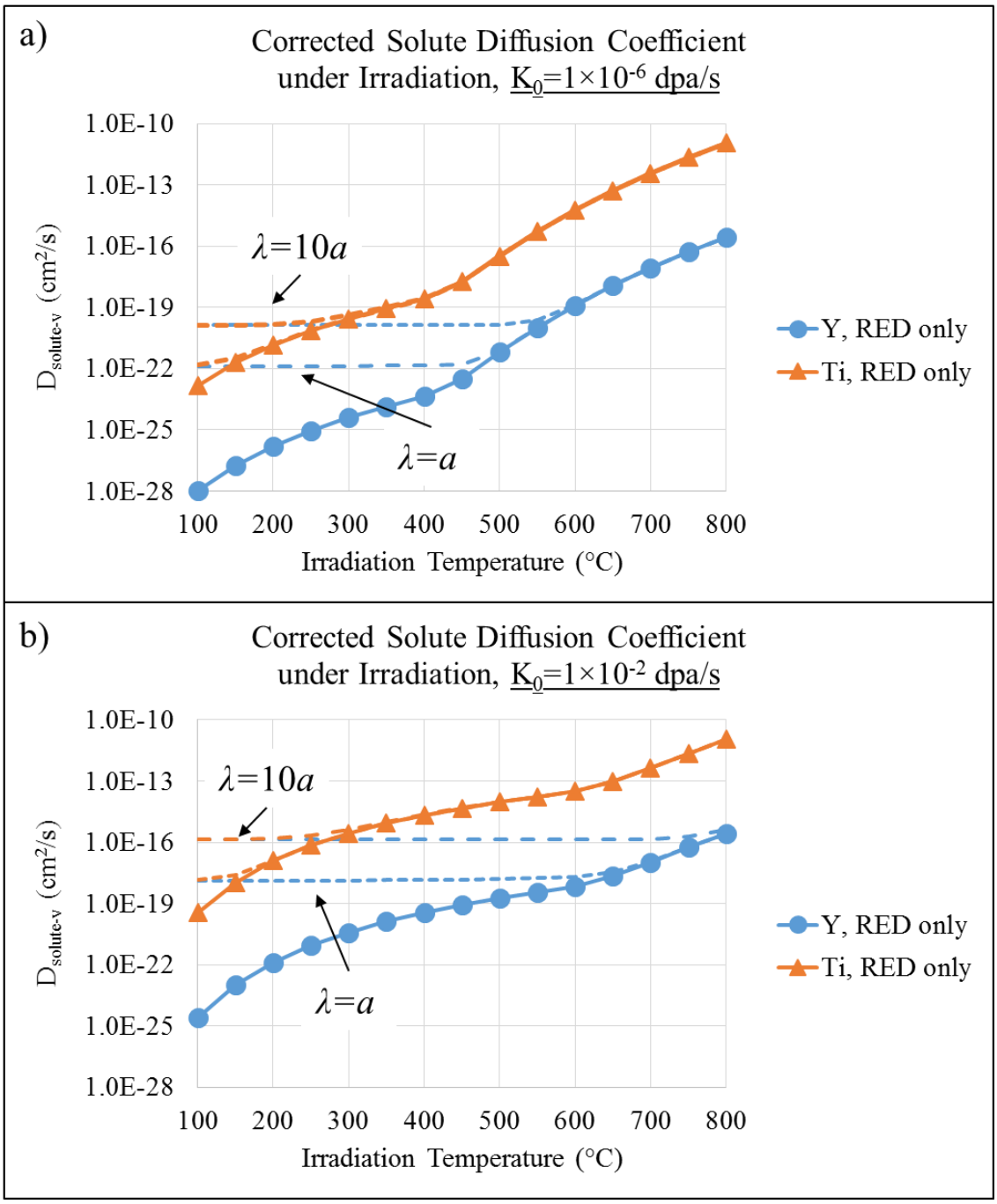

Figure 6-10. Comparison among radiation enhanced diffusion coefficients of Y and Ti with D_B modifications. Two test cases, $\lambda = a$ and $10a$, where a is lattice constant, are plotted for demonstration.

6.4.3 Temperature Shift and Dose Rate Effects

Temperature shift was developed with the intention to alter irradiation temperatures to compensate dose rate dependence effects to make defect flux invariant. It was conceptualized based on several rate theory models for void swelling and influenced by "peak swelling temperature shift" in void swelling experimental data [17, 183, 197] during that time of periods. Later studies have shown that the observed shift is likely a misconception, where analyzed data was combinations of incubation and steady state swelling [Private discussions with Frank Garner][22]. The temperature shift concept, on the other hand, has been carried over and continue to be discussed widely. In a later review by Mansur [183] and a book chapter by Was [8], the void growth rate was found possible to be dose rate invariant if defect annihilation at sinks is the dominant mechanism. In this section, we will show derivation of dose rate dependence for a slightly generalized diffusion-control microstructural evolution.

From perspectives of rate theory models, temperature shift originated from the solutions to the defect balance equations. Since solute diffusion is essential to microstructural evolutions and is heavily dependent on point defect concentrations, solute diffusion coefficients rely on both temperature and defect production rate. The link between defect concentration and solute diffusivity has been expressed above in equation (6.2). An analytical solution assuming thermal interstitial concentration is negligible has been given in section 5.1.3, equation (5.13) and (5.14). Calculated steady state defect concentrations using MA957 material parameters within a wide temperature range have been shown in Figure 6-8 in section 6.4.1. The steady state solutions can be approximated at two extreme cases, the recombination dominant regime, where point defect annihilation mostly via recombination, as in the equation (6.3), and the sink dominant regime, where point defect annihilation mostly via defect sinks, as in the equation (6.4) [8]:

$$C_v^{ss} = \left[\frac{K_0 K_{is}}{K_{iv} K_{vs}}\right]^{\frac{1}{2}}, C_i^{ss} = \left[\frac{K_0 K_{vs}}{K_{iv} K_{is}}\right]^{\frac{1}{2}} \tag{6.3}$$

$$C_v^{ss} = \frac{K_0}{K_{vs}C_s}, C_i^{ss} = \frac{K_0}{K_{is}C_s} \tag{6.4}$$

where K_0 is dose rate, K_{iv}, K_{vs}, and K_{is} are defect reaction rates between vacancy and interstitial, between vacancy and sinks, and between interstitial and sinks. Theses parameters can be calculated in approaches described in section 5.1.3.

Assuming there are some microstructural quantities, such as solute concentrations, proportional to solute or defect diffusivity, an abstract dose dependent form master equation can be written as below, assuming diffusion coefficients are not compositional dependent:

$$\frac{dM}{K_0 dt} \propto \frac{1}{K_0} \sum m_j D_{solute,j} \tag{6.5}$$

where M is a microstructural quantity, D is the solute diffusivity, and m_j is some other factors that are model-specific, which could be defect concentration gradient for example. Note that it is the accumulated dose we are interested in rather than actual irradiation time for microstructural correlation. The master equation is in an abstract form for a variety of microstructural evolution models, such as void growth, precipitates stability, and solute segregations [160, 167, 183, 191, 198]. The ratio between solute diffusivity and dose rate is that important to know and it can be obtained by combining equation (6.2) and (6.5):

$$\frac{D_{solute}}{K_0} = \frac{D_{solute,v}^{thermal}}{C_v^{eq}} \frac{C_v}{K_0} + D_{solute,i}^{thermal} \frac{C_i}{K_0} + \frac{D_B}{K_0} \tag{6.6}$$

In defect recombination regime, equation (6.5) can be re-organized by combining equations (6.1), (6.3) and (6.6):

$$\frac{dM}{K_0 dt} \propto \sum m_j \left(\frac{a_j}{K_0^{1/2}} + \frac{b_j}{K_0^{1/2}} + \frac{1}{6}\lambda^2 \right) \tag{6.7}$$

where a_j and b_j are some temperature dependent quantities related to vacancy and interstitial diffusion coefficients at thermal equilibrium. As a result, change of microstructural quantity M per dpa is inverse proportional to square root of dose rate. Compared with higher dose rate K_0, irradiation temperature need to be elevated for low

dose rate cases to increase a_j and b_j to keep defect flux invariant. Similarly, the formula for sink dominant regime can be obtained by using equation (6.4) (6.3):

$$\frac{dVar}{K_0 dt} \propto \sum m_j \left(a_j + b_j + \frac{1}{6}\lambda^2 \right) \tag{6.7}$$

in which change of microstructural quantity *M* per dpa is dose rate independent. Thus there is no need to shift temperature to accommodate different dose rate.

According to above approximations, it is the solute diffusivity-to-dose rate ratio, D/K_0, that determines whether defect flux is invariant to dose rate or not. A set of comparisons for D/K_0 of Ti and Y are plotted in Figure 6-11 with and without consideration of the ballistic mixing contribution to diffusivity. If ballistic mixing is ignored, as shown in a), we can see that dose rate dependence of D/K_0 for each element can be roughly divided into three temperature regimes. When irradiation temperature <150°C, D/K_0 is dose rate dependent by square root of K_0 due to a recombination dominant defect annihilation. In temperature range ~150-400°C, D/K_0 are the same between two dose rate cases, which can be attributed to sink dominant defect annihilation. At higher temperature above 450°C, solute diffusivity follows thermal diffusion in low dose rate case while in high dose rate irradiation radiation enhanced diffusion is still larger than thermal diffusion. As a result, D/K_0 becomes much higher in low dose rate than in high dose rate.

If ballistic mixing modification is applied, as shown in b), the dose rate dependence of D/K_0 for solute needs to be assessed individually. For example, contribution from ballistic mixing is orders of magnitude smaller than radiation enhanced diffusion for Cr so that it is won't affect Cr much. For Ti, ballistic mixing induced diffusion is comparable or larger than radiation enhanced diffusion only at temperatures lower than 150°C. As a result, sink dominant regime and thermal dominant regime for Ti remains the same as those prior modification. For Y, ballistic mixing completely takes over temperature regime below 450°C due to extremely small values of Y diffusivity via vacancy mechanism. In this case, we noticed that at 400-450°C, a small temperature window exists that Ti is dose rate dependent while Y is dose rate independent.

In order to reproduce microstructural features in ion irradiation, application of temperature shift need to be analyzed case by case, which depends on the regime that D/K_0 belongs to. According to above demonstration, ideally, no temperature shift is needed for sink dominant and ballistic mixing regimes, in which D/K_0 is dose rate independent. The D/K_0 ratio in high dose rate case is lower than low dose rate if it falls into recombination dominant or thermal dominant regimes. Temperature shift estimation for recombination dominant scenarios can be found in references [8, 17]. For thermal dominant regime, temperature shift is estimated to be on the order of hundreds of degree Celsius to keep D/K_0 similar.

Using current parameters, rate theory calculation suggests that no temperature shift is needed at lower temperature (385-500°C) and ion irradiation may reproduce microstructural features as those in neutron irradiated specimens. At higher temperatures, however, thermal diffusion become dominant in neutron irradiation. This may be responsible for the coarsening of YTiO particles in neutron irradiated specimens. The rate theory calculation seems in excellent qualitative agreement with experimental data in this study.

We need to caution that above results are only demonstrations using our material specific parameters and derived quantities within rate theory models framework. The accuracy of calculated variables are thus strongly dependent on model as well as parameters of choice. For example, as previously mentioned, including interstitialcy mechanism for Y diffusion would shift take-off temperature of ballistic mixing to lower value and would shift thermal diffusion dominant temperature upward to higher values. Since these models are greatly simplified, a variety of factors from atomistic details to local variations, which may be crucial to microstructural evolution, are not included. For example, the cell model in section 5.2.2 shows that if atoms are displaced further away in neutron irradiation due to higher average PKA energy, local concentration field may be altered. Solute diffusivity is assumed to be concentration independent is another simplification. In reality, diffusivity is related to local free energy. Whether applying a

large temperature shift could reproduce similar microstructural features or not need more investigations.

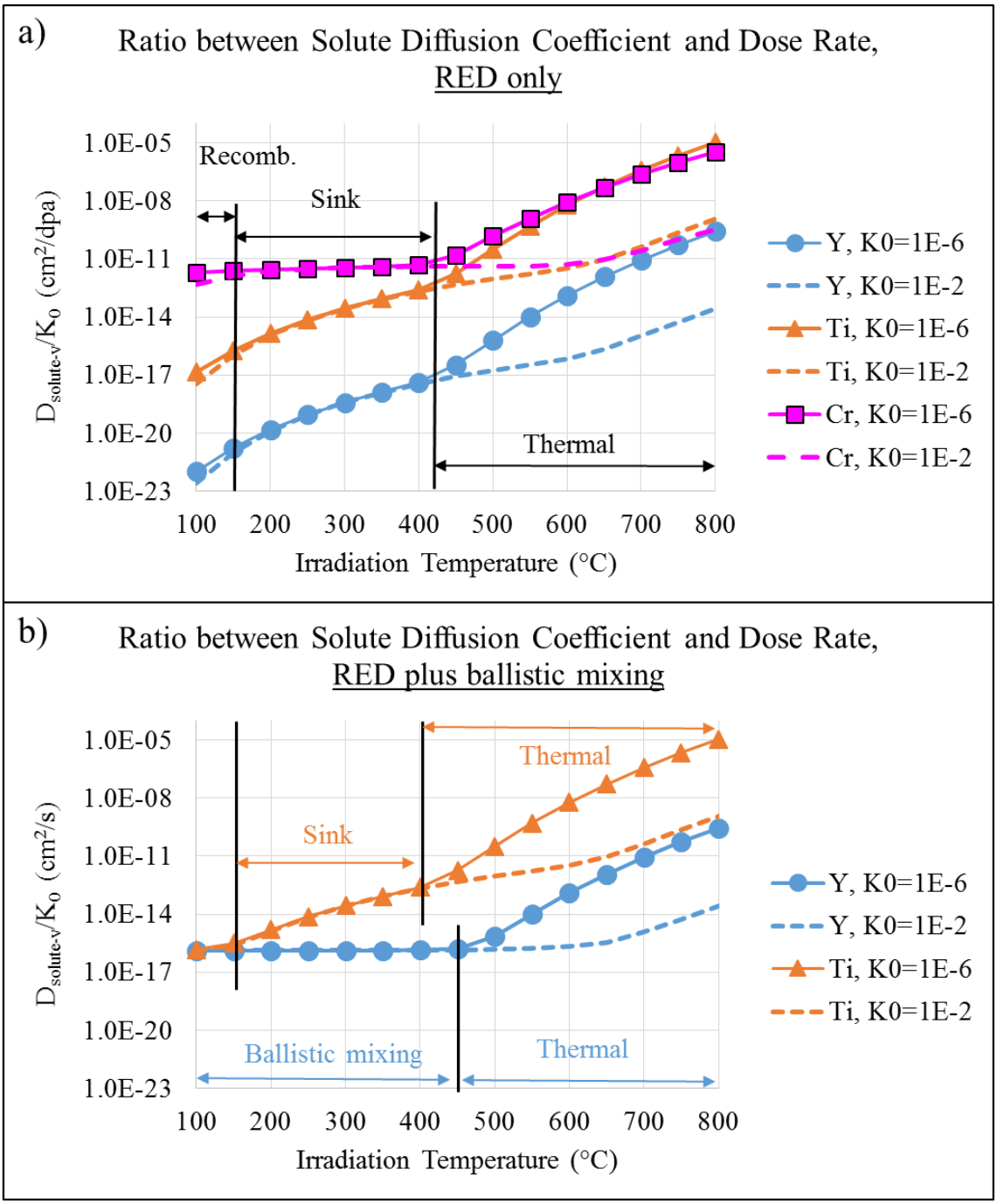

Figure 6-11. Comparisons among solute diffusivity-to-dose rate ratios for low and high dose rate irradiations. a) without ballistic mixing modification, and b) with ballistic mixing modification, $\lambda = a$. "Sink", "thermal", "recomb." and "ballistic mixing" are identified temperature ranges where corresponding mechanism is dominant. Contribution from ballistic mixing is negligible for Cr so that it is not plotted.

6.4.4 Use a Different Vacancy Formation Energy

The choice of vacancy formation energy also greatly affect the magnitude of calculated radiation enhanced diffusion coefficients. Merely change it from 1.6 eV to 2.2 eV, both of which are validate choices [145, 195], would result in ~7 orders of magnitude increase in radiation enhanced diffusion for all solutes via vacancy mechanism. This effect arises from our treatment in calculating radiation enhanced diffusion coefficient. Since experimental data was used to estimate solute diffusivity at thermal equilibrium, the radiation enhanced diffusion coefficient is estimated by equation (5.5). The treatment is equivalent to calculate solute migration energy by subtracting measured activation energy by vacancy formation energy. Therefore, from physics perspective, it is the unknown solute migration energy that truly affect radiation enhanced diffusion coefficients. The vacancy formation energy affect the calculated temperature range for thermal diffusion dominant. In this section, the vacancy formation energy will be assumed to 2.2 eV instead of previously used 1.6 eV, and its effects on result will be briefly discussed.

Solute diffusion coefficients for Cr, Ti and Y re-calculated using vacancy formation energy of 2.2 eV are shown in Figure 6-12a). As mentioned above, all diffusion coefficients are elevated by several orders of magnitude in radiation enhanced diffusion temperature range. The take-off temperature for thermal diffusion become dominant is postponed to ~600°C compared to ~450-500°C in previous calculations (Figure 6-9). Since calculated radiation enhanced diffusion is greatly increased, ballistic mixing driving diffusion dominant temperature range is shifted further down to lower temperatures. For example, the transition from radiation enhanced diffusion to ballistic mixing for Y is < 100°C in this case. Figure 6-12b) shows the re-calculated diffusion coefficient-to-dose rate ratios. From 100 to 800°C, the temperature can be divided into three distinctive regimes, the recombination dominant (100-200°C), the sink dominant (200-600°C), and the thermal diffusion dominant (> 600°C).

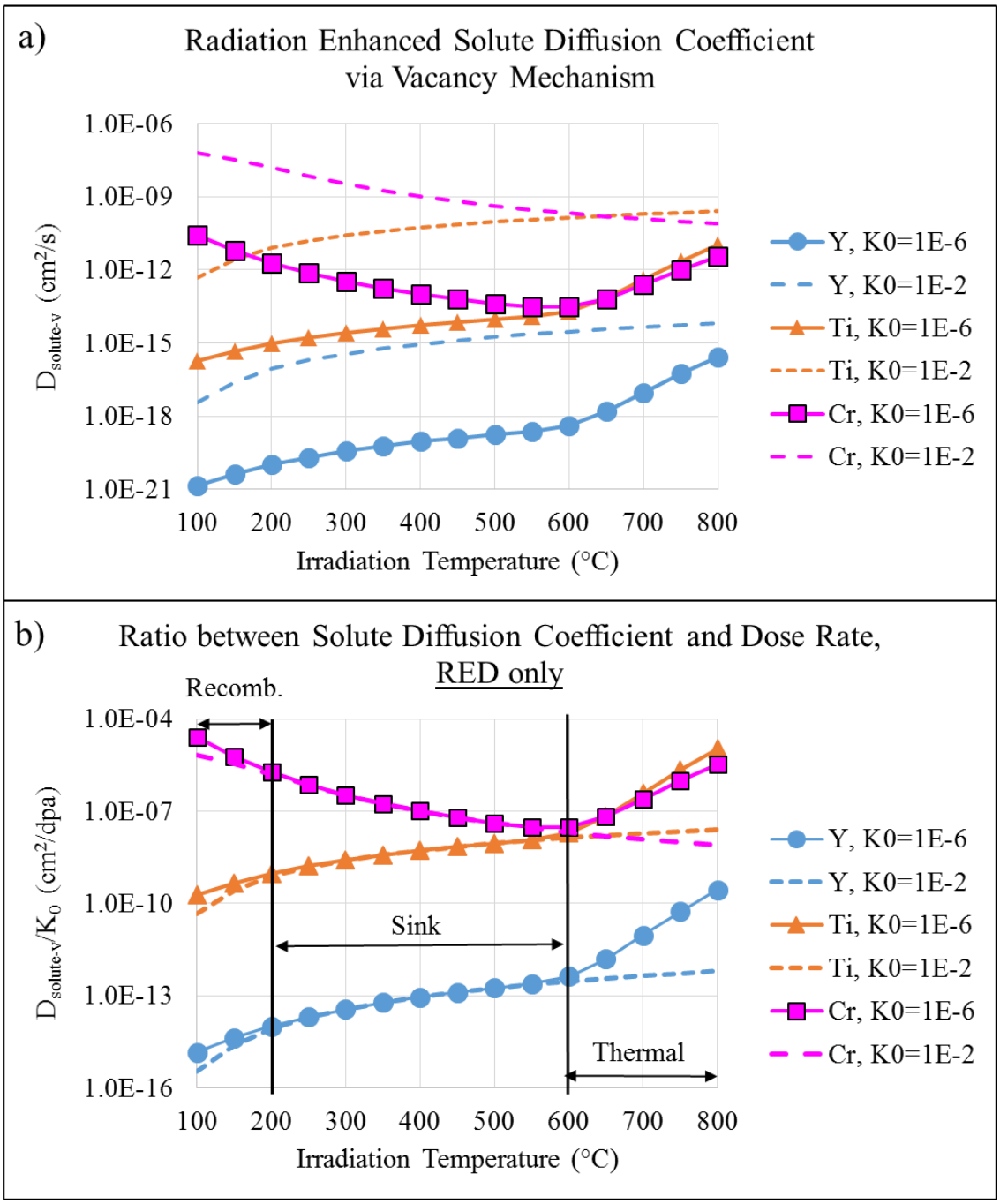

Figure 6-12. a) Re-calculated solute diffusion coefficients; and b) diffusion coefficient-to-dose rate ratio, using vacancy formation energy of 2.2 eV in BCC Fe instead of 1.6 eV. All other parameters remain the same as used for Figure 6-9 and Figure 6-10.

As a consequence, the re-precipitate rate for oxide particles will be enhanced as well, according to equation (5.18). The dissolution rate of YTiO particles is then calculated as the re-precipitation rate subtracted by the particle radius change rate. The measured radius change is taken as the slope between unirradiated and 100 dpa ion irradiated specimens, as in Figure 5-16. Table 6-7 listed dissolution rates for oxide particles following this procedure. Note that we are aware this is a rough approximation due to limited number of experimental data points. For comparison, dissolution rate obtained using vacancy formation energy of 1.6 eV is 1.2-4.8×10^{-10} cm/dpa, which is much smaller than using vacancy formation energy of 2.2 eV.

Table 6-7. Estimated dissolution rate using measured radius change rate and re-calculated re-precipitation rate. The measured radius change is taken from Figure 5-16 for ion irradiation. The re-precipitation rate is calculated according to equation (5.18). The dissolution rate is calculated by subtracting the re-precipitation rate by the radius change rate.

Temperature (°C)	Radius change rate (×10^{-10} cm/dpa)	Re-precipitation rate (×10^{-10} cm/dpa)	Dissolution rate (×10^{-10} cm/dpa)
400	-4.77	19.85	24.62
420	-2.27	24.26	26.53
450	-2.39	28.45	30.84
500	-1.05	39.03	40.08

7 CONCLUSIONS AND FUTURE WORK

This research presents detailed microstructural characterizations by APT for a neutron-ion irradiation intercorrelation investigation regarding microstructural features, like phase stability, second phases and grain boundary chemistry, in ODS alloy MA957. Similarities and differences among them are analyzed and discussed. Rate theory based calculations have been conducted to gain mechanistic insight for neutron-ion intercorrelations. Temperature and dose rate effects on microstructural evaluations, such as phase stability, have been analyzed. A general guideline for future neutron-ion intercorrelation investigation has been proposed.

The APT characterization result shows that YTiO particles' responses to irradiation are very similar between neutron and ion irradiation at temperatures below 450°C, while larger discrepancies occur at higher temperatures. These nano-oxides are found to be shrinking at all temperatures in ion irradiated specimens and at temperatures <495°C in neutron irradiated ones. At higher temperature for neutron irradiation, coarsening of oxide particles have been observed. Their number density seems to be strongly temperature and dose rate dependent, which suggest complexities in oxide particle nucleation. Under all irradiation condition, a large fraction of YTiO particles are still present in specimen to ~100 dpa, suggesting excellent radiation tolerance. Chemical compositions of oxide particles are found mostly stable in neutron irradiated specimens. But Y/Ti ratio in ion irradiated MA957 at 400°C is increased significantly.

The formation of alpha-prime has been identified in both neutron and ion irradiated specimens at temperatures below 450°C. In general, average size and number density against temperature shares the same shape between neutron and ion irradiations. The average sizes of alpha prime in both neutron and ion irradiated specimens exhibit a non-monotonic response with irradiation temperatures with peak size observed at 420°C for ion and 412°C for neutron. The number density monotonic decreasing rapidly as irradiation temperature increased from ~400°C to ~450°C for both neutron and ion irradiated specimens. No alpha-prime was observed in APT analyzed volume for

specimens irradiated above 450°C. The absence of Cr-enriched precipitates at higher temperatures could be attributed to the increasing Cr solubility. Our experimental result suggest that for the critical temperature for Cr precipitation under irradiation in MA957 (14 wt% Cr) is likely to be sitting in the temperature range between 450-500°C, which agrees with other reports neutron irradiated or thermally aged 14Cr alloys [133-136].

Grain boundary chemistry is also similar between neutron and ion irradiation specimen, although we expect that self-ion irradiation has its limitations on this microstructural feature. Radiation-induced segregation of chromium underwent a transition from depletion to enrichment with increasing irradiation temperature. The same trend has been observed in ion irradiation as well. However, interference from alpha-prime formation makes deconvolution Cr GB segregation difficult. Ti and O rich particles, many are enriched with Y as well, have been observed to be strongly enriched at grain boundary in some temperature ranges (385-412°C for neutron and 450-500°C for ion). It may be attributed to preferential reformation of YTiO particles on grain boundaries or grain boundary migration pinned by oxide particles.

Rate theory calculations suggest that experimentally good agreements between neutron and ion irradiated specimens below 500°C could be attributed to sink dominant defect annihilation, in which microstructural feature development is dose rate independent. At higher temperature, discrepancies arise due to thermal diffusion dominance in low dose rate experiments. The diffusivity-to-dose rate ratio D/K_0 has been identified to be a good measure in determination whether temperature shift is needed and how large it would be. Four different regimes for D/K_0 corresponded to different dominant diffusion contributions have been explored and characteristic dose rate dependence in each regime are discussed. In general, when defect concentration is governed by annihilation at defect sinks or ballistic mixing is the primary diffusion driving force, microstructures, like void and precipitate growth kinetics, are independent of dose rate. Thus ion irradiation could be a good tool to investigate those features in these temperature regimes. If defect annihilation is governed by mutual recombination or if thermal diffusion is dominant, temperature shift needs to be considered for neutron-ion

intercorrelation studies. In addition, we need to caution about temperature shift in thermal diffusion regime since the estimated value could be quite large if dose rates are very different.

Current experimental and theoretical results indicate that ion irradiation could be an effective validated surrogate technique to investigate irradiation effects caused by neutron. Many future work could be done to further our understanding in this subject. First of all, the dislocation structures and grain structures need to be characterized so that their correlation can be evaluated. Since dose rate has strong influence on precipitate number density, nucleation models of precipitate need to be studied and understood. In our literature review over experiments under similar conditions, opposite trends, results, or conclusions are common. A natural reaction for us would be to understand if other factors that are equally if not more important as commonly well-recognized heat treatment, temperature and dose rate. One of them could be to investigate whether or not there are accelerator dependence or specimen preparation procedure dependence on final microstructure. To better understand neutron-ion correlations, more advanced techniques are needed. One potential powerful tool is the phase-field modeling, in which thermal dynamics and temporal, spatial variations can be added while using similar kinetics as in rate theory. Characterization, data analysis and interpretation as have been mentioned several time previously would have a huge influence on final results and conclusion even for the same specimen. Another direction for better performing neutron-ion correlation investigations would be to find or build common consensus, standardized microstructural characterization and analysis procedures.

REFERENCES

[1] S.J. Zinkle, J.T. Busby, Structural materials for fission & fusion energy, Materials Today 12(11) (2009) 12-19.

[2] P. Hejzlar, R. Petroski, J. Cheatham, N. Touran, M. Cohen, B. Truong, R. Latta, M. Werner, T. Burke, J. Tandy, Terrapower, LLC traveling wave reactor development program overview, Nuclear Engineering and Technology 45(6) (2013) 731-744.

[3] F. Garner, M. Toloczko, B. Sencer, Comparison of swelling and irradiation creep behavior of fcc-austenitic and bcc-ferritic/martensitic alloys at high neutron exposure, Journal of Nuclear Materials 276(1) (2000) 123-142.

[4] M. Toloczko, F. Garner, C. Eiholzer, Irradiation creep and swelling of the US fusion heats of HT9 and 9Cr-1Mo to 208 dpa at~ 400 C, Journal of nuclear materials 212 (1994) 604-607.

[5] B.H. Sencer, J. Kennedy, J. Cole, S.A. Maloy, F.A. Garner, Microstructural analysis of an HT9 fuel assembly duct irradiated in FFTF to 155dpa at 443° C, Journal of Nuclear Materials 393(2) (2009) 235-241.

[6] O. Anderoglu, J. Van den Bosch, P. Hosemann, E. Stergar, B. Sencer, D. Bhattacharyya, R. Dickerson, P. Dickerson, M. Hartl, S. Maloy, Phase stability of an HT-9 duct irradiated in FFTF, Journal of Nuclear Materials 430(1) (2012) 194-204.

[7] J.A. Brinkman, Production of atomic displacements by high-energy particles, American Journal of Physics 24(4) (1956) 246-267.

[8] G.S. Was, Fundamentals of radiation materials science: metals and alloys, Springer2016.

[9] G. Kinchin, R. Pease, The displacement of atoms in solids by radiation, Reports on progress in physics 18(1) (1955) 1.

[10] R.E. Stoller, M.B. Toloczko, G.S. Was, A.G. Certain, S. Dwaraknath, F.A. Garner, On the use of SRIM for computing radiation damage exposure, Nuclear Instruments and Methods in Physics Research Section B: Beam Interactions with Materials and Atoms 310 (2013) 75-80.

[11] M.T. Robinson, I.M. Torrens, Computer simulation of atomic-displacement cascades in solids in the binary-collision approximation, Physical Review B 9(12) (1974) 5008-5024.
[12] S. Myers, Ion-beam-induced migration and its effect on concentration profiles, Nuclear Instruments and Methods 168(1-3) (1980) 265-274.
[13] A.D. Marwick, The primary recoil spectrum in the simulation of fast-reactor radiation damage by charged-particle bombardment, Journal of Nuclear Materials 55(3) (1975) 259-266.
[14] R.E. Stoller, The role of cascade energy and temperature in primary defect formation in iron, Journal of nuclear materials 276(1) (2000) 22-32.
[15] G.S. Was, Fundamentals of radiation materials science: metals and alloys, Springer Science & Business Media2007.
[16] G.S. Was, T. Allen, Radiation-induced segregation in multicomponent alloys: Effect of particle type, Materials characterization 32(4) (1994) 239-255.
[17] L. Mansur, Correlation of neutron and heavy-ion damage: II. The predicted temperature shift if swelling with changes in radiation dose rate, Journal of Nuclear Materials 78(1) (1978) 156-160.
[18] L.K. Mansur, Void swelling in metals and alloys under irradiation: an assessment of the theory, Nuclear Technology 40(1) (1978) 5-34.
[19] N. Packan, K. Farrell, J. Stiegler, Correlation of neutron and heavy-ion damage: I. The influence of dose rate and injected helium on swelling in pure nickel, Journal of Nuclear Materials 78(1) (1978) 143-155.
[20] E. Lee, L. Mansur, Unified theoretical analysis of experimental swelling data for irradiated austenitic and ferritic/martensitic alloys, Metallurgical Transactions A 21(4) (1990) 1021-1035.
[21] L. Shao, C.-C. Wei, J. Gigax, A. Aitkaliyeva, D. Chen, B. Sencer, F. Garner, Effect of defect imbalance on void swelling distributions produced in pure iron irradiated with 3.5 MeV self-ions, Journal of Nuclear Materials 453(1) (2014) 176-181.

[22] F. Garner, L. Shao, M. Toloczko, S. Maloy, V. Voyevodin, Use of self-ion bombardment to study void swelling in advanced radiation-resistant alloys, 17th Int. Conf. Environ. Degrad. Mater. Nucl. Power Syst.–Water React. Canadian Nuclear Society, Ottawa (Canada), 2015, pp. 163-181.
[23] J.G. Gigax, E. Aydogan, T. Chen, D. Chen, L. Shao, Y. Wu, W. Lo, Y. Yang, F. Garner, The influence of ion beam rastering on the swelling of self-ion irradiated pure iron at 450° C, Journal of Nuclear Materials 465 (2015) 343-348.
[24] M.P. Short, D.R. Gaston, M. Jin, L. Shao, F.A. Garner, Modeling injected interstitial effects on void swelling in self-ion irradiation experiments, Journal of Nuclear Materials 471 (2016) 200-207.
[25] E. Getto, Z. Jiao, A. Monterrosa, K. Sun, G. Was, Effect of irradiation mode on the microstructure of self-ion irradiated ferritic-martensitic alloys, Journal of Nuclear Materials 465 (2015) 116-126.
[26] E. Getto, Z. Jiao, A. Monterrosa, K. Sun, G. Was, Effect of pre-implanted helium on void swelling evolution in self-ion irradiated HT9, Journal of Nuclear Materials (2015).
[27] F. Garner, Impact of the injected interstitial on the correlation of charged particle and neutron-induced radiation damage, Journal of Nuclear Materials 117 (1983) 177-197.
[28] E.H. Lee, L.K. Mansur, M.H. Yoo, Spatial variation in void volume during charged particle bombardment — the effects of injected interstitials, Journal of Nuclear Materials 85 (1979) 577-581.
[29] K. Vörtler, M. Mamivand, L. Barnard, I. Szlufarska, F. Garner, D. Morgan, Simulated spatial and temporal dependence of chromium concentration in pure Fe and Fe 14% Cr under high dpa ion irradiation, Journal of Nuclear Materials 479 (2016) 23-35.
[30] J. Wang, M.B. Toloczko, N. Bailey, F.A. Garner, J. Gigax, L. Shao, Modification of SRIM-calculated dose and injected ion profiles due to sputtering, injected ion buildup

and void swelling, Nuclear Instruments and Methods in Physics Research Section B: Beam Interactions with Materials and Atoms 387 (2016) 20-28.
[31] F. Garner, L. Greenwood, Recent progress in fusion reactor materials studies: focus on transmutation and radioactivation aspects, Materials Transactions, JIM 34(11) (1993) 985-998.
[32] L. Greenwood, F. Garner, D. Edwards, Calculation of transmutation in copper and comparison with measured electrical properties, Proc. Eighth ASTM-Euratom Symposium on Reactor Dosimetry, Vail, CO, 1993, pp. 500-508.
[33] L. Greenwood, F. Garner, Transmutation of Mo, Re, W, Hf, and V in various irradiation test facilities and STARFIRE, Journal of nuclear materials 212 (1994) 635-639.
[34] C. Forty, Activation response of martensitic steels, Journal of fusion energy 16(3) (1997) 277-283.
[35] L.R. Greenwood, F.A. Garner, Impact of transmutation issues on interpretation of data obtained from fast reactor irradiation experiments, Journal of nuclear materials 329 (2004) 1147-1150.
[36] R. Klueh, Reduced-activation bainitic and martensitic steels for nuclear fusion applications, Current Opinion in Solid State and Materials Science 8(3) (2004) 239-250.
[37] S.I. Maydet, K.C. Russell, Precipitate stability under irradiation: Point defect effects, Journal of Nuclear Materials 64(1) (1977) 101-114.
[38] R. Cauvin, G. Martin, Radiation induced homogeneous precipitation in undersaturated solid-solutions, Journal of Nuclear Materials 83(1) (1979) 67-78.
[39] C. Cawthorne, E. Fulton, Voids in irradiated stainless steel, (1967).
[40] L. Walters, C. Walter, Observations of dilation and bowing in Experimental Breeder Reactor II ducts and cladding, Nuclear Technology 46(1) (1979) 134-148.
[41] J. Straalsund, R. Powell, B. Chin, An overview of neutron irradiation effects in LMFBR materials, Journal of Nuclear Materials 108 (1982) 299-305.
[42] A. Brailsford, R. Bullough, The rate theory of swelling due to void growth in irradiated metals, Journal of Nuclear Materials 44(2) (1972) 121-135.

[43] E. Little, Microstructural evolution in irradiated ferritic-martensitic steels: transitions to high dose behaviour, Journal of nuclear materials 206(2) (1993) 324-334.
[44] M.B. Toloczko, F.A. Garner, S.A. Maloy, Irradiation creep and density changes observed in MA957 pressurized tubes irradiated to doses of 40–110dpa at 400–750° C in FFTF, Journal of nuclear materials 428(1) (2012) 170-175.
[45] M.B. Toloczko, F. Garner, V. Voyevodin, V. Bryk, O. Borodin, V. Mel'nychenko, A. Kalchenko, Ion-induced swelling of ODS ferritic alloy MA957 tubing to 500dpa, Journal of Nuclear Materials 453(1) (2014) 323-333.
[46] J. Stiegler, L. Mansur, Radiation effects in structural materials, Annual Review of Materials Science 9(1) (1979) 405-454.
[47] R.L. Klueh, D.R. Harries, High-chromium ferritic and martensitic steels for nuclear applications, ASTM West Conshohocken, PA, 2001.
[48] J. Gittus, Theory of dislocation-creep due to the frenkel defects or interstitialcies produced by bombardment with energetic particles, Philosophical Magazine 25(2) (1972) 345-354.
[49] W. Duffin, F. Nichols, The effect of irradiation on diffusion controlled creep processes, Journal of Nuclear Materials 45(4) (1973) 302-316.
[50] P. Heald, M. Speight, Steady-state irradiation creep, Philosophical Magazine 29(5) (1974) 1075-1080.
[51] W. Wolfer, M. Ashkin, Diffusion of vacancies and interstitials to edge dislocations, Journal of Applied Physics 47(3) (1976) 791-800.
[52] F. Garner, 4.02-Radiation Damage in Austenitic Steels," Oxford: Elsevier, 2012, pp. 33-95.
[53] M.B. Toloczko, D.S. Gelles, F.A. Garner, R.J. Kurtz, K. Abe, Irradiation creep and swelling from 400 to 600° C of the oxide dispersion strengthened ferritic alloy MA957, Journal of nuclear materials 329 (2004) 352-355.
[54] J. Wang, M.B. Toloczko, Phase 1 Effort to Produce an Optimized 9-Chromium Ferritic-Martensitic Steel for Transmutation Fast Reactor Fuel Duct, 2015.

[55] M.B. Toloczko, 17th International Symposium on Effects of Rad. On Materials STP1270, 1996.
[56] A. Rowcliffe, J. Robertson, R. Klueh, K. Shiba, D. Alexander, M. Grossbeck, S. Jitsukawa, Fracture toughness and tensile behavior of ferritic–martensitic steels irradiated at low temperatures, Journal of nuclear materials 258 (1998) 1275-1279.
[57] T.S. Byun, M. Li, K. Farrell, Dose Dependence of Strength After Low-Temperature Irradiation in Metallic Materials, Metallurgical and Materials Transactions A 44(1) (2013) 84-93.
[58] T.S. Byun, W.D. Lewis, M.B. Toloczko, S.A. Maloy, Impact properties of irradiated HT9 from the fuel duct of FFTF, Journal of Nuclear Materials 421(1) (2012) 104-111.
[59] R. Klueh, K. Shiba, M. Sokolov, Embrittlement of irradiated ferritic/martensitic steels in the absence of irradiation hardening, Journal of Nuclear Materials 377(3) (2008) 427-437.
[60] R.S. Nelson, D.J. Mazey, J.A. Hudson, The use of ion accelerators to simulate fast neutron-induced voidage in metals, Journal of Nuclear Materials 37(1) (1970) 1-12.
[61] C. Cawthorne, E. Fulton, Voids in irradiated stainless steel, Nature 216(5115) (1967) 575-576.
[62] G.L. Kulcinski, J. Laidler, D. Doran, Simulation of high fluence fast neutron damage with heavy ion bombardment, Radiation Effects 7(3-4) (1971) 195-202.
[63] proceedings of the workshop on correlation of neutron and charged particle damage, in: J. Stiegler (Ed.) Oak Ridge National Laboratory, 1976.
[64] F. Garner, R. Powell, D. Keefer, Summary report on the alloy development intercorrelation program experiment, Hanford Engineering Development Lab., Richland, Wash.(USA), 1977.
[65] F. Garner, H. Brager, Swelling of austenitic Fe-Ni-Cr ternary alloys during fast neutron irradiation, Hanford Engineering Development Lab., Richland, WA (USA), 1984.

[66] W.G. Johnston, J.H. Rosolowski, A.M. Turkalo, K.D. Challenger, Surface observations of nickel ion-bombarded stainless steels, Scripta Metallurgica 6(10) (1972) 999-1005.
[67] W.G. Johnston, J.H. Rosolowski, A.M. Turkalo, T. Lauritzen, Nickel ion bombardment of type 304 stainless steel: Comparison with fast reactor swelling data, Journal of Nuclear Materials 47(2) (1973) 155-167.
[68] W. Johnston, T. Lauritzen, J. Rosolowski, A. Turkalo, Void swelling in fast reactor materials: a metallurgical problem.[Fe--Cr--Ni], J. Met.;(United States) 28(6) (1976).
[69] W. Johnston, T. Lauritzen, J. Rosolowski, A. Turkalo, Effect of metallurgical variables on void swelling, General Electric Co., Sunnyvale, CA (USA). Fast Breeder Reactor Dept., 1976.
[70] W. Johnston, J. Rosolowski, A. Turkalo, T. Lauritzen, An experimental survey of swelling in commercial Fe-Cr-Ni alloys bombarded with 5 MeV Ni Ions, Journal of Nuclear Materials 54(1) (1974) 24-40.
[71] R. Bullough, T.M. Quigley, The correlation of electron, heavy-ion and fast-neutron irradiation damage in M316 steel, Journal of Nuclear Materials 113(2) (1983) 179-191.
[72] D. Gilbon, C. Rivera, Behaviour of different ferritic steels under ion, electron and fast neutron irradiation, Journal of Nuclear Materials 155 (1988) 1268-1273.
[73] D.J. Mazey, Fundamental aspects of high-energy ion-beam simulation techniques and their relevance to fusion materials studies, Journal of Nuclear Materials 174(2) (1990) 196-209.
[74] K. Farrell, M.B. Lewis, N.H. Packan, Simultaneous bombardment with helium, hydrogen, and heavy ions to simulate microstructural damage from fission or fusion neutrons, Scripta Metallurgica 12(12) (1978) 1121-1124.
[75] R. Schäublin, M. Victoria, Differences in the microstructure of the F82H ferritic/martensitic steel after proton and neutron irradiation, Journal of Nuclear Materials 283–287, Part 1 (2000) 339-343.
[76] C. Abromeit, Aspects of simulation of neutron damage by ion irradiation, Journal of nuclear materials 216 (1994) 78-96.

[77] J.F. Ziegler, M.D. Ziegler, J.P. Biersack, SRIM–The stopping and range of ions in matter (2010), Nuclear Instruments and Methods in Physics Research Section B: Beam Interactions with Materials and Atoms 268(11) (2010) 1818-1823.
[78] L. Shao, C.-C. Wei, J. Gigax, A. Aitkaliyeva, D. Chen, B.H. Sencer, F.A. Garner, Effect of defect imbalance on void swelling distributions produced in pure iron irradiated with 3.5 MeV self-ions, Journal of Nuclear Materials 453(1) (2014) 176-181.
[79] W.G. Johnston, J.H. Rosolowski, A.M. Turkalo, T. Lauritzen, A direct measurement of gross swelling in nickel-ion-bombarded stainless steel, Journal of Nuclear Materials 46(3) (1973) 273-280.
[80] T. MUROGA, T. MIYAZAWA, T. NAGASAKA, H. WATANABE, Correlation of Microstructural Evolution in V-4Cr-4Ti by Heavy Ion and Neutron Irradiations, Plasma and Fusion Research 11 (2016) 2405007-2405007.
[81] M. Swenson, C. Dolph, J. Wharry, The effects of oxide evolution on mechanical properties in proton-and neutron-irradiated Fe-9% Cr ODS steel, Journal of Nuclear Materials 479 (2016) 426-435.
[82] C.D. Hardie, G.R. Odette, Y. Wu, S. Akhmadaliev, S.G. Roberts, Mechanical properties and plasticity size effect of Fe-6%Cr irradiated by Fe ions and by neutrons, Journal of Nuclear Materials 482 (2016) 236-247.
[83] G. Was, J. Busby, T. Allen, E. Kenik, A. Jensson, S. Bruemmer, J. Gan, A. Edwards, P. Scott, P. Andreson, Emulation of neutron irradiation effects with protons: validation of principle, Journal of nuclear materials 300(2) (2002) 198-216.
[84] G.S. Was, Z. Jiao, A. Van der ven, S. Bruemmer, D. Edwards, Aging and Embrittlement of High Fluence Stainless Steels, Washington, DC, 2012.
[85] G.S. Was, Challenges to the use of ion irradiation for emulating reactor irradiation, Journal of Materials Research 30(09) (2015) 1158-1182.
[86] G. Was, Z. Jiao, E. Getto, K. Sun, A. Monterrosa, S. Maloy, O. Anderoglu, B. Sencer, M. Hackett, Emulation of reactor irradiation damage using ion beams, Scripta Materialia 88 (2014) 33-36.

[87] E. Getto, K. Sun, A.M. Monterrosa, Z. Jiao, M.J. Hackett, G.S. Was, Void swelling and microstructure evolution at very high damage level in self-ion irradiated ferritic-martensitic steels, Journal of Nuclear Materials 480 (2016) 159-176.
[88] J. Gigax, T. Chen, H. Kim, J. Wang, L. Price, E. Aydogan, S. Maloy, D. Schreiber, M. Toloczko, F. Garner, Radiation response of alloy T91 at damage levels up to 1000 peak dpa, Journal of Nuclear Materials 482 (2016) 257-265.
[89] C. Pareige, V. Kuksenko, P. Pareige, Behaviour of P, Si, Ni impurities and Cr in self ion irradiated Fe–Cr alloys–Comparison to neutron irradiation, Journal of Nuclear Materials 456 (2015) 471-476.
[90] J. Ribis, E. Bordas, P. Trocellier, Y. Serruys, Y. de Carlan, A. Legris, Comparison of the neutron and ion irradiation response of nano-oxides in oxide dispersion strengthened materials, Journal of Materials Research 30(14) (2015) 2210-2221.
[91] N.A. Bailey, E. Stergar, M. Toloczko, P. Hosemann, Atom probe tomography analysis of high dose MA957 at selected irradiation temperatures, Journal of Nuclear Materials 459 (2015) 225-234.
[92] M. Swenson, J. Wharry, The comparison of microstructure and nanocluster evolution in proton and neutron irradiated Fe–9% Cr ODS steel to 3 dpa at 500° C, Journal of Nuclear Materials 467 (2015) 97-112.
[93] P. Gilman, J. Benjamin, Mechanical alloying, Annual review of materials science 13(1) (1983) 279-300.
[94] G. Odette, M. Alinger, B. Wirth, Recent developments in irradiation-resistant steels, Annu. Rev. Mater. Res. 38 (2008) 471-503.
[95] L. Mansur, Theory and experimental background on dimensional changes in irradiated alloys, Journal of Nuclear Materials 216 (1994) 97-123.
[96] M.L. Hamilton, D.S. Gelles, R.J. Lobsinger, G.D. Johnson, W.F. Brown, M.M. Paxton, A.J. Puigh, C.R. Eiholzer, C. Martinez, M.A. Blotter, Fabrication Technological Development of the Oxide Dispersion Strengthened Alloy MA957 for Fast Reactor Applications, 2000.

[97] M.L. Hamilton, D.S. Gelles, R.J. Lobsinger, M.M. Paxton, W.F. Brown, Fabrication Technology for ODS alloy MA957, 2000.
[98] P. Dubuisson, Y. de Carlan, V. Garat, M. Blat, ODS ferritic/martensitic alloys for sodium fast reactor fuel pin cladding, Journal of Nuclear Materials 428(1) (2012) 6-12.
[99] J. Wang, M.B. Toloczko, Continued Microstructural Studies on Neutron Irradiated MA957, FCRD-FUEL-2016-XXXXXX, 2016.
[100] M.B. Toloczko, D.S. Gelles, F.A. Garner, R.J. Kurtz, K. Abe, Irradiation creep and swelling from 400 to 600 C of the oxide dispersion strengthened ferritic alloy MA957, Journal of nuclear materials 329 (2004) 352-355.
[101] S. Yamashita, N. Akasaka, S. Ukai, S. Ohnuki, Microstructural development of a heavily neutron-irradiated ODS ferritic steel (MA957) at elevated temperature, Journal of Nuclear Materials 367 (2007) 202-207.
[102] J. Ribis, S. Lozano-Perez, Nano-cluster stability following neutron irradiation in MA957 oxide dispersion strengthened material, Journal of Nuclear Materials 444(1) (2014) 314-322.
[103] M.J. Alinger, G.R. Odette, D.T. Hoelzer, The development and stability of Y–Ti–O nanoclusters in mechanically alloyed Fe–Cr based ferritic alloys, Journal of Nuclear Materials 329–333, Part A (2004) 382-386.
[104] H. Sakasegawa, M. Tamura, S. Ohtsuka, S. Ukai, H. Tanigawa, A. Kohyama, M. Fujiwara, Precipitation behavior of oxide particles in mechanically alloyed powder of oxide-dispersion-strengthened steel, Journal of Alloys and Compounds 452(1) (2008) 2-6.
[105] H. Sakasegawa, L. Chaffron, F. Legendre, L. Boulanger, T. Cozzika, M. Brocq, Y. De Carlan, Correlation between chemical composition and size of very small oxide particles in the MA957 ODS ferritic alloy, Journal of Nuclear Materials 384(2) (2009) 115-118.
[106] A. Hirata, T. Fujita, Y. Wen, J. Schneibel, C.T. Liu, M. Chen, Atomic structure of nanoclusters in oxide-dispersion-strengthened steels, Nature materials 10(12) (2011) 922-926.

[107] M.C. Brandes, L. Kovarik, M.K. Miller, M.J. Mills, Morphology, structure, and chemistry of nanoclusters in a mechanically alloyed nanostructured ferritic steel, Journal of Materials Science 47(8) (2012) 3913-3923.
[108] Y. Wu, E. Haney, N. Cunningham, G. Odette, Transmission electron microscopy characterization of the nanofeatures in nanostructured ferritic alloy MA957, Acta Materialia 60(8) (2012) 3456-3468.
[109] M.J. Alinger, G.R. Odette, D.T. Hoelzer, On the role of alloy composition and processing parameters in nanocluster formation and dispersion strengthening in nanostuctured ferritic alloys, Acta Materialia 57(2) (2009) 392-406.
[110] C.A. Williams, G.D.W. Smith, E.A. Marquis, Quantifying the composition of yttrium and oxygen rich nanoparticles in oxide dispersion strengthened steels, Ultramicroscopy 125 (2013) 10-17.
[111] E. Aydogan, N. Almirall, G.R. Odette, S.A. Maloy, O. Anderoglu, L. Shao, J.G. Gigax, L. Price, D. Chen, T. Chen, F.A. Garner, Y. Wu, P. Wells, J.J. Lewandowski, D.T. Hoelzer, Stability of nanosized oxides in ferrite under extremely high dose self ion irradiations, Journal of Nuclear Materials 486 (2017) 86-95.
[112] M.K. Miller, D.T. Hoelzer, Effect of neutron irradiation on nanoclusters in MA957 ferritic alloys, Journal of Nuclear Materials 418(1) (2011) 307-310.
[113] B. Gault, M.P. Moody, F. De Geuser, A. La Fontaine, L.T. Stephenson, D. Haley, S.P. Ringer, Spatial resolution in atom probe tomography, Microscopy and Microanalysis 16(01) (2010) 99-110.
[114] B. Gault, M.P. Moody, J.M. Cairney, S.P. Ringer, Atom probe microscopy, Springer Science & Business Media2012.
[115] B. Gault, D. Haley, F. De Geuser, M. Moody, E. Marquis, D. Larson, B. Geiser, Advances in the reconstruction of atom probe tomography data, Ultramicroscopy 111(6) (2011) 448-457.
[116] P. Bas, A. Bostel, B. Deconihout, D. Blavette, A general protocol for the reconstruction of 3D atom probe data, Applied Surface Science 87 (1995) 298-304.

[117] B. Geiser, D. Larson, E. Oltman, S. Gerstl, D. Reinhard, T. Kelly, T. Prosa, Wide-field-of-view atom probe reconstruction, Microscopy and Microanalysis 15(S2) (2009) 292-293.
[118] B.P. Geiser, T.F. Kelly, D.J. Larson, J. Schneir, J.P. Roberts, Spatial distribution maps for atom probe tomography, Microscopy and Microanalysis 13(6) (2007) 437-447.
[119] E.A. Marquis, F. Vurpillot, Chromatic aberrations in the field evaporation behavior of small precipitates, Microscopy and microanalysis 14(06) (2008) 561-570.
[120] D. Larson, E. Marquis, P. Rice, T. Prosa, B. Geiser, S.-H. Yang, S. Parkin, Manganese diffusion in annealed magnetic tunnel junctions with MgO tunnel barriers, Scripta Materialia 64(7) (2011) 673-676.
[121] K. Torres, B. Geiser, M. Moody, S. Ringer, G. Thompson, Field evaporation behavior in [001] FePt thin films, Ultramicroscopy 111(6) (2011) 512-517.
[122] T. Petersen, S. Ringer, Electron tomography using a geometric surface-tangent algorithm: Application to atom probe specimen morphology, Journal of Applied Physics 105(10) (2009) 103518.
[123] F. Vurpillot, M. Gilbert, B. Deconihout, Towards the three‐dimensional field ion microscope, Surface and interface analysis 39(2‐3) (2007) 273-277.
[124] D. Edwards, M. Toloczko, Microstructural Changes in a Highly Irradiated ODS Ferritic MA957 Alloy, Microscopy and Microanalysis 21(S3) (2015) 1019-1020.
[125] Structural Material Irradiations in FFTF, Hanford Engineering Development Lab, Richland, WA(USA), 1985.
[126] A.G. Certain, M.B. Toloczko, Report on FY12 MA957 ODS Ferritic Alloy Microstructure Examinations, FCR&D-XXXX-2013-XXXXXX, 2013.
[127] M.B. Toloczko, Report on FY14 TEM Characterization of Unirradiated MA957 at PNNL, FCR&D-XXXX-2014-XXXXXX, 2014.
[128] K. Thompson, D. Lawrence, D. Larson, J. Olson, T. Kelly, B. Gorman, In situ site-specific specimen preparation for atom probe tomography, Ultramicroscopy 107(2) (2007) 131-139.

[129] M.K. Miller, K.F. Russell, K. Thompson, R. Alvis, D.J. Larson, Review of atom probe FIB-based specimen preparation methods, Microscopy and Microanalysis 13(06) (2007) 428-436.
[130] N.A. Bailey, E. Stergar, M. Toloczko, P. Hosemann, Atom Probe Tomography Analysis of High Dose MA957 at Selected Irradiation Temperatures, Journal of Nuclear Materials (2015).
[131] O.C. Hellman, J.A. Vandenbroucke, J. Rüsing, D. Isheim, D.N. Seidman, Analysis of three-dimensional atom-probe data by the proximity histogram, Microscopy and Microanalysis 6(05) (2000) 437-444.
[132] J.P. Wharry, M.J. Swenson, K.H. Yano, A review of the irradiation evolution of dispersed oxide nanoparticles in the b.c.c. Fe-Cr system: Current understanding and future directions, Journal of Nuclear Materials 486 (2017) 11-20.
[133] M. Bachhav, G. Robert Odette, E.A. Marquis, α′ precipitation in neutron-irradiated Fe–Cr alloys, Scripta Materialia 74 (2014) 48-51.
[134] G. Bonny, D. Terentyev, L. Malerba, On the α – α′ miscibility gap of Fe–Cr alloys, Scripta Materialia 59(11) (2008) 1193-1196.
[135] A. Alamo, V. Lambard, X. Averty, M.H. Mathon, Assessment of ODS-14%Cr ferritic alloy for high temperature applications, Journal of Nuclear Materials 329–333, Part A (2004) 333-337.
[136] J. Ribis, S. Lozano-Perez, Orientation relationships and interface structure of α′-Cr nanoclusters embedded in α-Fe matrix after α – α′ demixing in neutron irradiated Oxide Dispersion Strengthened material, Materials Letters 74 (2012) 143-146.
[137] E.A. Marquis, S. Lozano-Perez, V. De Castro, Effects of heavy-ion irradiation on the grain boundary chemistry of an oxide-dispersion strengthened Fe–12wt.% Cr alloy, Journal of Nuclear Materials 417(1) (2011) 257-261.
[138] A. Brailsford, R. Bullough, M. Hayns, Point defect sink strengths and void-swelling, Journal of Nuclear Materials 60(3) (1976) 246-256.
[139] R. Bullough, M.R. Hayns, M.H. Wood, Sink strengths for thin film surfaces and grain boundaries, Journal of Nuclear Materials 90(1) (1980) 44-59.

[140] D.R. Olander, Fundamental aspects of nuclear reactor fuel elements, California Univ., Berkeley (USA). Dept. of Nuclear Engineering, 1976.
[141] N. Cunningham, Y. Wu, D. Klingensmith, G.R. Odette, On the remarkable thermal stability of nanostructured ferritic alloys, Materials Science and Engineering: A 613 (2014) 296-305.
[142] R.E. Stoller, S.I. Golubov, C. Domain, C.S. Becquart, Mean field rate theory and object kinetic Monte Carlo: A comparison of kinetic models, Journal of Nuclear Materials 382(2–3) (2008) 77-90.
[143] S. Yamashita, K. Oka, S. Ohnuki, N. Akasaka, S. Ukai, Phase stability of oxide dispersion-strengthened ferritic steels in neutron irradiation, Journal of Nuclear Materials 307–311, Part 1 (2002) 283-288.
[144] J.P. Wharry, Z. Jiao, G.S. Was, Application of the inverse Kirkendall model of radiation-induced segregation to ferritic–martensitic alloys, Journal of Nuclear Materials 425(1) (2012) 117-124.
[145] S. Choudhury, L. Barnard, J. Tucker, T. Allen, B. Wirth, M. Asta, D. Morgan, Ab-initio based modeling of diffusion in dilute bcc Fe–Ni and Fe–Cr alloys and implications for radiation induced segregation, Journal of Nuclear Materials 411(1) (2011) 1-14.
[146] S. Huang, D.L. Worthington, M. Asta, V. Ozolins, G. Ghosh, P.K. Liaw, Calculation of impurity diffusivities in α-Fe using first-principles methods, Acta Materialia 58(6) (2010) 1982-1993.
[147] M.I. Mendelev, Y. Mishin, Molecular dynamics study of self-diffusion in bcc Fe, Physical Review B 80(14) (2009) 144111.
[148] Y.N. Osetsky, A. Serra, Vacancy and interstitial diffusion in bcc-Fe, Defect and Diffusion Forum, 1997, pp. 155-160.
[149] A.W. Bowen, G.M. Leak, Diffusion in Bcc iron base alloys, Metallurgical Transactions 1(10) (1970) 2767-2773.
[150] N. Soneda, T. Diaz de La Rubia, Migration kinetics of the self-interstitial atom and its clusters in bcc Fe, Philosophical Magazine A 81(2) (2001) 331-343.

[151] S. Takaki, J. Fuss, H. Kuglers, U. Dedek, H. Schultz, The resistivity recovery of high purity and carbon doped iron following low temperature electron irradiation, Radiation Effects 79(1-4) (1983) 87-122.
[152] C. Hin, B. Wirth, J. Neaton, Formation of Y 2 O 3 nanoclusters in nanostructured ferritic alloys during isothermal and anisothermal heat treatment: A kinetic Monte Carlo study, Physical Review B 80(13) (2009) 134118.
[153] D. Murali, B.K. Panigrahi, M.C. Valsakumar, C.S. Sundar, Diffusion of Y and Ti/Zr in bcc iron: A first principles study, Journal of Nuclear Materials 419(1–3) (2011) 208-212.
[154] C. Hin, B.D. Wirth, Formation of Y 2 O 3 nanoclusters in nano-structured ferritic alloys: Modeling of precipitation kinetics and yield strength, Journal of Nuclear Materials 402(1) (2010) 30-37.
[155] P. Klugkist, C. Herzig, Tracer diffusion of titanium in α - iron, Physica status solidi (a) 148(2) (1995) 413-421.
[156] C. Nellis, C. Hin, Radiation induced segregation in quaternary Fe-Ti-Y-O alloys, Journal of Alloys and Compounds 701 (2017) 82-93.
[157] R.S. Nelson, J.A. Hudson, D.J. Mazey, The stability of precipitates in an irradiation environment, Journal of Nuclear Materials 44(3) (1972) 318-330.
[158] A. Barbu, G. Martin, Radiation induced precipitation in nickel silicon solid solutions: Dose rate effects, Scripta Metallurgica 11(9) (1977) 771-775.
[159] K.Y. Liou, P. Wilkes, The radiation disorder model of phase stability, Journal of Nuclear Materials 87(2) (1979) 317-330.
[160] P. Wilkes, Phase stability under irradiation — a review of theory and experiment, Journal of Nuclear Materials 83(1) (1979) 166-175.
[161] G. Martin, Phase stability under irradiation: Ballistic effects, Physical Review B 30(3) (1984) 1424-1436.
[162] C.F. Bilsby, A theoretical examination of the effect of irradiation-enhanced dissolution on diffusion-controlled coarsening kinetics, Journal of Nuclear Materials 55(2) (1975) 125-133.

[163] F.S. Ham, Theory of diffusion-limited precipitation, Journal of Physics and Chemistry of Solids 6(4) (1958) 335-351.
[164] A. Baldan, Review progress in Ostwald ripening theories and their applications to nickel-base superalloys Part I: Ostwald ripening theories, Journal of materials science 37(11) (2002) 2171-2202.
[165] H.Y. Xiao, F. Gao, W.J. Weber, Threshold displacement energies and defect formation energies in Y 2 Ti 2 O 7, Journal of Physics: Condensed Matter 22(41) (2010) 415801.
[166] C. Hin, B.D. Wirth, Formation of oxide nanoclusters in nanostructured ferritic alloys during anisothermal heat treatment: A kinetic Monte Carlo study, Materials Science and Engineering: A 528(4–5) (2011) 2056-2061.
[167] A.D. Brailsford, Precipitate re-solution in low dose irradiations, Journal of Nuclear Materials 91(1) (1980) 221-222.
[168] H.J. Frost, K.C. Russell, Recoil resolution and particle stability under irradiation, Journal of Nuclear Materials 104 (1981) 1427-1432.
[169] H.J. Frost, K.C. Russell, Particle stability with recoil resolution, Acta Metallurgica 30(5) (1982) 953-960.
[170] D.S. Gelles, F.A. Garner, An experimental method to determine the role of helium in neutron-induced microstructural evolution, Journal of Nuclear Materials 85 (1979) 689-693.
[171] H. Okamoto, Comment on Fe-Y (Iron-Yttrium), Journal of phase equilibria 16(5) (1995) 473-473.
[172] J.W. Christian, The theory of transformations in metals and alloys, Newnes2002.
[173] K.C. Russell, The theory of void nucleation in metals, Acta Metallurgica 26(10) (1978) 1615-1630.
[174] A. Claisse, P. Olsson, First-principles calculations of (Y, Ti, O) cluster formation in body centred cubic iron-chromium, Nuclear Instruments and Methods in Physics Research Section B: Beam Interactions with Materials and Atoms 303 (2013) 18-22.

[175] A. Certain, S. Kuchibhatla, V. Shutthanandan, D. Hoelzer, T. Allen, Radiation stability of nanoclusters in nano-structured oxide dispersion strengthened (ODS) steels, Journal of Nuclear Materials 434(1) (2013) 311-321.
[176] J. He, F. Wan, K. Sridharan, T.R. Allen, A. Certain, V. Shutthanandan, Y. Wu, Stability of nanoclusters in 14YWT oxide dispersion strengthened steel under heavy ion-irradiation by atom probe tomography, Journal of Nuclear Materials 455(1) (2014) 41-45.
[177] C.K. Dolph, D.J. da Silva, M.J. Swenson, J.P. Wharry, Plastic zone size for nanoindentation of irradiated Fe–9%Cr ODS, Journal of Nuclear Materials 481 (2016) 33-45.
[178] K. Yano, M. Swenson, Y. Wu, J. Wharry, TEM in situ micropillar compression tests of ion irradiated oxide dispersion strengthened alloy, Journal of Nuclear Materials 483 (2017) 107-120.
[179] G. Pells, The temperature dependence of the threshold displacement energy in MgO, Radiation Effects 64(1-4) (1982) 71-75.
[180] S.J. Zinkle, C. Kinoshita, Defect production in ceramics, Journal of Nuclear Materials 251 (1997) 200-217.
[181] E.A. Marquis, Core/shell structures of oxygen-rich nanofeatures in oxide-dispersion strengthened Fe–Cr alloys, Applied Physics Letters 93(18) (2008) 181904.
[182] D. Doran, G. Odette, R. Simons, L. Mansur, Damage correlation in theory and practice, Hanford Engineering Development Lab., Richland, Wash.(USA); California Univ., Santa Barbara (USA); Oak Ridge National Lab., Tenn.(USA), 1977.
[183] L.K. Mansur, Theory of transitions in dose dependence of radiation effects in structural alloys, Journal of Nuclear Materials 206(2) (1993) 306-323.
[184] T. Chen, J.G. Gigax, L. Price, D. Chen, S. Ukai, E. Aydogan, S. Maloy, F. Garner, L. Shao, Temperature dependent dispersoid stability in ion-irradiated ferritic-martensitic dual-phase oxide-dispersion-strengthened alloy: Coherent interfaces vs. incoherent interfaces, Acta Materialia 116 (2016) 29-42.

[185] T. Chen, E. Aydogan, J.G. Gigax, D. Chen, J. Wang, X. Wang, S. Ukai, F. Garner, L. Shao, Microstructural changes and void swelling of a 12Cr ODS ferritic-martensitic alloy after high-dpa self-ion irradiation, Journal of Nuclear Materials 467 (2015) 42-49.
[186] P.D. Edmondson, A. London, A. Xu, D.E.J. Armstrong, S.G. Roberts, Small-scale characterisation of irradiated nuclear materials: Part I – Microstructure, Journal of Nuclear Materials 462 (2015) 369-373.
[187] M.L. Lescoat, J. Ribis, Y. Chen, E.A. Marquis, E. Bordas, P. Trocellier, Y. Serruys, A. Gentils, O. Kaïtasov, Y. de Carlan, A. Legris, Radiation-induced Ostwald ripening in oxide dispersion strengthened ferritic steels irradiated at high ion dose, Acta Materialia 78 (2014) 328-340.
[188] R. Cauvin, G. Martin, Solid solutions under irradiation. I. A model for radiation-induced metastability, Physical Review B 23(7) (1981) 3322-3332.
[189] J.-L. Bocquet, G. Martin, Irradiation-induced precipitation: A thermodynamical approach, Journal of Nuclear Materials 83(1) (1979) 186-199.
[190] J.J. Penisten, The mechanism of radiation-induced segregation in ferritic-martensitic steels, The University of Michigan, 2012.
[191] J.P. Wharry, G.S. Was, The mechanism of radiation-induced segregation in ferritic–martensitic alloys, Acta Materialia 65 (2014) 42-55.
[192] G.S. Was, J.P. Wharry, B. Frisbie, B.D. Wirth, D. Morgan, J.D. Tucker, T.R. Allen, Assessment of radiation-induced segregation mechanisms in austenitic and ferritic–martensitic alloys, Journal of Nuclear Materials 411(1) (2011) 41-50.
[193] J.P. Wharry, G.S. Was, A systematic study of radiation-induced segregation in ferritic–martensitic alloys, Journal of Nuclear Materials 442(1–3) (2013) 7-16.
[194] O. Senninger, F. Soisson, E. Martínez, M. Nastar, C.-C. Fu, Y. Bréchet, Modeling radiation induced segregation in iron–chromium alloys, Acta Materialia 103 (2016) 1-11.
[195] L. Messina, M. Nastar, T. Garnier, C. Domain, P. Olsson, Exact ab initio transport coefficients in bcc $\mathrm{Fe}\ensuremath{-}X$ ($X=\mathrm{Cr}$,

Cu, Mn, Ni, P, Si) dilute alloys, Physical Review B 90(10) (2014) 104203.
[196] G. Martin, Phase stability under irradiation: Ballistic effects, Physical Review B 30(3) (1984) 1424.
[197] L.K. Mansur, Correlation of neutron and heavy-ion damage, Journal of Nuclear Materials 78(1) (1978) 156-160.
[198] K.C. Russell, Phase stability under irradiation, Progress in Materials Science 28(3) (1984) 229-434.